Ion Acceleration Mechanisms of Helicon Thrusters

A Dissertation
Presented to
The Academic Faculty

By

Logan Todd Williams

In Partial Fulfillment
Of the Requirements for the Degree
Doctor of Philosophy in
Aerospace Engineering

Georgia Institute of Technology

May 2013

Ion Acceleration Mechanisms of Helicon Thrusters

Thesis Committee:

Dr. Mitchell L. R. Walker, Advisor
Associate Professor
School of Aerospace Engineering
Georgia Institute of Technology

Dr. Alan W. Wilhite
Langley Professor of the Practice
School of Aerospace Engineering
Georgia Institute of Technology

Dr. Jechiel I. Jagoda
Professor
School of Aerospace Engineering
Georgia Institute of Technology

Dr. Benjamin Longmier
Assistant Professor
School of Aerospace Engineering
University of Michigan

Dr. Jerry M. Seitzman
Professor
School of Aerospace Engineering
Georgia Institute of Technology

Date Approved: March 29, 2013

Be strong and courageous! Do not be afraid; do not be discouraged, for the Lord your God will be with you wherever you go.

Joshua 1:9

ACKNOWLEDGEMENTS

The acknowledgements section is interesting, because it is the first section the reader will see, but it is the last section that I write. I must confess that I've had moments where I daydreamed about writing this, not the least because it would signify completion of this dissertation. Really though, it is because often over the past few years I've been reminded of the impact others have had on me and my progress in this program. The process of completing as large and involved a project as a doctoral dissertation and the associated research is not one that can be done in a vacuum (pun intended), but one where I've been aided by many people over the years. Therefore, as you begin your reading and as I finish my writing, I want to commit to words all those who have made a difference in making this document a reality.

Firstly I want to thank my advisor, Dr. Mitchell Walker, for all the support and guidance for the past seven years. This research has involved the combination of several different disciplines, each requiring considerable time and effort to master, and I want to thank Dr. Walker for having the patience and understanding while I worked through each one. The atmosphere here at HPEPL is one where I've been free to carry out this research from first principles all the way to finished product, and I thank him for his trust and confidence in me to see this work through. Likewise, my thanks to Dr. Jagoda for integrating me into the graduate experience here in the Aerospace Engineering department and assisting me over the years when I had the occasional random question. I also wish to thank the other members of my committee for all their time and effort that they put into this document and their expertise provided. My appreciation also goes to

international members, Gabriella and Sebastiano; you two not only brought technical knowledge, but also broadened our horizons. To Scott "the Swedish King;" if HPEPL were a party, you'd be the life of it. Finally, I salute and thank Gabe, aka "Der Kommissar," "Dr. Moneybags," and "Prof. X." You are a good friend and going through all the ropes of grad school was all the easier having you as a sounding board. You were right Der Kommissar, I will indeed see you on the other side. Everyone, the Lab Tyrant has finished!

There was also network of support I had outside of the lab, and that was my church family at Second Ponce de Leon Baptist Church. Were I to try to list names I'd be here all day, but suffice to say that words cannot express how grateful I am to all of you for your support, love, and prayers. You all believed in me and continually would inquire about my progress, even if the answers gave you headaches. During times of stress you were a place to find peace; during times of success, celebration; during times of frustration, sanity. Thank you all, and know that what you've done will never be forgotten.

Finally I wish to thank my family. My grandparents, for all their support and encouragement, and for showing me what hard work and diligence can do. My brothers, Nathan and Tristan, for never doubting me, but reminding me that I can do anything I set my mind to. My parents, Diane and Jeff, who not only gave encouragement, love, and support, but also a good amount of technical advice. Dad, it was something I always saw in you as a kid, but it took grad school for me to finally realize it: the only way one can ever solve a problem is to just sit down, roll up your sleeves, and do it. The power of perseverance and dogged determination to identify a problem and solve it is what

separates students from engineers. Mom, you always said I'd end up working in fields and waves, and I guess you're right. Thanks for letting me borrow your text books, as well as being Chief Editor of this dissertation. You're probably the only one other than me who will ever read the appendices in their entirety. Thank you all.

TABLE OF CONTENTS

ix

LIST OF TABLES

LIST OF FIGURES

NOMENCLATURE

A_a	=	Anode area
A_c	=	Collector area
$A_{c,eff}$	=	Effective collector area
A_g	=	Grid area
A_p	=	Probe area
a	=	Discharge chamber radius/conductor radius/matched line ratio
B	=	Magnetic flux density
B_0	=	DC magnetic field
b	=	Outer conductor radius
C	=	Capacitance
C'	=	Capacitance per unit length
C_j	=	j^{th} arbitrary constant
C_p	=	Parasitic capacitance
C	=	Wave velocity
D	=	Distance between two conductors in a balanced line
D_i	=	Ion diffusion coefficient
d_a	=	Acceleration grid aperture diameter
d_s	=	Screen grid aperture diameter
E	=	Electric field
E_e	=	Electron energy
e	=	Electron charge, 1.6×10^{-19} C
f	=	RF frequency
G'	=	Conductance per unit length
g	=	Gravitational acceleration, 9.81 m/s^2
H	=	Magnetic field intensity
h_c	=	Height of the Faraday probe collector
h_s	=	Height of the Faraday probe guard ring
I_b	=	Beam current
I	=	Current
I_A	=	Accel grid current
I_a	=	Anode current
I_b	=	Beam current
I_D	=	Discharge current
I_e	=	Electron current
$I_{e,w}$	=	Electron current to the wall
I_F	=	Current of the forward wave
I_i	=	Ion current
$I_{i,w}$	=	Ion current to the wall
I_p	=	Ion production rate
I_R	=	Current of the reflected wave
I_s	=	Screen grid current
I_{sat}	=	Ion saturation current

I_{sp}	=	Specific impulse
I^*	=	Rate of neutral excitation
j	=	Current density
j_{Bohm}	=	Bohm ion current density
j_c	=	Current density at the center of the plume
j_e	=	Ion current density
j_i	=	Electron current density
j_{max}	=	Maximum allowable electron current density
k	=	Axial wave number
k_b	=	Boltzmann's constant, 1.38×10^{-23} m^2-kg/s^2
L	=	Inductance
L'	=	Inductance per unit length
L_A	=	Antenna inductance
L_{ML}	=	Matched line loss
$L_{MML,db}$	=	Mismatched line loss, in dB
l_e	=	Effective sheath length
l_g	=	Grid separation distance
m	=	Wave mode number
m_e	=	Electron mass, 9.11×10^{-31} kg
m_i	=	Ion mass
$\dot{m}$	=	Mass flow rate
$\dot{m}_p$	=	Propellant flow rate
$\dot{m}_i$	=	Ion mass flow rate
N	=	Longitudinal index of refraction/Number of turns
N_a	=	Number of apertures
n_i	=	Ion number density
n_e	=	Electron number density
n_0	=	Neutral number density
n_s	=	Ion number density at the sheath edge
P	=	Perveance
P_{abs}	=	Power absorbed by the plasma
P_{in}	=	Input power
P_{jet}	=	Jet power
P_{RF}	=	RF power
P_t	=	Thrust power
p_b	=	Base pressure
p_g	=	Gauge pressure
p_o	=	Operating pressure
Q	=	Quality factor
q	=	Particle charge
R	=	Resistance/Grid voltage ratio
R'	=	Resistance per unit length
R_A	=	Antenna resistance
R_{AC}	=	AC resistance
R_V	=	Accelerating voltage ratio
r_1	=	Inner radius of a ferrite toroid

r_2	=	Outer radius of a ferrite toroid
r_c	=	Radius of the Faraday probe collector
r_c	=	Inner radius of the Faraday probe guard ring
T	=	Thrust/Transverse wave number/Temperature
T_e	=	Electron temperature
T_{max}	=	Maximum thrust
T_s	=	Grid transparency
t_s	=	Grid thickness
V	=	Voltage
V_A	=	Accel grid voltage
V_a	=	Anode voltage
V_b	=	Beam voltage
V_{ctg}	=	Cathode to ground voltage
V_D	=	Discharge voltage
V_d	=	Volume of the discharge chamber
V_f	=	Floating potential
V_F	=	Voltage of the forward wave
V_p	=	Plasma potential
$V_{p,raw}$	=	Raw plasma potential
V_R	=	Voltage of the reflected wave
V_s	=	Screen grid potential
V_T	=	Total voltage drop between discharge plasma and accel grid
v_a	=	Ion acoustic velocity
v_{Bohm}	=	Bohm velocity
v_e	=	Electron velocity
v_i	=	Ion velocity
v_n	=	Neutral velocity
v_φ	=	Phase velocity
X	=	Reactance
Y'	=	Admittance per unit length
Z	=	Impedance
Z'	=	Impedance per unit length
Z_0	=	Characteristic impedance
Z_A	=	Impedance of the antenna
Z_{eq}	=	Equivalent impedance
Z_C	=	Impedance of the capacitor
Z_L	=	Impedance of the load or inductor
Z_s	=	Impedance of the source
α	=	Wave number/attenuation constant
α_d	=	Divergence half angle
β	=	Phase constant
β_j	=	Wave number of the jth wave solution
δ	=	Skin depth
ε	=	Permittivity of a medium
ε^+	=	Ionization energy

ε^*	=	Excitation energy
ε_0	=	Permittivity of free space, 8.85×10^{-12} A^2-s^4/m^3-kg
φ	=	Sheath potential/propagation phase
φ_a	=	Anode sheath potential
φ_{Bohm}	=	Bohm sheath potential
φ_s	=	Screen sheath potential
φ_w	=	Wall sheath potential
χ	=	Gas correction factor
γ	=	Collisional damping/Plume divergence factor/propagation constant
η_a	=	Anode efficiency
η_d	=	Ion production efficiency
η_m	=	Mass utilization efficiency
η_o	=	Grid optics efficiency
η_T	=	Thrust efficiency
ζ	=	Phase shift at the load
κ_g	=	Gap correction term
λ	=	Mean free path
λ_D	=	Debye length
μ	=	Permeability of a medium/magnetic moment
μ_e	=	Electron collisional mobility
μ_i	=	Ion collisional mobility
μ_r	=	Relative permeability
μ_0	=	Permeability of free space, 1.26×10^{-6} m-kg/s^2
ν_e	=	Electron collision frequency
ν_{en}	=	Electron-neutral collision frequency
ν_{ei}	=	Electron-ion collision frequency
ν_i	=	Ion collision frequency
ρ_i	=	Reflection coefficient for current
ρ_v	=	Reflection coefficient for voltage
σ_i	=	Ionization cross section
σ_{ei}	=	Electron-ion collisional cross section
τ	=	Ion confinement time
ω	=	Angular frequency of the wave
ω_e	=	Electron cyclotron frequency
ω_p	=	Plasma frequency
x, y, z	=	Cartesian coordinate system
r, θ, z	=	Cylindrical coordinate system
r, θ, φ	=	Spherical coordinate system

SUMMARY

Helicon plasma sources are devices that are capable of efficiently producing high density plasmas. There is growing interest in utilizing helicons in space propulsion as an ion thruster or a component thereof. However, it is not yet known if the helicon plasma source is able to function as both an ion source and ion accelerator, or whether an additional ion acceleration stage is required. In order to evaluate the capability of the helicon source to accelerate ions, the acceleration and ionization processes must be decoupled and examined individually. To accomplish this, a case study of two helicon thruster configurations is conducted. The first is an electrodeless design that consists of the helicon plasma source alone, and the second is a helicon ion engine that combines the helicon plasma source with electrostatic grids used in ion engines. The electrodeless configuration is used to examine the structure of the plasma plume and the resulting ion acceleration the plume generates. The gridded configuration is a unique design that utilizes a magnetically shielded anode to bias the discharge plasma potential and electrostatic grids to accelerate the ions. This configuration separates the ionization and ion acceleration mechanisms and allows for individual evaluation not only of ion acceleration, but also of the components of power expenditure and the ion production cost.

In this study, both thruster configurations are fabricated and experimentally characterized. The metrics used to evaluate ion acceleration are ion energy, ion beam current, and the plume divergence half-angle, as these capture the magnitude of ion acceleration and the bulk trajectory of the accelerated ions. The thrust of each

configuration is also measured to compare with the estimated thrust contribution from the accelerated ions. The electrode-less thruster is further studied by measuring the plasma potential, ion number density, and electron temperature inside the discharge chamber and in the plume up to 60 cm downstream and 45 cm radially outward. The two configurations are tested across several operating parameter ranges: 343-600 W RF power, 50-450 G magnetic field strength, 1.0-4.5 mg/s argon flow rate, and the gridded configuration is tested over a 100-600 V discharge voltage range. Most of the operating conditions selected are identical between configurations to allow performance comparisons, although there are several cases where one configuration is tested beyond the other to determine operating parameter effects.

Both configurations are found to have thrust and efficiency below contemporary thrusters of similar power, but the distinction between the performances is in the ion acceleration mechanisms and degree of the power losses. For the gridded variant, the primary losses are under-focusing of the ions due to low grid voltages and poor RF coupling to the plasma. Despite this, the generated ion beam current is in the range of 65-120 mA with ion energies in the hundreds of volts in a collimated beam. In contrast, the loss mechanisms in the electrodeless configuration affect all three performance metrics. The beam current is generally less than 20 mA, which demonstrates few ions are accelerated. Furthermore, those ions that are accelerated have low energies in the range of 20-40 V, restricted by the change in plasma potential across the plume. Finally, these ions are highly divergent due to the formation of regions of high plasma potential that create radial electric fields. In total, few ions are accelerated, while those that are have

low energies and do not form a collimated beam, all of which is prohibitive for propulsive application.

Another basis of comparison between the two configurations is the degree of parametric control of the ion acceleration. Initial performance evaluations can often be mitigated by demonstrable control over the ion acceleration, as it suggests the behavior of the device can be improved through optimization. Variance of the operating parameters of the gridded configuration demonstrated a high degree of control of all three performance metrics. A set of modifications is determined using extrapolation of the empirical data that should increase performance to match other ion engines of similar specifications. In contrast, the electrodeless configuration ehibits negligible control of the performance metrics. There are fewer operational parameters available for variation compared to the gridded configuration, and optimization of one metric often adversely affects another. Furthermore, while ion trajectory is impacted primarily by the magnetic field, it has negligible effect on the beam divergence half-angle. Rather than collimating the plume, an increase in the magnetic field deflects ions at large angles. Therefore while the initially poor performance of the gridded configuration is mitigated by the fact that parametric optimization will yield significant gains, the electrodeless configuration has not such clear pathway for improvement.

A primary benefit to using the gridded configuration in this study is that it separates the ionization and ion acceleration mechanisms and allows for accurate measurement of both. Using measurements of the plasma structure of the helicon plasma source along with performance measurements of the gridded configuration, the ion production cost of the helicon plasma source is estimated. This is the first work where ion beam current is

directly measured without the use of Faraday or Langmuir probes, which can overestimate the ion current and lead to large uncertainties in the ion production cost. Discharge efficiency was found to range from 132-212 eV/ion for argon, the lower bound of which is comparable to the 157 eV/ion in contemporary DC discharges. The upper bound is generally due to high ion loss to the walls and high discharge plasma temperature. Optimization of the discharge chamber is predicted to further decrease the ion production cost below that of DC discharges.

There are three unique contributions of this work. The first is the development and testing of a gridded helicon ion thruster that uses a magnetically shielded anode to bias the thruster discharge plasma. This approach decouples the ionization and ion acceleration processes and allows for individual examination of each. The second is estimation of the ion production cost of a helicon plasma source as an integrated component of a gridded engine. The third contribution is measurement of the structure of the plasma plume of an expanding helicon plasma and the impact of region of high plasma potential on ion trajectory.

CHAPTER I

INTRODUCTION

1.1 Rocket Propulsion

1.1.1 Chemical Propulsion

The basic premise of rocket propulsion is to accelerate a working fluid (the propellant) away from the vehicle along the axis of desired motion. By Newton's third law, as the propellant is accelerated away from the vehicle, the vehicle is propelled in the opposite direction. There are several ways to accelerate the propellant, but the ubiquitous rocket archetype is the chemical engine, which uses the combustion of one or more propellants to generate a high enthalpy fluid which is accelerated through a nozzle to produce thrust. The specific impulse, I_{sp}, of an engine is defined as the thrust per unit mass of propellant normalized by the acceleration due to gravity at sea level.

$$I_{sp} = \frac{T}{\dot{m}g} \tag{1.1}$$

The specific impulse is directly related to the exit velocity of a gas. A fundamental limitation of chemical rockets is that the energy of the exhaust is extracted from the energy of the chemical bonds in the propellant, which places an upper limit on the exhaust velocity. Therefore, if a rocket with high specific impulse is desired, another method must be used to accelerate the propellant.

1.1.2 Electric Propulsion

Electric propulsion (EP) is the concept of using electrical energy, rather than chemical energy, to accelerate the propellant. There are three categories of EP devices based on the method of propellant acceleration: electrothermal, electrostatic, and electromagnetic. Electrothermal thrusters use Ohmic heating through a resistor or an electrical arc to increase the enthalpy of the propellant and expand the gas through a nozzle to create thrust. Electrostatic and electromagnet thrusters ionize the propellant and use either electric fields or the Lorentz force, respectively, to accelerate the ions and generate thrust. A common example of an electrostatic thruster is the ion engine, which uses a series of aligned metallic grids to accelerate ion. Figure 1 shows a picture of a typical ion engine. The common premise in all EP devices is that the exhaust energy of the propellant is not extracted from internal energy, but instead is deposited from an external power source. This implies that the specific impulse has no limit, although in practice it is limited by spacecraft design and power allocation.

Figure 1. 13-cm Xenon Ion Propulsion System (XIPS) thruster.[1]

For electrostatic and electromagnetic EP devices, one of the most critical components is the ion source. Since the most acceleration mechanisms in EP devices only affect ions, such as an electric field, the overall acceleration of the propellant is dependent on the ionization efficiency of the ion source. The vast majority of EP devices use collisional ionization between a cathode and an anode as the ion source. Electrons are created in the cathode and are accelerated towards the anode; neutral propellant is fed into the discharge where the energetic electrons collide with the neutrals, creating ions.

While collisional excitation is well understood, there is potential for improvement over anode-cathode discharge plasmas by moving to a more efficient and flexible ion source. Helicon ion sources offer increased ionization efficiencies and the ability to operate over a wide range of operational parameters and gases. Helicon sources also offer a key capability to adjust electron energy, which can alter the collisional cross section and selectively ionize specific chemical species.[2] This capability is of particular interest in dual-use propellant systems, where a chemical engine is paired with an EP system that share a joint propellant source. A helicon source would allow for a more efficient method of ionization that could ionize the molecular propellant and avoid dissociating the propellant into multiple fragments and waste power. Despite the great potential of helicons and their observed high efficiency as a plasma source, there is limited understanding on the behavior and performance of helicons as part of a propulsion system.

1.2 Helicons and RF Thrusters

1.2.1 Helicon Source

A helicon plasma source is a highly efficient device capable of creating a high density, low temperature plasma using RF waves transmitted from an antenna.[3-9] The RF waves couple to the helicon wave that propagates through a plasma, depositing energy into the plasma. The RF energy is deposited into the free plasma electrons, creating an energy distribution within the electron population. The electron energy distribution function (EEDF) can be manipulated by changing various operational parameters, such as RF power, RF frequency, and applied DC magnetic field strength. Electron-neutral collisions where the electrons have energy exceeding the neutral atom ionization energy result in the creation of an ion-electron pair. Thus for a mixture of propellants, the ion species produced by the helicon source can be tuned by altering the EEDF to target specific ionization energies.

1.2.2 Helicon Thrusters

A helicon thruster is a device that uses a helicon source to create and accelerate ions. There are two approaches to helicon thrusters: a single stage device that creates and accelerates ions simultaneously, or a two-stage device that separates ionization and ion acceleration. Most attempts to create a helicon thruster have focused on the single-stage approach.[10-20] The advantage to this configuration is that it has no electrode exposed to the plasma, and thus erosion, which is one of the primary lifetime determining factors, is greatly mitigated. The problem with this thruster design is that every test has been characterized by a few millinewtons of thrust and efficiency below 3%. Since the helicon

4

plasma source has a high efficiency, the low thrust efficiency is likely created in the ion acceleration stage of the helicon thruster.

In addition to the propulsion research using helicons focused on the helicon source as the entire thruster, there has been some investigation into two-stage helicon thrusters that use an additional ion accelerator in conjunction with a helicon source. The first research efforts were not directed toward propulsion, but instead focused on ion beam generation for general applications using single aperture setups.[21-23] Recently there has been development of thruster systems that combine the helicon plasma source with an additional acceleration stage for the explicit purpose of thrust generation.[24-26] By separating the ion generation and the ion acceleration mechanisms, the two-stage design potentially preserves the high ionization efficiency of the helicon source and avoids the low efficiency apparent in most helicon thrusters. A greater degree of development has been done for two-stage engines that use an inductive RF discharge instead of a helicon discharge.[27-29] Figure 2 shows two examples of RF thrusters. However, research into application of a helicon plasma source in a two-stage thruster design remains limited.
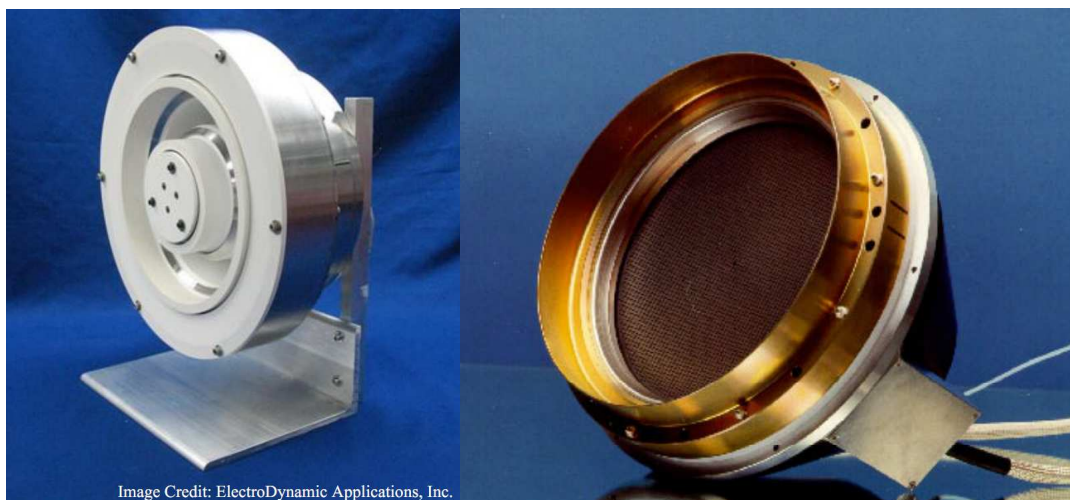
Image Credit: ElectroDynamic Applications, Inc.

Figure 2. Example RF thrusters: the helicon Hall thruster[26] (left) and an RF ion thruster[28] (right)

As a result of the lack of research in the area of helicon thrusters, there is limited experimental measurement of the ion production cost. Thus while the helicon plasma source is theoretically a very efficient ion source, there is very little experimental confirmation. Investigations into the ion production cost is further complicated by the fact that for single-stage helicon thrusters there is no accurate method to directly measure the ion beam current. Previous research relied on measurement of the beam current using multiple planar Langmuir probes downstream,[30] or through measurements of the helicon plasma density using a Langmuir probe and assuming some overall ion diffusion.[31] The difficulty with the first approach is that probes within a plasma form a plasma sheath, which tends to increase collection area and overestimate overall ion current. The second approach neglects the plasma structure, which strongly impacts ion diffusion rates, and assumes an ion exit velocity without direct measurements. Even research into two-stage helicon thrusters has met with difficulty in determining the ion production cost, as the Hall thruster stage allows electron backstreaming to the anode, which prevents accurate measurements of the beam current.[26]

1.3 Problem Statement and Research Aim

While research has been conducted on both single and two-stage thruster approaches, there has been no evaluation of the relative capability for ion acceleration. Most experimental development has focused on one concept or the other without determining the relative merits of each approach. The one example[26] of concurrent work that does examine both single-stage and two-stage helicon thrusters does not fully examine the ion acceleration mechanism of the single-stage configuration. Therefore, the goal of this

work is to determine whether a two-stage thruster design is a more effective design approach to developing a helicon thruster.

1.4 Research Methodology

In order to evaluate the ion acceleration capability of helicon thrusters, two thruster configurations, single-stage and two-stage, are fabricated and tested. The first configuration is a single-stage, electrodeless helicon thruster (EHT) that consists solely of the helicon plasma source. In this device, the presumed ion acceleration mechanism is a current-free double layer that forms near the exit plane of the helicon. While the double layer is reviewed in Chapter II, the mechanism itself is not studied; instead the resulting ion acceleration is the subject of interest. The other configuration is a two-stage gridded helicon ion thruster (GHIT) that combines the helicon plasma source with electrostatic grids to accelerate ions. A magnetically shielded anode is placed within the helicon plasma to collect electrons and bias the discharge plasma. The ion acceleration mechanism in this configuration is the electrostatic potential drop between the helicon plasma and the downstream plume plasma and the electric field between the grids. In order to make the comparison between the two configurations as accurate as possible, both devices utilize the same helicon plasma source. Thus the only difference between the two thrusters is the addition of the acceleration stage of the two-stage variant.

Device feasibility is determined by comparing two qualities: the performance of each thruster and the degree of control over the performance by manipulating operating conditions. Thruster performance provides several direct quantitative metrics for comparison, while performance control is a more qualitative figure of merit that can be

used to compare the relative difficulty to optimize the thruster. As an example, a thruster with substandard performance that demonstrates a highly predictable degree of control is still a feasible design, as it can easily be optimized for a different set of operating conditions. Conversely, a thruster that has higher performance with a much lower degree of control over the thruster behavior can be a liability for design and mission planning purposes.

The chosen ion acceleration performance metrics for the case study are the ion energy, the beam current, and the amount of divergence of the ion beam created. The ion energy quantifies the amount of acceleration each ion undergoes, while the beam current demonstrates the number of ions that can be accelerated. The beam divergence describes the overall trajectory of the ions and degree of beam collimation. While other metrics, such as thrust or specific impulse, are measured as a part of the performance evaluation, they are not used in comparing thruster feasibility. This is due to such metrics being large scale qualities that do not capture how each device accelerates ions, as it is ion acceleration that is the function of interest.

1.5 Research Contributions

This work makes several novel contributions to the field of electric propulsion. The first is the development of a gridded helicon ion thruster that utilizes a magnetically shielded anode to bias the thruster discharge plasma. While inductive RF ion engines have already been developed, this is the first occurrence of an ion engine that incorporates the architecture of a helicon plasma source to create the discharge plasma. Likewise, while magnetically shielded anodes have been used in standard ion engines,

this is the first use of one in conjunction with a helicon plasma source. The presence of the grids separates the ionization and ion acceleration processes and allows individual evaluation of the two.

As a result of the GHIT's unique design, the second contribution this work presents is an accurate estimation of the discharge efficiency of a helicon plasma source. Generally such calculations are difficult to perform, as it requires measurement of the beam current. While such measurements can be done using a Faraday probe, discussed in Chapter V, they are often inaccurate and lead to high uncertainties. The use of grids on the GHIT restricts ion and electron flow such that the beam current can be accurately measured using grid and anode currents. These currents, in addition to measurements of the plasma density and potential structure, allow for accurate modeling of the discharge efficiency and ion production cost of the helicon plasma source.

The final contribution of this work is a 2-D mapping of the plasma characteristics of a helicon plasma inside the discharge chamber and in the plume, as well as the determination of the primary ion acceleration mechanism in a single-stage helicon thruster. Ions are found to be primarily accelerated across a decrease of the plasma potential as the plasma expands downstream of the thruster. Radial electric fields result in high beam divergence. In addition, conical regions of high plasma potential form off of the discharge chamber wall at higher magnetic fields that cause the ions to oscillate along the radial position and lead to increased collisional damping of ion energy.

1.6 Organization

There are four primary sections to this dissertation: background material (Chapters II and III), presentation of thruster configurations, facilities, and diagnostics (Chapters IV and V), performance evaluation and analysis of the EHT (Chapters VI and VII), and performance evaluation and analysis of the GHIT (Chapters VIII and IX).

Chapters II and III provide a brief review of the material to familiarize the reader with the subjects discussed in this work. Chapter II covers helicon plasma sources, helicon wave propagation, coupling modes, and the potential ion acceleration mechanism of the double layer. Chapter III gives a brief review of ion engines, plasma sheaths, gridded ion optics, and calculation of the discharge efficiency.

Chapters IV and V present the design and operation of all experimental hardware used in this work. Chapter IV details the design of the two thruster configurations studied, including the helicon plasma source common between the two and the components added to convert the EHT into the GHIT, as well as a performance model for the GHIT. Chapter V describes the vacuum facilities used to conduct the experiments, as well as the diagnostics used to characterize the two thrusters. Review of each diagnostic instrument includes a summary of the general theory, specifications of the construction, instructions on operation, and calculation of the uncertainty.

Chapters VI and VII present the performance evaluation of the EHT and analysis of the ion acceleration, while Chapters VIII and IX present the same for the GHIT. Chapter VI entails overall EHT performance such as thrust, specific impulse, beam divergence, and ion energy, as well as 2-D spatial mapping of the helicon plasma characteristics. Chapter VII covers the analysis of the ion energies, as well as the effects of the plume

electric field on the ion trajectories at different magnetic fields. Chapter VIII contains the discharge analysis of the GHIT to determine density and temperature, as well as a study of the ion optics as a function of the operating conditions. Plume divergence and thrust are also measured. Chapter IX presents several modifications that can increase the performance of the GHIT. An analysis of the discharge efficiency is also performed.

Finally, Chapter X compares the two thruster configurations and suggests several areas for future work.

CHAPTER II

HELICON PLASMA THEORY

As the aim of this research is to evaluate the ion acceleration capability of helicon thrusters, the helicon plasma source is a fundamental component. In both engine configurations it generates the ions utilized to create thrust, and for the EHT it is also the source of the ion acceleration. Therefore, an understanding of the physics of a helicon plasma source is required to properly design, operate, and characterize either thruster configuration. This chapter serves as an introduction to the four key areas of helicon source design and operation. The first section provides a definition of helicon waves, a description of a helicon plasma source, and a summary of helicon wave propagation. The second section covers energy deposition of RF waves into a plasma, the various coupling modes between the antenna and the plasma, and the transitions between modes. The third section describes Trivelpiece-Gould waves and the potential implications to helicon plasma sources. The fourth section discuses electrodeless helicon thrusters and the current-free double layer as the assumed ion acceleration mechanism.

2.1 Helicon Waves

2.1.1 Definition of Helicon Waves

There are many types of waves that can propagate through a plasma, such as plasma waves, electrostatic waves, electromagnetic waves, and ion acoustic waves.[32] One subset of electromagnetic (EM) waves is called a whistler wave, which is a right-handed,

circularly polarized wave that has a frequency much less than the electron cyclotron frequency. Helicon waves are bounded whistler waves that have a frequency above the lower hybrid frequency such that the electron gyration is neglected and electron motion consists only of the motion of the guiding center.[3] The imposition of a radial boundary condition by the discharge chamber wall changes the nature of the helicon wave from electromagnetic to partially electrostatic.[4] Plasma sources that use helicon waves for ionization are capable of efficiently creating high density, uniform plasmas in low pressure conditions without direct contact of the electrodes to the plasma.[3-9]

2.1.2 Helicon Plasma Source

A helicon plasma source consists of several components: a discharge chamber, an antenna, and a DC magnetic field source. Figure 3 shows a diagram of the helicon plasma source and its constituent components.
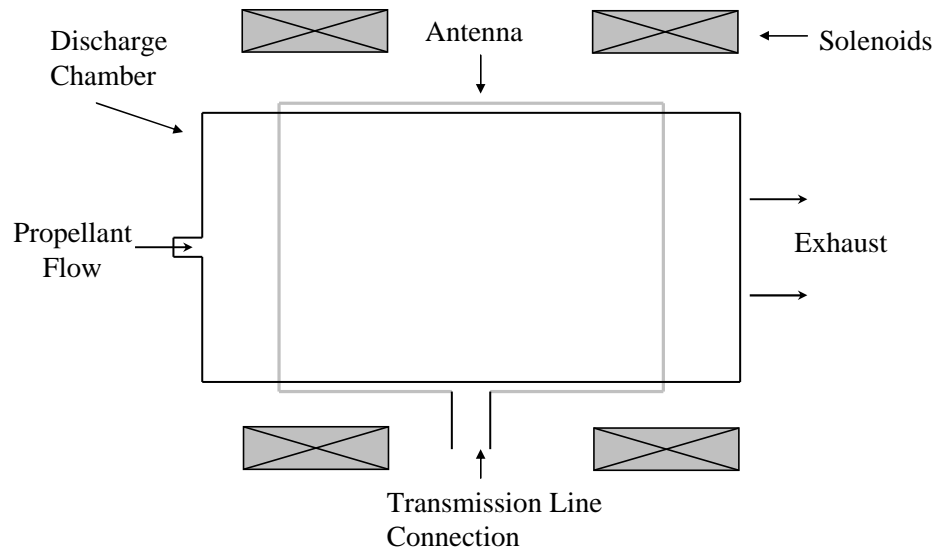
Figure 3. Diagram of a helicon plasma source.

2.1.2.1 Discharge Chamber

The discharge chamber is generally an insulating cylinder open at one end and closed at the other except for a propellant inlet. The insulating walls contain the plasma radially while allowing the RF waves to penetrate into the plasma. The size of the discharge chamber generally sets the axial length of the RF antenna used, and thus the wavelength of the helicon wave propagated. The diameter of the discharge chamber also affects the transition from capacitive coupling to inductive coupling, more of which will be discussed later.

2.1.2.2 RF Antenna

The antenna is a conductor wrapped around the exterior of the discharge chamber, generally made of copper. Four common types of antennas, shown in Figure 4, that are used in helicon research are: three Nagoya type III configurations (straight, right 180º helical, and left 180º helical) and the double saddle antenna. The different antenna configurations excite different helicon wave modes. Straight Nagoya III antennas excite the m = 0 mode; the right and left Nagoya III antennas excite the m = 1 and m = -1 modes, respectively;[33] and the double saddle antenna excites either the m = 0 or the m = 1 mode, depending on the operating conditions.
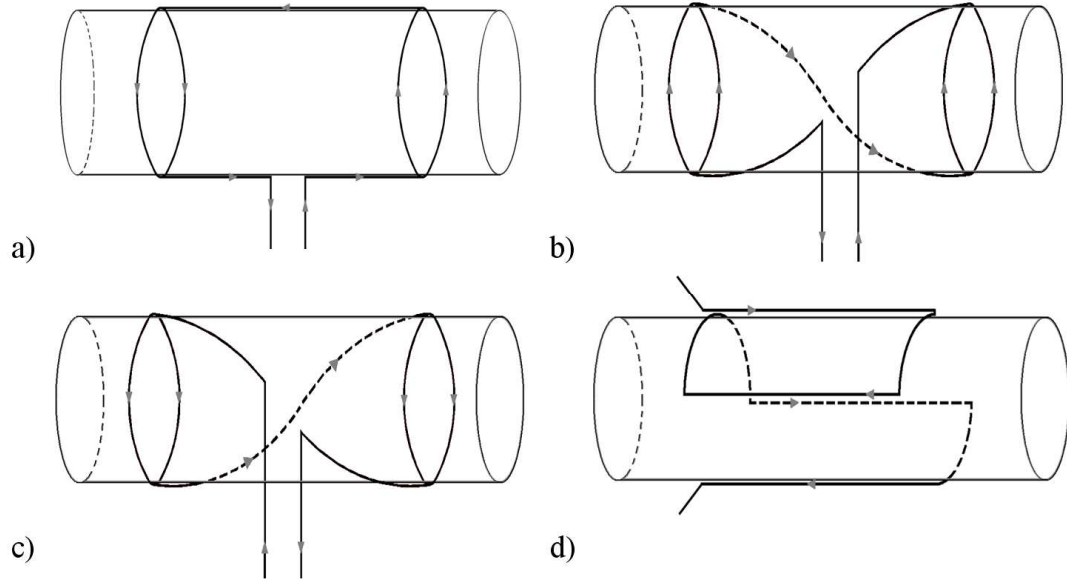
Figure 4. Helicon antenna configurations. (a) Nagoya III, (b) Nagoya III R, (c) Nagoya III L, (d) Double Saddle. Current paths of the antennas are denoted by the arrows.

2.1.2.3 DC Solenoids

The DC magnetic field is supplied by two or more solenoids placed around the discharge chamber. The DC magnetic field serves to restrict electron radial mobility and direct the plasma towards the outlet of the discharge chamber. Reducing radial electron mobility is generally desired to limit wall neutralizations, as this is a loss mechanism that reduces the efficiency of the plasma discharge. In addition, the helicon wave requires the presence of an axial DC magnetic field in order to propagate.

2.1.3 Helicon Wave Propagation

The propagation of the helicon wave is determined from the dispersion relation of the wave. The dispersion relation relates the longitudinal wave number of the helicon wave, k, to the plasma density, n_0, DC magnetic field strength, B_0, RF angular frequency, ω, discharge chamber radius, a, and the mode number of the wave, m. The dispersion relation for a uniform density plasma column with electron mass neglected is given

below in Equation (2.1) with a full derivation in Appendix A, which describes the parameters Z_m and α_m that are derived from Bessel functions.

$$\frac{\omega}{k}\frac{\mu_0 e n_0}{B_0} = \frac{1}{a}\left[\left(\frac{ka}{\alpha_m m}+Z_m\right)^2 + k^2 a^2\right]^{\frac{1}{2}} \tag{2.1}$$

A helicon wave, like all other EM waves, contains an electrostatic and a magnetic component. For the simplest case where the electron mass is neglected, the axial electric field is zero and the radial and azimuthal electric fields are related to the magnetic fields as shown in Equations (2.2) and (2.3) taken from Appendix A.

$$E_r = \frac{\omega}{k}B_\theta \tag{2.2}$$

$$E_\theta = -\frac{\omega}{k}B_r \tag{2.3}$$

At each point the magnetic field is orthogonal to the electric field. The magnetic field components are given by Equations (2.4) and (2.5),

$$\vec{B}_r = C_1 J_{m+1}(Tr) + C_2 J_{m-1}(Tr) \tag{2.4}$$

$$\vec{B}_\theta = iC_1 J_{m-1}(Tr) - iC_2 J_{m+1}(Tr) \tag{2.5}$$

where C_1 and C_2 are constants, T is the transverse wave number, r is the radial distance from the centerline axis of the discharge chamber, and J is Bessel's function of the first

kind of order denoted by the subscript. Substitution of Equations (2.4) and (2.5) into (2.2) and (2.3) results in the components of the electric wave.

$$E_r = \frac{i\omega}{k}\left(C_1 J_{m-1}(Tr) - C_2 J_{m+1}(Tr)\right) \tag{2.6}$$

$$E_\theta = -\frac{\omega}{k}\left(C_1 J_{m+1}(Tr) + C_2 J_{m-1}(Tr)\right) \tag{2.7}$$

Since these functions describe waves, the values of the field strengths oscillate in space and time. Equations (2.4) through (2.7) describe the amplitude of each wave component; the time-dependent value of each wave is defined by the real component of the exponential perturbation. Thus E and B can be described by Equation (2.8).[33]

$$f = fe^{i(m\theta + kz - \omega t)} \tag{2.8}$$

In general there are only three mode numbers of interest, m = -1, 0, 1. Mode numbers beyond this range are often difficult to generate and are not as efficient for plasma production as the other three modes. For the m = ± 1 modes, the field patterns do not change with position but rather with the value of k/α. The field shapes of the m = ± 1 modes are shown in Figure 5. As the wave propagates down the axis of the device, the wave pattern rotates in the positive θ direction for m = 1, and the negative θ direction for m = -1.
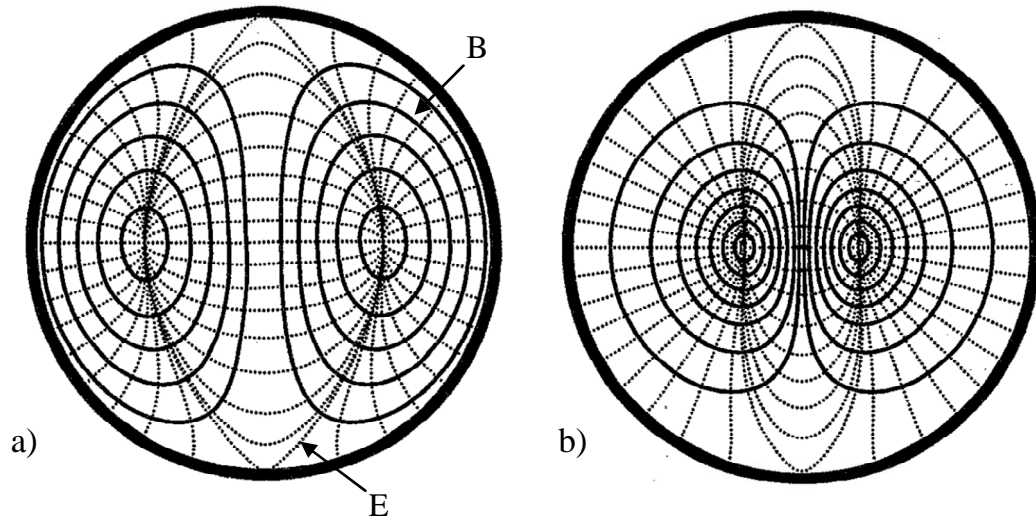
Figure 5. Cross section of the field structure of helicon wave in for (a) m = 1 and (b) m = -1 modes. Solid lines denote magnetic field lines, dotted lines denote electric field lines.[33]

In contrast, the wave shape in the m = 0 mode changes along the axis of propagation. When the quantity $(kz - \omega t)$ is zero, E_r vanishes and the wave becomes purely magnetic. When the quantity equals $\pi/2$, the field becomes purely radial and the wave is electrostatic. For other values, both qualities exist and the wave structure is spiral. Figure 6 shows the progression of these structures as the wave propagates down the axis of the discharge chamber.[3]
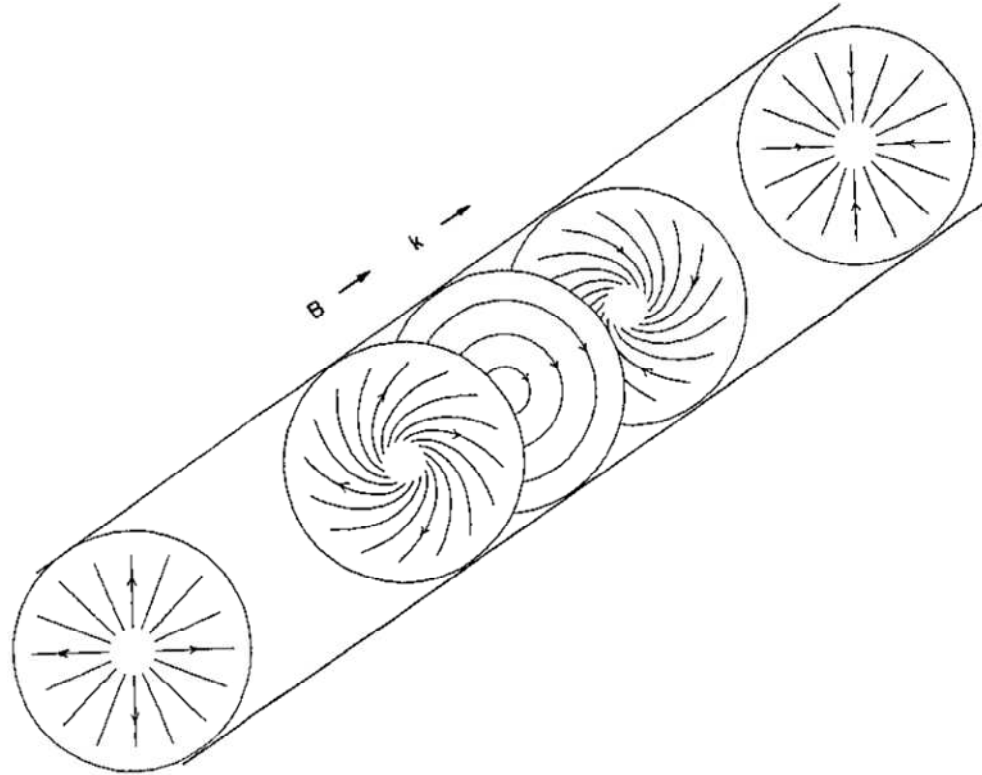
Figure 6. Electric field structure of m = 0 mode.[3]

2.2 Energy Deposition

2.2.1 Overview of Wave Coupling Modes

The formation of a plasma in a helicon source consists of several steps, as there are several coupling modes of plasma operation that are possible.[9-34] In the first mode, the RF wave is called a capacitively coupled plasma (CCP), where the electrostatic field generated between the leads of the antenna strip electrons from the propellant gas. The electric field accelerates these free electrons which then collide with other neutral species to cause additional ionization. This process is predominantly driven by the voltage drop between the electrodes of the antenna (a product of the power transmitted through the antenna) and thus creates only a low density plasma focused at the edge of the containment vessel.[35]

The second mode occurs when the oscillating magnetic field from the antenna couples to the plasma current, creating an inductively coupled plasma (ICP). The antenna thus induces current oscillations within the plasma that deposit energy into free electrons. ICPs have a higher plasma density than CCPs though the plasma is still focused at the edge of the containment vessel where the majority of the wave energy is absorbed.[34] In an ICP plasma only the radial and azimuthal components of the RF magnetic field couple to the plasma, while the axial component cannot penetrate into the plasma.

The final mode, the helicon wave mode, is characterized by the RF wave coupling to the helicon wave propagating down the axis of the device. Plasmas heated by helicon wave coupling differ from CCPs and ICPs by having the density profile peak at the center, rather than at the walls. This results in a radial density profile that is parabolic in appearance with a peak in the center. Figure 7 shows a graphical comparison of the density profiles of the three coupling modes.
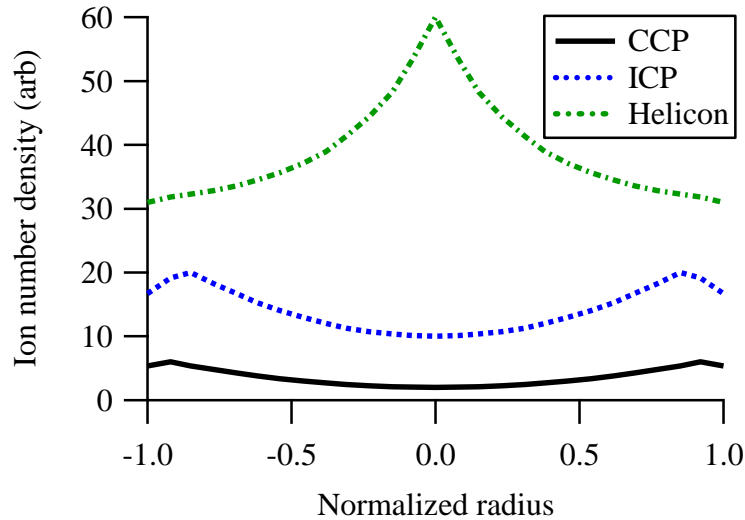
Figure 7. Qualitative radial ion density profiles in a cylindrical plasma chamber for a CCP, an ICP, and a helicon plasma. CCP and ICP tend to have higher densities near the wall, while the helicon mode peaks along the centerline.

Originally it was thought that the power deposition mechanism was Landau damping.[3,4,37-39] Landau damping is a collisionless process where a wave interacts with particles that have similar energy as the wave. For particles with slightly more energy than the wave, the wave gains energy at the expense of the particles; for particles with slightly less energy than the wave, the particles gain energy at the expense of the wave. Since electrons in a helicon plasma generally have a Maxwellian distribution, more of the electrons have low energies than high. Thus the RF wave couples to and drives the helicon wave, which is damped by the plasma through Landau damping, depositing the RF power into the plasma.

While the above theory about Landau damping was the dominant explanation for the efficient operation of the helicon for over ten years, it is now thought Landau damping is insufficient to explain the high energy deposition rate in helicon plasmas. Recent work shows that electrons accelerated by Landau damping are too sparse to explain the high ionization rate.[40] Equations (2.1) through (2.7) are derived under the assumption that the

21

electron mass is negligible. This requires that E_z is equal to zero, which is not satisfied during operation. There are two approaches to correct this: the first is to allow for finite electron mass while enforcing the zero E_z condition, called the transverse electric (TE) approximation; the second approach is to allow finite electron mass and a nonzero E_z, which gives rise to radial electrostatic waves, called Trivelpiece-Gould (TG) waves.[41]

2.2.2 Coupling Mode Transition

The transition from one coupling mode to another occurs when conditions within the plasma change the dominant mechanism for power deposition between the antenna and the plasma. These different modes are reached sequentially as the plasma forms and the transitions between them can be described by thresholds in the device operating parameters.

2.2.2.1 CCP and Plasma Ignition

The first transition is the ignition of a neutral gas to a CCP. Prior to ionization, the propellant gas acts as a dielectric medium, which will not attenuate the RF wave and thus no energy will be absorbed. Suppose a free electron enters a region of an oscillating electric field produced by the antenna. The electron undergoes successive cycles of acceleration and deceleration as the electric field oscillates with time. The time-averaged result is that the electron gains no net energy (excluding the case of an electron cyclotron wave). However, if the electron collides with a neutral atom before the electric field reverses energy is transferred from the electric field to the gas. Therefore energy is only deposited if the electron-neutral mean free path is less than the distance the electron travels before the electric field reverses. The mean free path can be modeled as

$$\lambda = \frac{1}{n_0 \sigma} \tag{2.9}$$

where σ is the collision cross section and n_0 is the number density of the species the electron is colliding with (in this case neutral atoms). The neutral number density can be related to the pressure using the Ideal Gas Law,

$$p = n_0 k_b T \tag{2.10}$$

where T is the temperature of the gas and k_b is Boltzmann's constant. The probability of an electron colliding with a neutral within a certain distance, x, is as follows.

$$f(x) = 1 - e^{-x/\lambda} \tag{2.11}$$

Substituting Equations (2.9) and (2.10) into (2.11) yields a relation between the probability of a collision and the neutral pressure.

$$f(x) = 1 - \exp\left(\frac{-xp\sigma}{k_b T}\right) \tag{2.12}$$

It is seen from Equation (2.12) that there is a pressure dependence of the ability to ignite a plasma from a neutral gas. One requirement for ignition is that the neutral pressure is above some minimum threshold. It is possible to reduce this threshold by

increasing the power of the wave propagated by increasing the voltage across the antenna, and thus the electric field. As the electric field increases, the probability of electron field emission from neutral atoms increases, which also increases the amount of free electrons, and thus the amount of energy absorption. Full ignition occurs when a sufficient number of free electrons exist such that the energy absorbed from the incident wave balances the energy lost due to wall collisions or ion-electron neutralization collisions.

2.2.2.2 ICP

While a CCP attenuates some of the RF wave to absorb energy, most of the wave is still transmitted through the plasma. Transition to an ICP occurs when the majority of the RF wave is absorbed by the plasma. Treating the plasma as a simplified conductor, as the gas is progressively ionized, the conductivity σ, of the plasma increases, which means the skin depth of the plasma, δ, decreases according to Equation (2.13)[42]

$$\delta = \frac{1}{\sqrt{f\pi\mu\sigma}} \qquad (2.13)$$

where f is the frequency of the RF wave and μ is the permeability of the medium (in this case the plasma). The skin depth is a measure of how far through the medium the wave penetrates before it is absorbed. Quantitatively, after a distance of δ into the plasma the amplitude of the electric and magnetic fields have decreased by a factor of 1/e (36.8%). However, a helicon plasma is not a simple conductor and is neither homogenous nor

isotropic, which means the conductivity and permeability are no longer scalar. A more appropriate definition for skin depth of a plasma is

$$\delta = \frac{c}{\sqrt{\omega_p^2 - \omega^2}} \qquad (2.14)$$

where c is the phase velocity of the RF wave, ω is the RF angular frequency, and ω_p is the plasma frequency, defined as

$$\omega_p = \left(\frac{n_0 e^2}{\varepsilon_0 m_e} \right)^{1/2} \qquad (2.15)$$

where ε_0 is the permittivity of free space and m_e is the mass of an electron. The plasma frequency describes sinusoidal oscillations of electrons around an equilibrium position in a plasma relative to the ions. These oscillations arise from perturbations in the plasma displacing the electrons from the equilibrium position and the restoring electric field causing the electrons to overshoot the equilibrium position, shown in Figure 8. The plasma frequency is not dependent on the wave number, which means $d\omega/dk$ (the group velocity) is zero. Therefore, in the absence of collisions, this characteristic plasma oscillation does not propagate.
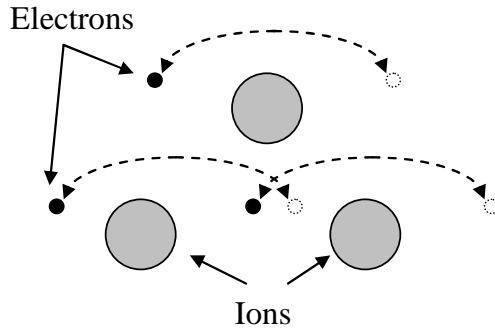
Figure 8. Diagram of plasma oscillations

Returning to the previous discussion, once the skin depth is the same order as the diameter of the plasma column, the magnetic fields generated by the antenna induce oscillating currents in the plasma. As additional free electrons become available, a positive feedback loop occurs, which increases the plasma density until the entire RF wave is absorbed by the plasma. This marks the transition to the inductive mode.

2.2.2.3 Helicon Mode

The transition to helicon mode does not yet have a clear demarcation due to the ambiguities in the coupling mechanism. A commonly used definition for the transition to helicon mode is when the wavelength of the helicon wave is on the order of the length of the antenna, or equivalently of the device itself.[8,34] However, if the primary power coupling mechanism is not related to the helicon wave but to something else, such as TG waves, then this criteria would be inaccurate. Thus, before any meaningful exploration of helicon mode transition can take place, the TG wave must be examined.

2.3 Trivelpiece-Gould Waves

2.3.1 Boundaries, Collisions, and the Rise of Trivelpiece-Gould Waves

Whistler waves are classified as unbounded electromagnetic waves, yet for plasma sources an unbounded geometry is impossible. The primary impact of a radially bounded system is it changes the structure of the waves propagating in the device. Past work by Trivelpiece and Gould (for whom the TG waves are named) found that the presence of a radial boundary caused the propagation of radial space-charge (aka electrostatic) waves to occur.[43] This becomes particularly important when the radial boundary is insulating (as is common with most helicon plasma sources) as it imposes a boundary condition in which the radial current vanishes. In order for this to be possible, a second wave must arise at the edge of the plasma that cancels out the radial current at the plasma boundary – the TG wave.

To begin an investigation into the nature of TG waves, one must first remove two erroneous assumptions: zero axial electric field and zero electron mass. As a result, electrons can now carry and transfer RF energy. The mechanism for this energy transfer is the collisions of electrons with other electrons, as well as with neutrals and ions. Electron collisions change the physics of the plasma in several ways; first, the form of Ohm's Law changes in the derivation of the helicon dispersion relation. The use of this modified Ohm's Law, (derived in Appendix B) brings about an interesting scenario. Instead of a single solution, two solutions appear, each with a distinct wave number β,

$$\beta_{1,2} = \frac{1 \mp \sqrt{1 - 4\alpha\gamma}}{2\gamma} \qquad (2.16)$$

27

with

$$\alpha = \frac{\omega}{k} \frac{\omega_p^2}{\omega_c c^2} \qquad (2.17)$$

$$\gamma = \frac{\omega + i \nu_e}{k \omega_c} \qquad (2.18)$$

$$\omega_c = \frac{e B_0}{m_e} \qquad (2.19)$$

where ν_e is the collision frequency of an electron in the plasma and ω_c is the electron cyclotron frequency. While α corresponds to the wave number derived from the collisionless plasma derivation, γ is a collisional damping term, and ω_c is the electron cyclotron frequency. The electron cyclotron frequency is the frequency electrons will gyrate on a magnetic field line.

A more thorough exploration into the two solutions is done in Appendix B. As a quick summary, the first solution corresponds to the helicon wave, while the second represents a radial electrostatic wave - the TG wave. The operating conditions of the plasma itself determine whether the helicon wave and/or the TG wave can propagate.

2.3.2 Propagation Conditions

In order to examine the boundaries for which each wave can propagate, the assumption of a collisionless plasma is resumed.[44,45] With that assumption, the wave number β must be a real number. The wave number is composed of two components: the

28

longitudinal component, k, which is parallel to the magnetic field, and the transverse component, T, which is orthogonal to the magnetic field.

$$\beta^2 = k^2 + T^2 \tag{2.20}$$

The longitudinal wave number must also be real, as it is quantized by the discharge vessel length L,

$$k \propto \frac{\pi}{L} \tag{2.21}$$

If both the longitudinal and the total wave numbers are real, it follows that the transverse wave number must also be real. Equation (2.16) can therefore be rewritten as

$$T_{1,2}^2 = \frac{\left(1 \mp \sqrt{1 - 4\alpha\gamma}\right)^2 - 4\gamma^2 k^2}{4\gamma^2} \tag{2.22}$$

Equation (2.22) reveals that there are two requirements that must be met for the transverse wave number to be real. First, the discriminant must be positive, and second, is that the right hand side of the equation be positive.

$$1 - 4\alpha\gamma \geq 0 \tag{2.23}$$

$$\frac{\left(1 \mp \sqrt{1 - 4\alpha\gamma}\right)^2 - 4\gamma^2 k^2}{4\gamma^2} \geq 0 \tag{2.24}$$

29

Solving for the case of the helicon wave and substituting in Equation (2.18) for γ, the first requirement is found to be

$$\frac{\alpha\omega}{k\omega_c} \leq \frac{1}{4} \tag{2.25}$$

The second requirement is found by taking a first order Taylor approximation of the radical of Equation (2.24) and solving the inequality.

$$\frac{\alpha}{k} \geq 1 \tag{2.26}$$

Solving the second requirement for the TG wave yields the following.

$$\frac{\omega_c}{\omega} \geq \frac{\alpha}{k} \tag{2.27}$$

Since the electron cyclotron frequency is much greater than the driving frequency while α is of a similar order to k, Equation (2.27) can be considered always true. Thus while the helicon wave has two requirements for propagation, the TG wave only has one.

Using the longitudinal refractive index, N, defined as

$$N = \frac{kc}{\omega} \tag{2.28}$$

30

two parameters can be used to describe the propagation conditions.

$$\alpha_0 = \left(\frac{\omega_p}{N\omega_c}\right)^2 \qquad (2.29)$$

$$\beta_0 = \frac{\omega\omega_c N^2}{\omega_p^2} \qquad (2.30)$$

Substituting Equation (2.29) into (2.25) and (2.30) into (2.26) yields the final propagation conditions.

$$\alpha_0 \leq \frac{1}{4} \qquad (2.31)$$

$$\beta_0 \leq 1 \qquad (2.32)$$

Helicon wave propagation requires fulfillment of both requirements, while a TG wave only needs to satisfy Equation (2.31). These conditions create boundaries for regions of wave propagation in the space of plasma density and magnetic field strength for a fixed axial wave number and angular frequency.[46] Figure 9 shows a qualitative illustration of the propagation boundaries for both waves.
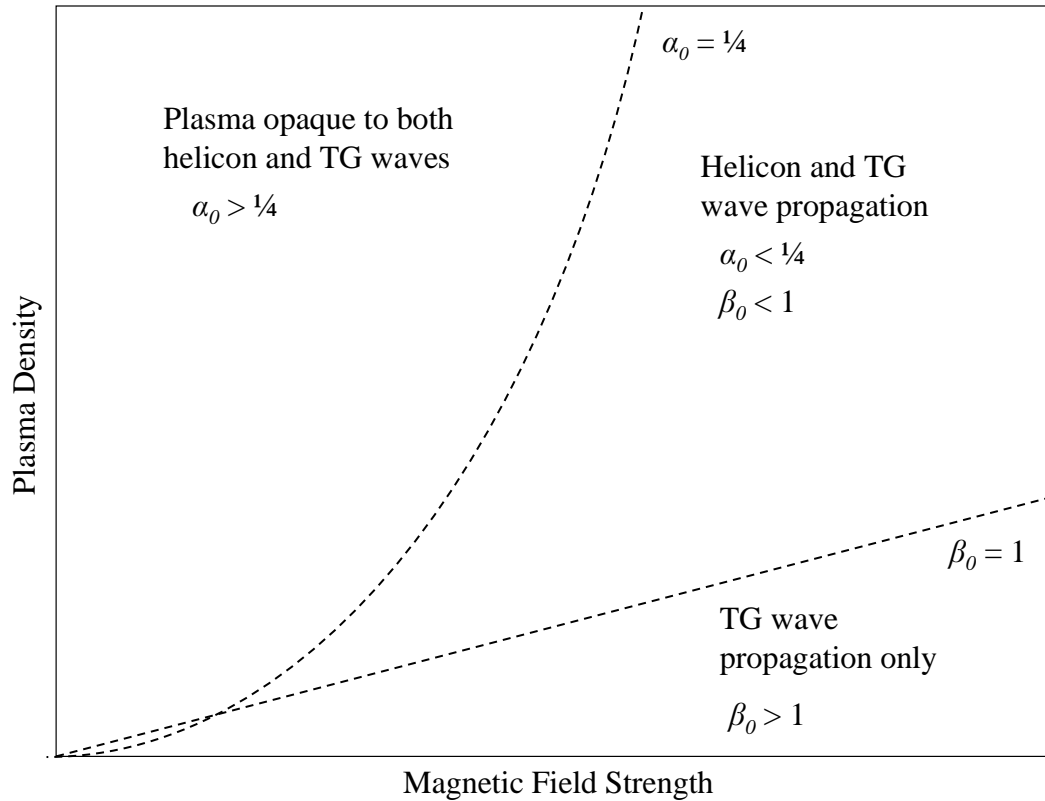
Figure 9. Wave propagation map for fixed k and ω.[46]

2.4 Electrodeless Helicon Thruster

While the helicon plasma source has mostly been studied as an ion source for various applications, there is growing interest in its use as an electrodeless thruster. One of the primary limiters to thruster lifespan is electrode erosion, so a thruster configuration with no electrode would conceivably have an unlimited lifespan. The primary concern with such a design would be whether the thruster has parametric control of the ion energy. Most electrostatic thrusters use electrodes in contact with the plasma to create a drop in electric potential that accelerates the ions. In contrast, the most likely ion acceleration mechanism for the electrodeless thruster is the double layer. Thus, the electrodeless configuration is reliant on passive control of the ion acceleration using variation of the

operating conditions. Therefore, the performance of the thruster is dependent on how the double layer mechanism responds to changes in operating conditions.

2.4.1 Double Layers

The next chapter introduces the topic of plasma sheaths, which describe the interaction between a plasma and a boundary, such as an insulating wall or a conductive electrode. At this boundary, a thin region of the plasma shifts in potential to maintain net zero charge flux out of the plasma. If, instead of a wall or electrode, the boundary is another plasma at a different potential, then a double-sided sheath would form as thin regions of both plasmas adjust their potentials. This double sheath, also known as a double layer, creates a continuous transition of the potential between the two plasmas.

In such a system there are four main particle groups: high potential ions and electrons, and low potential ions and electrons. The high potential ions and low potential electrons are accelerated by the double layer and pass into the other plasma. In contrast, the low potential ions and high potential electrons do not have the energy to pass the potential barrier and are trapped. In most cases these trapped populations have some finite temperature and thus have some particles from the high energy tail of the distribution that can pass through the double layer freely. A qualitative illustration of a double layer and the particle groups is shown in Figure 10.
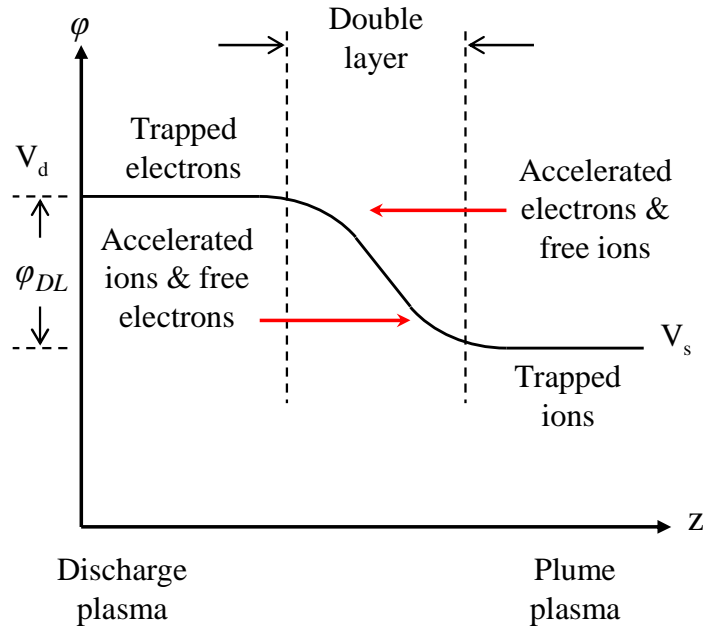
Figure 10. Double layer structure.[11]

Assuming that the free portion of the trapped ions and electrons is negligible, quasi-neutrality breaks down within the double layer, as the ion and electron current flux differs by a factor of the square root of the mass ratio.[47]

$$j_e = j_i \sqrt{\frac{m_i}{m_e}} \qquad (2.33)$$

This is often the case when the double layer occurs in a current driven device, where a current source is located on one side and a current sink on the other. A classic example is a cathode placed upstream of a constriction of the discharge chamber. Inside this constriction the ion loss rate to the walls is greater than in the larger section of the chamber. Therefore in order to maintain quasi-neutrality, a sheath must form between the two regions to impart additional energy to electrons to increase the ionization rate.[47]

Another type of double layer is the current-free double layer, which does not have any net current passing through the system and thus does not violate quasi-neutrality. This would arise in situations where one side of the double layer does not have any net current sources or sinks. Therefore in steady state, the net current flow through the sheath for this one side must be zero. A helicon plasma source is an example of such a device; the discharge chamber consists of only the insulating wall, the inlet, and the outlet. Since the inlet carries only neutral gas, and the wall cannot accept a non-zero current as it is floating, then the outlet must also pass zero net current. If the helicon plasma is expanding out of the inlet into a lower density plasma, then a double layer should form at some point downstream of the exit plane and likewise have no net current.[11] Such a double layer would have the high potential ions limited by ambipolar diffusion in order to accelerate additional high potential electrons through the potential barrier. Similarly, low potential electrons would accelerate trapped ions into the double layer. A net mass flow exists if the energy of the trapped electrons of the high potential plasma exceeded the energy of the trapped ions of the low potential plasma, allowing more ion-electron pairs from the high potential plasma to pass through the double layer than from the low potential plasma.

2.4.2 Ion Acceleration and Propulsive Applications

Recent work has investigated performance of electrodeless helicon thrusters by measuring the ion energy profiles of the ion beam[11-16] and direct thrust measurements.[17-20] These works measured beam voltages that ranged from 15-30 V and no greater than 5 mN of thrust. However, these works were primarily at single operating conditions and did not examine the plasma characteristics in detail. Thus, it remains to be seen what the

parametric effects are of operation and how the operational behavior of the thruster varies at different operating conditions.

The two key requirements to the efficacy of a thruster are its performance and the controllability of that performance. For an electrodeless double layer thruster, this infers that beyond providing adequate performance in the metrics of thrust, specific impulse, and efficiency, the device must also demonstrate the ability to alter these metrics through the variation of the operating conditions. For an electric propulsion device, a critical control parameter is the amount of energy deposited into each ion. The ion energy determines exit velocity, which contributes to thrust and specific impulse. Furthermore, since the primary thrust generation mechanism is the acceleration of ions, control of the ion trajectory is equally important. Should the electrodeless thruster lack control over either of these two mechanisms, it would be ineffective as a propulsive unit. Therefore the metrics for evaluating an electrodeless thruster are the values and controllability of the ion energy and ion trajectories.

2.5 Conclusions

To conclude, the helicon plasma source is an ion source that functions by coupling RF power in the antenna to the plasma electrons. This process is dependent on the following operating parameters: axial magnetic field strength, RF power, RF frequency, propellant flow rate, and discharge chamber geometry. The first four parameters can be varied during operation, and thus are the parameters that will be used during testing to control EHT performance. Since the GHIT utilizes a helicon plasma source as an ion

source, these parameters are also a subset of the control parameters of the two-stage thruster configuration as well.

The two functions of the helicon plasma source to be evaluated are ion production and ion acceleration. The characteristics of the helicon plasma source that describe its performance as an ion source are the ion number density and electron temperature. The presumed ion acceleration mechanism is the current-free double layer, which can be measured as a change in plasma potential through the plasma expansion plume. Thus, the characteristic of interest for ion acceleration is a spatial map of the plasma potential. The measured change in plasma potential can then be compared against direct measurement of the ion energy distribution to verify the predicted source of the ion acceleration.

CHAPTER III

ION ENGINES & GRIDDED ION EXTRACTION

While the first helicon thruster configuration is essentially a helicon plasma source alone, the second configuration utilizes metallic grids to extract ions from the helicon plasma inside the discharge chamber and accelerate them to produce thrust. This separates ion acceleration and ionization into two distinct stages that can be individually examined. Ion acceleration is performed by the grids, which extract the ions from discharge plasma through a plasma sheath that forms off the grids. The ions are accelerated as they pass through this grid sheath and form an ion beam downstream of the grids. The grids also force an equal number of electrons to be collected at the thruster anode, and since the grids prevent electron backstreaming, this allows for an accurate measurement of the ion beam current. With the beam current accurately known, a model of the thruster discharge chamber can be used to determine the ion production cost.

This chapter gives a brief overview of ion engines and the physics of ion extraction. The first section presents a brief history of ion engines and how they operate. The second section reviews the physics of plasma sheaths and how they interact with the grids and the discharge plasma. The third section details how ion engine discharges operate, both DC and RF. A model of ion engine discharge efficiency is presented as a means to calculate the ion production cost. This value serves as a performance metric to evaluate the helicon plasma against DC collisional discharge chambers.

3.1 Overview of Ion Engines

Ion engines are a subtype of electric propulsion thrusters that utilize electrostatic ion acceleration to produce thrust. What distinguishes ion engines from other electrostatic thruster configurations is that ion engines use gridded ion extraction rather than bulk plasma acceleration. There are two main consequences to such an approach. The first is extraction of a non-neutral plasma through gridded apertures is limited by the repulsion of similarly charged species. This effect is called the space-charge limitation and defines a maximum ion current that can pass through an aperture for a given geometry and set of operating conditions.

The second consequence of using gridded extraction is the ionization and acceleration stages of the thruster are distinctly separated. As a comparison, in a Hall effect thruster the propellant is ionized by an electron current confined in the downstream portion of the discharge channel. The location of this Hall current overlaps the region where the electrostatic potential decreases, causing the ionization and acceleration regions to merge slightly. It is advantageous to separate these two stages, as it allows for individual optimization of each stage, as well as avoiding the risk of propellant ionization occurring partially through the acceleration region and only gaining a fraction of the total energy.

Ion engines are composed of three primary components: the discharge chamber, the grid assembly, and the neutralizer cathode. The function of the discharge chamber is to ionize the propellant and serve as the ion source for the engine. The grid assembly then extracts ions produced in the discharge and accelerates them to generate thrust. The purpose of the neutralizer cathode is to emit electrons to neutralize the ion plume. As previously mentioned, grid assemblies only extract ions from the discharge, which

necessitates a pathway for the electrons to exit the discharge and rejoin the plume to avoid a buildup of electric charge on the spacecraft. Figure 11 shows a schematic of an example ion engine.
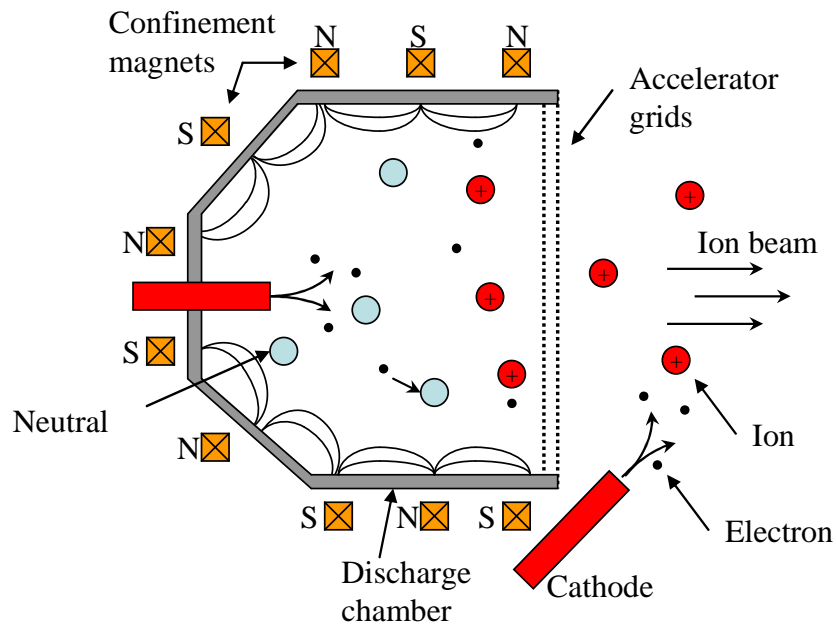
Figure 11. Ion engine schematic.

While the concept of electric propulsion dates back to 1906 with Robert Goddard and independently in 1911 with Konstantin Tsiolkovsky, the first ion engine was only developed in 1959 by Dr. Harold Kaufman.[1] The early ion engines used cesium or mercury as a propellant due to the low ionization cost and high mass. Over time the design was altered to use less reactive propellants, such as xenon. Several other modifications made over the evolution of the ion engine include: replacing the axial confinement magnetic field with a cusp field geometry, a three-grid assembly that used a domed architecture, and the semi-conical discharge chamber shape shown in Figure 11. Commercial use of ion engines began in 1997 with the launch of a Hughes Xenon Ion

Propulsion System (XIPS), while NASA launched the first deep-space mission using an ion engine in 1998 on Deep Space 1. Since then there has been a rapid increase in the use of ion engines, such as the 25 cm XIPS shown in Figure 12, and Hall effect thrusters on geosynchronous satellites for station keeping.

Figure 12. Photograph of 25 cm XIPS thruster.[1]

3.2 Electrostatic Gridded Ion Acceleration

Ion engines generate thrust by accelerating ions through an electric field generated by a set of biased grids. The force on the spacecraft is the reactive force of the electric field on the grids as they accelerate the ions. Thus, the three primary functions of the ion engine are to: create ions in the discharge chamber, extract ions from the discharge plasma at the grids, and accelerate the ions to create thrust. In this section, the extraction and acceleration of ions are discussed, while ionization and the discharge plasma are covered in Section 3.3. One of the key design considerations with electrostatic grids is that the grids extract ions through a plasma sheath. Additionally, the size and placement

of this sheath affects the ion trajectory in the grid and defines the ion optics of the grids. Therefore, a thorough consideration of the plasma sheath formation is required in ion engine design.

3.2.1 Plasma Sheaths

The basic function of a gridded ion accelerator is to extract ions from a plasma using a biased electrode. If the ion extraction electrode is at a lower electric potential than the plasma potential, ions are accelerated along the electric field lines and can be exhausted from the engine to produce thrust. There is a temptation to view the plasma-electrode from a fluid mechanics analogy: the potential difference between the plasma and the extraction electrode is the pressure head, the extracted ion plasma is the fluid flow, and the electrode geometry is the pipe geometry. From that viewpoint one could say that increasing the potential drop between the plasma and the extraction electrode should increase the ion current. However, this statement is incorrect as it erroneously assumes the bulk plasma and the extraction electrode have any direct interaction.

Suppose there is a volume of plasma with some arbitrary boundary, shown in Figure 13. In the interior region of the volume, quasi-neutrality requires that the electron number density be equal to the ion number density. At the boundary there will be diffusion of both charged species out of the volume. The ratio of the fluxes of electrons and ions is the ratio of their thermal velocities.
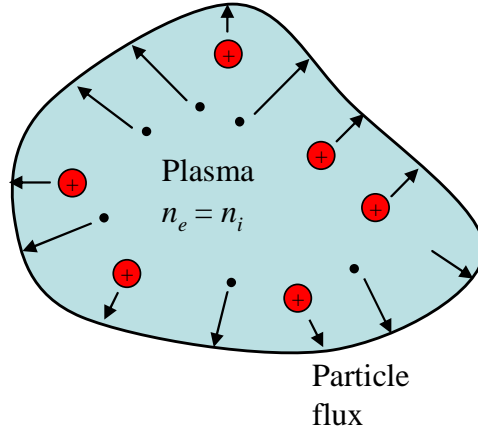
Figure 13. Arbitrary quasi-neutral plasma volume. Ions and electrons diffuse outwards with $v_i \ll v_e$.

$$\frac{j_e}{j_i} = \frac{en_e v_e}{en_i v_i} \qquad (3.1)$$

Equation (3.1) assumes the plasma is in thermal equilibrium and that ion temperature is equal to electron temperature. However, in most plasma discharges, especially those used in ion engines, energy deposition is primarily focused on electrons rather than ions. Furthermore, the residence time and ion-electron collision frequency is sufficiently low to prevent thermal equilibrium between the ions and electrons. Therefore, ion temperature is often much lower than the electron temperature for both DC[48] and helicon[49] discharges. Thus, the velocity of the electrons and the current flux out of the plasma volume is much higher than that of the ions. This would result in a buildup of positive charge within the plasma as electrons exit the volume at a faster rate. Therefore, in order for there to be a steady-state quasi-neutral plasma, a boundary condition must exist that reduces electron velocity and increases ion velocity at the boundary.

Now suppose this plasma volume is contained by an insulating wall. Initially the electron flux into the wall is higher than the ion flux, which leads to an accumulation of

negative charge on the wall, creating a potential difference between the wall and the bulk plasma. The parameter φ describes the difference in potential from one point to the potential in the bulk plasma. The convention adopted here is that φ is zero at the plasma potential, V_p, which means φ will generally be negative. As the wall potential decreases, it begins to accelerate ions and repel electrons. A length scale for this effect is called the Debye length,

$$\lambda_D = \left(\frac{\varepsilon_0 k_b T_e}{n_0 e^2} \right)^{\frac{1}{2}} \tag{3.2}$$

where T_e is the electron temperature of the plasma and ε_0 is the permittivity of free space. Assuming that the ions at the plasma potential have negligible velocity, the ions must be accelerated to at least the Bohm velocity, defined in terms of the electron temperature and ion mass, m_i.

$$v_{Bohm} = \sqrt{\frac{k_b T_e}{m_i}} \tag{3.3}$$

Under the convention where the sheath edge is the location at which the ions have reached the Bohm velocity, shown in Figure 14, the sheath potential at this location is

$$\phi_{Bohm} = -\frac{k_b T_e}{2e} \tag{3.4}$$

where the value of T_e is from the bulk plasma.
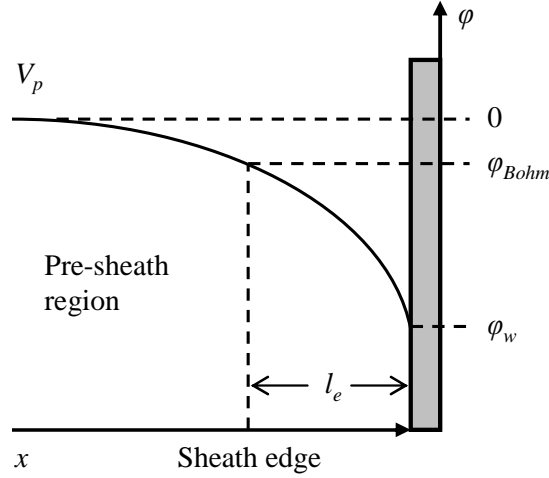
Figure 14. Wall sheath structure.

Outside the plasma sheath the plasma is still quasi-neutral; therefore the plasma density at the sheath edge, n_s, is limited by the electron number density.

$$n_s = n_0 \exp\left(\frac{e\phi_{Bohm}}{k_b T_e}\right) = 0.61 n_0 \qquad (3.5)$$

Here it is assumed that the electrons have a Maxwellian energy distribution. Substituting Equations (3.5) and (3.3) into the ion flux portion of (3.1), the Bohm ion current flux is

$$j_{Bohm} = 0.61 e n_0 \left(\frac{k_b T_e}{m_i}\right)^{1/2} \qquad (3.6)$$

The electron current density is determined in a similar fashion, but uses the RMS value of the electron velocity for a Maxwellian distribution and the potential drop to the wall ϕ_w.[50]

$$j_e = \frac{1}{4} e n_0 \left(\frac{8 k_b T_e}{\pi m_e} \right)^{1/2} \exp\left(\frac{e\phi_w}{k_b T_e} \right) \tag{3.7}$$

In order for a steady state solution to exit, the ion and electron fluxes into the sheath must balance. Equating Equations (3.6) and (3.7) yields

$$\phi_w = \frac{kT_e}{e} \ln\left(0.61 \sqrt{\frac{2\pi m_e}{m_i}} \right) \tag{3.8}$$

For sheaths with a thickness on the order of the Debye length, called Debye sheaths, it is assumed the potential drop across the sheath is small compared to the electron temperature. This assumption allows for a finite electron flux into the sheath, and is typically employed where electrically floating surfaces are used. Another case is when the potential drop across the sheath is much larger than the electron temperature, which causes the electron flux to become negligible according to Equation (3.7). Sheaths of this type are called Child-Langmuir sheaths. The maximum ion flux through a Child-Langmuir sheath is

$$j_{max} = \frac{4\varepsilon_0}{9} \left(\frac{2e}{m_i} \right)^{1/2} \frac{|\phi|^{3/2}}{l_e^2} \tag{3.9}$$

where l_e is the sheath thickness. Since no electrons pass through the sheath, Equation (3.9) also describes the total current density through the sheath.

If no assumptions are made, a general equation describing the sheath can be found using Poisson's equation in one dimension, which is done in Appendix C. Regardless of the assumptions chosen, a plasma sheath will form between the bulk plasma and the surface of any disturbance, such as an electrode. Ions will enter the sheath at a rate largely independent of the potential between the plasma and the electrode, although the electron current is a function of this potential drop. Since it is within the sheath that ions are accelerated, the sheath is the region of interest when designing extraction electrodes for ion engines. These electrodes, and the focusing and acceleration of the ions, is called ion optics.

3.2.2 Ion Optics

The most common ion extraction electrode is a grid, as it offers both high ion transparency and small apertures that can be sized to match the plasma sheath. Most ion extractors consist of two grids: the screen grid and the acceleration (accel) grid. The accel grid is the actual extraction electrode with which the plasma sheath interacts. The screen grid is biased slightly below the plasma potential and shields the accel grid from any ions that are not aligned properly with the accel grid apertures. Ions exiting the grids occasionally collide with neutral atoms in charge-exchange collisions. These collisions result in low energy ions that are accelerated back towards the accel grid and cause sputtering of the grid. A third grid, the deceleration (decel) grid, is often placed downstream of the accel grid to shield the accel grid from these charge-exchange ions in much the same manner as the screen grid. In this study the decel grid is neglected for simplicity. Figure 15 shows a qualitative diagram of a three-grid setup and the corresponding electric potentials through the grid assembly.
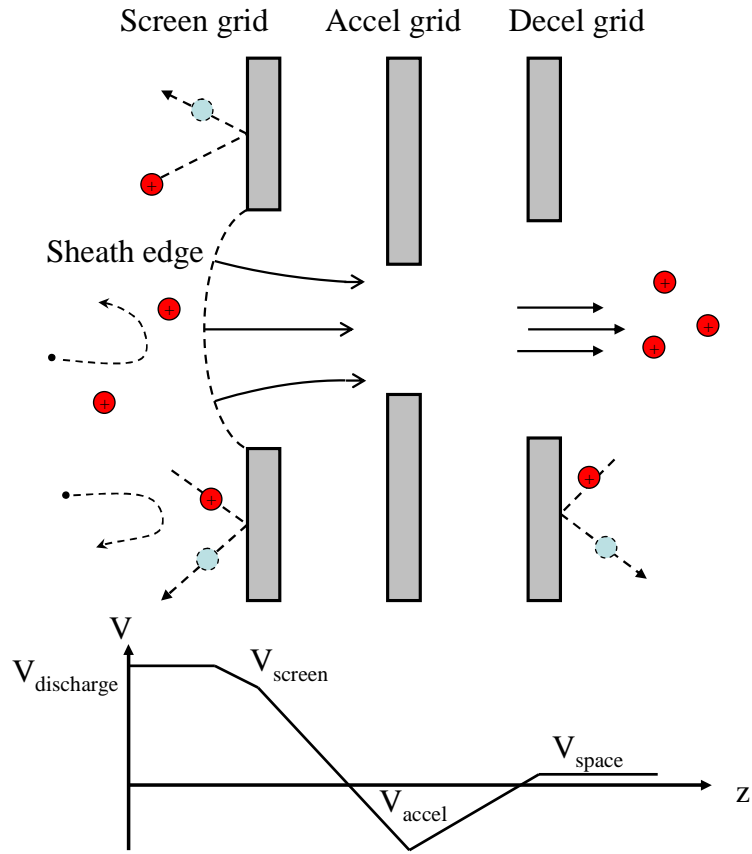
Figure 15. Example of a three-grid configuration and electric potentials.

The ideal configuration of the two-grid setup is to have the sheath between the accel grid and the bulk plasma and extend just past the screen grid apertures. This prevents any ions that are misaligned from accelerating along the electric field and striking the accel grid, causing erosion. Once past the accel grid, the ions return to the plasma potential of the plume, which means the total acceleration voltage is set by the potential difference between the discharge plasma and the space potential, not the difference in grid potentials. The potential difference between the grids is the total potential drop through the sheath and thus sets the maximum current density that can pass through. Since the potential difference between the accel grid and the discharge plasma is generally very large compared to the electron temperature, the sheath around the grid is a Child-

Langmuir sheath. The current density is therefore comprised solely of ion flux. Substituting the grid potentials into Equation (3.9) yields

$$j_{max} = \frac{4\varepsilon_0}{9}\left(\frac{2e}{m_i}\right)^{1/2}\frac{(V_s - V_a)^{3/2}}{l_e^2}$$ (3.10)

where V_s and V_a are the screen and acceleration grid potentials. When designing the grid assembly, the goal is to match the sheath thickness, l_e, with the actual distance between the grids. Since the sheath will form a slight dome as it extends past the screen grid apertures, the desired sheath thickness is therefore

$$l_e = \sqrt{\left(l_g + t_s\right)^2 + \frac{d_s^2}{4}}$$ (3.11)

where l_g is the distance between grids, t_s is the grid thickness, and d_s is the aperture diameter of the screen grid. Figure 16 shows an illustration of the approximation with the relevant parameters.
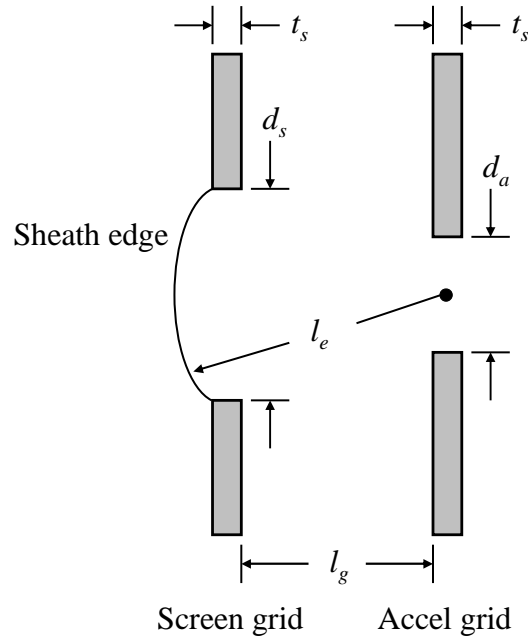
Figure 16. Effective sheath approximation.

The design of a two-grid system for a given discharge chamber focuses on four design parameters: the screen grid aperture diameter, the accel grid aperture diameter, the grid thickness, and the distance between the grids. The screen grid aperture diameter has a maximum value of an order of magnitude higher than the Debye length. The accel grid aperture diameter and the grid separation distance are not as clearly defined and require simulation to determine. The ions are aligned by the screen grid to pass through the accel grid apertures, and the electric field between the two grids focuses the ions, allowing the accel grid apertures to be smaller than those of the screen grid. The ion focusing creates a duality of the grid transparency: for ions the transparency is determined by the screen grid, while for neutrals the transparency is set by the accel grid. Therefore, it is advantageous to maximize the transparency of the screen grid while minimizing the transparency of the accel grid and prevent neutrals from escaping. However, there is a lower bound to the accel grid aperture diameter, otherwise high energy ions will collide

with the grid and erode the material. Similarly, the optimum distance between the grids is smaller than the screen grid aperture diameter with a minimum separation of 1 mm per 2.4 kV of potential difference between the grids to prevent electric breakdown and arcing between the grids.

Thus far the only potential difference used has been the difference in potential of the two grids. There is another potential to consider: the plasma potential of the discharge relative to the plasma potential of the plume, called the space potential. The total potential drop that accelerates the ions is the difference between the discharge potential and the space potential, called the beam voltage, V_b. Figure 17 shows a qualitative plot of the potential from the discharge chamber to the plume. The potential drop between the grids generally exceeds the beam voltage, as the accel grid is generally biased below common. The negatively biased accel grid repels downstream electrons from the neutralizer cathode entering the discharge chamber through the grids, a process called backstreaming. Electron backstreaming causes the electron current to be recycled through the discharge anode to the neutralizer cathode, which is a source of inefficiency. Furthermore, this recycled electron current prevents accurate measurement of the beam current using the anode and grid currents. Therefore, biasing the accel grid below common to eliminate electron backstreaming improves efficiency and enables easy determination of the beam current.
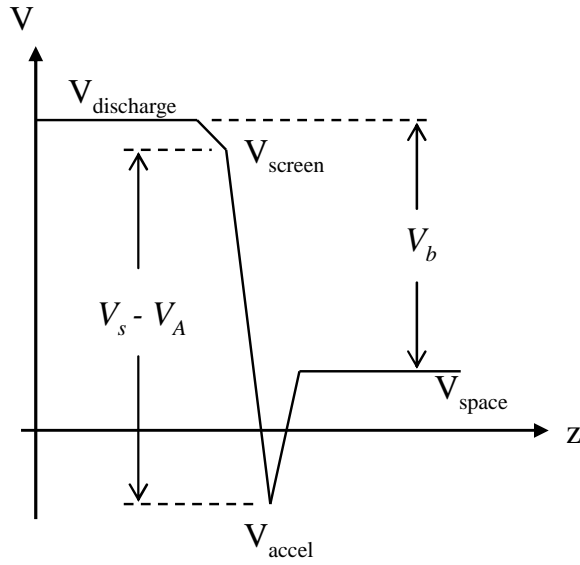
Figure 17. Beam voltage compared to grid potentials.

While maximizing the potential drop between the grids maximizes the current that can be passed through the grids, having a large grid potential drop relative to the beam voltage can cause ion impingement on the accel grid and limit thruster lifetime. This is represented by the voltage ratio, R, which is typically designed to be between 0.8-0.9.[1]

$$R = \frac{V_b}{V_s - V_A} \tag{3.12}$$

The design parameters discussed so far encompass only the grid assembly. However, the actual acceleration mechanism is the plasma sheath that forms between the grid and the discharge plasma. Equation (3.2) and Appendix C show that the thickness of a sheath is dependent on the temperature and density of bulk plasma. Therefore, the trajectory of the accelerated ions is not solely dependent on the electrode geometry, but also dependent on the shape of the plasma sheath. The shape of the sheath is not fixed, but rather varies

with the potential drop through the grids compared to the bulk plasma parameters. This variance is described by a parameter called the perveance.

3.2.3 Perveance

Perveance is a measure of how much current is accelerated through an aperture for a given potential drop, defined as

$$P = \frac{I}{V_T^{3/2}} \tag{3.13}$$

where I is the total current transmitted through the aperture and V_T is the total potential drop through the aperture. The maximum perveance through a round aperture can be found by using Equation (3.9) for the current density and equating the total potential drop to the sheath potential.

$$P_{max} = \frac{\pi \varepsilon_0}{9} \left(\frac{2e}{m_i} \right)^{1/2} \frac{d_s^2}{l_e^2} \tag{3.14}$$

The above equation sets an upper bound to the current that can pass through an aperture for a given voltage drop. A useful design and characterization tool is to normalize the perveance by the ratio of the squares of the aperture diameter and the sheath thickness,[52] as this allows an easy comparison of the perveance to the allowable limit. Since Equation (3.14) describes the perveance for a single aperture, Equation (3.13) must also be divided by the number of apertures, N_a.

$$P_{norm} = \frac{I}{N_a V_T^{3/2}} \left(\frac{l_e}{d_s} \right)^2 \tag{3.15}$$

$$P_{norm,\max} = \frac{\pi \varepsilon_0}{9} \left(\frac{2e}{m_i} \right)^{1/2} \tag{3.16}$$

The perveance serves as a measure of the sheath placement in relation to the screen grid. In the ideal case the sheath extends through the screen grid aperture and forms a convex "lens" to focus the ions through the smaller accel grid aperture, shown in Figure 18. This only happens for a certain match between the discharge plasma and the applied potential on the grids. There are two competing parameters that set the location of the sheath edge: the incoming ion current and the total potential drop across the sheath. The ion current, described by Equation (3.6), has two variable components: the electron temperature and density of the bulk plasma. As these parameters vary, the location of the sheath edge can move either back into the discharge plasma, or further into the grid assembly.
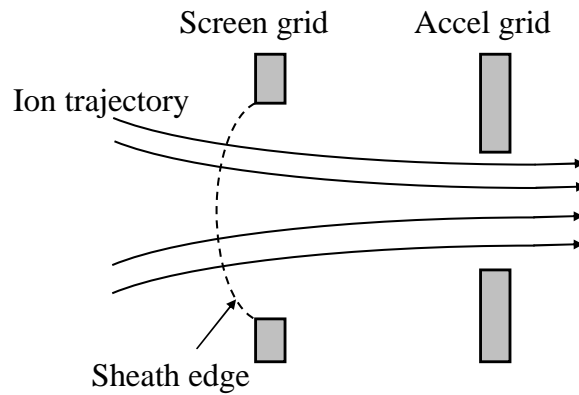
Figure 18. Optimum perveance.

An increase in the discharge plasma density (or a reduction of the electron temperature) for constant grid potentials reduces the sheath thickness and pushes the "lens" further towards the accel grid. This causes some of the ions to have insufficient focusing and increases ion impingement on the accel grid. In this condition, the perveance is higher than the optimal case, called "over-perveance," shown in Figure 19. Similarly, an increase in the potential drop across the grids increases the sheath thickness and extends the boundary towards the discharge plasma. In this scenario, called "under-perveance," the ions are over-focused and will cross trajectories with neighboring apertures, shown in Figure 20.
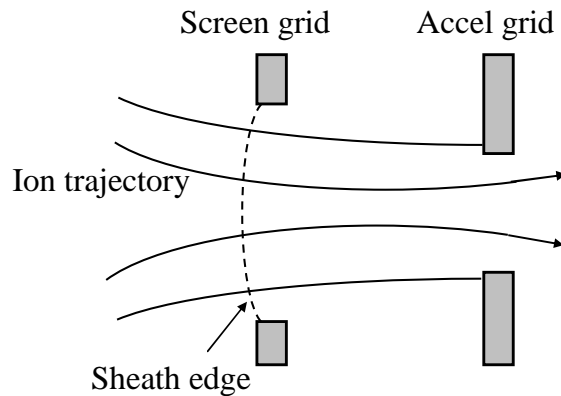
Figure 19. Over-perveance where some ions are insufficiently focused
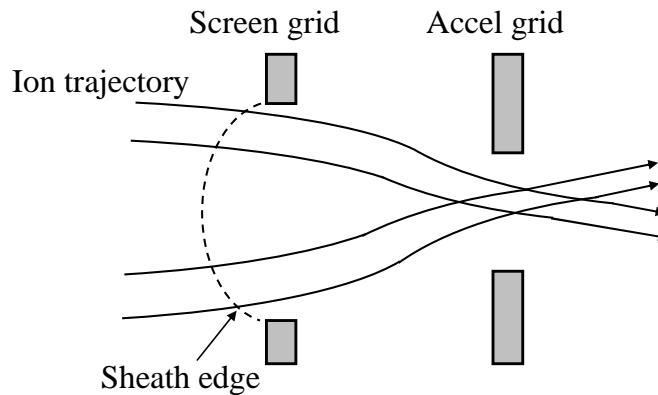
Figure 20. Under-perveance and over-focusing of ions.

The determination of the optimal perveance can be performed experimentally by varying the grid potentials and measuring the ion current into the accel grid. The optimal perveance occurs at a minimum of the ratio of the accel grid current to beam current as a function of the normalized perveance. A general design target is to operate at half the maximum perveance.[51]

3.3 Plasma Discharge

The primary function of the plasma discharge is to supply the device with a source of ions that can be accelerated by the grid assembly. A secondary function of the discharge chamber is to bias the plasma above the downstream space potential, which sets the net ion energy and ultimately the specific impulse. There are two types of discharges that can be used: DC and RF discharges. The distinction between the two groups is the methods used to ionize and confine the propellant.

3.3.1 DC Discharges

DC discharges create a plasma through electron-neutral collisions where the electrons are supplied by a cathode inside the discharge chamber. An anode is placed inside the chamber (or more commonly the walls of the discharge chamber are the anode) with an applied potential drop between the anode and the cathode. As electrons are emitted by the cathode they are accelerated by the difference in potential and collide with neutral gas fed into the chamber. Given sufficient electron energy, the electron-neutral collisions result in the ionization of the gas. The ions produced are then accelerated through the grid assembly, while the electrons are collected by the anode and fed to the external

neutralizer cathode to neutralize the exhaust plume. Figure 21 shows a qualitative illustration of an ion engine discharge chamber using argon gas.
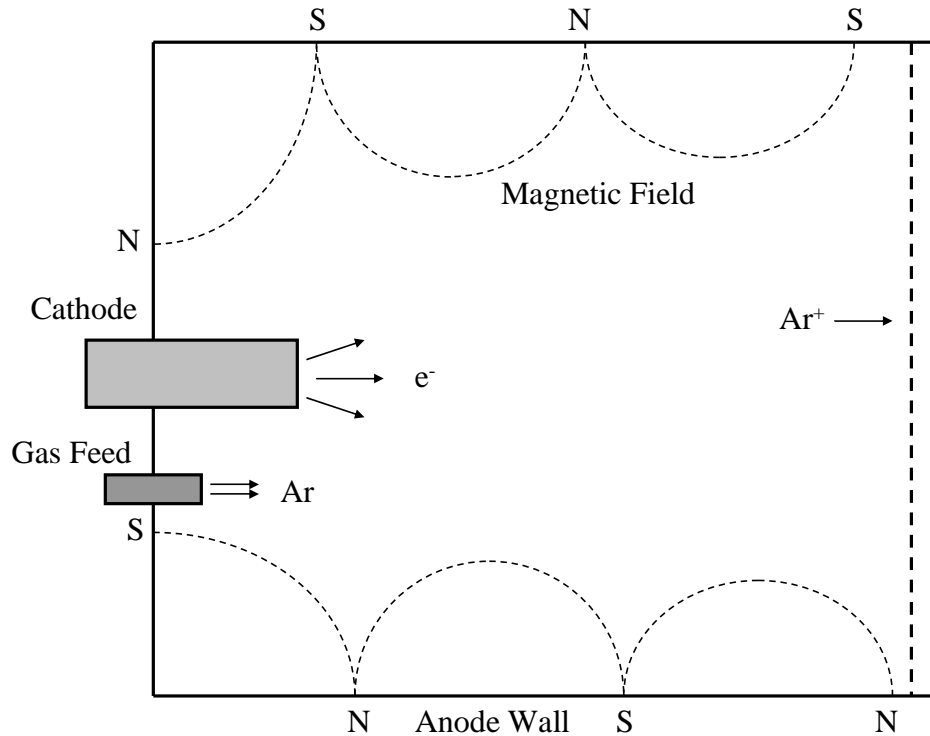
Figure 21. Conceptual DC plasma discharge chamber.

While the anode creates the potential drop that sets the electron energy and provides a pathway for electrons to the ion plume, the anode also creates a source of inefficiency. Every electron that reaches the anode that does not correspond to an extracted ion is passed through the discharge cathode and re-enters the discharge. Should an electron pass from the cathode to the anode without colliding with a neutral and create an ion, the energy spent accelerating the electron is wasted. The most common solution is to create a magnetic barrier that causes the electrons to gyrate around the magnetic field lines. By creating a magnetic field roughly parallel with the wall (which is approximately

perpendicular to the electric field to the anode), the path length for an electron to the wall is greatly increased. For a given mean-free path this results in a greater chance that an electron will collide with a neutral before reaching the wall. There are many different configurations possible for the magnetic field; the one depicted in Figure 21 is a system of ring cusp magnets that are wound around the exterior of the discharge chamber.

3.3.2 RF Plasma Discharges

RF discharges are similar to DC discharges in that the primary goal is to energize electrons to collide with neutrals and cause ionization. Whereas DC discharges rely on electron acceleration between a cathode and an anode, RF discharges primarily use oscillating electromagnetic fields in the Medium Frequency (MF) and High Frequency (HF) bands to deposit energy into the electrons. A common approach is to create an inductively coupled plasma discharge using an RF coil wrapped around the discharge chamber as the antenna.[27-29,1] An ion engine that utilizes such a discharge is classified as a radiofrequency ion engine (RIT).

There are several ways the behavior of RF discharges differs from that of DC discharges. The first is that in an ICP the electrons gain energy in proportion to the amplitude of the incident wave. However, since the plasma is a conductive medium it will attenuate the wave as it passes through, as described by the skin depth. Generally, RF discharges are designed so that the skin depth is on the order of the diameter of the discharge chamber. With the RF coil located on the exterior of the discharge chamber, energy deposition, and thus propellant ionization, will mostly occur near the discharge chamber wall and not in the center. The second difference from a DC discharge is that RF discharges often do not have a DC magnetic field to confine electrons, instead relying

58

on an oscillating axial magnetic field induced by the RF coil. Another other major

distinction is that since ionization is not dependent on a cathode-anode discharge, the

walls of the discharge chamber no longer have to serve as the anode. In fact, in order for

the RF wave to propagate into the discharge chamber at all, the chamber wall must be

insulating. An anode is still required to bias the discharge plasma and provide a pathway

for discharge electrons to be emitted into the ion plume, but the size and location of the

anode are more variable than in the case of a DC discharge.

One final consideration for an RF discharge is the conditions required to ignite the

plasma discharge. As already discussed in Section 2.2.2, an RF discharge can be ignited

given sufficient neutral gas pressure and RF power. However, such an approach requires

high power transmission through an antenna with no initial load. In RF discharges the

plasma itself is the load for the RF signal, and the reliance on high power to ignite the

plasma requires the RF system to either supply high power at mismatched impedance, or

to include a variable impedance tuning circuit to allow for changing the system

impedance after the plasma is ignited. Since transmitting high power across mismatched

impedances is generally undesirable, the latter option is usually required, which is

covered in Appendix D. An alternative is to use the neutralizer cathode as a free electron

source by placing no bias on the grids and drawing in the electrons using the anode. The

excess electrons then reduce the power needed to ignite the plasma.

3.3.3 Discharge Efficiency

The discharge efficiency is a ratio of the power absorbed by the plasma from the RF

system, P_{abs}, to the beam current created,

$$\eta_d = \frac{P_{abs}}{I_b}$$ (3.17)

Discharge efficiency has units of W/A, or more commonly eV per ion. The discharge efficiency, also referred to as the ion production cost, is a useful metric for evaluating an ion engine discharge chamber. The discharge efficiency is higher than the ionization energy, as not only is power expended to first create the ion, but also in various loss mechanisms, such as recombination, collisional excitation, and wall neutralization. Thus the discharge efficiency is a measure of the energy cost to create and transport an ion to the grids taking these losses into account. Generally the discharge efficiency is about a factor of ten greater than the ionization cost.[1]

While there is only one way for energy to enter the discharge, either through a DC or RF source, there are several pathways for energy to exit the discharge. The primary energy expenditures are: neutral ionization, neutral excitation, ion current flow to the grids and discharge chamber wall, ion current to the beam, electron flow to the wall, and electron collection by the anode. Since a Child-Langmuir sheath exists at the grids, the electron current to the grids can be assumed to be negligible. In the steady-state the power absorbed by the plasma must equal the power output, which can be written as[1]

$$P_{abs} = I_p \varepsilon^+ + I^* \varepsilon^* + \left(I_s + I_b + I_A\right)\left(\frac{k_b T_e}{2} + \phi_s\right) + I_{w,i}\left(\frac{k_b T_e}{2} + \phi_w\right) + I_{w,e}\left(2k_b T_e + \phi_w\right)$$

$$\underbrace{\qquad\qquad}_{\text{Ionization \&}} \underbrace{\qquad\qquad\qquad}_{\text{Grid ion extraction loss}} \underbrace{\qquad\qquad}_{\text{Wall ion loss}} \underbrace{\qquad\qquad}_{\text{Wall electron loss}}$$

Ionization &
excitation

$$+ I_{a,i}\left(\frac{k_b T_e}{2} + \phi_a\right) + I_{a,e}\left(2k_b T_e + \phi_a\right) \tag{3.18}$$

$$\underbrace{\qquad\qquad}_{\text{Anode ion loss}} \underbrace{\qquad\qquad}_{\text{Anode electron loss}}$$

where I^* is the rate of neutral excitation, I_s is the ion current to the screen grid, I_b is the ion beam current, I_A is the accel grid current, $I_{w,i}$ is the rate of ion loss to the walls, $I_{w,e}$ is the electron loss rate to the walls, I_a is the electron current to the anode, ε is energy of ionization and excitation, and φ_j is the potential difference of the sheath between the discharge plasma potential and j, where j is s, w, or a for the screen grid, the wall, or the anode, respectively.

The ion production rate can be expressed as a function of the ionization cross section of the neutral particle, σ_i, the volume of the discharge chamber, V_d, and the electron velocity, v_e.

$$I_p = n_n n_e \langle \sigma_i v_e \rangle V_d \tag{3.19}$$

The term in the brackets denotes the product averaged over the Maxwellian distribution of the electron velocity distribution function. The neutral excitation rate can similarly be expressed as

$$I^* = n_n n_e \left\langle \sigma^* v_e \right\rangle V_d \tag{3.20}$$

with a total excitation collision cross section for a 15 eV electron and a neutral argon atom is approximately 0.1×10^{-20} m^2.[53]

Ideally, the beam current is the Bohm current into the open area of the screen grid, which is the grid area, A_g, multiplied by the screen grid transparency, T_s.

$$I_b = 0.61 n_0 e A_g T_s v_{Bohm} \tag{3.21}$$

The transparency is defined as the ratio of the open area of the grid to the total area occupied by the grid.

$$T_s = \frac{A_{g,open}}{A_g} \tag{3.22}$$

This is a reasonable approximation for the sheath area, since the slightly convex shape of the sheath does not appreciably add to the surface area compared to the open area of the grids. However, Equation (3.21) assumes there is no ion impingement on the accel grid, which is not always the case. Instead, it is more accurate to state that the Bohm current is equal to the combined accel grid and beam currents.

$$I_b + I_A = 0.61 n_0 e A_g T_s v_{Bohm} \tag{3.23}$$

Similarly, the screen grid current is the Bohm current into the closed area of the screen grid.

$$I_s = 0.61 n_0 e A_g \left(1 - T_s\right) v_{Bohm} \tag{3.24}$$

The possibility exists that the anode will still collect an ion current from the discharge plasma. This occurs when the area of the anode is comparable to the area of the grids, or when the anode does not draw a very large current. Assuming that the anode collects both ions and electrons, the currents to the anode can be found using Equation (3.6) and Equation (3.7), as well as the area of the anode, A_a.

$$I_{a,e} = \frac{1}{4} e n_0 A_a \left(\frac{8 k_b T_e}{\pi m_e}\right)^{1/2} \exp\left(\frac{e \phi_a}{k_b T_e}\right) \tag{3.25}$$

$$I_{a,i} = 0.61 e n_0 A_a \left(\frac{k_b T_e}{m_i}\right)^{1/2} \tag{3.26}$$

The ion and electron currents to the discharge chamber wall differ from the other currents into a sheath due to the presence of the axial magnetic field. The magnetic field does not limit electron mobility parallel to the magnetic field, such as to the anode; however, it does limit transverse electron mobility, such as electron flow to the wall. Electrons are thus confined to the magnetic field lines and can only achieve transverse diffusion via collisions. The ion gyroradius is much larger than the electron gyroradius, and ions are much less confined than electrons. In order to maintain quasi-neutrality ions

63

must exit the discharge chamber (in this case by neutralizing at the wall) at the same rate as electrons, which requires ion mobility to be decreased. As a result, an electric field arises that accelerates electrons and decelerates ions, a mechanism called ambipolar diffusion. The transverse velocity for an ion or electron for ambipolar diffusion is expressed as[1]

$$v_{\perp} = \frac{\mu_e}{1 + \mu_e^2 B^2 - \dfrac{\nu_{ei}}{\nu_e}} \left(E_{\perp} + \frac{k_b T_e}{e} \frac{\nabla n_e}{n_e} \right) \tag{3.27}$$

where μ_e is the transverse electron mobility, B is the applied magnetic field strength, and ν is the collision frequency, with the subscript "ei" denoting electron-ion collisions, and "e" denoting electron collisions with either ions or neutrals. Figure 22 shows the transverse velocity and the associated components in relation to the axial magnetic field of the helicon discharge.
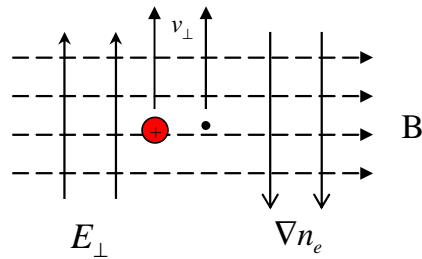
Figure 22. Transverse diffusion velocity components.

The above terms are defined as

$$\mu_e = \frac{e}{m_e \nu_e} \tag{3.28}$$

$$\nu_e = \nu_{en} + \nu_{ei} \tag{3.29}$$

$$\nu_{ei} = n_i \sigma_{ei} \bar{v}_e \tag{3.30}$$

while the electron-neutral collision frequency is[54]

$$\nu_{en} = 5 \times 10^{-19} n_n \sqrt{\frac{k_b T_e}{m_e}} \tag{3.31}$$

The average electron collision velocity is a function of the reduced mass, m^*, so the following can be said.

$$\bar{v}_e = \sqrt{\frac{8 k_b T_e}{\pi m_{e,i}^*}} \tag{3.32}$$

$$m_{e,i}^* = \frac{m_e m_i}{m_e + m_i} \approx m_e \tag{3.33}$$

For collisions between charged particles, called Coulomb collisions, electrostatic forces cause the impact parameter to be higher than just the radii of the particles. Instead, the cross section is

$$\sigma_{ei} = \frac{e^4 \ln \Lambda}{16 \pi \varepsilon_0^2 k_b^2 T_e^2} \tag{3.34}$$

where $\ln\Lambda$ is the Coulomb logarithm, defined in terms of the Debye length, λ_D.

$$\Lambda = 12\pi n_e \lambda_D^3 \tag{3.35}$$

Substituting Equations (3.32) through (3.35) into Equation (3.30) yields

$$v_{ei} = n_i \frac{e^4}{\varepsilon_0^2 (32 m_e)^{1/2} (\pi k_b T_e)^{3/2}} \ln\left(12\pi n_e \lambda_D^3\right) \tag{3.36}$$

The ion and electron wall currents are thus

$$I_{w,i} = I_{w,e} = n_0 e A_w v_\perp \tag{3.37}$$

The anode sheath potential is defined in relation to the discharge temperature by enforcing charge balance and equating the ion currents to the electron currents, shown in Figure 23.

$$I_{a,e} + I_{w,e} = I_{a,i} + I_{w,i} + I_s + I_A + I_b \tag{3.38}$$
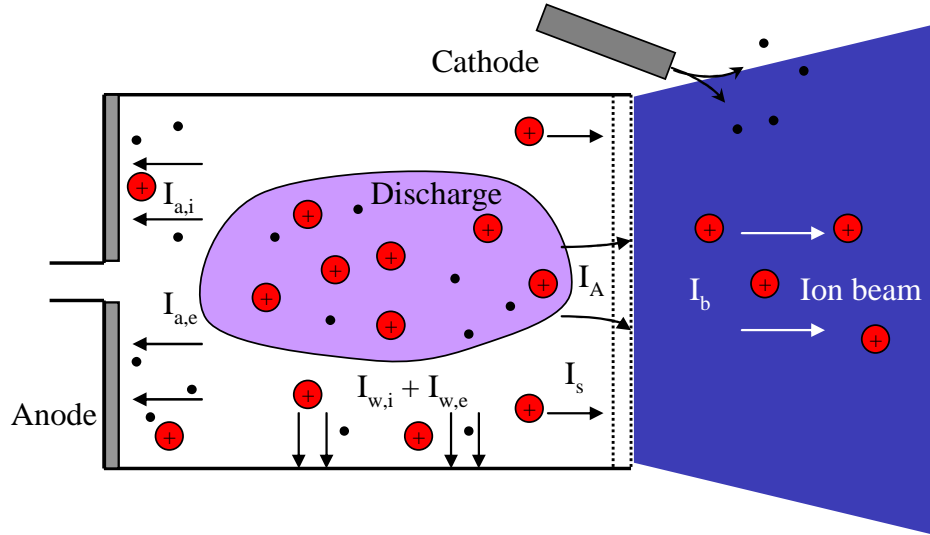
Figure 23. Discharge chamber currents.

Substituting Equations (3.23), (3.24), (3.25), (3.26), and (3.37) into Equation (3.38) yields

$$\phi_a = \frac{k_b T_e}{e} \ln\left(0.61 \frac{A_a + A_g}{A_a} \sqrt{\frac{2\pi m_e}{m_i}} \right) \qquad (3.39)$$

Thus, unless the grid area is much larger than the anode area, Equation (3.39) contains the natural log of a quantity less than one, which yields a negative anode sheath potential. This confirms the earlier assumption that the anode sheath collects ions in addition to electrons. Physically, this is due to the higher velocity of the electrons creating a larger electron current incident on the anode than is required to balance the grid currents. In order to maintain charge balance, the anode sheath must repel some of the electrons, which necessitates a negative sheath potential and the collection of ions.

The sheath potential to the screen grid can be found by relating the anode and screen potentials to the anode sheath potential.

$$\phi_s = \phi_a - \left(V_a - V_s\right) \tag{3.40}$$

If a cylindrical discharge chamber is assumed with an axial magnetic field, and the only insulating wall condition is on the radial boundary, then the ion and electron wall collision rate is already equal due to ambipolar diffusion across a magnetic field. Therefore no wall potential is required to ensure quasi-neutrality and φ_w is zero.

3.4 Conclusions

From the information presented in this chapter, there are several additional operating parameters that control the GHIT beyond previously mentioned the helicon plasma source operational parameters of RF power, RF frequency, magnetic field strength, and propellant flow rate. These additional parameters are the voltages of the screen and accel grids, and the voltage of the discharge plasma with respect to the cathode. This does not include the grid aperture geometry, as this cannot be easily modified during operation. However, the impact of the grid voltages on ion extraction and acceleration is also affected by the discharge plasma density and temperature. Thus it is more accurate to say that ion extraction and focusing is dependent on the combination of the discharge plasma characteristics and the grid voltages, a quantity captured by the perveance. Thus the GHIT has a greater number of variable operational parameters that can be used to control ion acceleration. Additionally, the separation of the ionization and ion acceleration mechanism allows for separate characterization of each process. These processes can be captured with measurements of the component grid currents, discharge plasma characteristics, and the beam divergence angle.

Furthermore, the discharge efficiency model describes the ionization of the discharge chamber in relation to the various power losses possible. The model reveals that measurements of the plasma structure inside the discharge chamber are necessary to calculate radial ion losses. However, such measurements are already required for the EHT in order to evaluate electrodeless ion acceleration. Therefore, the ion production cost can now be calculated more accurately utilizing a combination of measurements of both the EHT and the GHIT.

CHAPTER IV

THRUSTER CONFIGURATIONS

The goal of this research is to examine ion acceleration in helicon thrusters and determine the necessity of a separate ion accelerator. In the previous chapters the experimental methodology is established as a case study between two thruster configurations and the ion acceleration mechanisms of each is reviewed. Additionally, the operational parameters that can be used to control each thruster configuration is determined, along with the key performance characteristics and evaluation metrics.

This chapter outlines the design, fabrication, and operation of the two thruster configurations. The first is an electrodeless helicon thruster (EHT) that consists of a helicon plasma source exhausting a plasma into a diverging magnetic field to produce thrust. The second configuration is a gridded helicon ion thruster (GHIT) that uses an identical helicon plasma source to create a plasma discharge and a two-grid ion extractor to accelerate ions to produce thrust. Both thruster configurations share the same configuration of the helicon in terms of discharge chamber size, solenoids, and antenna. There are several additional components that convert the EHT to the GHIT. The first section of this chapter details the design of the EHT and the RF system. The second section introduces the additional components of the GHIT: the anode, grid assembly, and cathode. Additionally, the integrated thruster is presented along with a performance model to predict thrust based on the operating conditions.

4.1 Electrodeless Helicon Thruster

The helicon consists of a Pyrex discharge chamber 27.3 cm long and 14.0 cm in diameter. The axial magnetic field is provided by two 725-turn solenoids 7.6 cm wide with a 19.7 cm inner diameter. The solenoids are placed 10.2 cm apart. Figure 24 shows the on-axis magnetic field strength for the four solenoid currents used. The magnetic field strengths are referred to by the strength at the center of the antenna; thus while the device is tested at solenoid currents of 3.76, 6.26, 8.75, and 11.25 A, it is referred to as 150, 250, 350 and 450 G, respectively. Contour maps of the 150 G and 350 G cases are shown in Figure 25 and Figure 26, respectively.
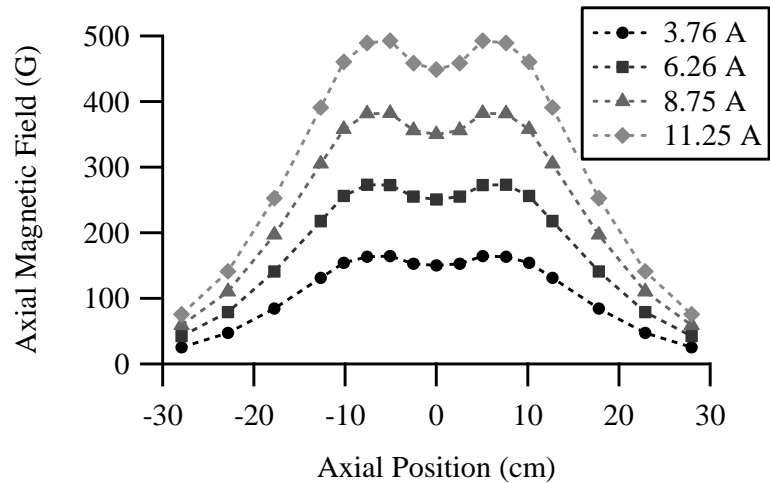
Figure 24. Measured centerline axial magnetic field at four currents.
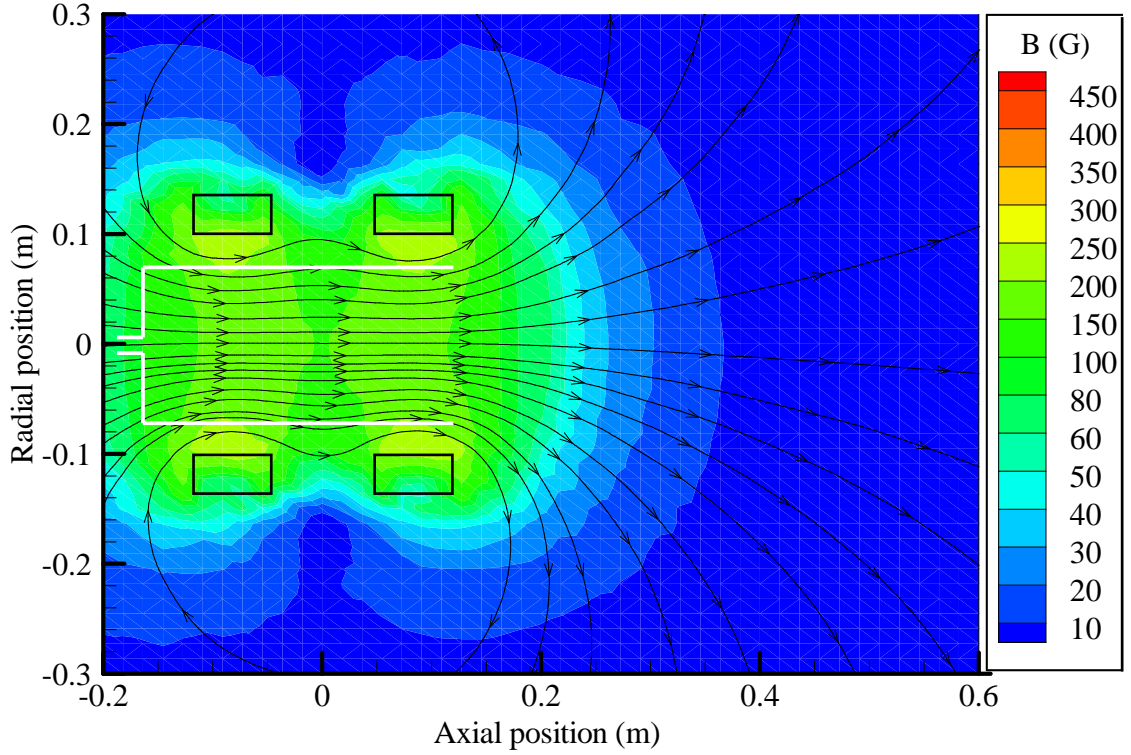
Figure 25. Helicon magnetic field contour at 3.76 A (150 G). Cross section of the solenoids denoted by black boxes, and discharge chamber wall by white lines.
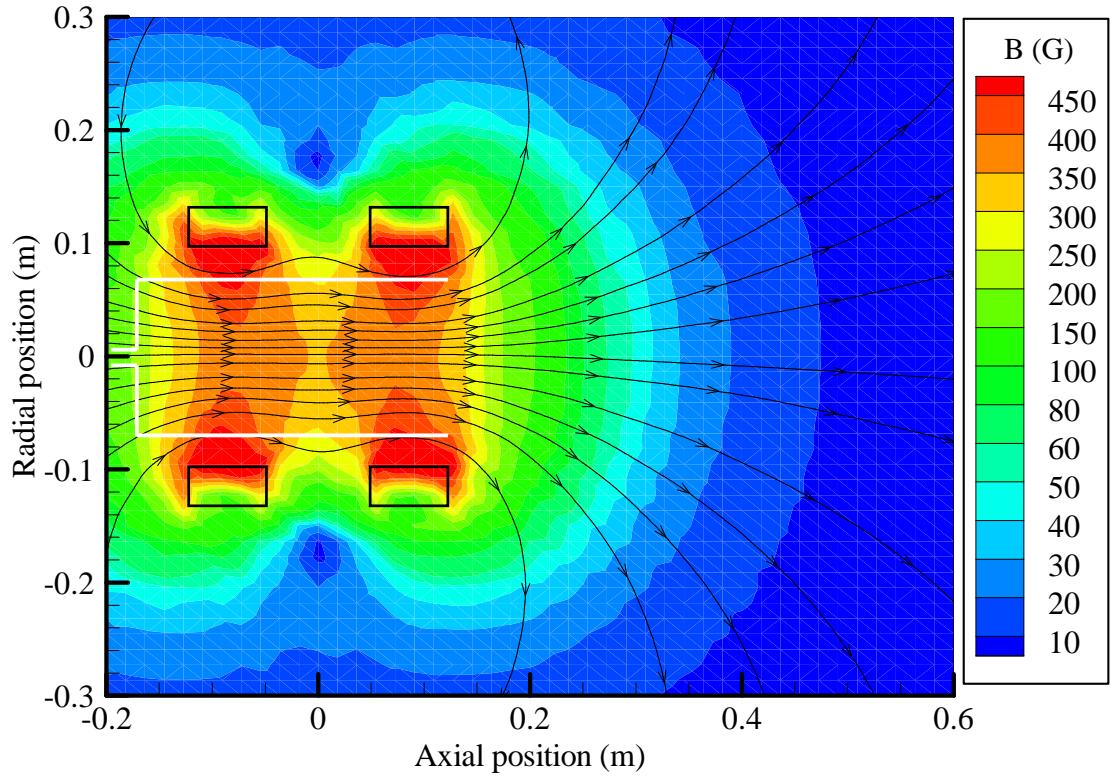
Figure 26. Helicon magnetic field contour at 8.76 A (350 G). Cross section of the solenoids denoted by black boxes, and discharge chamber wall by white lines.

Figure 27 shows the geometry of the helicon plasma source and a schematic of the RF system. The RF signal is provided by a Yaesu FT-540 HF transceiver and amplified by an ACOM 2000A linear amplifier. A LP-100 RF wattmeter monitors the RF power transmitted and measures the standing wave ratio (SWR) with an uncertainty of ± 1 W for power and ± 0.05 for the SWR. The signal is matched by a π-type matching network described in Appendix D. RF power is transmitted from the transceiver to the matching network through RG-8/U coaxial cable, and from the matching network to the antenna using RG-393.
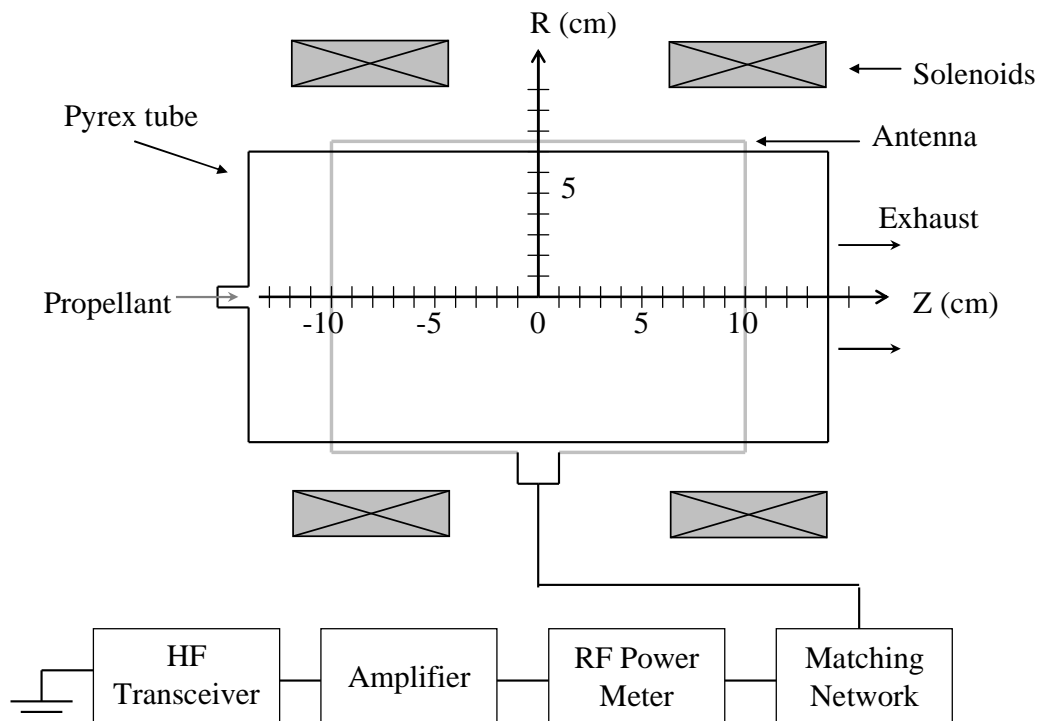
Figure 27. Helicon configuration and RF schematic.

The antenna is a double saddle antenna designed similarly to the type used by Chi and Boswell.[55] The antenna is 20.3 cm long and 15.9 cm in diameter. The antenna composed of copper strips 1.25 cm wide and 0.318 cm thick welded together. A gap of 0.635 cm

separates the two terminals that are connected to the coax cable. The antenna is wrapped in fiberglass tape to prevent direct electrical contact between the antenna and any stray plasma or the solenoids. A CAD model of the antenna is shown in Figure 28.
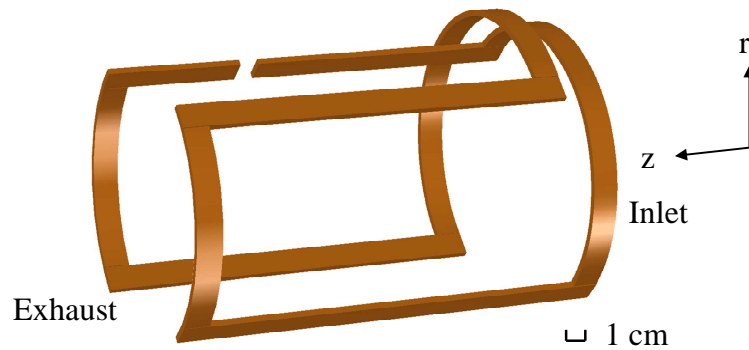
Figure 28. CAD model of the double saddle antenna.

Every connector, cable, and device has a characteristic impedance of 50 Ω. The procedure for determination of the attenuation of the transmission line is discussed in section D.4.3, but the following results summarize the findings. The matched-line loss is 0.8 and 1.5 dB at 11.9 MHz and 13.56 MHz, respectively, for the helicon thrust measurements. For all other tests the attenuation is 0.65 dB, which includes attenuation caused by the feedthrough. During thrust testing the SWR ranged from 1.01 to 1.10, which results at most in an additional 0.003 and 0.005 dB of attenuation for 11.9 and 13.56 MHz, respectively. For all other testing, the SWR did not exceed 1.04, which added an additional 0.0004 dB of attenuation. A picture of the EHT is shown in Figure 29.
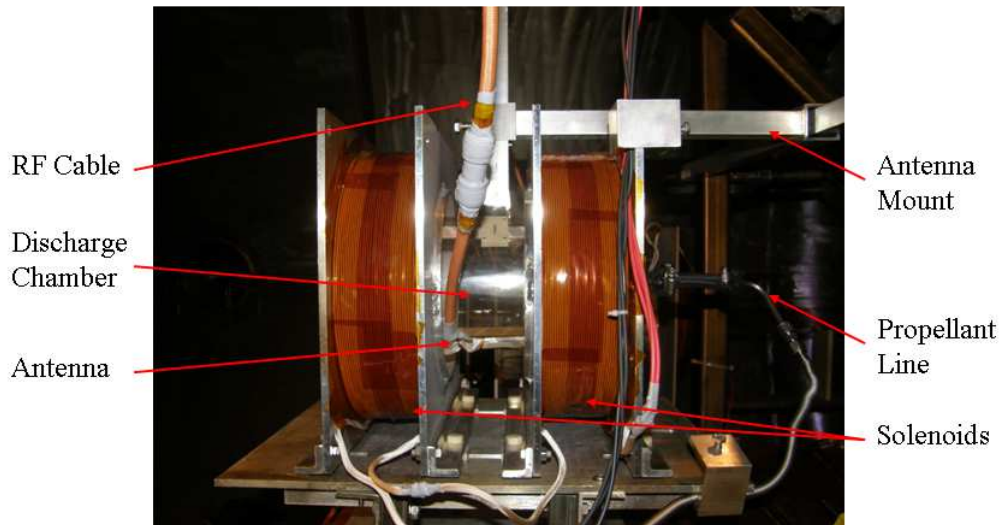
Figure 29. Electrodeless helicon thruster

4.2 GHIT Configuration

There are three main sub-systems to the helicon thruster. The first is the helicon plasma source described in Section 4.2, the second is the electrostatic grid assembly, and the third is the neutralizer cathode. The helicon plasma source ionizes the propellant gas to create a plasma, the grid assembly accelerates the ions to provide thrust, and the cathode neutralizes the ion plume to prevent charge buildup and back streaming. Within each sub-system are multiple components, such as magnetic solenoids and power supplies. A schematic of the thruster is given below in Figure 30.
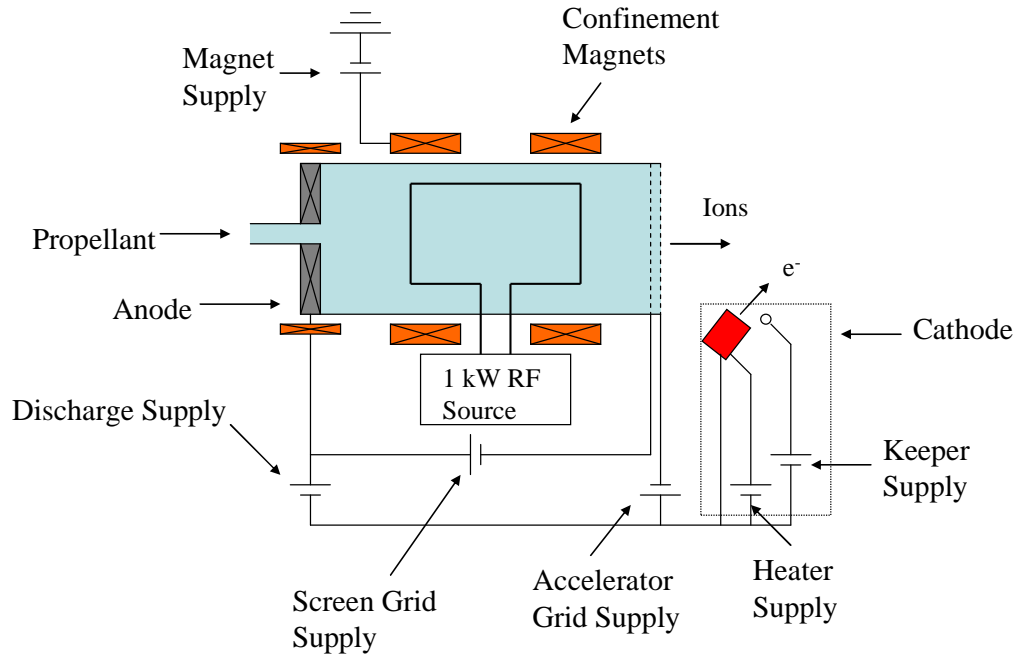
Figure 30. GHIT electrical schematic.

4.2.1 Helicon Discharge Additions

When the helicon is integrated into the thruster, two additions are made: an anode and a third solenoid. The anode is a 6.5 mm thick SS316 disc with a 13.85 cm outer diameter fit at the back of the interior of the discharge chamber. A 1.59 mm diameter, 25 mm long stainless steel rod is welded to the back of the anode and extends through a hole in the back of the discharge chamber to allow for an electrical connection to the anode. The additional solenoid has 525 turns with an inner diameter of 17 cm and is aligned with the previous two solenoids. The new solenoid is placed at the rear of discharge chamber such that the center of the anode coincides with the center of the solenoid.

As discussed in Chapter III, there are two reasons for the inclusion of the anode. The first is to allow a connection between the neutralizer cathode and the discharge plasma. As ions exit the discharge chamber, they leave behind their corresponding electrons; if left unchecked, this would create a buildup of negative charge in the discharge chamber.

76

Thus by including the anode and connecting it to the neutralizer cathode, the excess electrons can be collected and used to neutralize the ion plume.

The second purpose of the anode is to set the plasma potential within the discharge chamber. The net energy of the ions leaving the thruster is determined not by the potential drop across the grids, but by the net potential drop between the discharge plasma and the space potential, called the beam voltage. The potential drop between the grids only determines the maximum current density that can pass through the grids. Even if the acceleration grid provides a steep drop in potential, the ions would have to come back up the potential hill to end at the space potential. Thus the anode is required to push the potential of the discharge plasma above the space potential so a net potential exists to accelerate the ions. A qualitative illustration of this is shown in Figure 31.
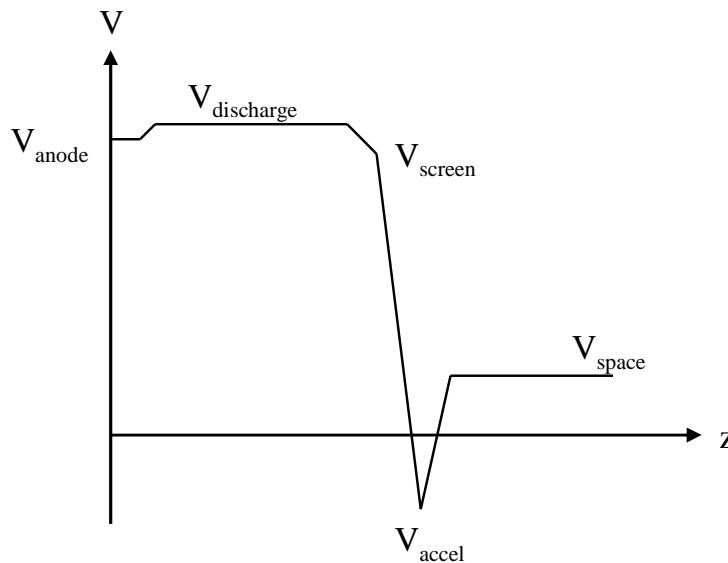
Figure 31. Qualitative plot of potential along thruster axis.

The third solenoid is added to provide variable magnetic shielding of the anode to control the flow of electrons to the anode. An increase in the axial magnetic field

strength near the anode would create a magnetic mirror effect that should decrease electron mobility to the wall. Since electrons must reach the anode to maintain discharge neutrality, the electron energy distribution will shift to a higher energy to allow sufficient electrons to pass through the barrier. Thus, it is hypothesized that increasing this magnetic barrier should increase the electron temperature of the discharge. Figure 32 shows a sample simulation of the magnetic field when the anode coil is included.
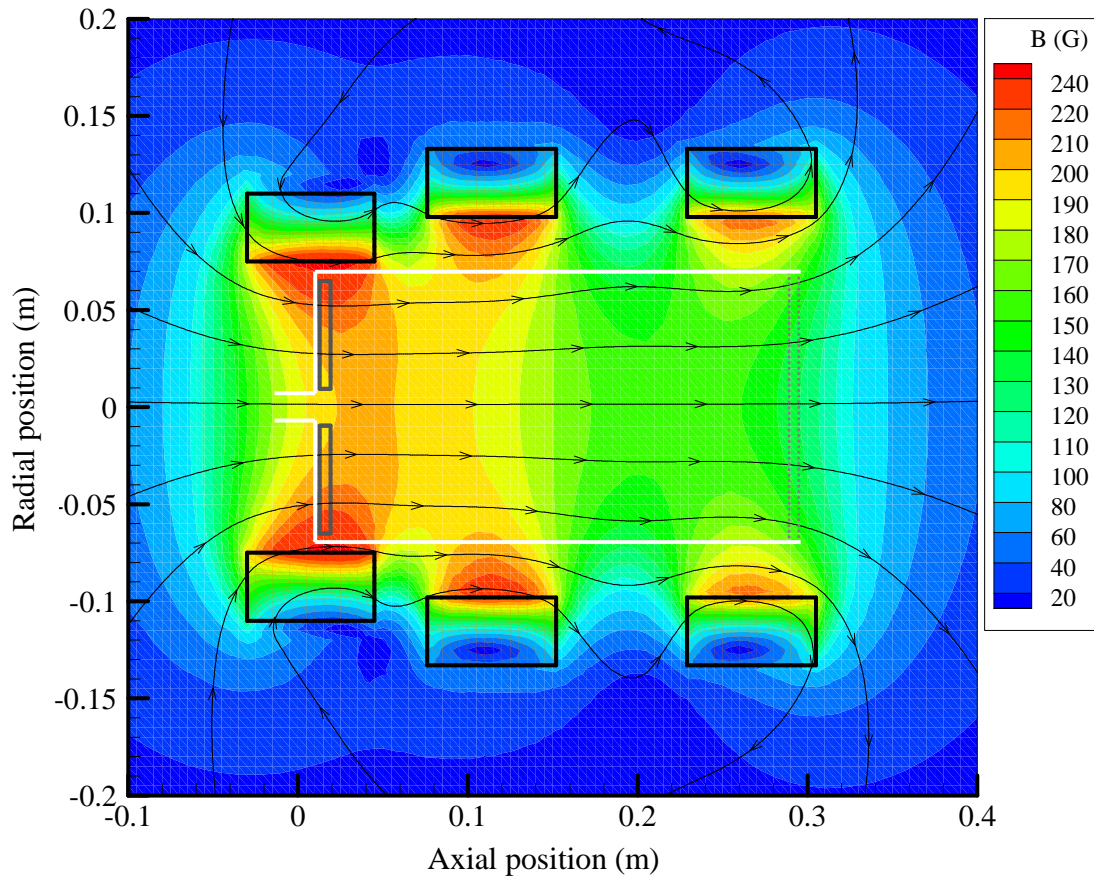
Figure 32. Magnetic field simulation of the primary solenoids at 3 A and the anode coil at 4 A. The cross section of the anode is represented by the grey boxes, the solenoids by the black boxes, the chamber wall by the white lines, and the grids by the dashed grey lines.

4.2.2 Grid Design

The grid design assumes an ion number density of 2×10^{16} m^{-3} and an electron temperature of 5 eV. The screen grid aperture diameter is set to be ten times larger than the Debye length from Equation (3.2), yielding 1.5 mm. The accel grid aperture diameter is chosen to be 1.2 mm, with a grid thickness of 0.635 mm and a grid separation of 1.0 mm. Both grids are laser-cut from SS 316 with the apertures arranged in a 60° hexagonal pattern with a 1.75 mm pitch.

The grid assembly starts with a base piece fabricated from polyether ether ketone (PEEK) sized to fit on the end of the discharge chamber. The screen grid is mounted on the base where four protrusions extend from the base and fit into side holes of the grid to restrict rotational motion of the grid. An imbedded aluminum electrode allows connection to the screen grid through the side of the base. Two 0.5 mm thick mica rings are placed on top of the screen grid to maintain the designed 1.0 mm grid separation distance. The accel grid is set within a PEEK holder that contains protrusions similar to the base for the same reason. The PEEK holder also has two protrusions on the side that match two recessions on the final piece, the grid press. The grid press is also fabricated from PEEK and bolts to the base part. The grid press serves two functions: sixteen set screws compress the grid stack together, and the grid press covers the sides of the grids, preventing arcing around the mica. The combination of the nested protrusions maintains aperture alignment. One of the set screws is aligned with a hole in the accel grid holder that allows electrical contact to the accel grid. Four screws mount the entire assembly to the discharge chamber. Figure 33 shows an exploded CAD view of the grid assembly.
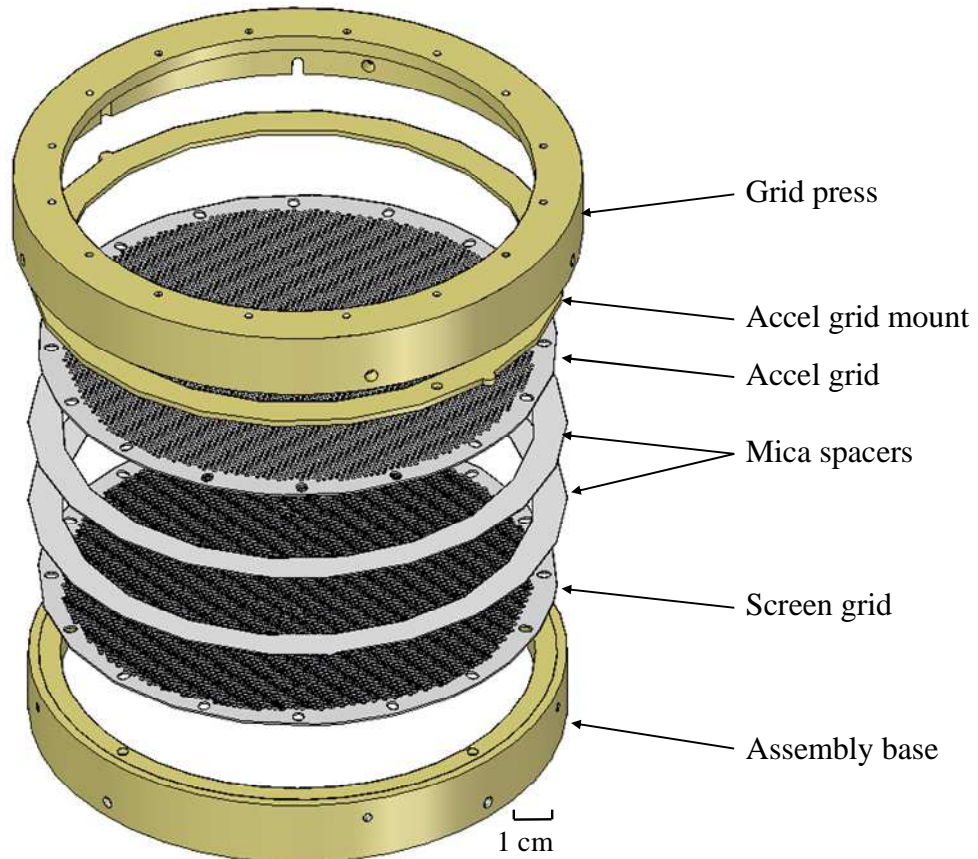
Figure 33. Exploded view of the grid assembly.

4.2.3 Neutralizer Cathode

The function of the neutralizer cathode is to draw excess electrons from the discharge plasma and eject them into the exhaust plume. This allows for the ions to neutralize downstream of the thruster and prevent charge buildup and back streaming. The cathode of choice for this thruster design is a lanthanum hexaboride (LaB_6) hollow cathode following the design of the Moscow Aviation Institute. The cathode consists of a pellet of LaB_6 as the electron emissive material placed in a molybdenum holder. A coil of tungsten is wrapped into a helical spring to fix the LaB_6 in place while also serving as the heater. A thin sheet of molybdenum is bent to form a cylindrical radiation shield that extends along the length of the heater coil. The radiation shield serves two purposes: it reduces radiation losses from the heater coil and acts as an electrical connection between

the heater coil and the heater connection rod that extends out the back of the cathode. Ceramic spacers fix the position of the radiation shield and heater connection relative to a center threaded rod that serves as a common cathode connection. The center assembly then fits inside a titanium shell with molybdenum foil wrapped around it, while a tantalum disc with a center bore is placed in front of the pellet; these both serve as thermal insulation to prevent the titanium shell from melting. Once the LaB_6 pellet reaches its operating temperature it emits electrons; by flowing a gas through the cathode the number of electrons emitted is increased by secondary emission via collisions of the primary electrons into the neutral atoms. An extraction wire called a keeper is placed just past the center orifice to aid in electron generation. A schematic of the cathode is shown in Figure 34.
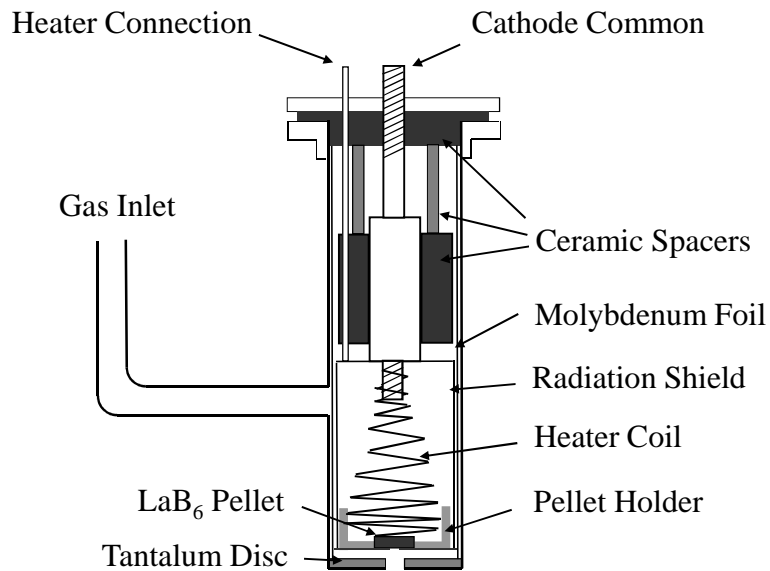
Figure 34. Cathode schematic.

81

4.2.4 GHIT Operation

Pictures of the fully assembled thruster are shown in Figure 35 and Figure 36.

Cathode

Anode coil

Discharge
chamber

Antenna
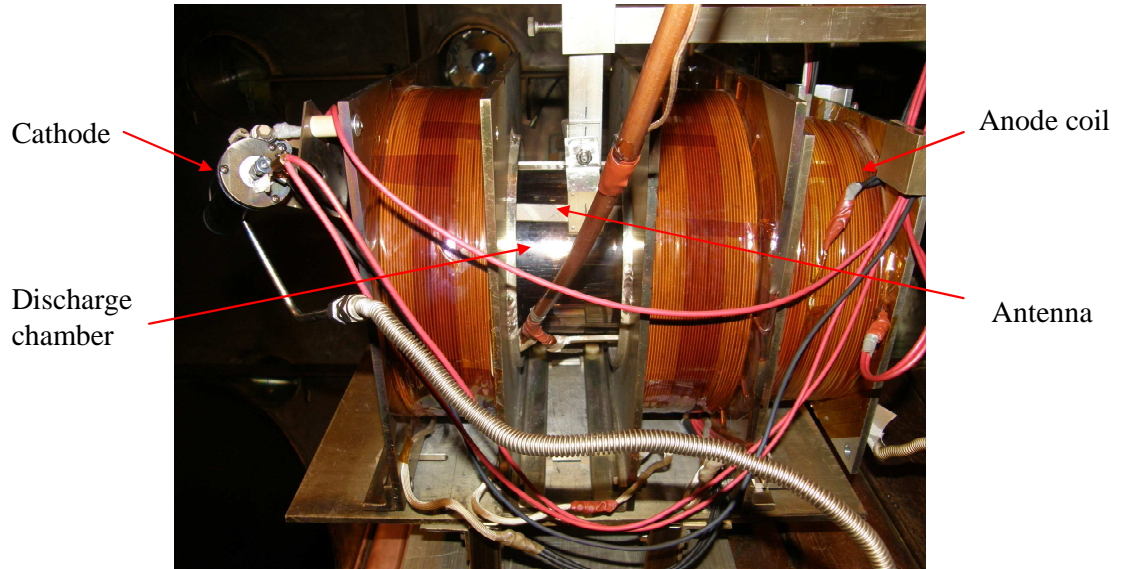
Figure 35. Side view of the GHIT.

Cathode
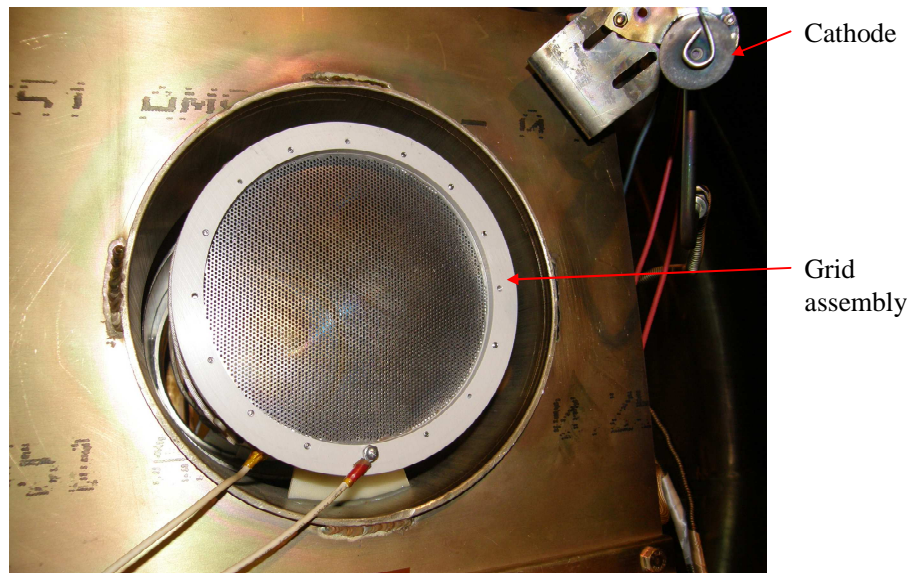
Grid
assembly

Figure 36. Front view of the GHIT and grid assembly.

GHIT operation is begun by first starting the cathode. The cathode is purged for 10 minutes with 5 sccm of argon. The cathode is progressively heated by running 5, 9, and then 11 A through the heater coil in 15 minute increments. When the heater current is at 11 A the gas flow through the cathode is increased to 9 sccm and the keeper is then biased to 100 V to start the electron extraction.

The next stage of the engine startup is to set the grid potentials and the axial magnetic field. The screen grid is biased 35 V below the anode, the voltage empirically found to repel all electron current to the grid. The accel grid is biased 150 V below cathode common; this potential is low enough to prevent electrons from the cathode back streaming into the discharge yet not low enough to decrease the voltage ratio R considerably. The discharge supply is initially set to 100 V in order to reduce total ion energy for any ions that might strike the accel grid during RF startup. The discharge propellant flow is then opened. The RF discharge is lit by matching the system impedance and then spiking the power up to 1.2 kW; the power is rapidly lowered to the desired operating point, and the matching network is re-tuned to the new load impedance. The discharge supply is set to the desired voltage. Figure 37 shows a picture of the GHIT operating at 600 W RF power, 150 G magnetic field, 600 V discharge, and 1.5 mg/s argon flow rate.
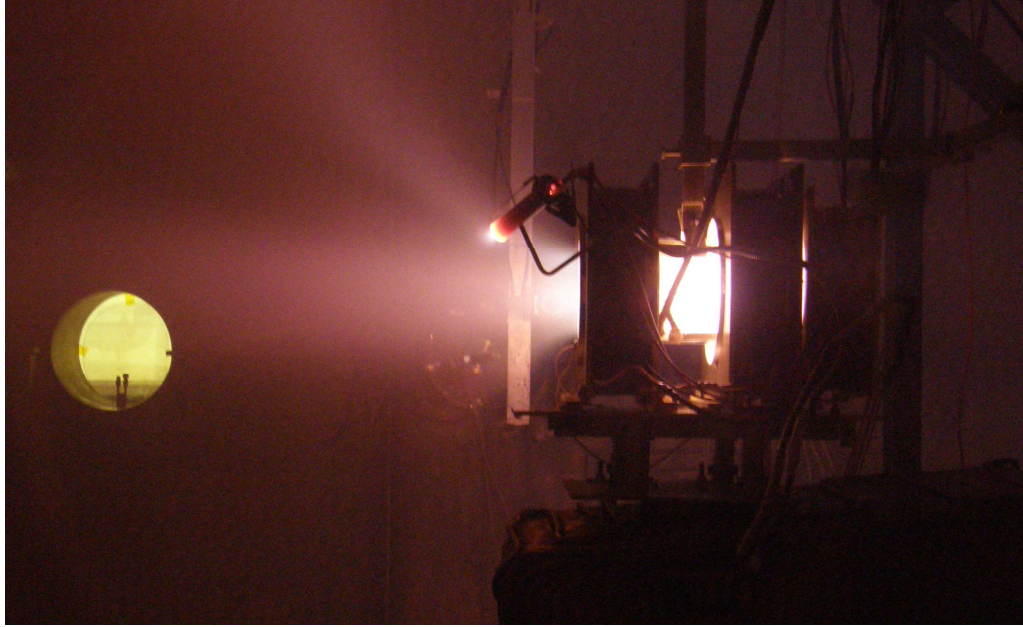
Figure 37. GHIT operation at 600 W, 150 G, 600 V, 1.5 mg/s argon.

4.2.5 Performance Model

The thrust, T, produced by an engine is

$$T = \gamma\left(\dot{m}_i v_i + \dot{m}_n v_n\right) \tag{4.1}$$

where γ is the plume divergence factor, $\dot{m}_i$ and $\dot{m}_n$ are the ion and neutral exit mass flow rates, respectively, and v_i and v_n are the ion and neutral exit velocities, respectively. Assuming the ions have negligible velocity inside the discharge chamber, the ion velocity is

$$v_i = \sqrt{\frac{2eV_b}{m_i}} \tag{4.2}$$

The ion mass flow rate can be related to the beam current as

$$\dot{m}_i = \frac{m_i}{e} I_b \qquad (4.3)$$

The beam current through the grids is dependent on two processes: the current flux from the discharge plasma into the grid sheath and the space charge limitation. Therefore the total beam current is the product of the ion current density over the transparent area of the grids.

$$I_b = j_i T_s A_g \eta_o \qquad (4.4)$$

Substituting Equation (4.4) into (4.3),

$$\dot{m}_i = \frac{j_i}{e} \eta_o T_s A_g m_i \qquad (4.5)$$

$$j_i = \begin{cases} j_{Bohm}, j_{Bohm} < j_{max} \\ j_{max}, j_{Bohm} > j_{max} \end{cases} \qquad (4.6)$$

The definitions of j_{Bohm} and j_{max} are given below from Equations (3.6) and (3.10).

$$j_{Bohm} = 0.61 e n_0 \left(\frac{k_b T_e}{m_i} \right)^{1/2} \qquad (3.6)$$

$$j_{max} = \frac{4\varepsilon_0}{9} \left(\frac{2e}{m_i} \right)^{1/2} \frac{(V_s - V_a)^{3/2}}{l_e^2} \qquad (3.10)$$

It should be noted that in Equation (4.5) the transparency used is the geometric transparency, which does not take into account ions that pass the screen grid and then strike the accel grid. Therefore an ion optics efficiency term is included in the ion mass flow definition to correct for this occurrence.

$$\eta_o = \frac{I_b}{I_b + I_A}$$ (4.7)

By Equation (3.6), the thrust varies with the discharge plasma density and temperature with a maximum allowable value set by the given grid potentials.

$$T = 0.61 \dot{m}_0 \eta_o T_s A_g \sqrt{2k_b T_e V_b e}$$ (4.8)

$$T_{max} = \gamma \varepsilon_0 \eta_o T_s A_g \sqrt{\frac{32}{81} V_b} \frac{(V_s - V_A)^{3/2}}{l_e^2}$$ (4.9)

Note that the thrust is independent of the mass of the propellant used. Instead, the choice of propellant is important in the discharge, where the ionization cost and collisional cross section is important in determining the di`scharge efficiency.   Equation (4.8) is an expression of the thrust in terms of the beam voltage and beam current with the beam current defined in terms of the discharge plasma parameters. However, it is still useful to conceptualize the component terms together as the beam current, shown below.

$$T = I_b \gamma \sqrt{\frac{2m_i V_b}{e}}$$ (4.10)

4.3 Conclusions

The two thruster configurations that make up the case study are presented. The EHT and GHIT both share the same helicon plasma source, which allows for measurements of the plasma structure inside the EHT discharge chamber to also be utilized with the GHIT. As outlined in Chapter III, this is advantageous, as gradients of the ion number density and plasma potential are required for the discharge efficiency model. With the two configurations fabricated, the next step is to determine the diagnostic equipment required to measure the selected performance metrics.

CHAPTER V

FACILITY AND DIAGNOSTICS

Thus far this dissertation has introduced the stated aim of evaluating the ion acceleration mechanisms between a single-stage and a two-stage helicon thruster, reviewed the physical processes of both acceleration mechanisms, and presented the two thruster configurations. In order to evaluate the two configurations, several figures of merit have been selected that encompass how well each thruster accelerates ions: the ion energy, the beam current, and the beam divergence half-angle. Direct thrust measurements are also desired to verify the predicted performance to the actual results.

In order to measure these quantities, several diagnostic instruments are required. The beam divergence half-angle, as well as beam current of the EHT, is determined using a Faraday probe, which measures the current density profiles across an angular sweep of the plume. A retarding potential analyzer is selected to measure the ion energy distributions, as it can selectively measure the change in ion current as a function of repulsion potential, much like a high pass filter. Finally, thrust is measured using an inverted pendulum thrust stand.

Additionally, in order to evaluate the ion acceleration of the EHT, measurements of the plasma plume structure are required to compare against the measured ion energies. The plasma structure inside the discharge chamber is also required to calculate the ion production cost of the GHIT. There are three plasma parameters that capture the structure of the plume: plasma potential, ion number density, and electron temperature.

These quantities can be determined using a combination of an emissive probe and a Langmuir probe. This chapter details the design and operation of each of the above diagnostic tools, as well as the vacuum system used during the experiments.

5.1 Vacuum Facility

All experiments are conducted in Vacuum Test Facility 1 (VTF-1). VTF-1 is a stainless steel vacuum chamber 4 m in diameter 7 m in length. Two 3800 CFM blowers and two 495 CFM rotary-vane pumps evacuate the chamber to a moderate vacuum (about 30 mTorr). High vacuum is reached by using six 48" diffusion pumps with a combined pumping speed of 485,000 l/s on argon. The presence of optical baffles at the inlet of the diffusion pumps reduces the effective pumping speed to 125,000 l/s. The chamber pressure is measured with a BA-571 ion gauge connected to a Varian SenTorr controller with an accuracy of 20%.[56] An MKS type 247 four-channel readout in conjunction with an MKS 1179 mass flow controller regulates the gas flow into the helicon with an accuracy of 1%.[57] The base pressure of VTF-1 for these experiments is 1.1×10^{-5} Torr. Figure 38 shows a schematic of the VTF.
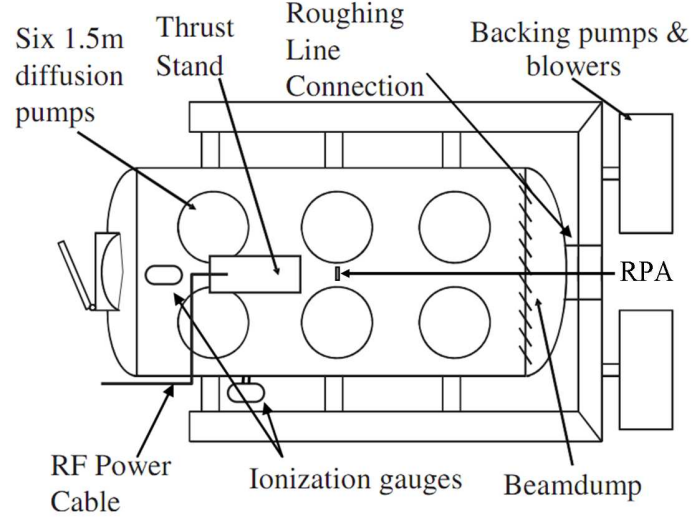
Figure 38. Schematic of VTF-1.

Operating pressure, p_o, is derived by a correction of the pressure measured by the ion gauge, given by

$$p_o = \frac{p_g - p_b}{\chi} + p_b \qquad (5.1)$$

where p_g is the pressure given by the ion gauge, p_b is the base pressure, and χ is the gas correction factor, which is 1.29 for argon. All pressures presented in this work, save for base pressures, are corrected for argon.

VTF-1 has a two-axis linear motion system and rotary table that enables the traversing of plasma diagnostics for spatial mapping. The linear tables are 1.5 m long model of the 406XR series by Parker Automation with a positional accuracy of ±134 microns and a bidirectional repeatability of ±3.0 microns. The rotary table is a 200RT from Parker Automation with an accuracy of ±10 arc-min and a unidirectional repeatability of ±0.5 arc-min.

5.2 Thrust Stand

The thrust of the helicon is measured using a null-type inverted pendulum thrust stand.[58] This type of stand maintains the thruster at a fixed position with a solenoid surrounding a center magnetic rod. By varying the current through the solenoid with a PID controller, the restoring force on the thrust stand, and therefore the thrust of the device, can be correlated to the solenoid current. The thrust stand is calibrated by the application of a series of known weights which allow a curve fit between solenoid current and applied weight. A water-cooled copper shroud surrounds the stand components to maintain a constant device temperature.

Figure 39. (*left*) **Thrust stand;** (*right*) **copper shroud**

Due to the design of the helicon, which includes an RF antenna, there are two issues that must be addressed during setup to ensure accurate thrust measurement of any device using the helicon. The first is drift of the thrust stand due to thermal expansion of the RF cable. As RF power is propagated through the cable, the power attenuated by the cable is absorbed into the cable by Ohmic heating. As the cable temperature increases, the cable expands, pushing on the antenna which in turn pushes on the device and ultimately deflects the thrust stand. To prevent this, the antenna is physically separated from the rest of the device and mounted to a three axis bracing mount, shown in Figure 40. This fixes the antenna in place such that it contacts neither the discharge chamber nor the solenoids, while allowing device to move smoothly along the axis of the thrust stand. Additionally, the RF cable makes a roughly 270º spiral to the antenna, allowing the cable to thermally expand along the arc, rather than directly into the device.
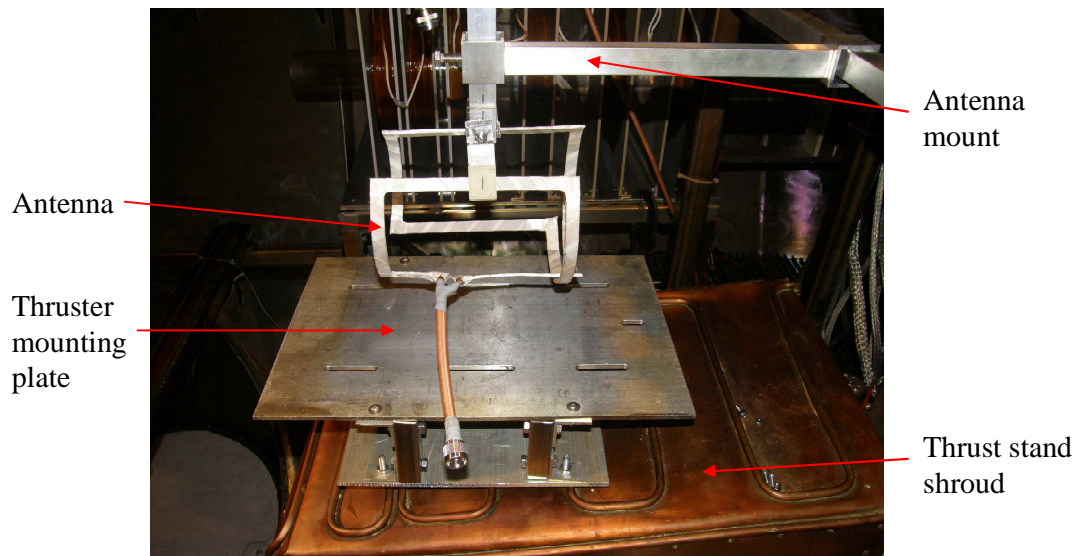
Figure 40. RF antenna mounted on brace above thrust stand.

The second issue with measuring the thrust of a helicon on a thrust stand is the elimination of any RF pickup in the thrust stand signal lines. Originally, it appeared as a DC offset to the measured thrust stand null coil current required to maintain the thrust stand position whenever the helicon was turned on. The problem occurred even when the helicon was removed from the thrust stand and placed on the floor of the chamber a meter away. This phenomenon is indicative of a ground loop caused by faulty RF shielding between the thrust stand electronics and the RF system. The solution is to separate the electronics ground from the RF ground and to shield the electronics and associated data lines from the RF signal. Inside the chamber, all signal lines are isolated from chamber ground while providing additional grounded shielding inside the chamber to prevent RF pickup. Outside the chamber, the signal lines are still isolated from chamber ground, but the cable shielding is connected to the thrust stand electronics common ground. Each electronic component of the thrust stand is placed in a grounded enclosure tied to the common ground, which is ultimately connected to the ground of a single wall outlet. This removes all RF offset during helicon operation.

There is a large amount of uncertainty in the thrust measurements due to the sensitivity of the thrust stand to vibrations. The load spring used in the thrust stand is one variable to control vibrations, with a looser spring to reduce vibrations. However, for heavier loads a stiffer load spring is needed to restrict thrust stand deflection, which increases sensitivity to vibrations. Generally this is mitigated by the fact that a heavier thruster produces higher thrust. In this case the helicon source has a mass of about 35 kg, which is comparable to a Hall effect thruster but with a much lower thrust. As a specific comparison, a T-140 Hall thruster has 200 mN of thrust with an uncertainty of ±2.3 mN,

which is only 1.1% of the measured value;[58] the helicon has an average thrust of 3 mN and an uncertainty of ±1.7 mN, which is approximately 57% of the measured value. For this study, thrust stand uncertainty is defined as the standard deviation of the null coil output from the mean value for the sample set used to determine the null coil position at each point.

5.3 Faraday Probe

A Faraday probe is a well-known diagnostic that measures ion current density in thruster plumes.[59-65] The primary function of the Faraday probe is to determine the plume shape in terms of the location of the plume beam current along a circular arc centered on the exit plane of the thruster. The shape is quantified by the beam divergence half angle, the angle from the center of the plume that captures 90% of the ion beam current, as illustrated in Figure 41. Ideally the divergence angle should be as low as possible, as this signifies a highly collimated beam where minimal ion energy is spent on radial motion and axial velocity is maximized.
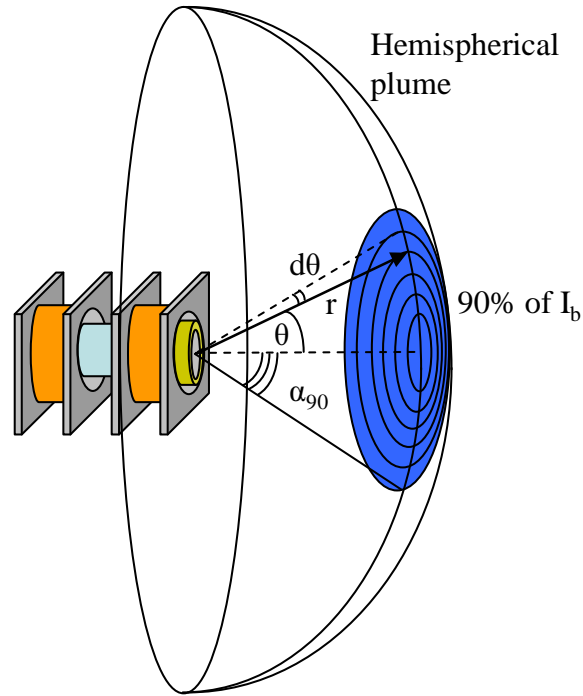
Figure 41. Illustration of 90% beam divergence half-angle. Blue shaded region denotes 90% of beam current content.[60]

5.3.1 Probe Construction

A Faraday probe consists of two primary elements: a collector and a guard ring. The collector is biased negatively to repel electrons, which ensures that the current collected by the probe is solely due to ions and not reduced by a partial electron collection. As the collector is biased a plasma sheath forms around the probe to transition from the negatively biased probe to the plasma potential. A concern is that as the sheath forms the edges of the sheath are curved, which enlarge the effective ion collection area. It is for this reason the guard ring is present. By biasing the collector and guard ring to the same potential, the sheath is extended so that the sheath above the collector is parallel to the plane of the collector, and only the guard ring collects ions from the edge of the sheath. Since the collector is isolated from the guard ring, the effective collection area is equal to

the area of the collector, giving a more accurate measurement of the current density. An illustration of this effect is shown in Figure 42.
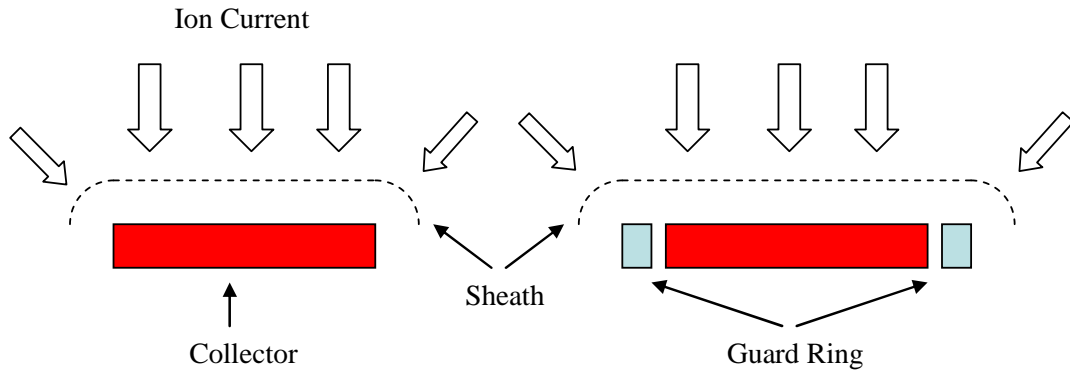
Figure 42. Guard ring effects. Probe on the left collects additional ion current from the curved edges, while the probe on the right has the guard ring to extend the plasma sheath and collect the ion current from the edge.

The collector is a tungsten coated aluminum disk 22.4 mm in diameter and 6.05 mm thick. The guard ring is 25.2 mm in outer diameter with a thickness of 0.75 mm and is 5.52 cm long. A threaded rod is attached to the back of the collector and passes through the back of the probe, serving as the electrical connection. Inside the probe the threaded rod is separated from the guard ring by a ceramic spacer. A schematic and picture of the probe are shown in Figure 43 and Figure 44, respectively
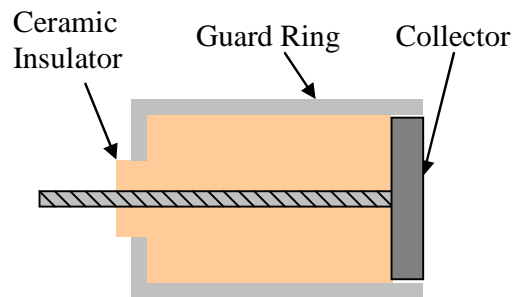
Figure 43. Faraday probe schematic.

Figure 44. HPEPL Faraday probe.

5.3.2 Divergence Angle Calculation

The current density is measured along a semicircle with the exit plane of the thruster at the center. The total beam current can then be calculated by integrating the current density across the surface area of the hemisphere,

$$I_b = \int_{-\pi/2}^{\pi/2} \int_{-\pi/2}^{\pi/2} j(\theta, \phi) r^2 \sin\theta \, d\theta \, d\phi \qquad (5.2)$$

where the angles θ and φ are defined in Figure 45.
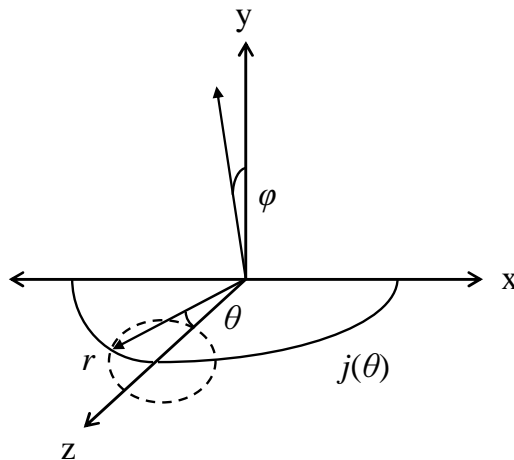
Figure 45. Current density integration geometry. Dashed circle represents differential area, and the ions exit in the positive z direction.

Assuming that the plume is radially symmetric, the current density is only a function of the angle θ. With this assumption, the integration can be conceptualized as the summation of a series of infinitesimally thin circular rings of radius $r\sin\theta$ and thickness $rd\theta$. Equation (5.2) becomes

$$I_b = \int_{-\pi/2}^{\pi/2} 2\pi r^2 j(\theta)\sin\theta d\theta \qquad (5.3)$$

Since the data is collected at discrete intervals, the integral can be converted into a series summation.

$$I_b = \sum_{-\pi/2}^{\pi/2} 2\pi r^2 j(\theta)\sin\theta(\Delta\theta) \qquad (5.4)$$

The divergence half angle, α_d, is arbitrarily defined as half of the sweep required to contain 90% of the beam current. Mathematically this is stated as

$$0.9I_b = \sum_{-\alpha_d}^{\alpha_d} 2\pi r^2 j(\theta)\sin\theta(\Delta\theta) \qquad (5.5)$$

The beam divergence factor quantifies the lost thrust caused by radial ion velocity in the plume, as radial velocity in a symmetric plume has no net force contribution. Instead, the net force on the thruster is the axial component of the velocity. Thus, the beam divergence factor is defined as

$$\gamma = \cos \alpha_d \qquad\qquad (5.6)$$

5.3.3 Measurement Circuit and Uncertainty

Both the collector and the guard ring are biased using a Xantrex XPD 60-9 power supply. The positive terminal of the XPD is grounded, which biases the probe below chamber ground. The two electrodes of the probe are biased using separate coaxial cables to eliminate RF pickup. A 99.4 Ω shunt in the collector line is used to measure the current using a 34970A data acquisition unit (DAQ). A schematic of the probe circuit is shown below in Figure 46.
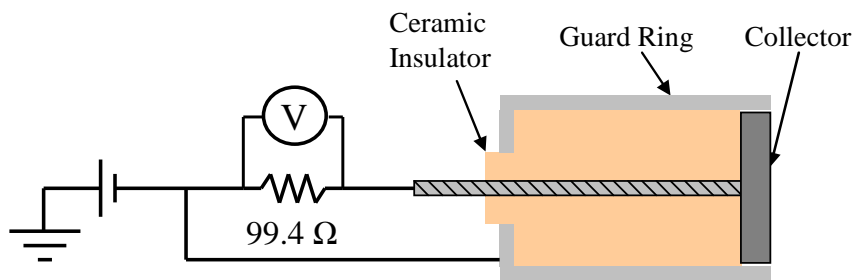
Figure 46. Faraday probe circuit.

There are three sources of uncertainty associated with the use of a Faraday probe: secondary electron emission, the area of the probe, and the measurement circuit. The first source of uncertainty with the probe is the potential for secondary electron emission (SEE). SEE is the phenomenon where a particle strikes a surface with sufficient energy to induce the emission of an electron from the surface. The probe therefore collects a positive charge and emits a negative charge, which is indistinguishable from the collection of two positive charges and results in an inaccurate measurement. In order to

reduce this occurrence, the aluminum collector is coated in tungsten, which has a lower

SEE coefficient of 0.1 electrons per ion,[66] which gives an uncertainty of $\pm 10\%$.

The other source of uncertainty within the probe is the effective collection area. In

theory, the collection area should be the area of the face of the collector disc. While the

purpose of the guard ring is to enforce this collection area, it is possible for ions to strike

the collector along the edge in between the collector and the guard ring. The effective

collection area is[64,65]

$$A_{c,eff} = A_c + \kappa_g \tag{5.7}$$

where A_c is the area of the face of the collector, and κ_g is the gap correction term,

$$\kappa_g = \pi\left(r_s^2 - r_c^2\right)\frac{2\pi r_c h_c}{2\pi r_c h_c + 2\pi r_s h_s} \tag{5.8}$$

where r and h are the radius and height of the collector and guard ring, denoted by

subscripts c and s, respectively. The effective area is 418 mm^2 compared to the collector

face area of 394 mm^2, which gives an uncertainty of $\pm 6.29\%$.

The uncertainty of the measurement circuit is dependent on the uncertainty of the

shunt resistance and the voltage measurement. The uncertainty of the DAQ is $\pm 0.0045\%$,

while the uncertainty of the resistance is $\pm 0.4\%$. Combining the uncertainties yields a

total uncertainty for the divergence angle of $\pm 12\%$.

5.4 Retarding Potential Analyzer

The retarding potential analyzer (RPA) is a diagnostic tool that measures the ion energy distribution function of a thruster plume.[67-69] A basic RPA consists of two grids and a collector coaxially aligned within, and isolated from, a stainless steel cylinder. The first grid, termed the electron repulsion grid, is negatively biased relative to ground to repel plasma electrons while the second grid, called the ion repulsion grid, is positively biased to retard ions. The electron repulsion grid prevents electrons from the plasma from reaching the collector and reducing the effective collection current. The potential of the ion repulsion grid determines the energy the ions need to pass through. Thus the probe acts as a high pass filter, allowing only ions with energy higher than the ion repulsion grid to pass through to the collector. By sweeping the potential of the ion repulsion grid, a plot of the collected ion current as a function of the applied potential can be created.

5.4.1 Theory of Operation

The ion current, I, collected by the RPA is defined as

$$I_i = qeA\Phi \qquad (5.9)$$

where q is the charge state of the ion, e is the charge of an electron, A is the area of the collector, and Φ is the ion flux incident on the collector surface. The ion flux is a function of the ion number density and the average ion velocity given by

$$\Phi = n_i \langle v_i \rangle \tag{5.10}$$

It should be noted that it is not the total average velocity that should be used but the average velocity orthogonal to the plane of the collector. As long as the axis of the RPA is aligned with the plume the two velocities are the same. However, if this is not the case, there is an additional $\cos\theta$ term that must be included, where θ is the angle between the axis of the RPA and the axis of the thruster plume. From here on it is assumed the RPA is aligned with the thruster plume so the $\cos\theta$ term is equal to one. The average velocity is defined as

$$\langle v_i \rangle = \int_{-\infty}^{\infty} v_i f(v_i) dv_i \tag{5.11}$$

where $f(v)$ is the velocity distribution function of the ions. Substituting the definitions of the average velocity and ion flux into the ion current collection equation yields the following.

$$I_i = qeAn_i \int_{v_{min}}^{\infty} v_i f(v_i) dv_i \tag{5.12}$$

The lower bound of the integral has been reset to v_{min} as only certain velocities of ions can reach the collector. At the very least, v_{min} must be greater than zero, as a negative velocity would indicate an ion traveling away from the collector.

Since the RPA operates by varying ion repulsion potential, it is worthwhile to perform a change of variable from velocity to potential. This is accomplished by relating the kinetic energy of an ion to electric potential energy.

$$v_i = \sqrt{\frac{2qeV}{m_i}} \tag{5.13}$$

Substituting into the above equation and setting the lower bound to V_{min} yields

$$I_i = qeAn_i \int_{V_{min}}^{\infty} \sqrt{\frac{2qeV}{m_i}} f(V) \frac{1}{2} \sqrt{\frac{2qe}{m_i V}} dV$$

$$I_i = \frac{q^2 e^2 An_i}{m_i} \int_{V_{min}}^{\infty} f(V) dV \tag{5.14}$$

where V_{min} is defined as the minimum potential an ion must exceed to pass through the repulsion grid to the collector. In practice this is the potential of the ion repulsion grid. Assuming the distribution function is finite as V goes to infinity, both sides of the equation can be differentiated to yield

$$f(V) = -\frac{m_i}{q^2 e^2 An_i} \frac{dI}{dV} \tag{5.15}$$

Thus with a sweep over a range of ion repulsion potentials, the generated plot of ion current versus potential can be used to determine the ion energy distribution function.[66]

One item to note with an RPA is the electric potential energy is a function of the charge state q. Since the ion is repelled as a function of only potential energy, the RPA cannot distinguish two singly charged ions at some set energy or one doubly charged ion at that same energy. Therefore the presence of doubly charged ions can potentially inflate the population of a certain energy in the energy distribution function. It is also possible that a doubly charged ion can be partially neutralized by a single electron after it is accelerated but before it reaches the RPA, and thus have twice the energy-to-charge ratio expected. This would appear in the energy distribution function as a secondary peak at high energy, generally around twice the average ion energy expected.

5.4.2 Probe Construction

A more advanced RPA has four grids, rather than just the two previously mentioned. In order from the aperture towards the collector they are the floating, electron repulsion, ion repulsion, and electron suppression grids. The floating grid has no active potential applied and becomes charged to the plasma potential. This serves to reduce perturbations in the plasma caused by the presence of the other biased grids. The electron suppression grid has a negative potential relative to the plasma to repel any secondary electrons emitted due to ion collisions with the ion repulsion grid.

The RPA used in this study is a four-grid design shown in Figure 47. Each grid is 203 μm thick 316 stainless steel 3.15 cm in diameter with a 31% transparency, 229 μm aperture diameter, 394 μm pitch with a hexagonal hole pattern. The grids are separated by Macor spacers; the thickness of the spacers, going from right to left in Figure 47, is 1.588 mm, 3.175 mm, 1.588 mm, 6.350 mm, and 6.350 mm. The collector is a 3.15 cm diameter copper disc 0.8 mm thick. Electrical wires are spot welded to each component

and run down a groove machined into the side of the grid-spacer stack. The stack is housed in a Macor tube which is placed inside an aluminum housing. The diameter of the aperture in the front face of the housing is 2.286 cm. A photograph of the RPA used is shown in Figure 48.
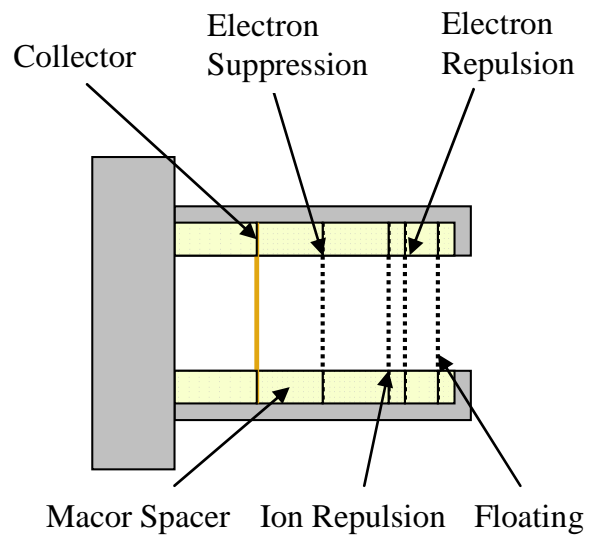
Figure 47. RPA cross-section schematic.

Figure 48. HPEPL four-grid RPA.

5.4.3 RPA Operation

A circuit diagram of the RPA is shown in Figure 49. The potential of the electron suppression and repulsion grids is negatively biased relative to ground and jointly supplied by a Xantrex XPD 60-9 power supply. As an aside, while it is possible to control the two electron grids separately, it was found to have no real advantage. The ion repulsion potential is biased above ground by a Keithley 2410 SourceMeter. The current from the collector is measured by a Keithley 6485 Picoammeter. The voltages of both power supplies are measured by an Agilent 34970A data acquisition unit. The current measured by the picoammeter is translated into an analog output by the unit which is measured by the DAQ. In order to eliminate RF pickup, each signal line to the RPA is an RG-58 coaxial cable with the shield grounded to the chamber if inside the chamber, and the electronics ground if outside the chamber. This effectively isolates the electronics from the RF signal while maintaining a continuous shield around the signal line. The feedthroughs used do not connect the shield of the BNC connector to the chamber.
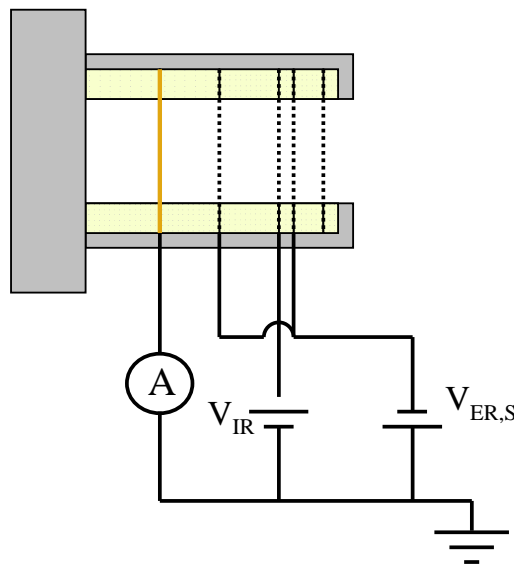
Before any measurement of an ion energy distribution can be done, there are several preliminary steps that must be taken. The first is determination of the electron repulsion and suppression grid voltages sufficient to eliminate electron current. This is done by placing the RPA at the desired location for measurement with no grid voltages applied. The ion current on the collector grid is then measured as the electron suppression and repulsion grid voltages are increased. The desired repulsion and suppression voltage is that which causes the collection current to be maximized, which demonstrates that electron current to the collector has been eliminated. An example sweep is shown in Figure 50.
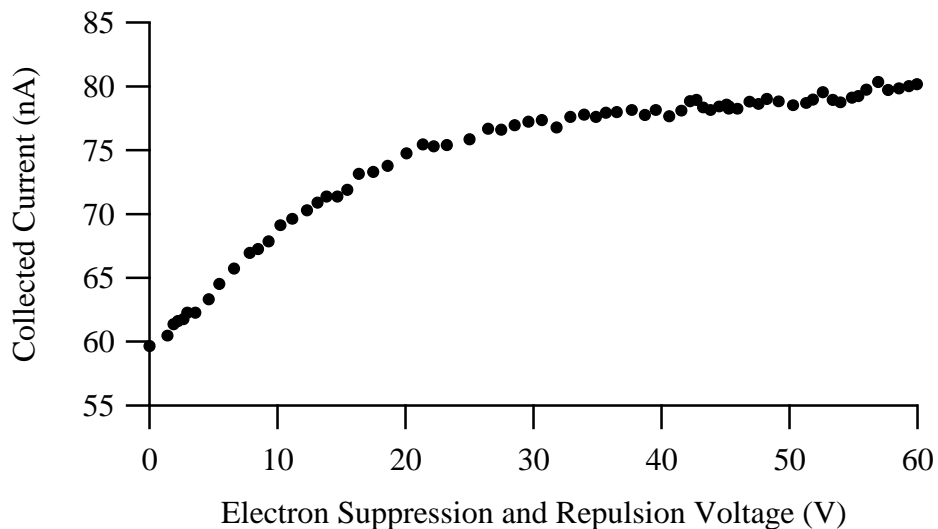
Figure 50. Example saturation sweep 50 cm downstream. 343 W RF power and 350 G.

The next step is to take a high voltage scan with a larger voltage interval to determine the maximum voltage needed on the ion repulsion grid to capture the entire energy profile. This ensures that voltage sweeps cover the minimum required voltage range

107

needed, and allows for a smaller resolution while ensuring that no features of the energy profile are missed. As an example, for the sweep shown in Figure 51, the required voltage range is 0-100 V to fully capture the energy profile.
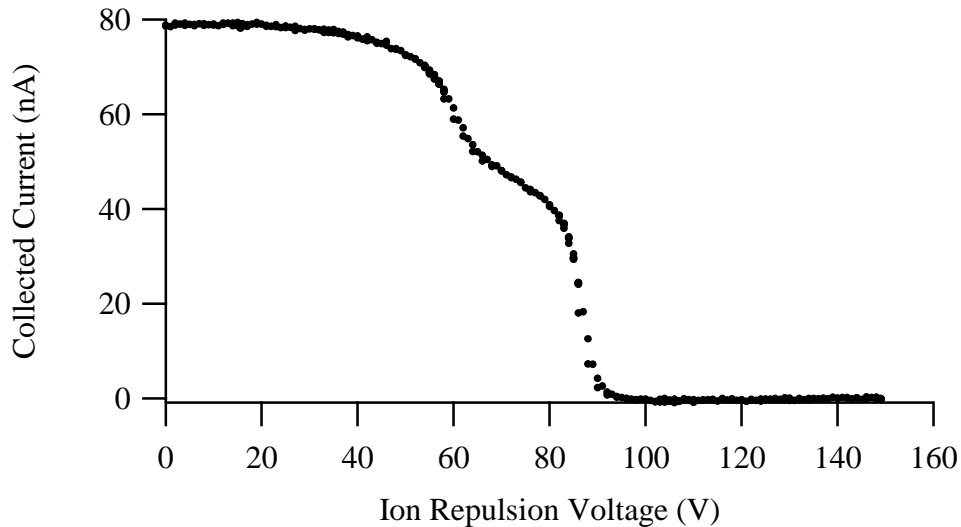
Figure 51. Example high voltage sweep 50 cm downstream. 343 W RF power and 350 G.

Once these preliminary steps are completed, six voltage sweeps are taken of the range of interest at intervals of 0.5 V with a delay of 400 ms at each voltage. The multiple scans are found to have excellent agreement that demonstrates a high degree of repeatability. Figure 52 shows an example plot of three such scans. During the voltage sweeps, the output of the picoammeter and the bias on the grids are measured every 300 ms. This creates several instances of multiple measurements at the same voltage, but these are subsequently averaged together to ensure one current measurement for a given ion repulsion voltage. The six scans are then averaged together and passed through a locally weighted scatter plot smoothing algorithm (LOESS) to remove irregularities.

While this process does introduce a small measure of uncertainty, it is required to eliminate small perturbations that are magnified when calculating the derivative.
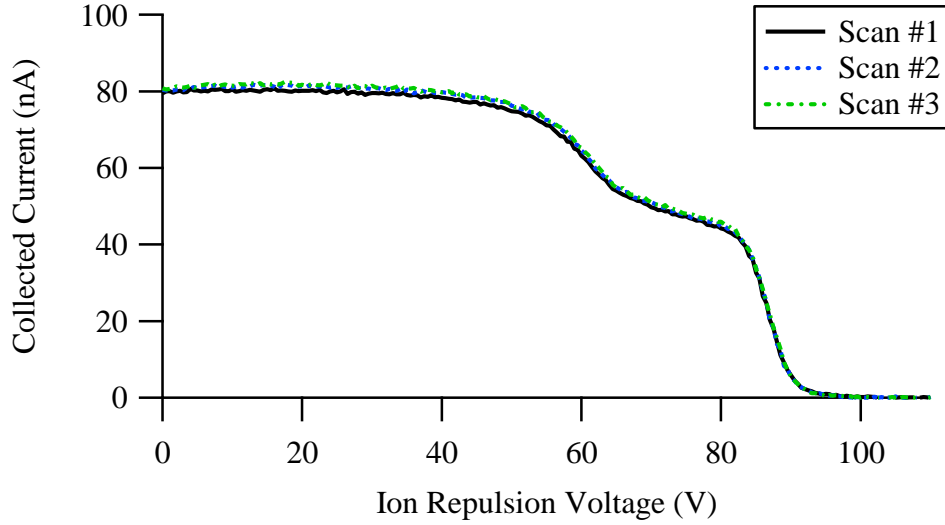
Figure 52. Example of three similar RPA voltage sweeps 50 cm downstream. 343 W RF power and 350 G.

The derivative is then numerically calculated using Newton's Difference Quotient. For terms not at either end of the sweep, the derivative is calculated as shown in Equation (5.16).

$$\left(\frac{dI}{dV}\right)_i = \frac{I_{i+1} - I_{i-1}}{V_{i+1} - V_{i-1}} \tag{5.16}$$

For terms at the beginning and end of the sweep the derivative is calculated as

$$\left(\frac{dI}{dV}\right)_0 = -\frac{I_1 - I_0}{V_1 - V_0} \tag{5.17}$$

$$\left(\frac{dI}{dV}\right)_N = -\frac{I_N - I_{N-1}}{V_N - V_{N-1}} \qquad (5.18)$$

An example of a LOESS-smoothed I-V trace and the resultant derivative is shown below in Figure 53.
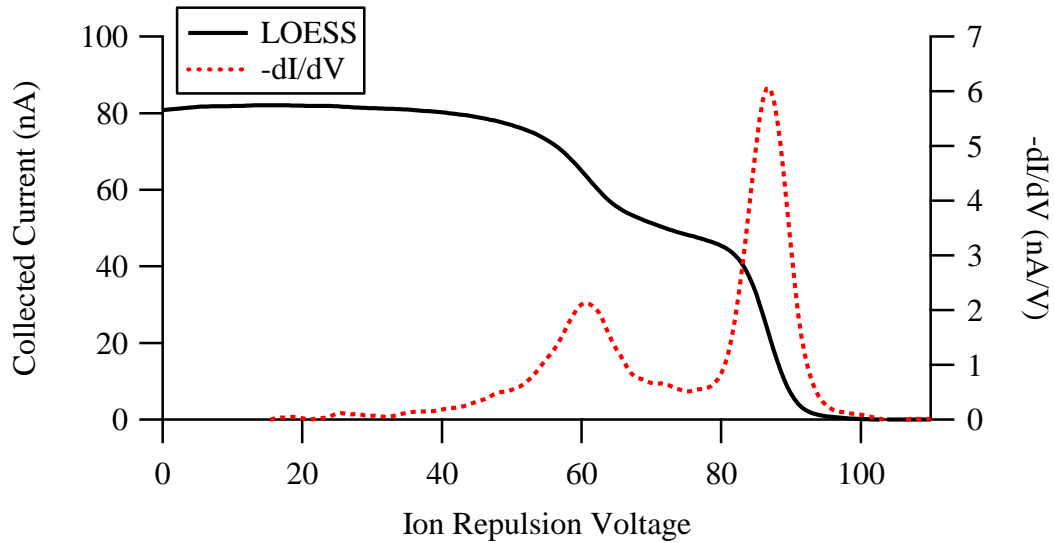
Figure 53. Example LOESS smoothed I-V trace and resultant derivative 50 cm downstream. 343 W RF power and 350 G.

5.4.4 Uncertainty Analysis

The first source of uncertainty is the measuring instruments. The 2410 SourceMeter has a voltage source accuracy of 0.02% with an additional $\pm$ 100 mV while in the 1000 V range.[70] The 6485 Picoammeter has an accuracy of 0.2 % with an additional $\pm$ 10 pA in the 200 nA range, and 0.15% with an additional $\pm$ 100 pA in the 2 μA range.[71] The DAQ has an accuracy of 0.0045%.[72] Combined, the instrument uncertainty at its highest is less than 0.25%. The next source of uncertainty is caused by LOESS-smoothing, which is calculated below in Equation (5.19).

$$E_{LOESS} = \frac{\sqrt{N \sum (I_{LOESS,i} - I_i)^2}}{\sum I_i} \qquad (5.19)$$

where N is the number of points in the sweep, I_i is the average current at point i, and $I_{LOESS,i}$ is the current at point i of the smoothed trace. This uncertainty is essentially the standard deviation of the LOESS curve compared to the average curve normalized by the average current. The final source of uncertainty is determined by comparing an RPA to a 45° parallel plate electrostatic energy analyzer, which found a 3.8% discrepancy in the location of the most probable voltage.[67,73] The total uncertainty of the RPA is thus the combination of all the components, shown in (5.20).

$$E_{RPA} = \sqrt{0.0025^2 + E_{LOESS}^2 + 0.038^2} \qquad (5.20)$$

5.5 Emissive Probe

Emissive probes are a category of internal plasma diagnostics that use an electron-emitting surface to measure the plasma potential.[74,75] The general form of this emitting surface is a thin metal filament heated to thermionic emission by passing a current through it. There are two methods for using an emissive probe: either as an emitting collector, or as a pure emitter. The first method applies a bias on the emitting probe relative to ground and measures the current emitted by the probe. By sweeping the probe bias much like a Langmuir probe, the plasma potential can be measured as the probe potential at which emission ceases.[76] This method is known as the inflection point method. The second approach to emissive probes is to heat the filament to emission and

allow the probe to float. If the filament wire is heated to a sufficient temperature the probe will float at the plasma potential; this method is called the floating method. Due to the simplicity of the approach, the floating method will be used.

5.5.1 Theory of Floating Operation

The basic premise of a floating emissive probe is to remove the plasma sheath between the probe and the bulk plasma. Suppose a floating electrode is inserted into a plasma. Since electrons are more mobile, they will collect on the electrode faster and reduce the potential. As the potential drops, more electrons are repelled and ions attracted until the rate of charge collection is balanced, which is the basis of the plasma sheath. The electrode is now at the floating potential.

Now suppose that this electrode is a thin filament that is a resistive element of a floating DC circuit. When heated, the filament thermionically emits electrons into the sheath, which reduces the net electron current into the filament and increases the potential of the filament away from the floating potential. As the amount of current passed through the filament is increased, the electron emission and probe potential are likewise increased. At a sufficient heater current, the filament emits enough electrons to remove the plasma sheath and the probe floats at the plasma potential; at this point the probe has reached saturation. Any additional heating past saturation produces very little additional emission, as the probe is now at the plasma potential and any additional electrons must overcome an adverse potential gradient. From another perspective, the emissive probe tip maintains charge flux balance by emitting the same number of electrons that the plasma sheath repelled, thus removing the need for a sheath to form. Figure 54 shows a diagram

of how the non-emissive and the emissive tips interact with the plasma and how the potential varies therein.
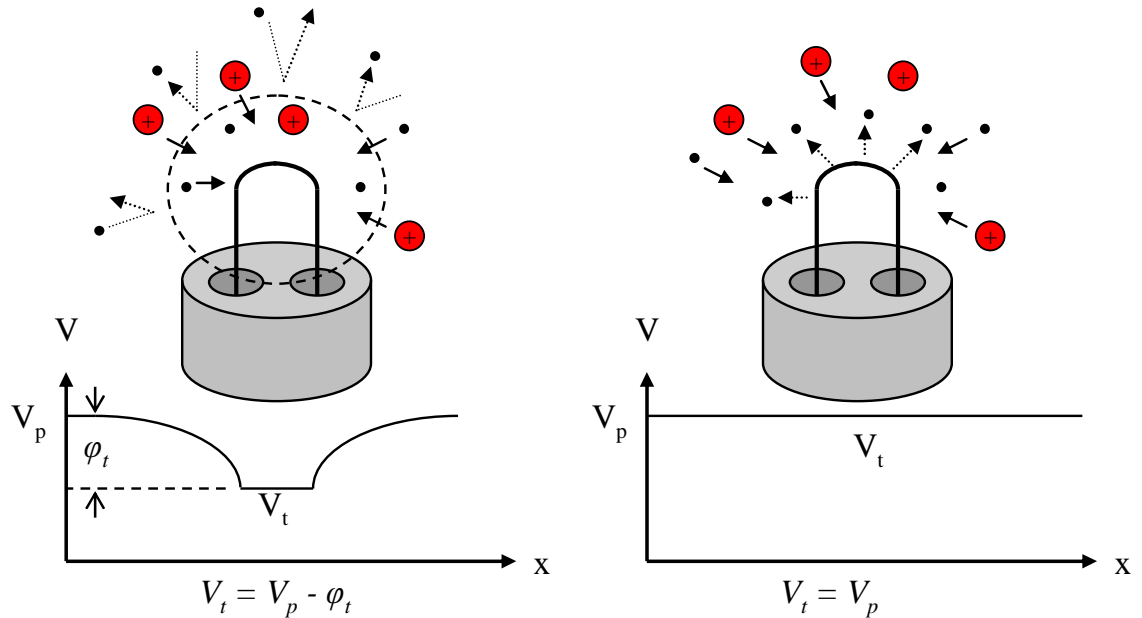
Figure 54. Emissive probe tip interacting with the plasma. The non-emissive tip with a plasma sheath (left) and the emitting tip at saturation (right) both collect zero net current. The non-emissive tip repels excess electron current using the plasma sheath, but a sheath potential separates the plasma and tip potentials. The emissive tip collects any incident electron and emits a current equal to the excess, and with no sheath, the tip potential is equal to the plasma potential.

While the above method is simple and easy to perform, there is one concern that must be addressed. In the presence of large magnetic fields there can be space charge limitations that can restrict emission and create a difference in potential between the saturated probe and the plasma. This can be avoided by having a filament with a diameter smaller than the Larmor radius of an electron. This criterion is described by the relation[74]

$$B \ll 4.8 \frac{\sqrt{T_e}}{d_f} \qquad (5.21)$$

where B is the magnetic field in gauss, T_e is the electron temperature in eV, and d_f is the filament diameter in cm.

5.5.2 Probe Construction

The probe tip is constructed using a 0.127 mm diameter thoriated tungsten wire filament inserted into a 12 cm long double bore ceramic tube with a 1.5 mm outer diameter and 0.375 mm diameter bores. The filament is bent around a 0.75 mm diameter stainless steel rod to ensure a rounded edge. A drawing of the probe tip geometry is shown in Figure 55. Inserted in the other end of both bores is 28 gauge copper wire with Kapton insulation, which is wedged against the tungsten to create a mechanical connection. The ceramic tube is inserted into one bore of a 4.65 mm outer diameter double bore tube with a bore diameter of 1.5 mm. This larger ceramic tube is then fed into a G-10 tube that is 14.3 mm in outer diameter and 4.76 mm in inner diameter. The G-10 tube fits inside an aluminum sleeve that is welded to an RF compensation box and secured with a set screw. The interface between tubes is sealed using fiberglass tape covered with ceramic paste. The total length of the probe is 32 cm from the tip to the RF compensation box.
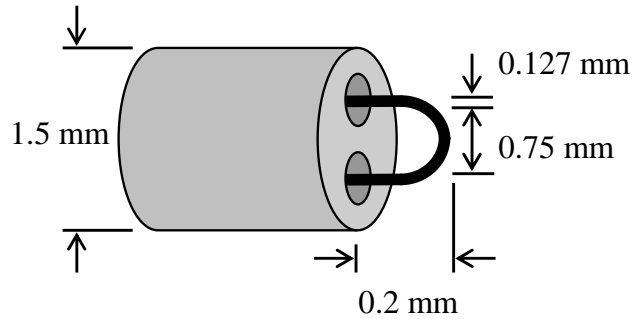
Figure 55. Emissive probe tip geometry.

The RF compensation box serves to choke any AC signal from contaminating the probe signal while allowing any DC signal to pass unimpeded. While the plasma potential is expected to oscillate in an RF plasma, it is the time-averaged DC component that is responsible for ion drift and therefore is the value of interest.[77] The two copper wires from the emissive probe tip are connected to a custom high temperature terminal made of aluminum and Teflon. The other side of the terminal is connected to two 22 gauge high temperature wires that are wrapped around ferrite toroids to create an RF choke. Each choke consists of a 1.27 cm inner diameter, 2.54 cm outer diameter series M ferrite from National Magnetics Group with 25 windings of the signal wire. At 13.56 MHz each choke provides an impedance of 5600 Ohms. Selection of the ferrite and the calculation of the impedance are detailed in Section 3.3 of Appendix D. The other end of the high temperature wire is connected to a BNC jack that is isolated from the box chassis. Figure 56 shows a picture of the interior of the RF compensation box. The chassis itself is left floating, and the compensation box is mounted on a G-10 bar with a 2.54 x 2.54 cm cross section that is 60 cm long. The G-10 bar is then mounted on an aluminum arm mounted on the two axis motion table. G-10 is used in place of a conductive material to eliminate the impact a grounded conductor would have on the plasma. Figure 57 shows a picture of the complete emissive probe.
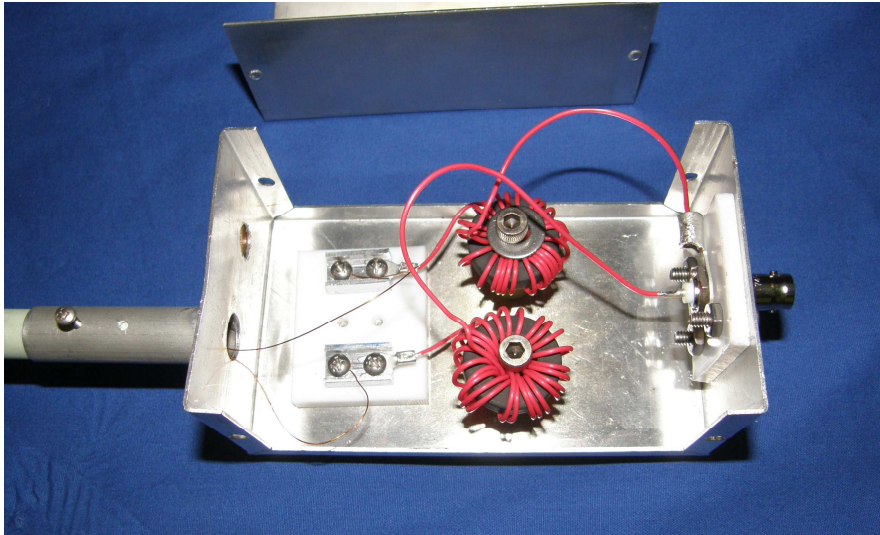
Figure 56. RF compensation box.
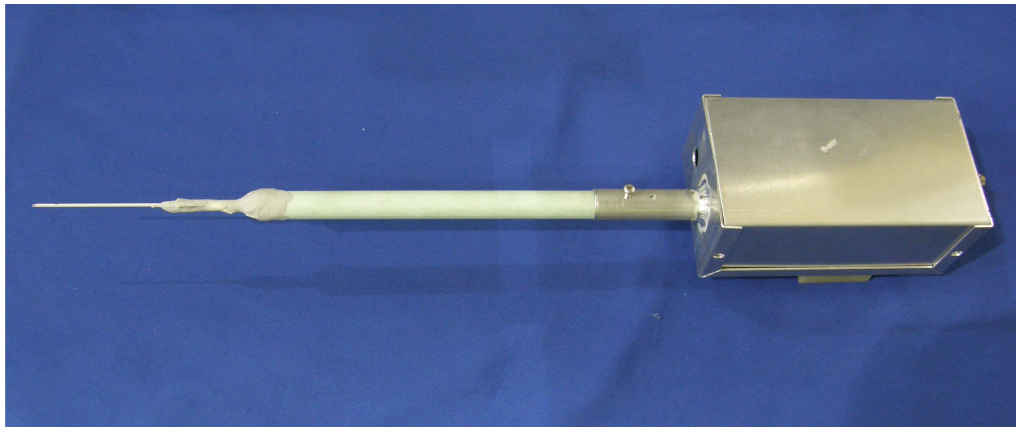
Figure 57. Complete RF-compensated emissive probe.

5.5.3 Measurement Circuit

The two leads of the emissive probe are connected to a DC power supply that is floated using an isolation transformer. A 25W, 0.1 Ω resistor is placed in series on each leg of the probe to provide for a low resistance current shunt to measure the heater current. A resistor is placed on both sides of the circuit to maintain similar resistance on each. The potential of each side of the probe is measured relative to ground through a 1 MΩ load resistor using an Agilent 34970A data acquisition unit that has an internal

resistance of 10 MΩ. The probe potential is calculated as the average of the two leg potentials.
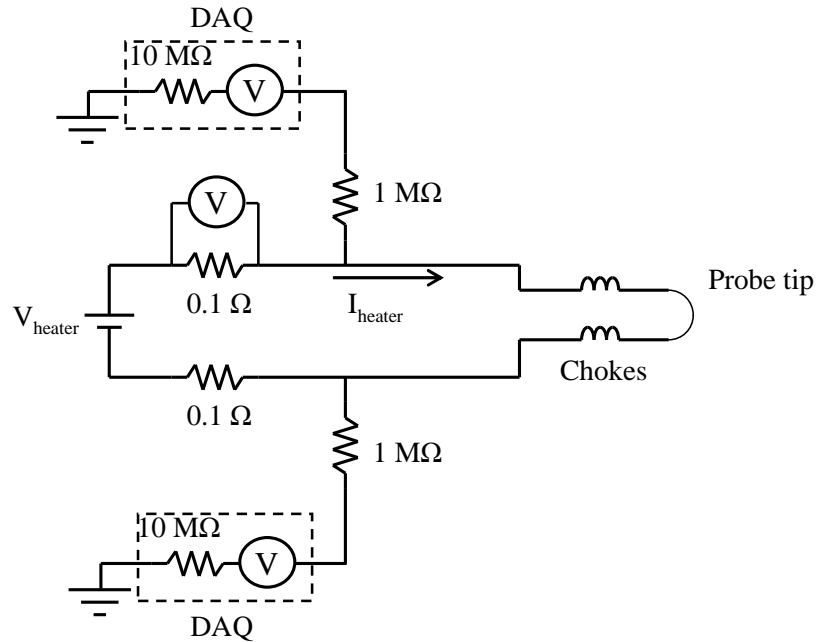
Figure 58. Emissive probe measurement circuit.

5.5.4 Data Analysis

Ideally, the emission of electrons from the tungsten filament should eliminate the sheath around the probe tip. In practice, the temperature of the emitted electrons is set by the temperature of the wire, which is much lower than the electron temperature of the plasma. This creates two electron populations: cold emitted electrons and hot plasma electrons. The two populations create a double sheath at the probe tip, which reflects some emitted electrons back into the probe and some plasma electrons away from the probe. The result is that the measured probe potential is actually slightly below the plasma potential. This can be corrected using[78]

$$V_p = V_{p,raw} + 0.6 \frac{kT_e}{e} \qquad (5.22)$$

The uncertainty of the corrected plasma potential is ± 0.9 kT$_e$/e.[78,79] An additional uncertainty is added by the presence of a finite potential drop across the filament to drive the heater current. The value varies with each probe due to minor differences in probe construction. The voltage drop ranges from 6.59-10.3 V, which gives on average an uncertainty of ± 4.36 V.

5.6 Langmuir Probe

A Langmuir probe is a conductive electrode inserted into a plasma for diagnostic purposes. While Langmuir probes have many variations in electrode shape and number, the simplest form is a single cylindrical rod. Langmuir probes are primarily utilized by applying a varying bias on the electrode and measuring the collected plasma current. From this I-V trace the plasma density, temperature, and potential can be determined. However, this process is time-consuming to conduct and calculation-intensive to process. A floating emissive probe can measure the plasma potential more accurately and conveniently, but cannot alone determine density or temperature. However, if an emissive probe is used in conjunction with limited Langmuir probe measurements, the parameters can be determined.

5.6.1 Theory of Operation

To determine electron temperature and density, there are two measurements that are needed: the floating potential and the ion saturation current. The floating potential is the

potential the Langmuir probe reaches in the plasma with no applied bias or path to ground. The electron temperature can be estimated by comparing the plasma potential measured by the emissive probe to the floating potential, since the difference in potentials is the sheath potential of the sheath surrounding the probe tip. Substituting the difference of the plasma potential and the floating potential into Equation (3.8) yields

$$V_p - V_f = -\frac{k_b T_e}{e} \ln\left(0.61 \sqrt{\frac{2\pi n_e}{m_i}} \right)$$
(5.23)

The uncertainty with this method is ±17%.[79]

The ion saturation current is the current the probe collects when it is biased sufficiently negative relative to the plasma such that all electrons are repelled. Since the electron temperature ranges from 2-12 eV, the probe is saturated as long as it is at least 60 V below the plasma potential. Since the ion current collected is the Bohm current through the sheath from the bulk plasma, the plasma density can be determined using Equation (3.6) multiplied by the area of the probe, A_p.

$$I_{sat} = 0.61 e n_0 A_p \left(\frac{k_b T_e}{m_i} \right)^{1/2}$$
(5.24)

5.6.2 Probe Construction

Since each point of data from the Langmuir probe must correspond to the same location for each point of the emissive probe, the Langmuir probe uses the emissive probe architecture and simply replaces the tip. Instead of the tungsten filament and the

1.5 mm diameter ceramic double-bore tube, a 0.76 mm diameter 304SS rod extends out of the same bore of the 4.65 mm diameter double-bore ceramic tube. The rod is soldered to a wire that runs to the RF compensation box, passes through one of the RF chokes, and is connected to a shielded coax cable. In order to have a defined probe area, only 7.37 mm of the rod is exposed to the plasma; the rest is insulated using Kapton. The probe is mounted to the motion table in the same manner as the emissive probe and measurements are taken after completing emissive probe measurements without altering the setup.

CHAPTER VI

EHT PERFORMANCE

The EHT is intended to evaluate the ion acceleration capability of the helicon plasma source as a single-stage device. Chapter II revealed the operating parameters that can be used to control the EHT are RF power, RF frequency, magnetic field strength, and propellant flow rate. Furthermore, the characteristic of interest for evaluating the plasma plume structure compared to the ion energy distribution is the plasma potential. Additionally, measurements of the ion number density and electron temperature inside the discharge chamber are needed to calculate the ion production cost of the GHIT.

This chapter presents the performance evaluation of the EHT and measurements of the plasma characteristics inside the helicon discharge chamber and the downstream plume. The ion acceleration performance metrics used are ion energy, ion beam current, and beam divergence half angle. The measured plasma characteristics are plasma potential, electron temperature, and ion number density. Thrust, specific impulse, and efficiency are also measured to quantify thruster performance capability and to compare against the contribution by ion acceleration. The EHT has an average beam divergence half angle of 82°, beam currents in the range of 7-47 mA, and 20-40 eV ion energy. The downstream plume structure is highly dependent on the axial magnetic field strength. Conical regions of high plasma potential and electron temperature form off the discharge chamber wall and extend downstream. The size and intensity of these regions increases as the axial magnetic field increases. Further analysis of these regions is done in Chapter

VII, but initial estimates of the thrust contribution due to ions show that very little power is spent accelerating ions. Instead, the EHT most likely produces thrust through thermal expansion of the propellant collisionally heated by the plasma.

6.1 Thrust Performance

The first steps in evaluating thruster performance are to measure the thrust of the device and calculate the specific impulse and thrust efficiency. These parameters are used to characterize the energy expended accelerating ions compared to ion production and thruster losses. In the specific case where a helicon double layer thruster is under evaluation, there is considerable interest in the thrust efficiency since the design has no direct control over the acceleration mechanism. Therefore, it is important to determine what effect the operating parameters have on the efficiency, as that would suggest which parameters could control the ion acceleration mechanism.

6.1.1 Thrust Measurements

To begin, a preliminary survey is conducted varying RF frequency, RF power, axial magnetic field strength, and mass flow rate. The results, shown in Figure 59 and Figure 60, reveal two observations. First, there is little discernable change in the thrust as the operational parameters are varied, given the average uncertainty of ±1.9 mN. The observed effects of the magnetic field or mass flow rate are almost completely within the measurement uncertainty. Only varying the RF power has any impact greater than the measurement uncertainty. The second observation is thrust is rather low for the power used. As a comparison, the thrust-to-power ratio of a T-220 Hall Effect thruster is at least

50 mN/kW,[64] while the observed thrust-to-power for the helicon thruster is at best around 8 mN/kW. To confirm whether this is an indicator of low ion acceleration, the thrust efficiency must be examined.
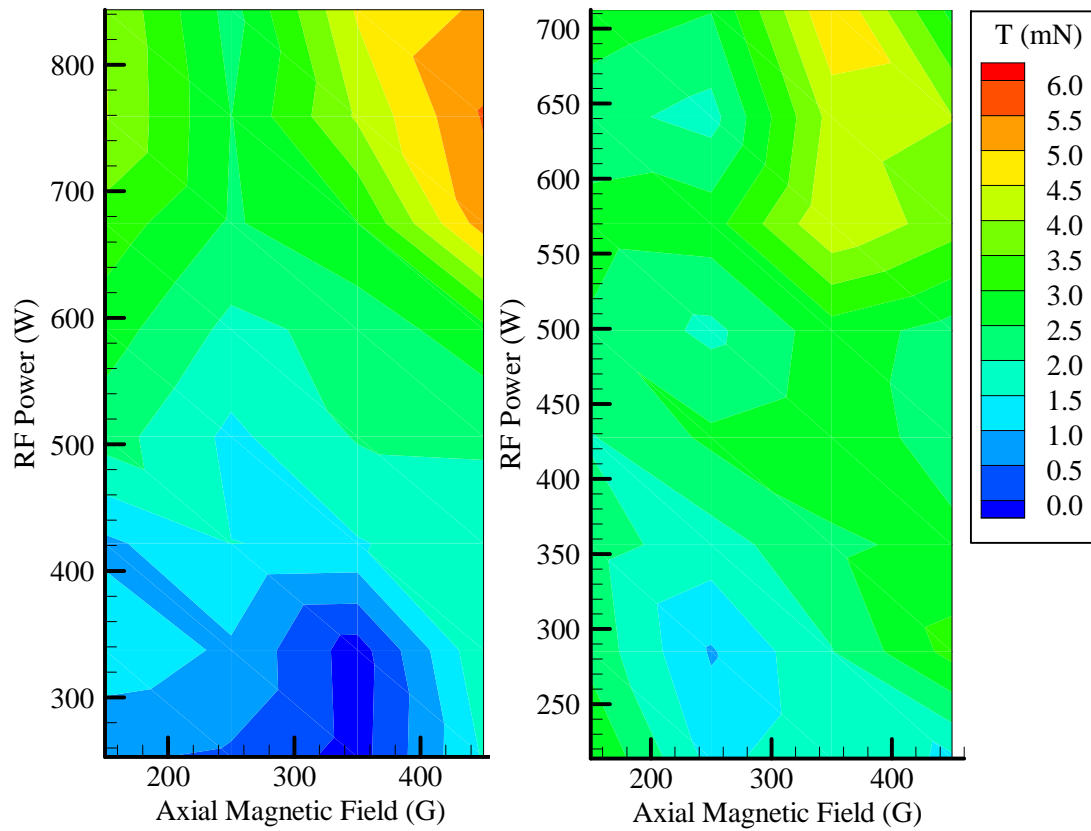
Figure 59. Helicon thrust with varying RF power and magnetic field at 11.9 MHz (*left*) and 13.56 MHz (*right*) with 1.5 mg/s argon flow rate.
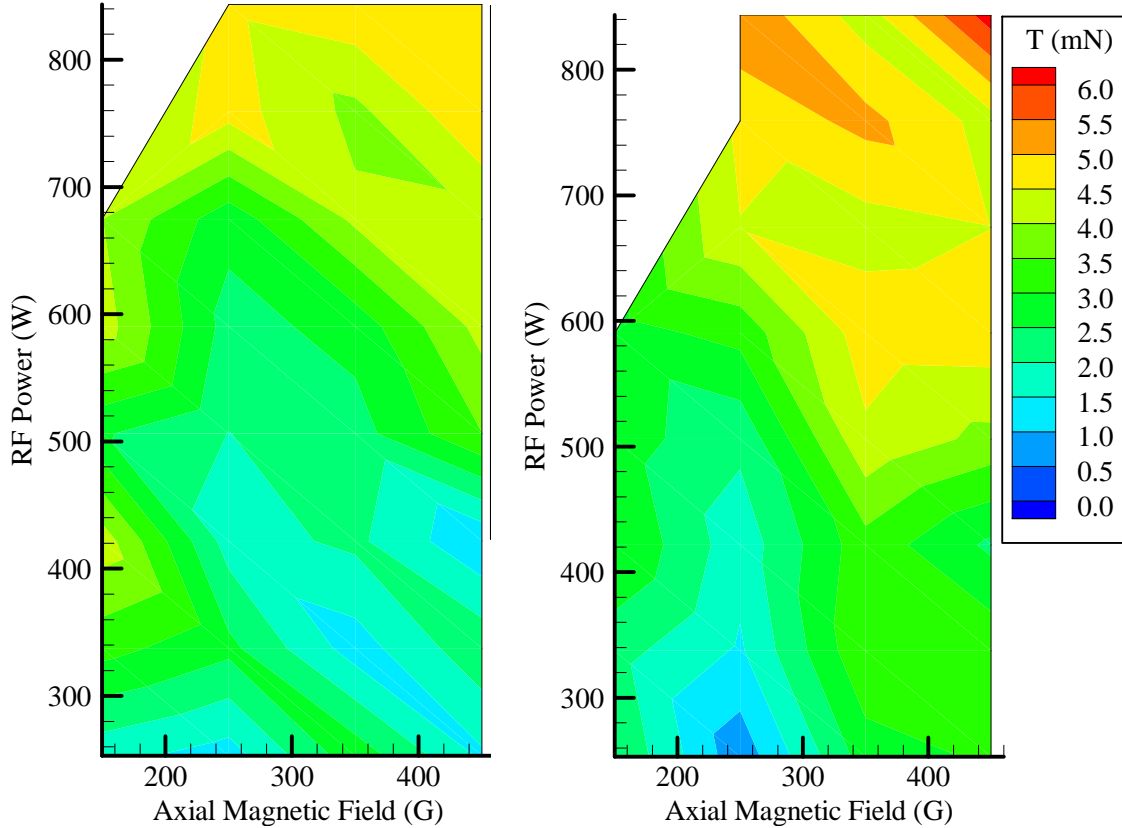
Figure 60. Helicon thrust with varying RF power and magnetic field at 11.9 MHz with 3.0 mg/s (*left*) and 4.5 mg/s (*right*) argon flow rate.

6.1.2 Thrust Efficiency

The thrust efficiency of the thruster is defined as

$$\eta_T = \frac{T^2}{2\dot{m}P_{in}} \tag{6.1}$$

where T is the thrust, $\dot{m}$ is the mass flow rate, and P_{in} is the total input power. The total input power consists of the RF power propagated through the antenna, the RF power lost in the transmission line, and the power used to run the solenoids. The latter two are dependent on the specific experimental setup used, so for the sake of comparison to other

work only the transmitted RF power is used in Equation (6.1). As a reminder, the transmitted RF power is determined by measuring forward power at the amplifier and correcting for power losses in the cable up to the antenna.

Figure 61 through Figure 63 show the calculated efficiencies. As expected from the low thrust-to-power ratio, efficiency is very low and suggests that very little of the power expended is spent accelerating ions. Another observation is that with the exception of two cases at high RF power and 450 G and one case at low power and 150 G, thrust efficiency is largely independent of every operating parameter.   While a weak relationship between the thrust efficiency and either magnetic field or power is observable, it is within the uncertainty of the data. This further suggests that the ion acceleration mechanism for the helicon is at best only weakly affected by the operating conditions, if at all.
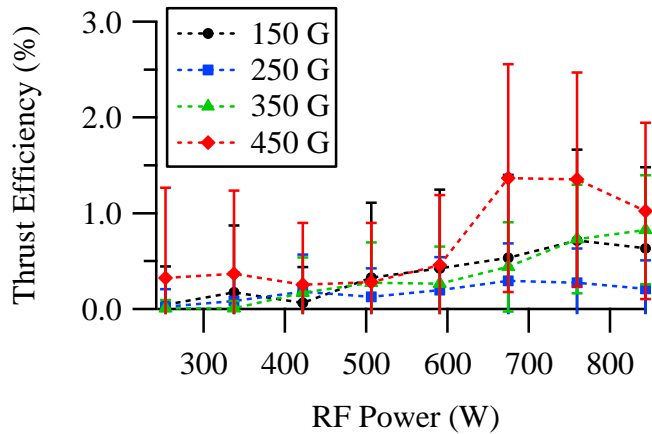
Figure 61. Helicon thrust efficiency as a function of power and magnetic field. 1.5 mg/s argon, 2.0x10^{-5} Torr-Ar, 11.9 MHz.

Figure 62. Helicon thrust efficiency as a function of power and magnetic field. 1.5 mg/s argon, 2.0x10^{-5} Torr-Ar, 13.56 MHz.

Figure 63. Helicon thrust efficiency as a function of argon mass flow rate. 350 G, 11.9 MHz, 2.0-2.6x10^{-5} Torr-Ar.

6.1.3 Helicon Specific Impulse

The other performance parameter of interest is the specific impulse, defined as

$$I_{sp} = \frac{T}{\dot{m}g} \tag{6.2}$$

where *g* is acceleration due to gravity. The specific impulse of the device is shown below

in Figure 64 through Figure 66. As before, specific impulse is largely independent of

operating conditions except for mass flow rate. The 1.5 mg/s cases at RF power above

600 W show an increase in specific impulse that is beyond the range of uncertainty. This

suggests two possibilities: either the amount of energy deposited into the ions increases

as the mass flow rate decreases, or the ion energy is largely unaffected and the increase in

specific impulse is caused by reducing the amount of neutrals that are never ionized.
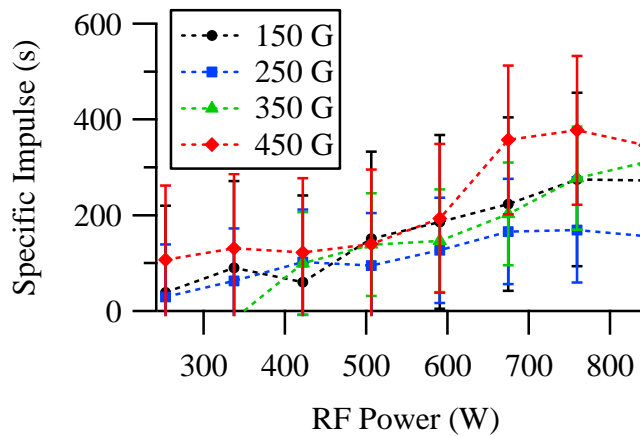
Figure 64. Helicon specific impulse as a function of RF power and magnetic field. 1.5 mg/s argon, 2.0x10^{-5} Torr-Ar, 11.9 MHz.

Figure 65. Helicon specific impulse as a function of RF power and magnetic field. 1.5 mg/s argon, 2.0×10^{-5} Torr-Ar, 13.56 MHz.
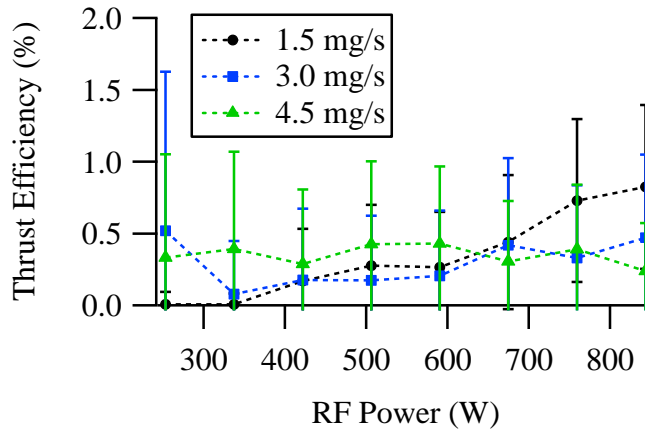
Figure 66. Helicon specific impulse as a function mass flow rate and RF power. 350 G, argon, 11.9 MHz, $2.0\text{-}2.6 \times 10^{-5}$ Torr-Ar.

In order to determine how the ions are accelerated, and thus determine the cause for the low thrust and thrust efficiency, the downstream plume of the thruster must be investigated. While the specific impulse can determine average exit velocity, it cannot determine the actually ion energy distribution. For this, a retarding potential analyzer is used. Prior to this, the structure of the plume must be determined in order to determine the direction of the ion velocities. While an ideal thruster has the majority of the ion

beam focused on the device centerline, this is not yet confirmed. Hence, measurements of the beam current density are required.

6.2 Plume Beam Current Density

Figure 67 illustrates the geometry of the Faraday probe sweeps, while Figure 68 shows a plot of the plume current density profiles. Rather than the central peak of a collimated beam, the plume of the helicon is very broad with peaks at the wings, located at approximately 60º and -70º. The current density distribution is characterized by asymmetry, not only in the angular location of the peaks, but also in the height and number of the peaks. The 600 W, 150 G case has only one peak at -70º, while the 600 W, 50 G case has three distinct peaks: 60º, -70º, and an additional peak at -26º. The 343 W, 150 G case has no distinct peak at all and appears as a broad dispersion. Furthermore, where the 60º peak is observed, it is the largest. This is marginal in the 50 G case, but quite pronounced for both cases at 350 G.
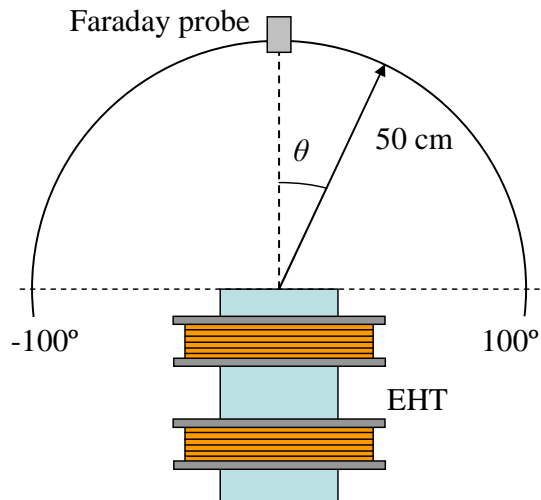
Figure 67. Faraday probe sweep geometry.
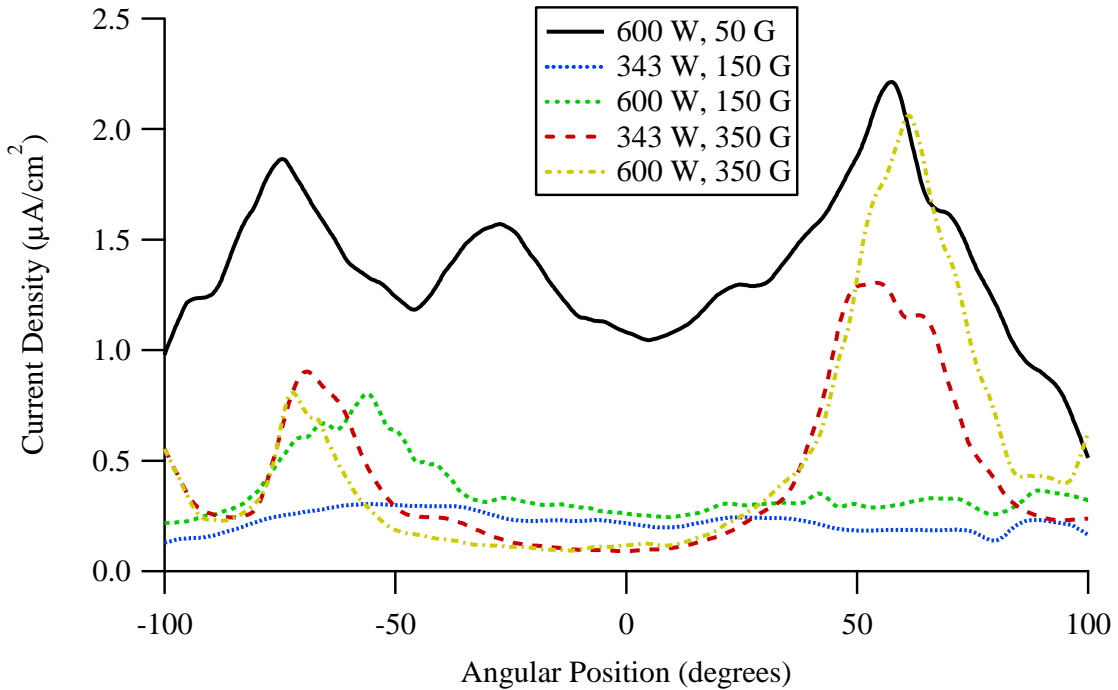
Figure 68. Current density profiles as a function of power and magnetic field. Probe is 50 cm downstream, 13.56 MHz, 1.5 mg/s Ar, 1.6x10^{-5} Torr-Ar.

Quantifiable metrics to describe the beam divergence are difficult to obtain in this situation, as a beam half-angle generally assumes a central plume structure. A central assumption in the analysis procedure outlined in Section 5.3 is radial symmetry. Figure 68 shows that neither assumption is valid for the data collected. Likewise, the Faraday probe generally overestimates beam current due to charge-exchange effects. However, in the absence of any alternative for qualitative comparison, these metrics will suffice. The beam half angles and beam currents for the five operating conditions are shown in Table 1. While the half-angle is not an ideal metric in this circumstance, the large values observed demonstrate quantitatively the broad structure of the plume. More importantly, the calculated beam currents show that the helicon does create an ion beam of significant size, especially considering that the Faraday probe is already overestimating the beam current.

Table 1. Beam half-angle and beam current.

Case	I_b (mA)	α_{90} (deg)	Uncertainty (%)
343 W, 150 G	7.20	84	12.2
600 W, 150 G	12.4	83	15.5
343 W 350 G	17.2	79	21.1
600 W 350 G	20.2	80	18.8
600 W 50 G	46.7	83	12.9

The lack of a centerline peak and the presence of large peaks on the wings strongly suggest that the ions are accelerated with a high degree of divergence. However, one consideration that must be taken when using a Faraday probe is the effects of charge-exchange collisions. A charge-exchange (CEX) collision occurs when an ion collides with a neutral and transfers charge while maintaining kinetic energy. This is problematic in thruster plume measurements, as a fast ion and a slow neutral become a fast neutral and a slow ion. The CEX collision also results in a random direction of travel for the slow ion, which statistically will favor the wings, rather than the centerline.[80]

For devices where the current density peaks on the center, such as an ion engine, CEX causes the measured current density on the wings to be higher and slightly lower along the center. However, since no discernible centerline peak exists in Figure 68, the goal is to determine to what extent the measured current density at these peak locations is due to CEX collisions. The most direct approach is to measure the energy distribution of the ions at these locations. Ions that are accelerated from the helicon at the wide angles measured will have an energy corresponding to the potential drop from the helicon to the location of the probe. In contrast, CEX ions will be closer to the plasma potential, since they are ionized further downstream and do not have the kinetic energy of the incident ion. Therefore, RPA measurements at the above three angles, along with the centerline

for comparison, are needed to quantify the contribution of CEX to the current density at the wings.

6.3 Ion Energy Distributions

The ion energy distributions are plotted below in Figure 69 to Figure 73 at each angular position of interest. A key value in energy distributions is the most probable energy, which is the voltage where the IEDF is locally maximized. Each relative maximum corresponds to an ion population distributed about that specific energy. The energy distributions for the helicon generally have two such relative maxima, or peaks. The first peak in each distribution corresponds to the plasma potential at the location of the RPA collector.[14,17-19] Since the collector is grounded, ions at the plasma potential will be accelerated by the potential drop between the plasma and the collector, despite not contributing to the ion beam. Higher potential peaks correspond to accelerated ion populations. For each test case, the potential of the first peak is very similar between angular positions. Since each position is 50 cm downstream of the exit plane, this suggests that the plasma potential should be approximately radially symmetric.
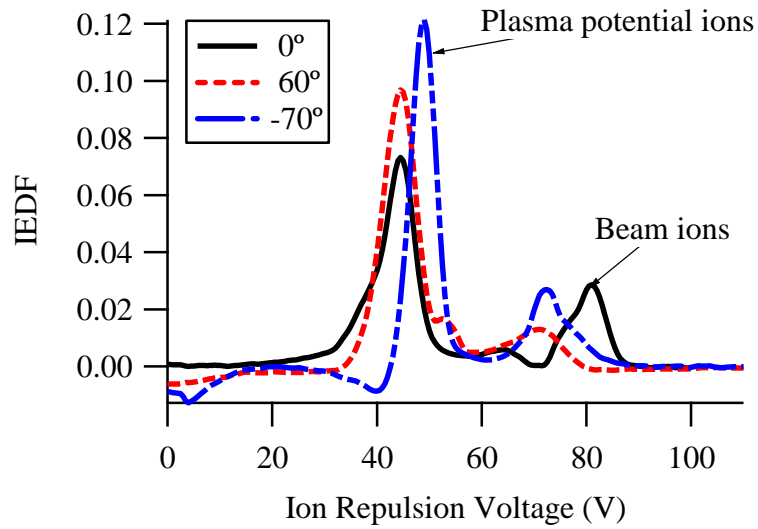
Figure 69. Ion energy distribution at varying angular positions 50 cm from the exit plane. 343 W, 150 G, 1.5 mg/s Ar, 1.6x10^{-5} Torr-Ar.
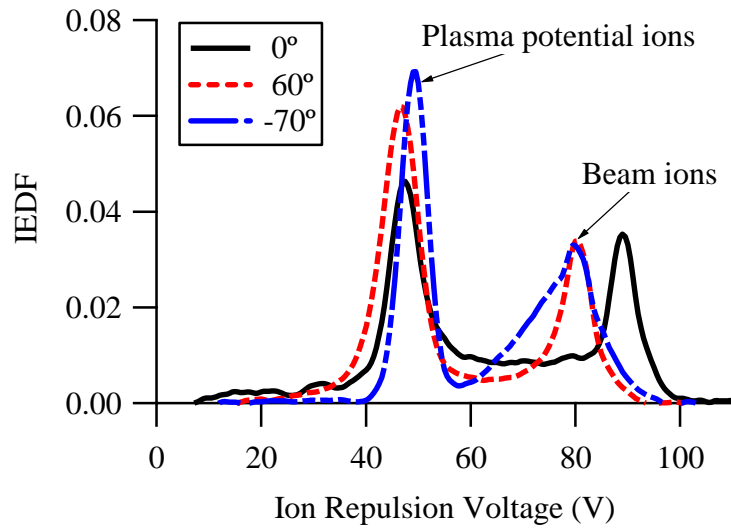
Figure 70. Ion energy distribution at varying angular positions 50 cm from the exit plane. 600 W, 150 G, 1.5 mg/s Ar, 1.6x10^{-5} Torr-Ar.
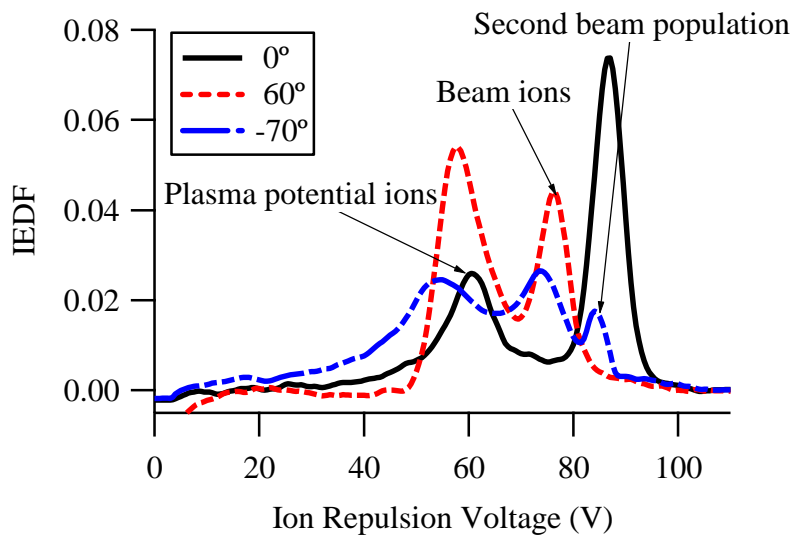
Figure 71. Ion energy distribution at varying angular positions 50 cm from the exit plane. 343 W, 350 G, 1.5 mg/s Ar, 1.6×10^{-5} Torr-Ar.
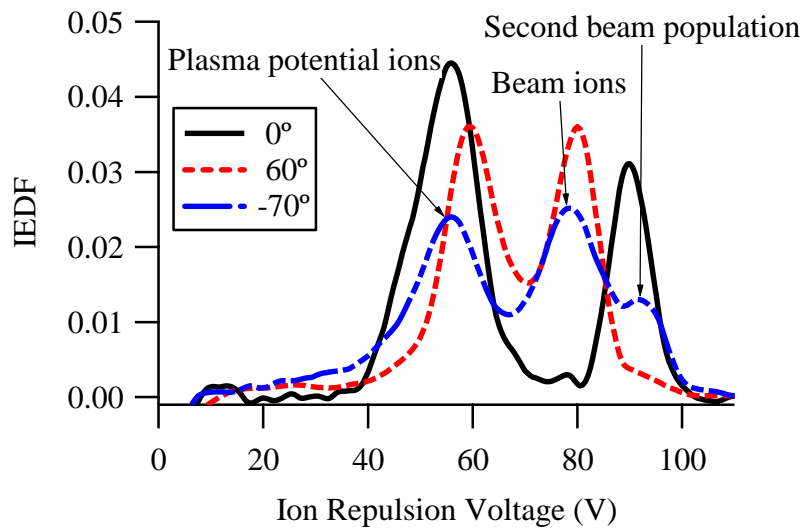
Figure 72. Ion energy distribution at varying angular positions 50 cm from the exit plane. 600 W, 350 G, 1.5 mg/s Ar, 1.6×10^{-5} Torr-Ar.
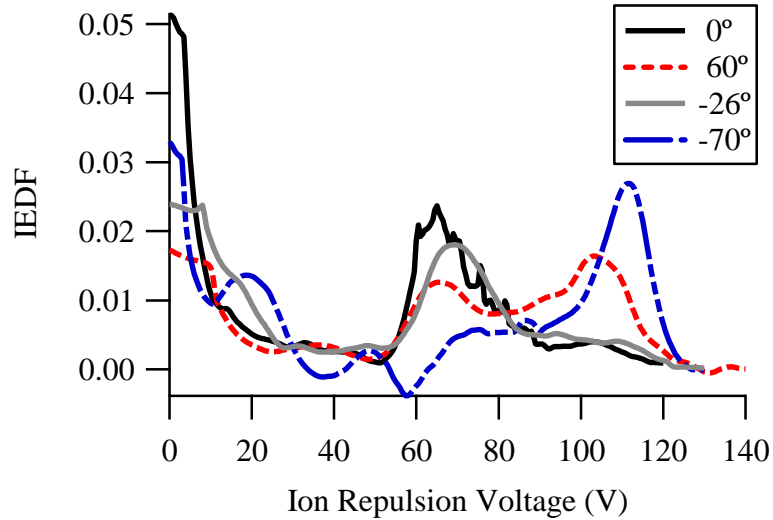
Figure 73. Ion energy distribution at varying angular positions 50 cm from the exit plane. 600 W, 50G, 1.5 mg/s Ar, 1.6x10^{-5} Torr-Ar.

A notable trend is the distinction between the different magnetic fields. For both powers at 150 G the first ion population is much larger than the accelerated ion population. At 350 G the accelerated ion population is of a similar size or larger than the plasma potential population. The 50 G case differs greatly from the other tested conditions, with a large population near ground in addition to the two populations corresponding to the plasma potential and the accelerated ions. The 50 G case is examined individually at a later point, and is excluded from the following discussion.

A closer examination of the most probable ion voltages, shown in Table 2, yields two additional trends of interest. For the same magnetic field, the first peak, representing the most probable voltage of the plasma potential, is approximately constant across both angular position and RF power. The maximum variation among the set is 5.5 V, which is only about 2 V larger than the uncertainty of the measurements. Similarly, for the same RF power, the second most probable voltages are very similar and within the uncertainty of the RPA. The exception is that the most probable voltage on the centerline is

approximately 10 V higher than on the wings. In addition, for both cases at 350 G, -70°, a third ion population is observed at the same energy as the ion beam on the centerline. This third ion population is smaller than the other two and suggests that the mechanism that reduces the ion beam energy on the wings does not affect a portion of the ions on that side.

Table 2. Most probable ion voltages 50 cm downstream

P_{RF} (W)	B (G)	θ (°)	V_{mp1} (V)	V_{mp2} (V)
343	150	0	44.5 ± 1.7	81.0 ± 3.2
		60	45.0 ± 1.8	71.0 ± 2.9
		-70	49.5 ± 2.6	73.0 ±3.8
	350	0	60.5 ± 2.3	87.0 ± 3.4
		60	57.5 ± 2.4	76.5 ± 3.2
		-70	55.0 ± 2.2	74.0 ± 3.0
600	150	0	47.5 ± 1.8	89.0 ± 3.4
		60	47.5 ± 2.1	81.0 ± 3.6
		-70	50.0 ± 1.9	80.5 ± 3.1
	350	0	56.5 ± 2.3	90.5 ± 3.7
		60	60.5 ± 2.4	81.0 ± 3.2
		-70	57.0 ± 2.2	80.0 ± 3.1

6.3 Plasma Potential

As outlined in Section 5.5 and 5.6, the most accurate method to measure the plasma potential with a floating emissive probe requires a correction for the electron temperature. The electron temperature is estimated by comparing the measured plasma potential to the floating potential measured with the Langmuir probe. Density can likewise be estimated using the measured ion saturation current and the electron temperature. Since calculation of these parameters involves multiple measurements at the same position, the position of the measurements must be consistent between experiments. All three measurements – plasma potential, floating potential, and ion saturation current – are taken every 2 mm in

the radial direction at different axial positions. A graphical representation of the measurement locations is shown in Figure 74.
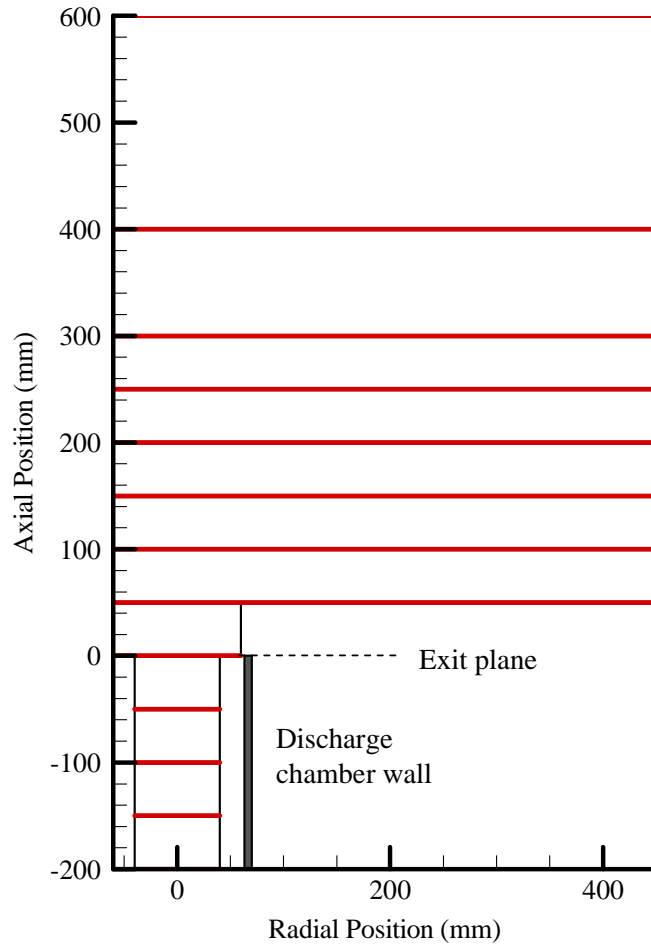
Figure 74. Spatial representation of probe measurements. Red lines denote radial sweeps with measurements taken every 2 mm.

Contour plots of the plasma potential of each operating condition are shown below in Figure 76 through Figure 80. With the exception of the 50 G case, the plots all share the following similarities. Inside the discharge chamber the plasma potential is minimized near the centerline of the device and maximized near the walls. Radial profiles at the exit plane, which run closer to the walls, show that the plasma potential decreases just before

the wall, which is consistent with the pre-sheath region of the wall plasma sheath. Figure 75 shows three example radial profiles of the plasma potential at the exit plane of the discharge chamber.
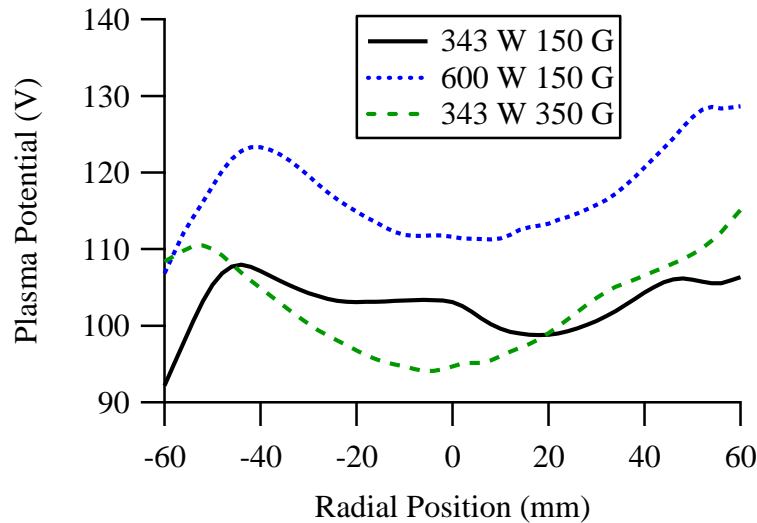
Figure 75. Radial plasma potential profile at the exit plane as a function of RF power and magnetic field. 1.5 mg/s Ar, 1.6x10^{-5} Torr-Ar.

Another similarity between the first four operating conditions is the highest plasma potential is located near the exit plane close to the walls of the discharge vessel. Downstream of the exit plane, the potential profile diffuses to a far-field value of approximately 59 V with negligible radial variation. Beyond these similarities, there are several varying characteristics in the contours that can be grouped by the axial magnetic field. The 50 G case is unique and shares very little with the other four cases beyond the diffusion of the plasma potential downstream.
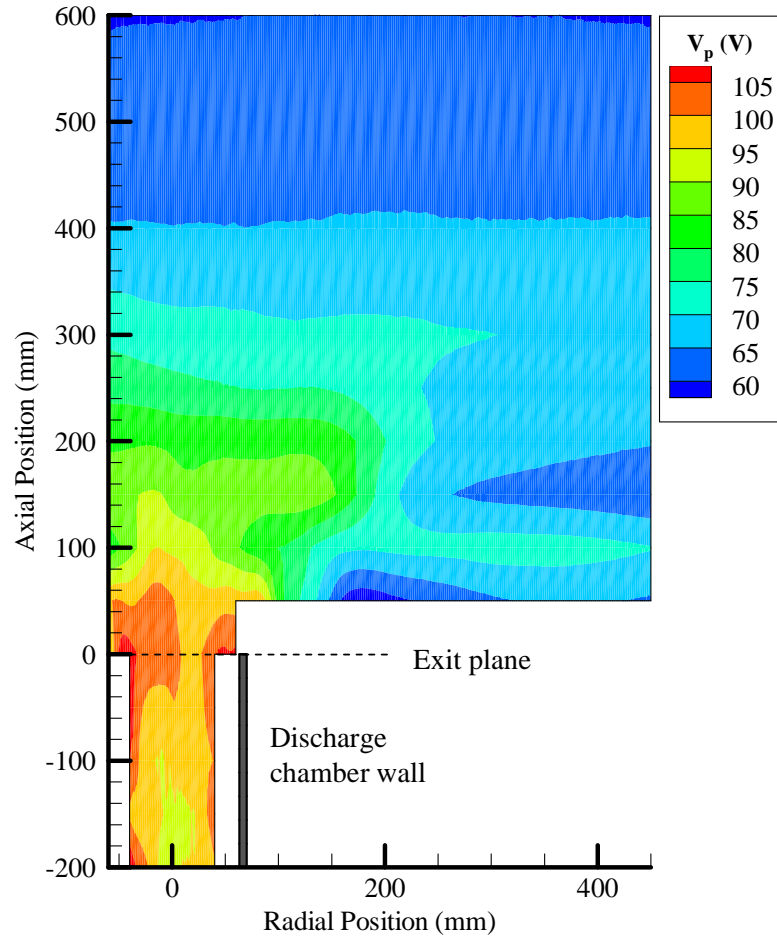
Figure 76. Plasma potential contour at 343 W, 150 G, 1.5 mg/s Ar, 1.6x10⁻⁵ Torr-Ar.
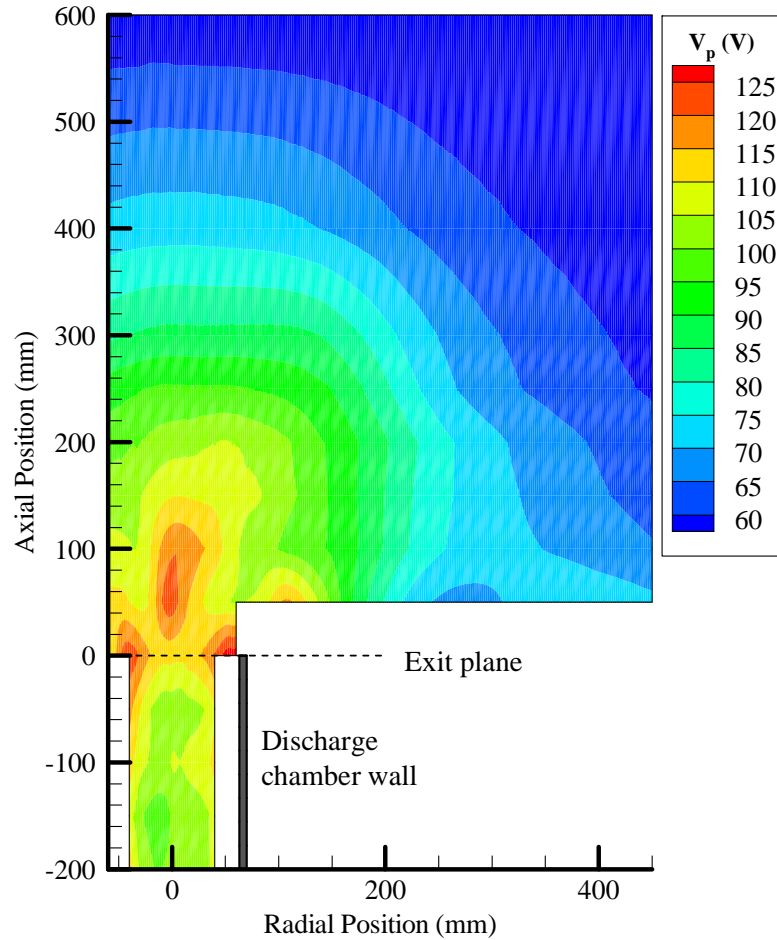
Figure 77. Plasma potential contour at 600 W, 150 G, 1.5 mg/s Ar, 1.6x10^{-5} Torr-Ar.

The two cases at 150 G share a similarity where the region of highest plasma potential is focused more towards the centerline of the device. This creates a convex region of high plasma potential immediately downstream of the exit plane. The primary difference between the two cases is that in the 600 W case the plasma potential is typically higher than in the 343 W case, with a difference in maxima of approximately 20 V.
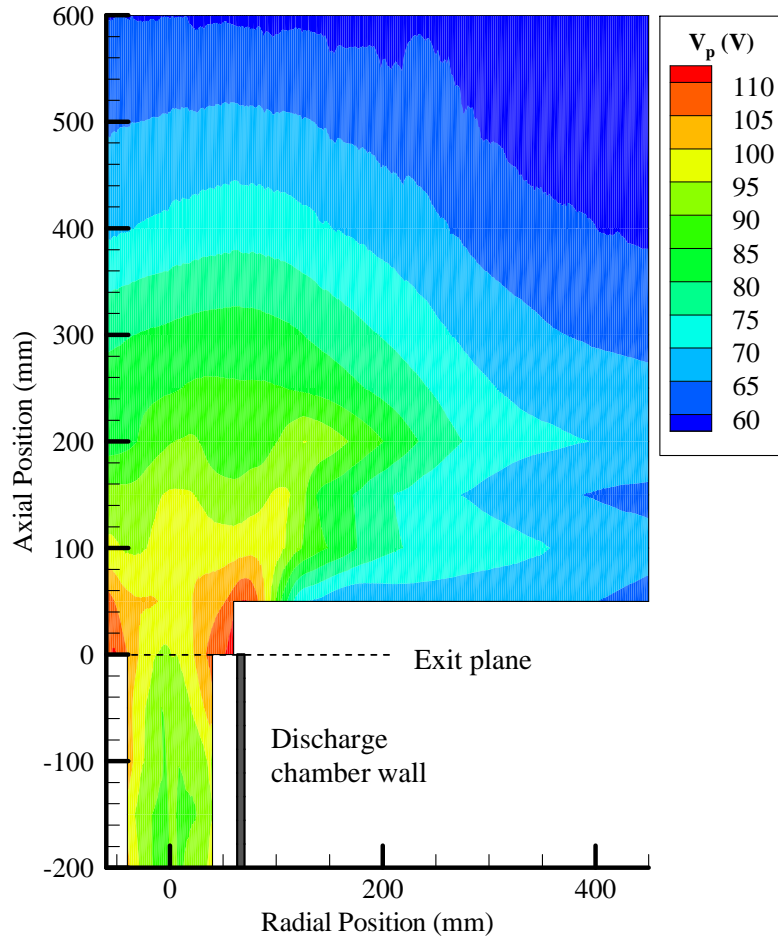
Figure 78. Plasma potential contour at 343 W, 350 G, 1.5 mg/s Ar, 1.6x10^{-5} Torr-Ar.
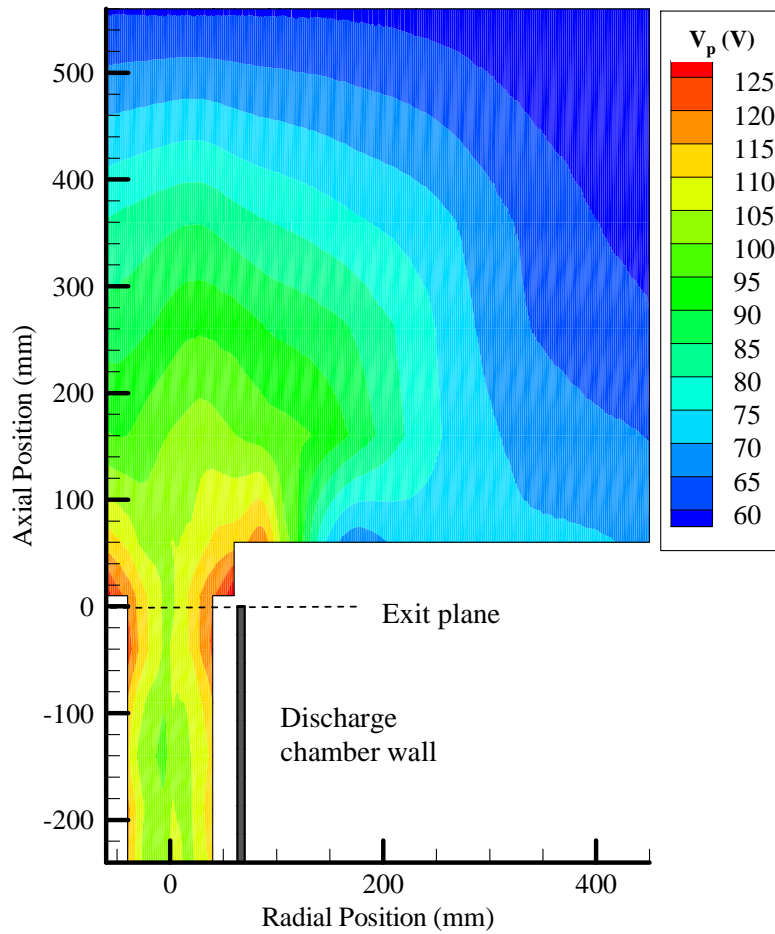
Figure 79. Plasma potential contour at 600 W, 350 G, 1.5 mg/s Ar, 1.6x10^{-5} Torr-Ar.

In contrast to the convex region of high plasma potential seen in the 150 G test cases, the 350 G data demonstrates a diverging annulus of high plasma potential around the exit plane of the discharge. This creates a converging-diverging structure out of the plasma potential centered on the exit plane of the device. As before, increasing the power increases the plasma potential while maintaining the overall shape.
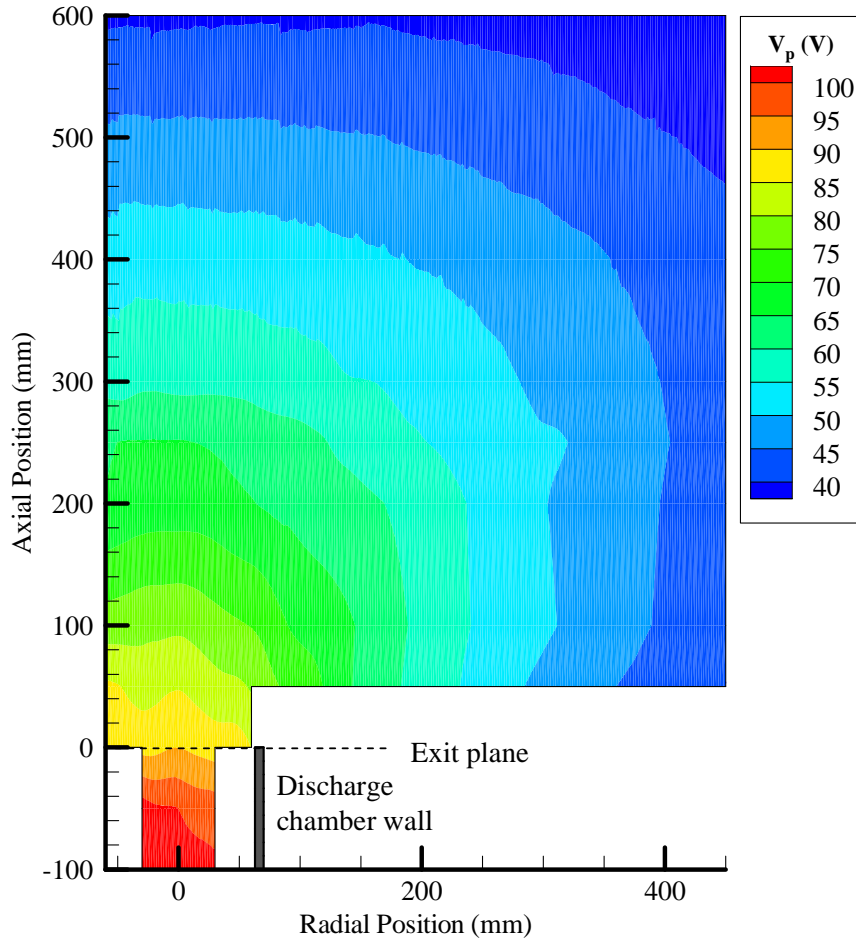
Figure 80. Plasma potential contour at 600 W, 50 G, 1.5 mg/s Ar, 1.6x10⁻⁵ Torr-Ar.

The 50 G case is distinct from the others in that there is no overall structure to the plasma potential either at the exit plane or downstream of it. Aside from some radial asymmetry inside the discharge chamber, the potential evenly diffuses downstream in an approximately spherical manner. Another difference between the 50 G case and the higher magnetic field tests is the far-field plasma potential is nearly 20 V lower for the 50 G condition.

Measurements are also taken along center line of the device in 2 mm intervals at each operating condition, shown in Figure 81. The axial profiles demonstrate the same approximate shape between tests at the same magnetic field. The cases at higher power

143

show a higher plasma potential at each position compared with the lower power case at the same magnetic field. This further suggests that the magnetic field sets the plasma potential shape, while the RF power controls the magnitude.
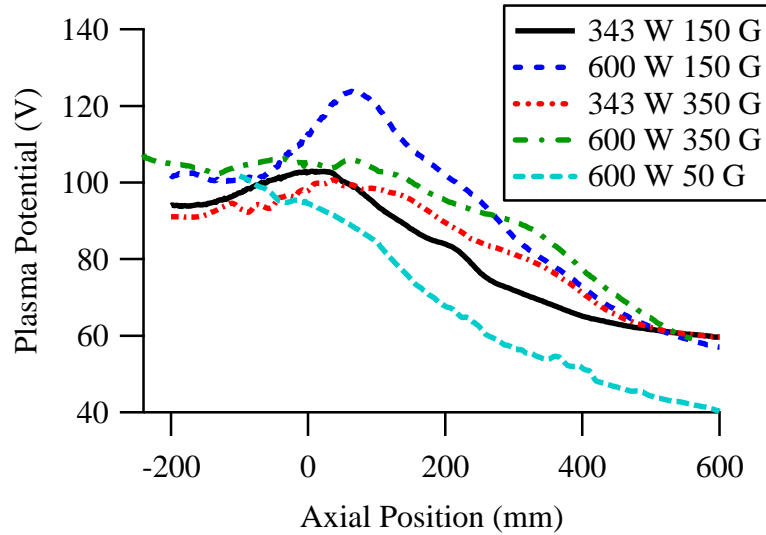
Figure 81. Plasma potential along the center line, 1.5 mg/s Ar, 1.6x10^{-5} Torr-Ar.

6.4 Electron Temperature

The floating potential, and thus the calculated electron temperature, is determined at the same measurement locations as in Figure 74. The contours of the electron temperature, shown below in Figure 82 through Figure 86, reveal the following traits common between all operating conditions. The first similarity is that inside the discharge chamber the electron temperature has a similar shape as the plasma potential, in that the radial profiles have the minima near the center and maxima near the walls. The second is that the electron temperature is lower inside the discharge than downstream of the exit plane. The third is that in all five contours the temperature is high in the region near the wall of the exit plane of the discharge chamber and in a conical region outwards and

downstream of the exit plane. As with the plasma potential, further comparisons of the

electron temperature contours can be made for the same magnetic field.
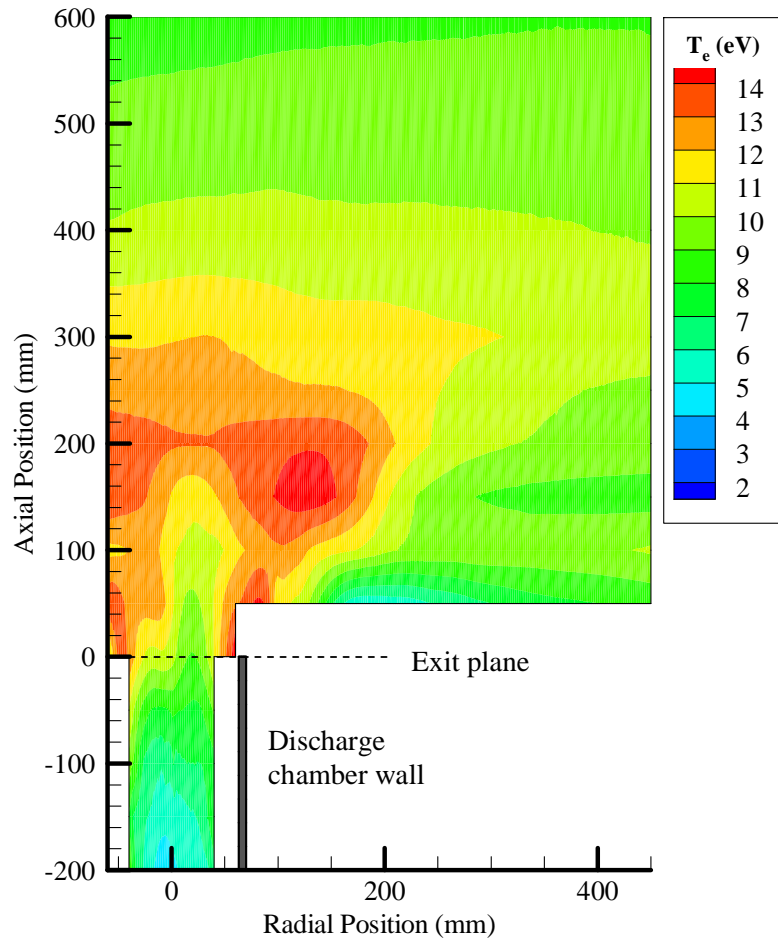
Figure 82. Electron temperature contour at 343 W, 150 G, 1.5 mg/s Ar, 1.6x10^{-5} Torr-Ar.
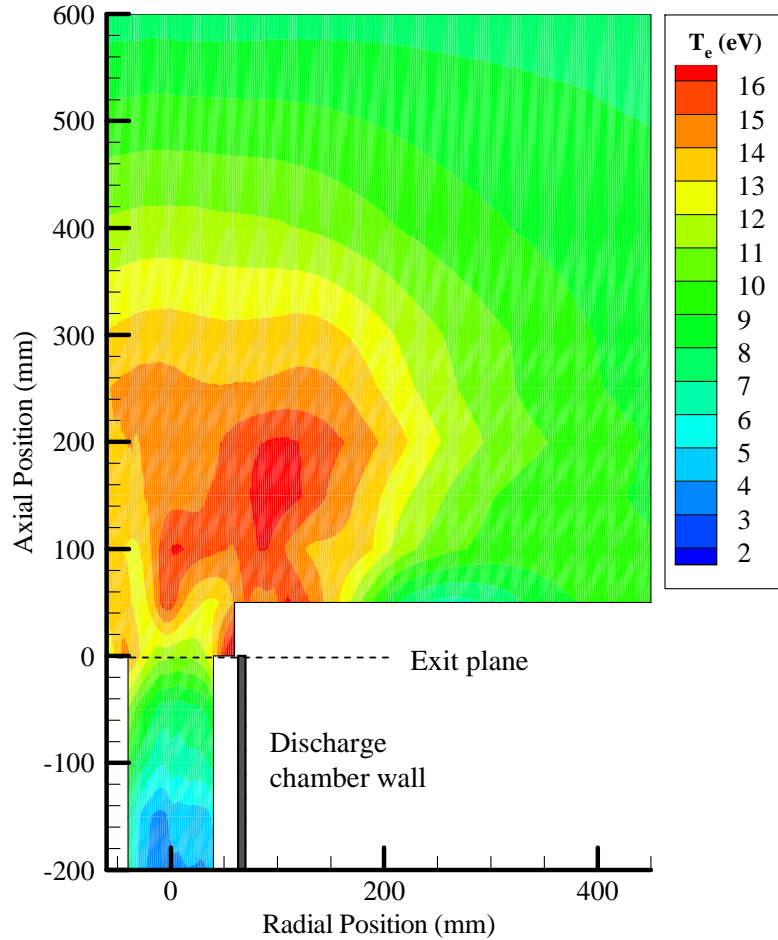
Figure 83. Electron temperature contour at 600 W, 150 G, 1.5 mg/s Ar, 1.6x10^{-5} Torr-Ar.

The two 150 G cases are distinguished by the downstream region of high temperature extending radially inward 100-200 mm downstream of the exit plane. It is worth noting that the 600 W case does not have the same degree of radial symmetry in this region as displayed by the 343 W case. The region immediately downstream of the exit plane for negative radial positions has a lower electron temperature compared to the positive radial quadrant. Furthermore, the negative radial quadrant corresponds to negative angular positions in the Faraday probe scans. It is observed that the 343 W, 150 G case has no observable peak in the current density distribution, while the 600 W, 150 G case has no peak at positive angles, and one peak at -70°. This asymmetry in the electron temperature

at 600 W could potentially explain the observance of only one peak, as any affect that the electron temperature has on ion trajectory favors one side over the other.
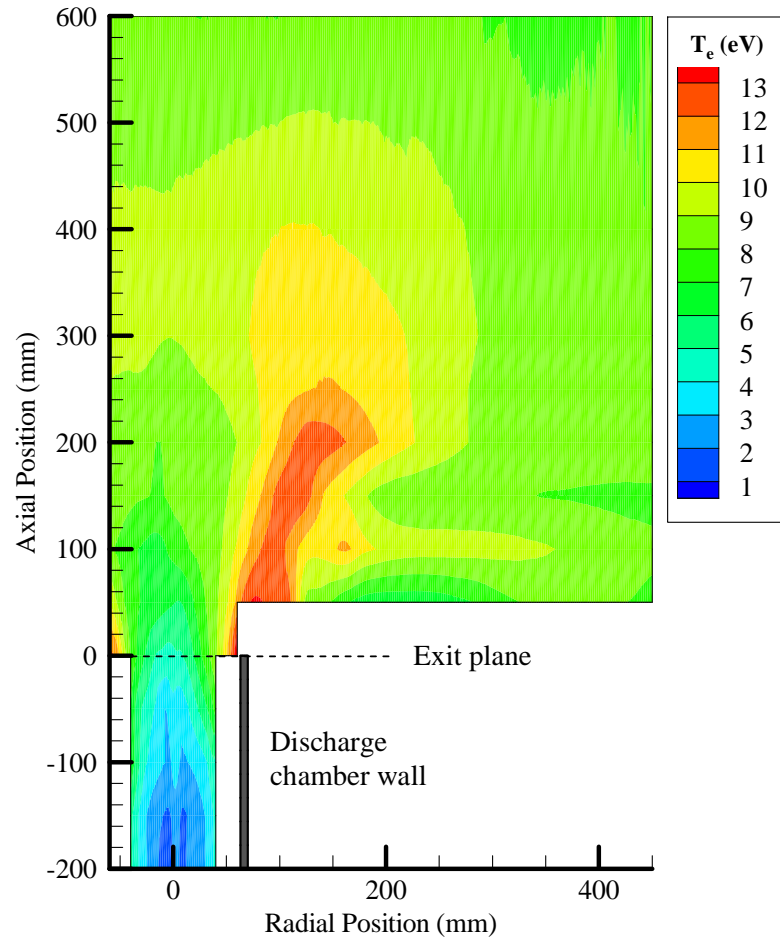
Figure 84. Electron temperature contour at 343 W, 350 G, 1.5 mg/s Ar, 1.6x10^{-5} Torr-Ar.
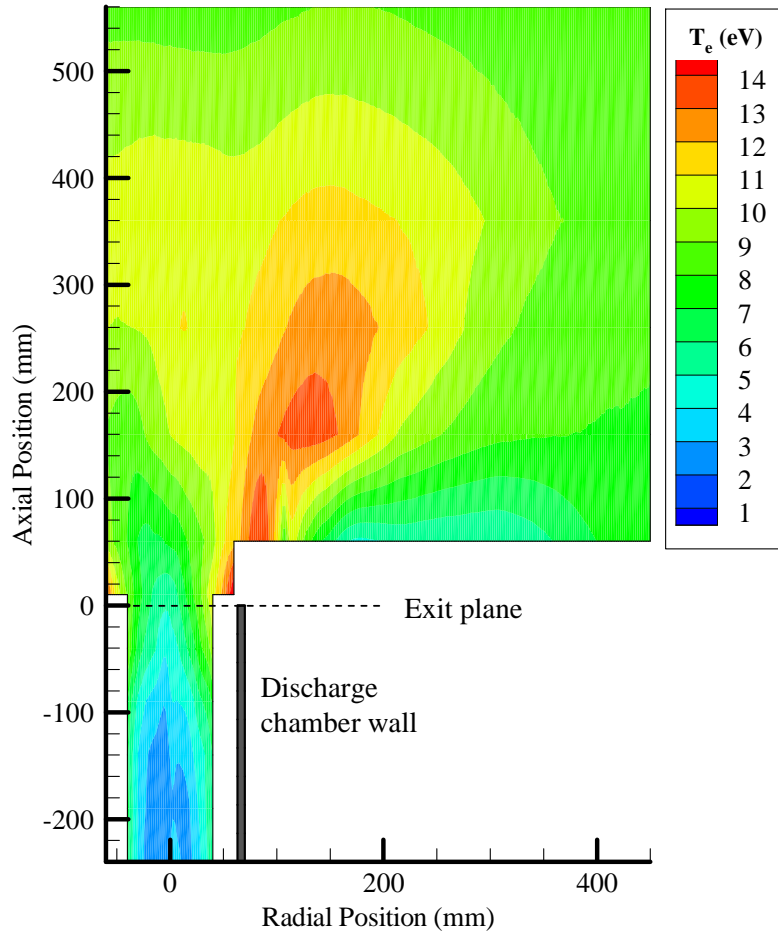
Figure 85. Electron temperature contour at 600 W, 350 G, 1.5 mg/s Ar, 1.6x10^{-5} Torr-Ar.

In contrast to the 150 G cases, the two cases at 350 G have no regions of high electron temperature along the centerline. While the temperature still increases along the centerline from within the discharge into the plume, the centerline always maintains a lower temperature than the radial region of 60-150 mm. For the 350 G cases, the parabolic shape of the radial temperature profiles inside the discharge is maintained downstream. The only change in the radial profiles with axial distance is as the axial position increases, the centerline increases while the edges decrease as the profile relaxes to approximately uniform. As is noted with the plasma potential, at both magnetic fields increasing the RF power has the effect of increasing the electron temperature.
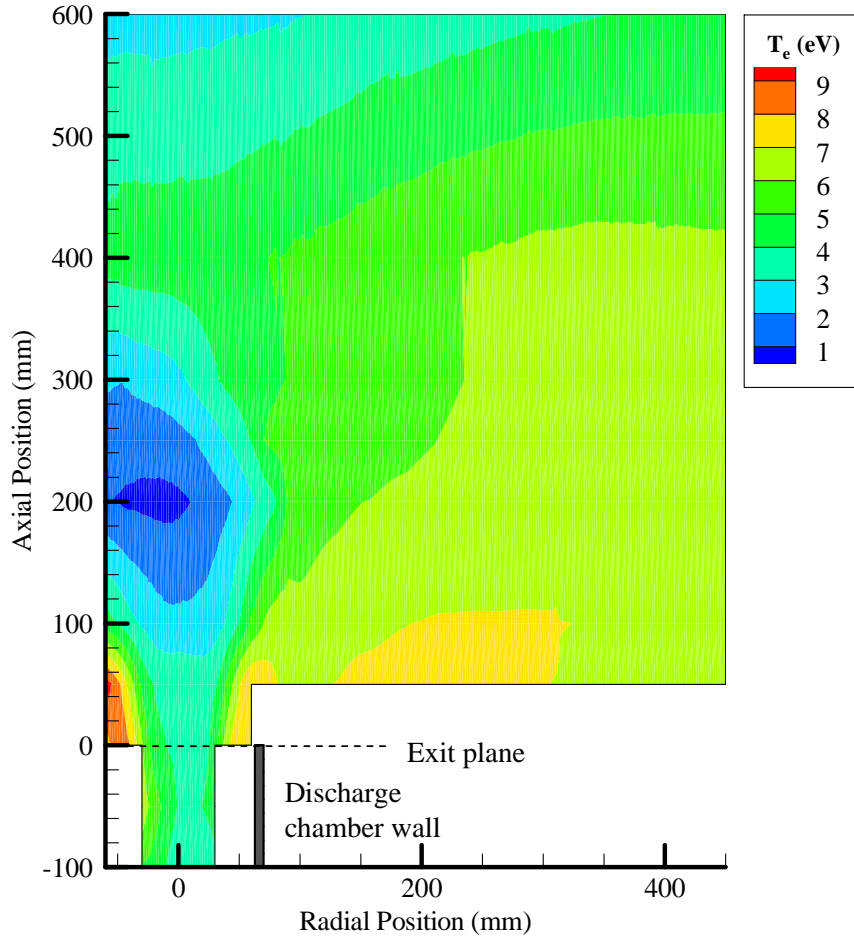
Figure 86. Electron temperature contour at 600 W, 50 G, 1.5 mg/s Ar, 1.6x10^{-5} Torr-Ar.

Figure 87 shows the axial profiles of the electron temperature along the center axis of the device. All five profiles show the same basic shape of the electron temperature starting at relatively low values that increase further downstream. At some point past the exit plane, the electron temperature peaks, after which the temperature decreases monotonically as the axial position increases. The profiles that share the greatest similarities are again those with the same magnetic field. Increasing the RF power has two observable effects on temperature: it increases the electron temperature relative to the lower power condition at the same magnetic field, and it decreases the axial position

where the temperature peaks. It is worth noting that the 150 G profiles peak closer to the exit plane than the 350 G profiles.
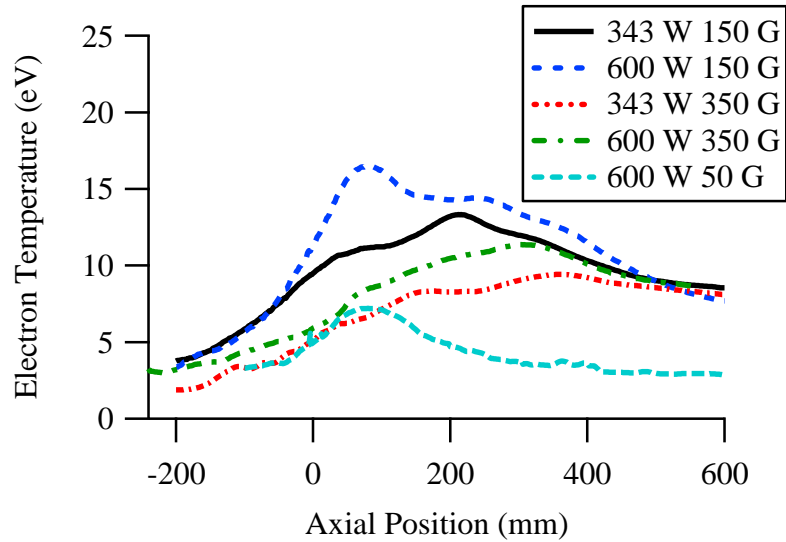
Figure 87. Electron temperature along the center line, 1.5 mg/s Ar, 1.6x10^{-5} Torr-Ar.

6.5 Ion Number Density

Figure 88 through Figure 92 show the electron number density contours for the five operating conditions tested. All five operating conditions share similar radial profiles inside the discharge chamber seen before, except now the maxima are located along the centerline of the device, similar to Figure 7. Additionally, the electron number density rapidly decreases downstream of the exit plane by more than an order of magnitude. The 50 G case is an exception to this, as the plume extends further downstream than the other four cases. As a quantitative comparison, the plume length is defined as the distance along the centerline from the exit plane where the number density is 10% of the exit plane density. Under this metric, the plume lengths for the 150 G and 350 G cases range from 157 to 172 mm, while the 50 G case has a plume that is 542 mm long, shown in

Table 3. The density at the maximum distance downstream of the exit plane is also higher for the 50 G case compared to the other cases.
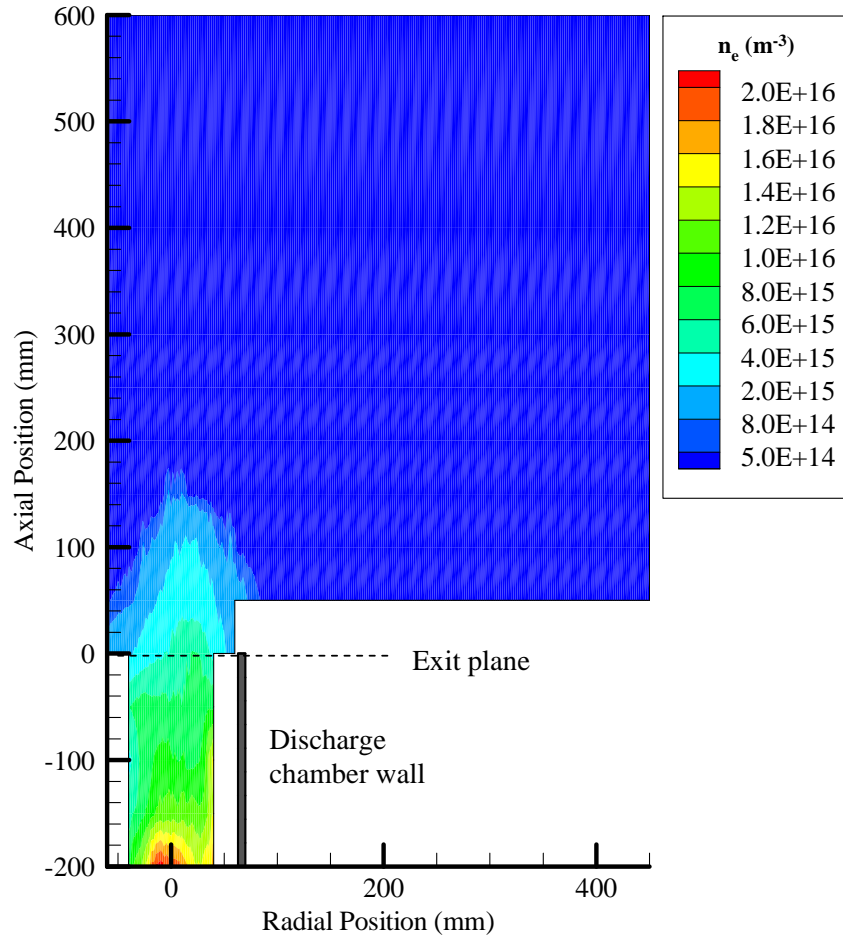
Figure 88. Electron number density contour at 343 W, 150 G, 1.5 mg/s Ar, 1.6x10^{-5} Torr-Ar.
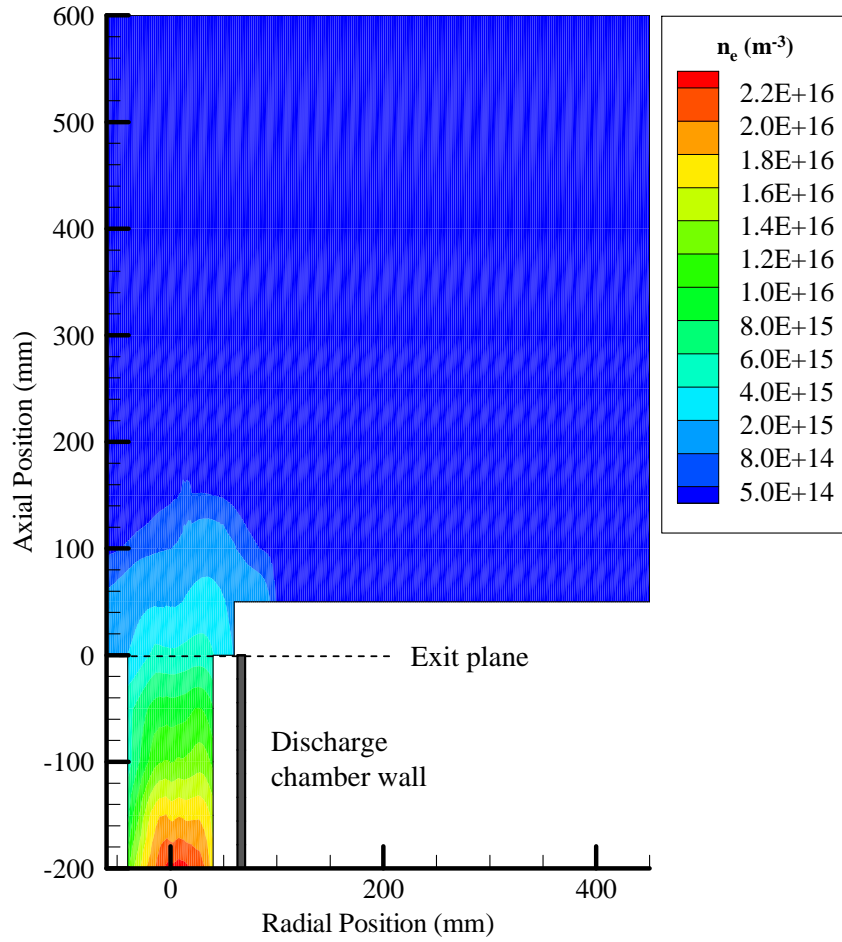
Figure 89. Electron number density contour at 600 W, 150 G, 1.5 mg/s Ar, 1.6x10⁻⁵ Torr-Ar.
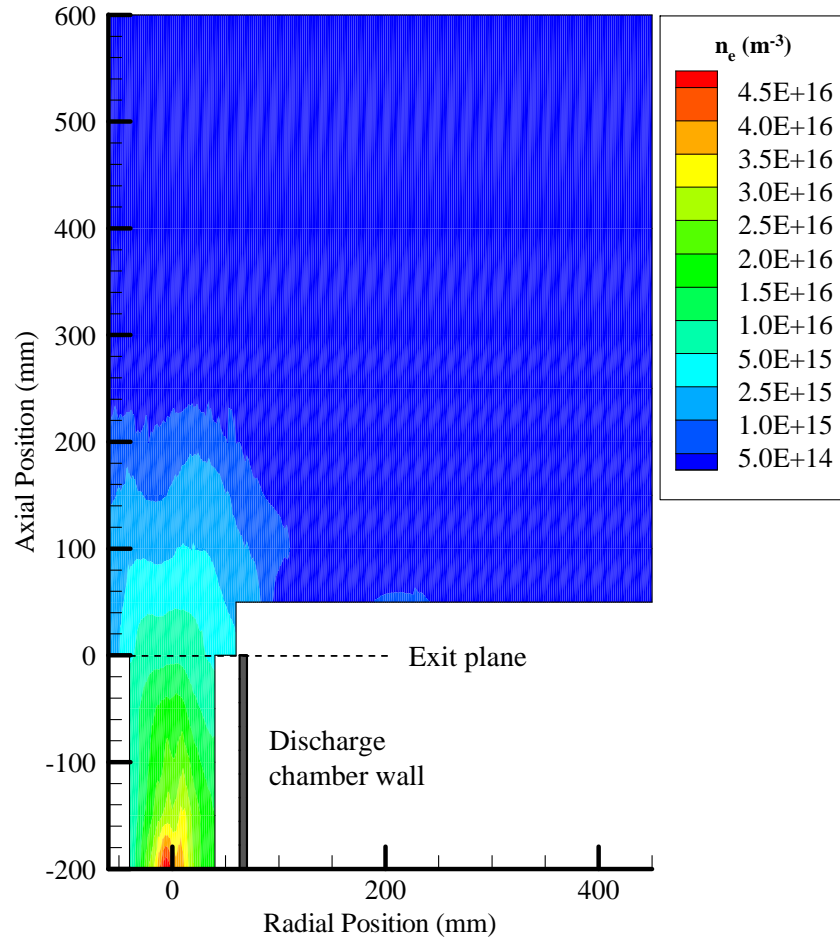
Figure 90. Electron number density contour at 343 W, 350 G, 1.5 mg/s Ar, 1.6x10^{-5} Torr-Ar.
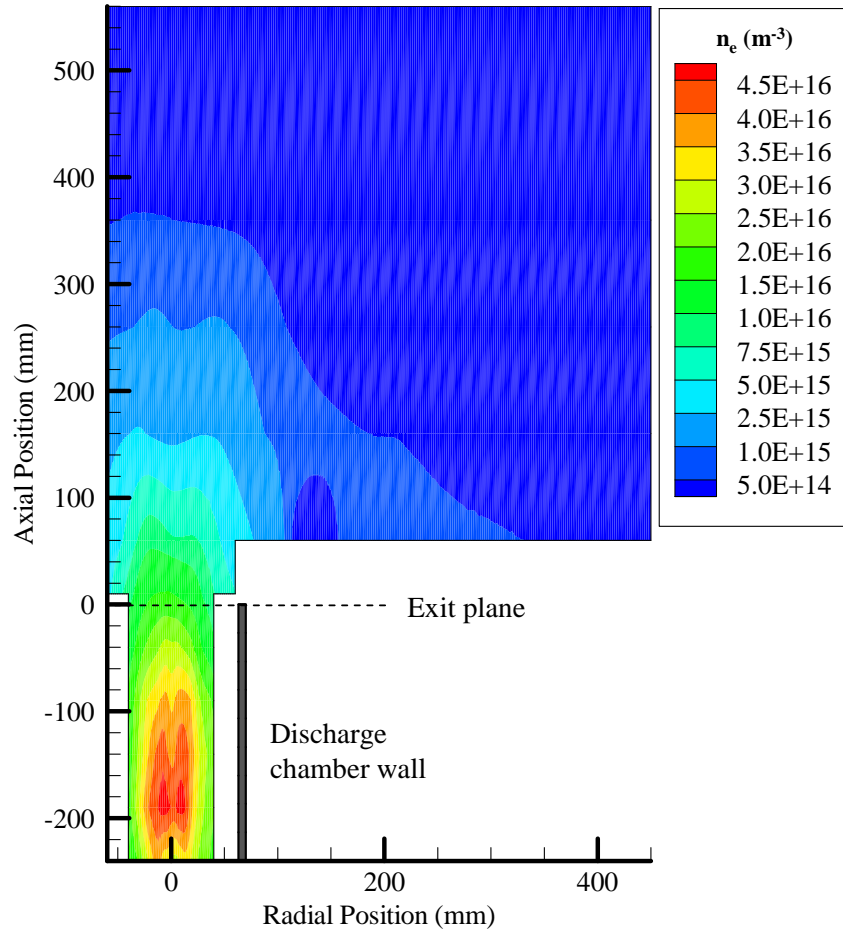
Figure 91. Electron number density contour at 600 W, 350 G, 1.5 mg/s Ar, 1.6x10^{-5} Torr-Ar.
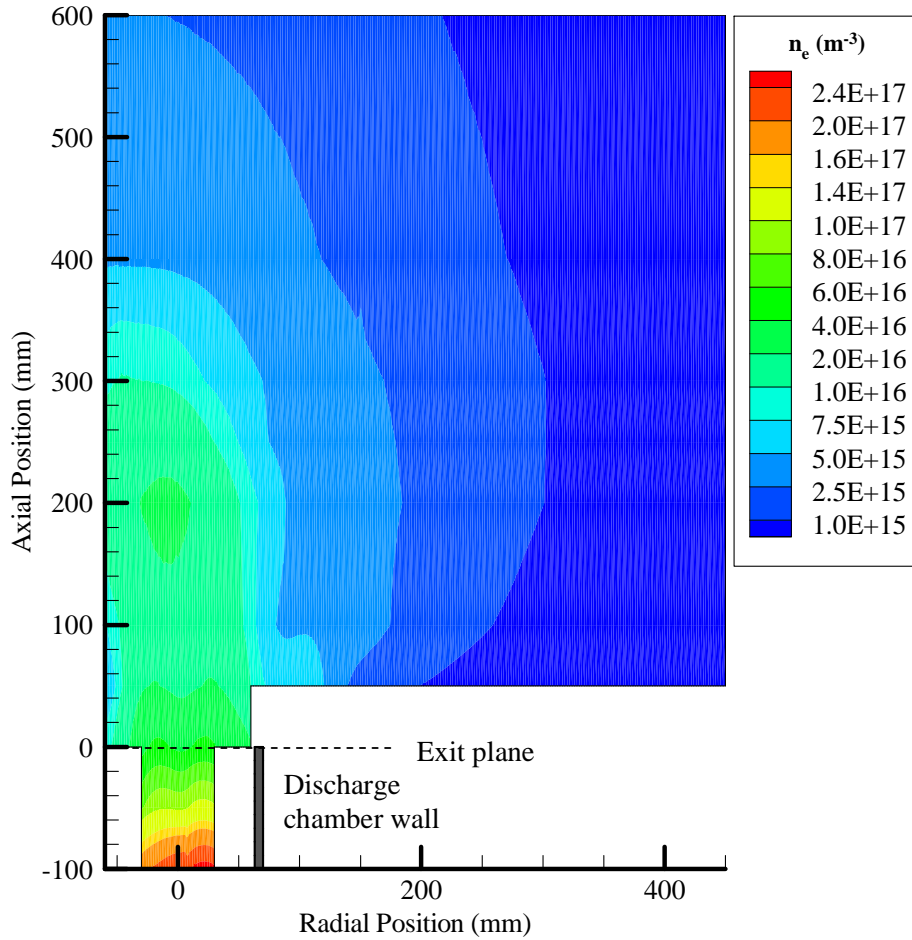
Figure 92. Electron number density contour at 600 W, 50 G, 1.5 mg/s Ar, 1.6x10^{-5} Torr-Ar.

Table 3. Helicon Plume Lengths

Operating Condition	Plume Length (mm)
343 W, 150 G	162
600 W, 150 G	157
343 W, 350 G	167
600 W, 350 G	172
600 W, 50 G	542

The contrast in the electron density between the first four cases and the 50 G case can be clearly seen in Figure 93, which shows the axial profiles of the electron number density. While the most similarities between profiles are for the same magnetic field, the 150 G and 350 G profiles exhibit a higher degree of similarity to each other as compared

with the 50 G profile. In addition to the higher density, the 50 G profile has a larger

decrease in density before the exit plane with a much smaller decrease downstream of the

exit plane compared with the other profiles.
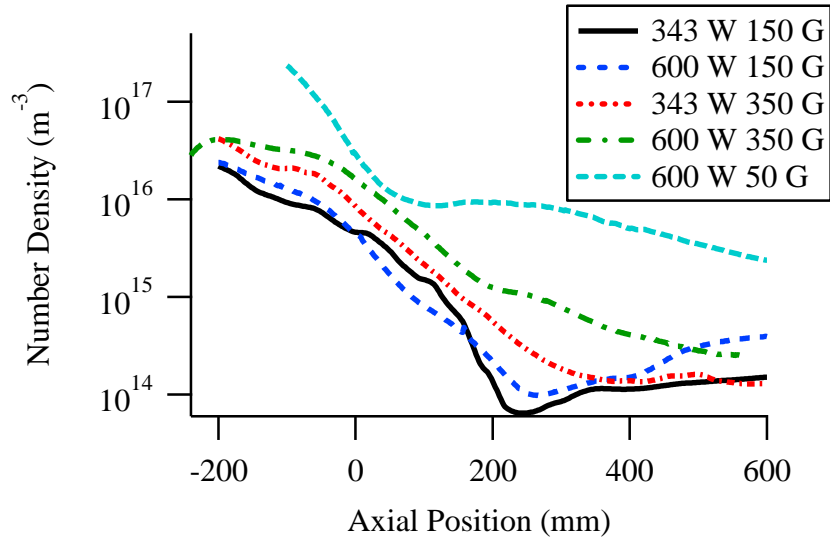
Figure 93. Electron number density along the center line, 1.5 mg/s Ar, 1.6×10^{-5} Torr-Ar.

6.6 Ion Thrust Contribution

In order to evaluate the EHT compared to the GHIT, the thrust contribution due to ion

acceleration must be determined. Using Equation (4.1), the thrust generated through ion

acceleration can be defined as

$$T = \gamma \frac{m_i}{e} I_b \bar{v}_i \qquad (6.3)$$

where the average ion velocity is calculated from the ion energy distributions

$$\bar{v}_i = \frac{\sum_{j=k+1}^{100} x_j \left(\frac{2e\left(V_j - V_p\right)}{m_i} \right)^{1/2}}{\sum_{j=k+1}^{100} x_j} \quad \left\{ k \mid V_k = V_p \right\} \tag{6.4}$$

In Equation (6.4), V_j is the voltage of the jth step of the voltage sweep, and x_j is the value of the probability distribution function at that voltage. The overall average ion velocity of each operating condition is the mean of the average ion velocity at the three angular positions. Using the average ion velocities along with the results in Table 1, the thrust contribution by ion acceleration is calculated and shown in Table 4.

Table 4. Ion thrust contribution and component parameters.

Operation Conditions	α (deg)	I_b (mA)	$v_{i,avg}$ (km/s)	T_{ion} (μN)
343 W, 150 G	83.5	7.20	5.97	2.02
600 W, 150 G	82.6	12.4	9.15	6.08
343 W, 350 G	79.0	17.2	7.56	10.3
600 W, 350 G	79.9	20.2	8.16	12.0

The results show that ion contribution to thrust is several orders of magnitude lower than the measured thrust. As a comparison, the cold gas thrust of the various propellant flow rates is in the range of 0.5-2 mN, as shown in Figure 94. This shows that very little of the power coupled to the helicon is transferred to axial ion energy. Even if the beam divergence factor is neglected, the ion thrust contribution only increases by a factor of 5-8, which still results in a negligible thrust contribution. The average ion velocity yields an expected specific impulse of approximately 600-900 s, but in practice the ionization fraction and beam currents are so low the thrust contribution from the ion beam is negligible. It is much more likely that the primary thrust contribution is a combination of

collisional heating of the neutral propellant and the resulting thermal exhaust, along with electron back-pressure on the discharge chamber.[81] The mean free path between ions and neutrals for momentum transfer would be on the order of a few centimeters, so significant thermal exchange between ions and neutrals should occur. However, ions typically have less thermal energy than electrons in helicon plasmas,[39,49] and thus thrust remains low.
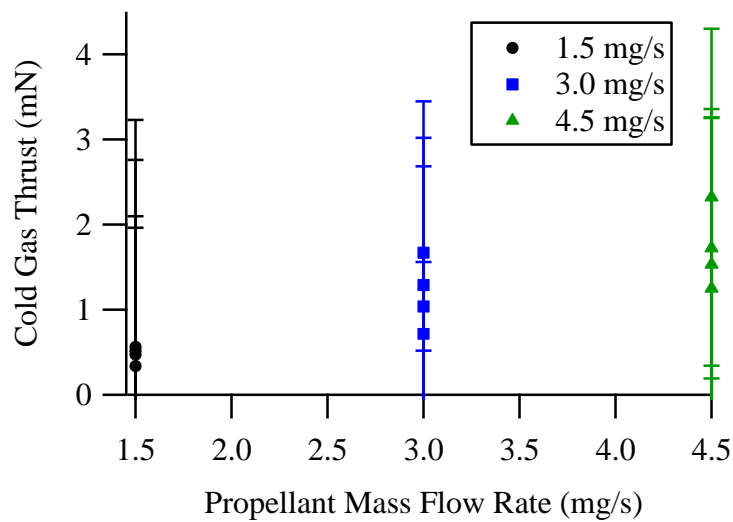
Figure 94. Cold gas thrust contribution of multiple tests as a function of mass flow rate.

From these findings, it is clear that the EHT is not effective as a thruster. It is possible that the EHT could be redesigned as an electrothermal thruster where the helicon plasma source is used to couple RF power to a plasma discharge to collisionally heat the propellant and expand it through a nozzle. However, given that ion temperatures are generally below 1 eV, this is very little energy deposited into the ions compared to the 15.76 eV required to ionize argon. This would still result in a thruster characterized by low specific impulse and efficiency. If a double layer is the ion acceleration mechanism, then it is characterized by small ion beam generation, large beam divergence, and low ion

energy. Therefore, unless there is a way to directly alter the ion acceleration mechanism to adjust these parameters, the EHT is unsuitable for thruster application.

6.7 Potential Trivelpiece-Gould Mode

The 600 W, 50 G case has so far been removed from much of the analysis. This is a result of the irregularities of the RPA measurements of the ion energy distributions. The other four operating conditions have RPA I-V plots that are generally constant until the plasma potential, and then decrease in two major sections, denoting the two ion energy populations. In contrast, the 600 W, 50 G case is characterized by an initial large decrease in ion current at low voltage, then a second drop in current without a clear region that would denote a distinct ion energy population. Figure 95 shows a comparison of the 600 W, 50 G case and the 343 W, 150 G case, the latter of which is more representative of the expected behavior.
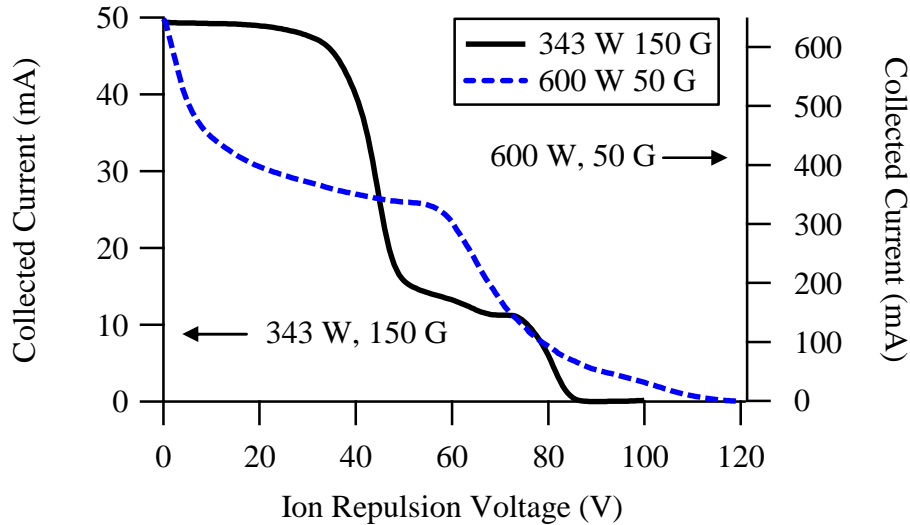
Figure 95. Comparison of I-V sweeps between expected behavior (black line) and unusual behavior at 600 W, 50 G (blue line).

The initial drop in collected current in the 600 G, 50 G case is unusual, as it would suggest that there is a large population of ions close to chamber ground. This stands in contrast to the emissive probe measurements, which show a plasma potential much higher than ground. Another possible explanation is that the 600 W, 50 G case has a much higher plasma density 50 cm downstream compared to the other four cases, which might adversely affect the RPA grid sheaths. However, even if this is the case, it does not explain the current decreasing at low voltages. As an example, if the sheath was too small on the electron repulsion grid, the RPA would not properly repel ions. As the ion repulsion grid voltage increases, the sheath off of the ion repulsion grid would expand and merge with the electron repulsion grid sheath and allow for design electron repulsion. Yet this would cause the current to increase as electrons are repelled, not decrease. Likewise, if the ion repulsion grid is too small and expands as the voltage on the grid increases, it would only repel ions with energy less than the repulsion grid voltage. This would still imply that a large number of ions are close to chamber ground.

Likewise, even supposing the initial drop in collected current is due to some adverse reaction of the RPA and is ignored, there would still be two distinct drops in the collection current that denotes the two ion populations at the plasma potential and the beam potential. Since these two populations cannot be clearly distinguished, analysis of the ion energy is difficult to perform and there is no definitive beam voltage that can be determined.

Despite this, the 600 W, 50 G case is unique in that the plasma density is much higher than the other four operating conditions despite the observed trend of a higher magnetic field yielding increased ion density. The most likely explanation is this operating

condition is in a Trivelpiece-Gould coupling mode, as TG coupled plasmas generally arise during operating at low magnetic field strengths.[82,83] By operating at 50 G, the electron cyclotron frequency is decreased to close to an order of magnitude higher than the RF frequency, which is a threshold to TG coupling.[83] Further investigation of low magnetic field operation of the helicon plasma source is required to confirm TG coupling, but this mode shows potential for higher efficiency operation compared to higher magnetic field operation. Figure 96 shows a comparison of operation at 600 W at 50 G and 350 G. One interesting observation from Chapter VIII is that the GHIT operating at 50 G does not observe a similar increase in ion density. Therefore, it is likely that this mode is inhibited by the presence of the grids, possibly due to requiring quasineutral plasma flow out of the discharge chamber. Despite the potential possibilities of this coupling mode, the beam current is still insufficient to justify the EHT as a thruster itself.
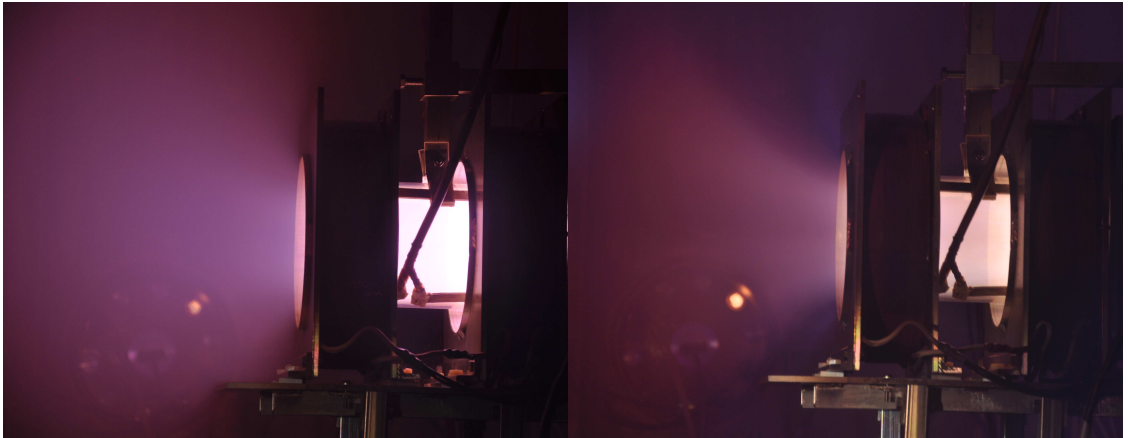
Figure 96. Operation of EHT at 600 W and 50 G (*left*) and 350 G (*right*). The discharge plasma at 50 G is demonstrably brighter and the plume does not follow the magnetic field lines.

CHAPTER VII

HELICON ION ACCELERATION

In the preceding chapter, the ion acceleration performance of the EHT is presented and found to be characterized by low beam current, low ion energy, and high beam divergence. The next step in the evaluation of the ion acceleration capability of the EHT is to determine the mechanisms responsible for the observed performance. Since the EHT couples ionization and ion acceleration into a single stage, the most effective method is to examine the plasma plume structure for the primary mechanisms that act on the ions. The plume structure is captured in contours of the ion number density, plasma potential, and electron temperature, measured in the previous chapter. The first task is to compare the plasma potential structure to the ion energy distributions to confirm ion energy is dependent solely on the change in plasma potential. The second task is to identify the primary forces acting on the ions during acceleration and compare them to the observed ion acceleration performance metrics.

This chapter examines the measurements of the plume structure from Chapter VI to determine the source of the ion energy and any potential losses. Calculation of the beam voltage using the ion energy profiles and the change in plasma potential measured by the emissive probe is found to be in agreement. The large beam divergence is found to be caused by radial electric fields downstream of the exit plane of the discharge chamber. These electric field lines follow the conical regions of high electron temperature and increase in intensity as the magnetic field is increased. Simulation of the ion trajectory

using the measured plasma plume characteristics show that an additional effect of increasing the magnetic field is to cause radial oscillations of the ions. These oscillations arise from competing electric forces from the conical regions of high plasma potential that form off of the edge of the discharge chamber wall. As the magnetic field increases, the potential in these regions increase and cause increased radial motion, which ultimately increases the ion path length. The region where this is most prevalent overlaps the region of highest neutral density, which leads to collisional dissipation of ion energy.

Ultimately this leads to a performance tradeoff with the magnetic field, as increasing the magnetic field increases ion density and beam current, but also increases beam divergence and collisional dissipation of ion energy. Furthermore, the beam divergence is not strongly impacted by any other operating parameter, which demonstrates that the EHT does not have clear and direct control over the ion trajectories.

7.1 Ion Energy Analysis

For propulsive application of the helicon, there are two primary operational metrics of interest: the beam current and the beam voltage. The beam current is the number of ions accelerated out of the thruster per unit time and is a measure of the ionized propellant flow rate. As such, thrust is directly proportional to the beam current. The beam voltage is the total potential drop experienced by the ions accelerated out of the thruster and describes the energy deposited into each ion. Table 1 from Chapter VI shows that the beam current from the helicon at every operating condition tested never exceeds 25 mA. The beam voltage, determined as the difference in potential between the two ion populations in the RPA scans, is found to be within the range of 19-42 V. The maximum

thrust possible from ion acceleration using these values would be less than 0.15 mN, which suggests that the measured thrust is due primarily to electron pressure[86] and thermal expansion of plasma-heated neutral gas, not ion acceleration.

While the performance metrics demonstrate that the helicon plasma source is not an effective thruster, examination of the ion energies is worthwhile in order to determine the cause of the substandard performance compared to similarly sized thrusters. The map of plasma potential for each operating condition provides an expected value for the beam voltage. The decrease in potential as the plasma expands downstream creates an electric field equal to the gradient of the potential. Normally, a plasma shields electric fields that occur using a sheath such that the bulk plasma does not encounter the electric field. In the case of the plume, the plasma is expanding to eventually contact the chamber wall (or disperse if in space) and can be thought of as one large sheath. More specifically, electric fields are present in regions of the plasma that are interacting with a boundary condition, and the plume is the interaction between the discharge plasma and the vacuum chamber wall (or the void of space) boundary condition. In this circumstance, quasi-neutrality might not apply and is instead replaced with the steady-state requirement that the divergence of the flux of ions is equal to that of electrons. By Poisson's Equation, given as Equation (C.1), the change in plasma potential is caused by small variations in the balance of the electron and ion number densities.

The result is that the downstream structure of the plasma potential creates a favorable potential gradient that accelerates the ions. The electrons are accelerated through ambipolar diffusion in order to maintain equivalent particle flux divergence, which applies an equivalent retarding force on the ions. Due to the large mass difference

between the ions and electrons, the change in ion energy is negligible. Therefore, the ion energy should be similar to the change in plasma potential from inside the discharge chamber to the measurement location of the RPA. Since no measurements of the plasma potential are made in the radial direction beyond -60 mm, radial symmetry is assumed and the plasma potential at -70º is equal to that at 70º. While the plasma inside the discharge chamber is not fully symmetric, at 50 cm downstream the contour is considerably more symmetric, justifying the assumption. The origin point for the plasma potential is selected as the point on the center axis furthest into the discharge chamber, which for most cases is -200 mm upstream of the exit plane. The beam voltage is calculated as the difference in voltage between the second and first peaks in the ion energy distribution in Table 2. Table 5 gives a summary of the beam voltages and the changes in plasma potential, and Figure 97 shows the data with respect to the measurement uncertainties. The second value in parenthesis for the beam voltage in Table 5 denotes the beam voltage of the third population observed in those two locations.

Table 5. Beam voltage and change in plasma potential between discharge chamber and RPA location

P_{RF} (W)	B (G)	θ (º)	V_b (V)	ΔV_p (V)
343	150	0	36.5 ± 3.6	32.4 ± 9.3
		60	26.0 ± 3.4	27.2 ± 9.5
		-70	23.5 ± 4.6	31.9 ± 8.8
	350	0	26.5 ± 4.1	28.9 ± 8.6
		60	19.0 ± 4.1	24.3 ± 9.1
		-70	$19.0 (30.0) \pm 3.7$	24.2 ± 8.6
600	150	0	41.5 ± 3.9	39.5 ± 9.6
		60	33.5 ± 4.2	41.8 ± 9.4
		-70	30.5 ± 3.7	28.9 ± 8.8
	350	0	34.0 ± 4.4	42.6 ± 9.0
		60	20.5 ± 4.0	46.7 ± 8.5
		-70	$23.0 (35.5) \pm 3.8$	43.8 ± 8.1
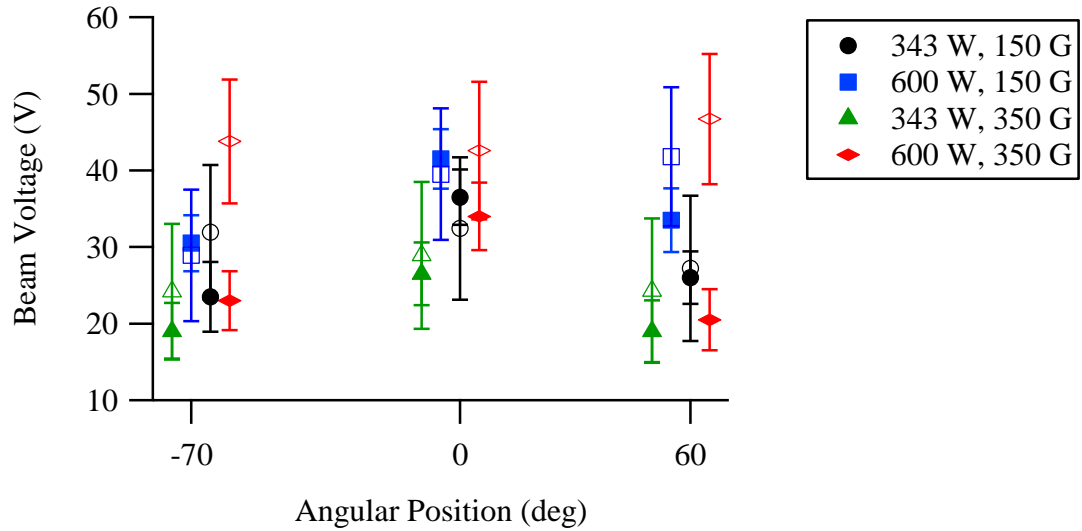
Figure 97. Beam voltage and change in plasma potential between the discharge chamber and the RPA location as a function of RF power, magnetic field, and angular position. Closed markers denote beam voltage measurements using the RPA, and open markers denote the change in plasma potential measured by the emissive probe. Angular positions for all measurements are either -70º, 0º, and 60º, separation of data points at these positions is done for clarity. 1.5 mg/s Ar, $1.6x10^{-5}$ Torr-Ar.

There is overall agreement, as the differences between the beam voltage and the change in plasma potential for most cases are within the uncertainty of the measurements. In particular, there are two observations: first, the beam voltage measured by the RPA is lower at -70º and 60º than on centerline by 8-13 V, depending on the operating conditions. Second, the change in plasma potential is independent of angular position within the measurement uncertainty, except for the 600 W, 150 G case. This suggests that for ions exhausted at an angle, some of the energy gained from the drop in potential is dissipated. For all but the 600 W, 350 G case, this loss of energy ranges from 1-8 V, which is within the uncertainty of the measurements. In three cases at 150 G, the beam voltage measured by the RPA is 1-4 V higher than what is measured with the emissive probe. These cases demonstrate the systemic uncertainty associated with conducting the same experiment at the same conditions but at different times. In contrast, the 600 W,

350 G is a clear example where the difference between the measured beam voltage and the change in plasma potential is larger than the measurement uncertainty. This supports the hypothesis that an energy loss mechanism occurs for ions at -70° and 60°, particularly at 350 G. The cause for the energy loss for ions accelerated at an angle can be further investigated by examining the electric field in the plume region.

7.2 Electric Field Effects

Since the primary source of the ion energy comes from the plasma potential structure, the accelerating electric field can be determined from the negative gradient of the potential across the area of the contour. The electric field is calculated using Newton's Difference Quotient of the measured plasma potential. Since the plasma potential is given in two dimensions, the radial and axial components of the field are solved individually.

$$E_{r,i} = \frac{\phi_{i+1} - \phi_{i-1}}{r_{i+1} - r_{i-1}} \qquad (7.1)$$

$$E_{z,i} = \frac{\phi_{i+1} - \phi_{i-1}}{z_{i+1} - z_{i-1}} \qquad (7.2)$$

Under the assumption that the plume is radially symmetric, there is no azimuthal variation of the plasma potential; therefore there is no azimuthal electric field. Even if the plume does not have perfect radial symmetry, any variation in θ should be small

compared to variations in *r* and *z*. Thus, only the radial and axial electric fields are considered.

An example of the calculated electric field lines plotted over the plasma potential contour is presented in Figure 98. One item to note from the overlay is the electric field has very strong radial components near the exit plane of the discharge chamber and in the region where *r* is greater than 100 mm. The presence of these radial electric fields potentially explains the high degree of divergence within the plume, as an ion exiting the discharge chamber would encounter a large radial electric field unless it is near the centerline of the device.
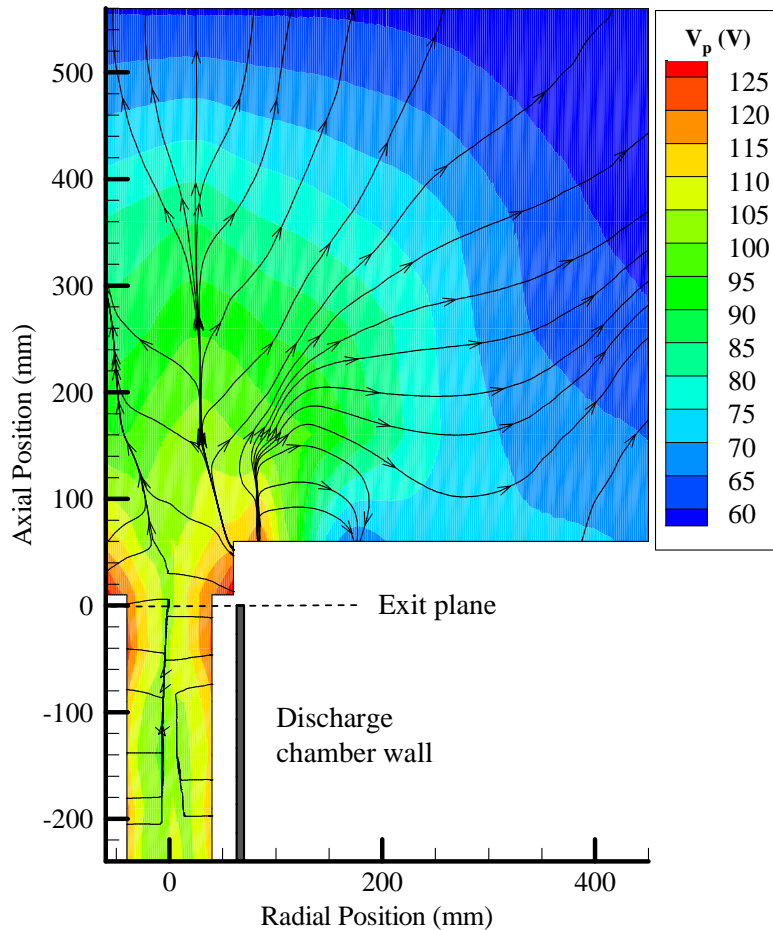
Figure 98. Plasma potential and electric field lines at 600 W, 350 G, 1.5 mg/s Ar, 1.6x10⁻⁵ Torr-Ar.

One particular structure in the electric field occurs at the radial position 75 mm, and axial position between 100 and 150 mm. At this point, there is a cluster of electric field lines that turn from purely axial to mostly radial, and some field lines turn back towards the thruster. The cause of this field line cluster can be seen by overlaying the electric field onto the contour for the electron temperature, shown in Figure 99. The field line cluster occurs at the high electron temperature region observed in the previous chapter. This region is most likely formed from high energy electrons escaping confinement on the magnetic field lines. The lower energy electrons remain confined and are turned back towards the thruster, which pulls the electric field lines back in the -z direction.
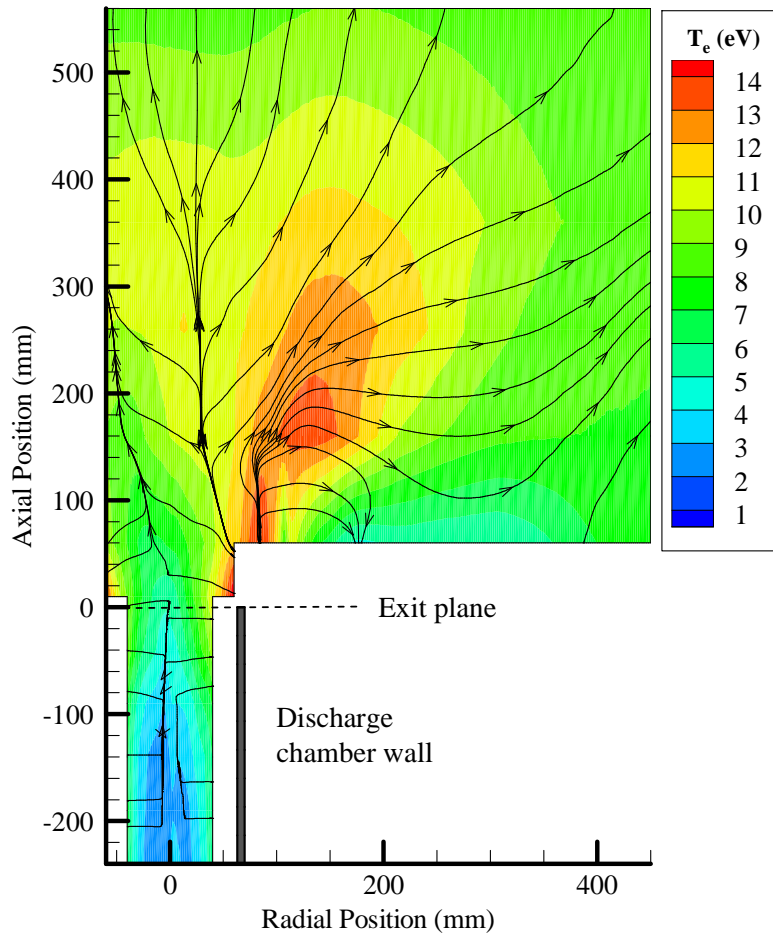
Figure 99. Electron temperature and electric field lines at 600 W, 350 G, 1.5 mg/s Ar, 1.6x10^{-5} Torr-Ar.

The above field structure would explain the high degree of beam divergence in the 600 W, 350 G case, and by extension the 343 W, 350 G case, as the two have similar electron temperature contours. Any ion that enters the high electron temperature regions would be accelerated radially outwards, and for certain regions receive a negative axial component as well. Conversely, at 150 G the high electron temperature regions are more broadly spread across the radius of the plume, as shown in Figure 100. This suggests the electric field lines are more evenly distributed, which promotes a wide plume with ions emitted evenly across all angles. The gap in this high electron temperature region in the negative radial position most likely explains why a current density peak occurs at -70º for this operating condition and not at 343 W, 150 G, which has a more symmetric electron temperature contour. Unfortunately, since measurements are not available for that side of the plume, the exact nature of the electric field lines are unknown.
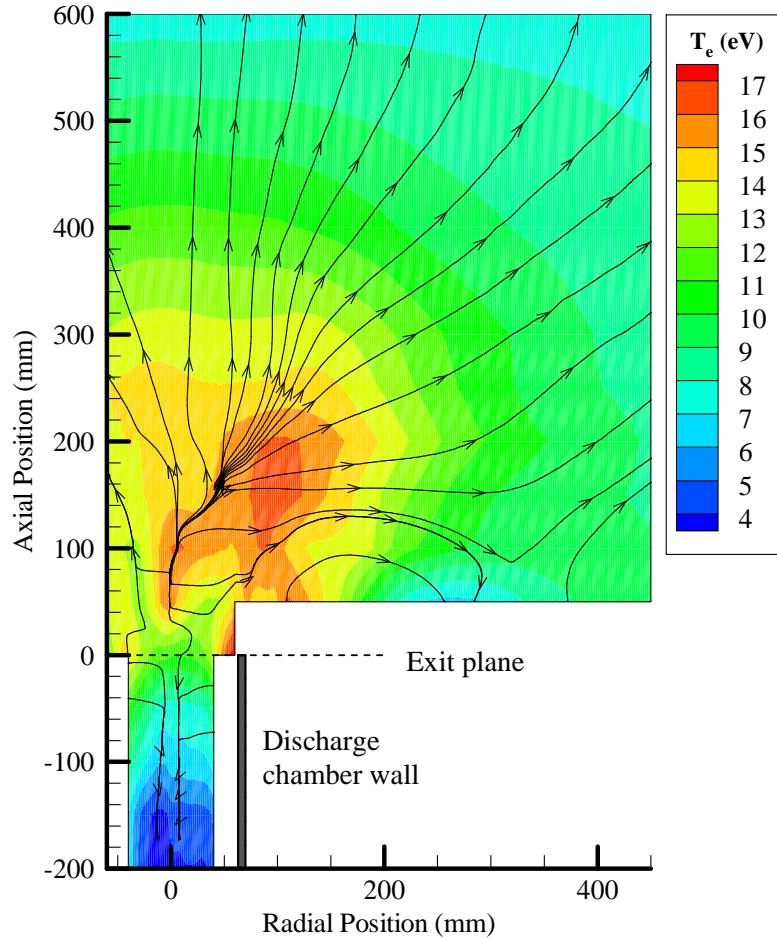
Figure 100. Electron temperature and electric field lines at 600 W, 150 G, 1.5 mg/s Ar, 1.6x10^{-5} Torr-Ar.

This mechanism also explains the current density distribution of the 50 G case. Recall that while the 50 G case has distinct peaks, the relative values of the peaks compared to the centerline current density are not as disparate as in the 350 G cases. At 50 G, the electrons are only weakly magnetized and only a very small region of high electron temperature forms near the exit plane. While these regions still direct some ions radially outward, it is much less pronounced. Thus the current density distribution is generally even with a few regions of higher current. The cause for the -26° peak is difficult to determine, as no data is available for that side of the plume. However, it is

most likely the result of asymmetry within the electron temperature distribution. It is worth noting that the central region of low electron temperature favors that side of the plume, so it is possible that this asymmetry causes the -26º peak.
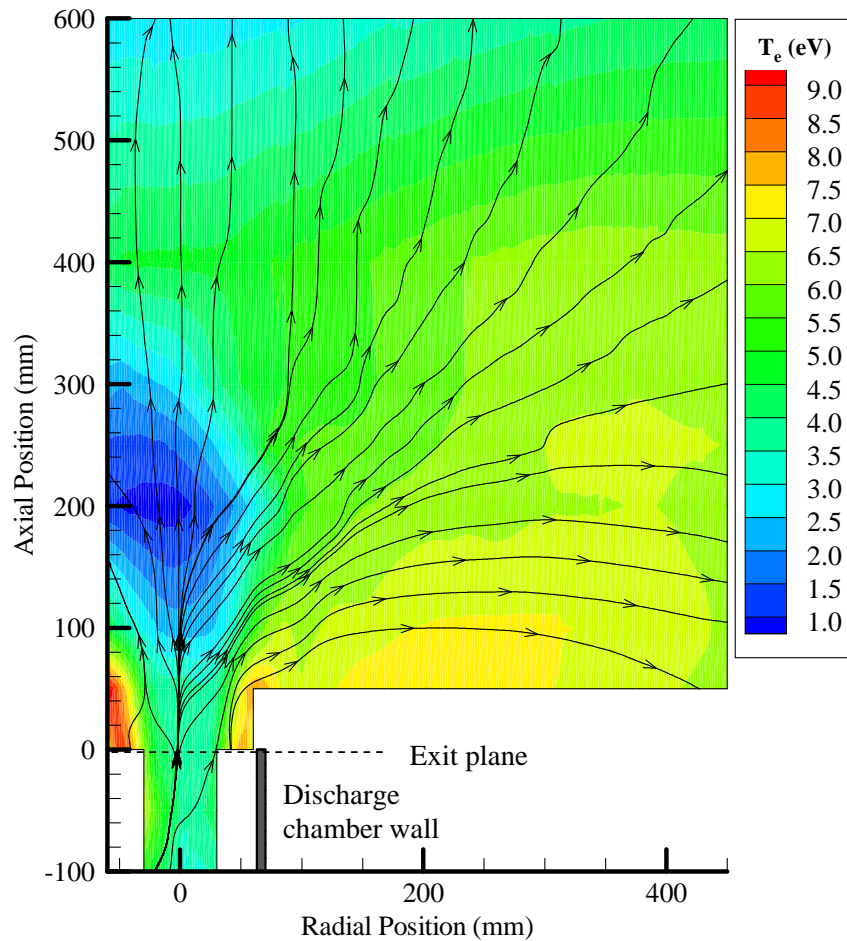
Figure 101. Electron temperature and electric field lines at 600 W, 50 G, 1.5 mg/s Ar, 1.6x10^{-5} Torr-Ar.

Thus far the discussion has been limited to a qualitative assessment of the observed contours of the plasma potential and the electron temperature with overlays of the electric field lines. While the electric field is an important component in determining the ion

172

path, it does not describe the pathlines of the ions. Therefore, in order to quantitatively discuss the effects of the operating conditions, the ion trajectories must be determined.

7.3 Ion Trajectories

There are two general approaches to modeling the expansion of the plasma into the plume: an Eulerian approach of solving the plasma flow using the magnetohydrodynamic (MHD) equations, and a Lagrangian approach of solving the momentum equations for a single ion in the plasma flow. The Eulerian approach involves solving the equations to determine the entire plume structure and ion velocities using boundary conditions of the experimental data. This method is difficult to conduct, as it requires solving a system of simultaneous equations for each point across the entire area of the plume. Even if simplified to a 2-D problem, this would be a difficult task. The Lagrangian approach is simpler, as it uses the data already measured to solve the momentum equations for a single ion placed at the exit plane of the discharge chamber. The momentum equations can be iteratively solved through discrete time steps until the ion reaches the edge of the measured data set, recording the position at each time step. This generates a pathline for the ion, and by solving for multiple starting positions, a sample of the ion trajectories can be generated.

For this model, all variations in the azimuthal direction are neglected, as radial symmetry is assumed. The ions are considered to be isothermal at 0.1 eV. The momentum equation from the MHD equations is

$$nm_i\left[\frac{\partial \bar{v}_i}{\partial t}+(\bar{v}_i\bullet\nabla)\bar{v}_i\right]=en_i\left(\bar{E}+\bar{v}_i\times\bar{B}\right)-\nabla(n_ik_bT_i)+m_in_iv_{in}\left(\bar{v}_n-\bar{v}_i\right) \quad (7.3)$$

Electron-ion collisions are neglected, as the large mass disparity results in negligible impact on the ion velocity. The term on the left hand side of the equation is the material derivative, which is only used in the Eulerian approach. This is easily converted to a Lagrangian system utilizing the definition of the total derivative. The example below is for the radial component of the term.

$$\left[\frac{\partial v_{i,r}}{\partial t}+v_{i,r}\frac{\partial v_{i,r}}{\partial r}+\frac{v_{i,\theta}}{r}\frac{\partial v_{i,r}}{\partial\theta}+v_{i,z}\frac{\partial v_{i,r}}{\partial z}-\frac{v_{i,\theta}^2}{r}\right]=\frac{\partial v_{i,r}}{\partial t}+v_{i,r}\frac{\partial v_{i,r}}{\partial r}+v_{i,z}\frac{\partial v_{i,r}}{\partial z}$$

The 1/r terms are dropped to avoid forming a singularity on the centerline axis.

$$\frac{\partial v_{i,r}}{\partial t}+v_{i,r}\frac{\partial v_{i,r}}{\partial r}+v_{i,z}\frac{\partial v_{i,r}}{\partial z}=\frac{\partial v_{i,r}}{\partial t}+\frac{dr}{dt}\frac{\partial v_{i,r}}{\partial r}+\frac{dz}{dt}\frac{\partial v_{i,r}}{\partial z}\equiv\frac{dv_{i,r}}{dt}$$

The resulting radial and axial momentum equations are

$$\frac{dv_{i,r}}{dt}=\frac{e}{m_i}E_r-\frac{e}{m_i}v_{i,z}B_\theta-\frac{k_bT_i}{m_in_i}\frac{\partial n_i}{\partial r} \quad (7.4)$$

$$\frac{dv_{i,z}}{dt}=\frac{e}{m_i}E_z-\frac{e}{m_i}v_{i,r}B_\theta-\frac{k_bT_i}{m_in_i}\frac{\partial n_i}{\partial z} \quad (7.5)$$

The collisional term is dropped since it applies to a bulk fluid element, not to an individual particle. While ion-neutral collisions are no longer captured in the trajectory model, they should not be removed from qualitative consideration. The azimuthal magnetic field term is also neglected; since the solenoids provide no azimuthal magnetic field, this field would only be induced by plasma currents. The induced azimuthal magnetic field can be estimated using Ampere's law.

$$\nabla \times \vec{B} = \mu_0 \vec{j} \tag{7.6}$$

Isolating the *z*-axis component and substituting ion and electron flux for the current density,

$$-\frac{\partial B_\theta}{\partial z} = \mu_0 e\left(n_i v_{i,r} - n_e v_{e,r}\right) \tag{7.7}$$

Ambipolar diffusion of the plasma exhaust requires a net zero charge flux, and since radial diffusion requires crossing magnetic field lines where electrons are bound, the diffusion rates of electrons and ions should be approximately equal. This results in negligible azimuthal magnetic field. As an upper bound estimate, even if the charge fluxes were not equal, the largest value the net current could reach is the case where both ions and electrons are at their thermal velocities (i.e. ions are not accelerated, thus giving a large disparity in velocities). As an example, integration along the centerline through the range of measured axial positions for the 343 W, 150 G case results in an upper

bound for the total induced magnetic field of approximately 8.5 G. In practice, ambipolar diffusion results in a much lower value.

Additionally, only motion in the *r-z* plane is modeled, as under the radial symmetry assumption any ion that drifts out of the plane of the page will be replaced by one drifting into the plane. Furthermore, the *ExB* drift is small compared to the magnitude of the electric field, which means any azimuthal drift is negligible. In essence, the model is a 2-D projection of the ion pathlines through the plume.

Equations (7.4) and (7.5) are solved iteratively in time steps of 5 µs, and the values of the plasma parameters are interpolated from the measured data using bilinear interpolation. The interpolated value of some parameter *f* at a position of (*r,z*) is given by

$$f(r,z) = \frac{1}{(r_2 - r_1)(z_2 - z_1)} [f(r_1, z_1)(r_2 - r)(z_2 - z) + f(r_2, z_1)(r - r_1)(z_2 - z)$$

$$+ f(r_1, z_2)(r_2 - r)(z - z_1) + f(r_2, z_2)(r - r_1)(z - z_1)] \tag{7.8}$$

where $r_2 > r > r_1$, and $z_2 > z > z_1$, and the numbered coordinates correspond to positions of measured data points. The position and velocity is incremented each step by

$$\delta r = \frac{1}{2} \frac{dv_{i,r}}{dt} (\delta t)^2 + v_{i,r} \delta t \tag{7.9}$$

$$\delta z = \frac{1}{2} \frac{dv_{i,z}}{dt} (\delta t)^2 + v_{i,z} \delta t \tag{7.10}$$

$$\delta v_{i,r} = \frac{dv_{i,r}}{dt} \delta t \tag{7.11}$$

$$\delta v_{i,z} = \frac{dv_{i,z}}{dt} \delta t \tag{7.12}$$

Most parameters of the model are set by the measured data of the plume, but there are a few assumed initial conditions. The ions are assumed to start at an initial axial position of 5 mm past the exit plane of the discharge chamber. This allows enough calculation space to determine if ions backstream into the discharge chamber or accelerate downstream. A sample set of ions are modeled with varying initial radial positions, from -60 to 60 mm in 10 mm steps. The ions are assumed to have an initial velocity equal to the average thermal velocity at 0.1 eV (approximately 500 m/s) in both the radial and axial velocity components. Ions with a negative initial radial position are initialized with a negative radial velocity, and ions with a positive initial radial position have a positive radial velocity. All ions are assumed to have a positive axial velocity. Variation of the initial velocities shows that the model is generally insensitive to initial ion energies within the range of reasonable estimates (less than 1 eV) due to the large electric fields. Figure 102 shows an example of the effects of initial ion thermal velocity.
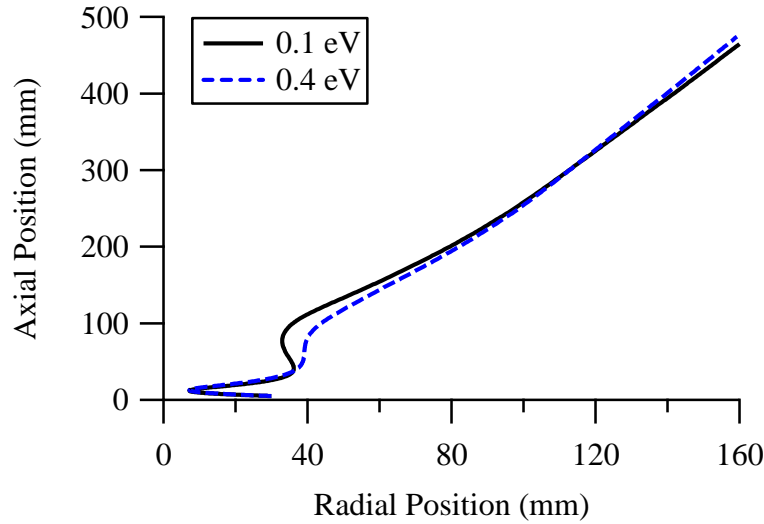
Figure 102. Variation in simulated ion pathlines due to initial ion thermal velocity for 343 W, 150 G.

The trajectories for a sample of ion initial positions are shown in Figure 103 through Figure 105. Only one simulation per magnetic field is shown, as the shape of the data contours is strongly set by the magnetic field and other parameters are less significant. At 50 G the trajectories are evenly spread, though ions placed close to the walls near the high electron temperature region have highly radial trajectories. As the magnetic field increases, the trajectories begin to be focused more radially outwards, until at 350 G very few trajectories are primarily axial. Some of the ions are found to be immediately accelerated back into the discharge chamber. This is caused by the ion's initial position being placed near an adverse potential gradient.
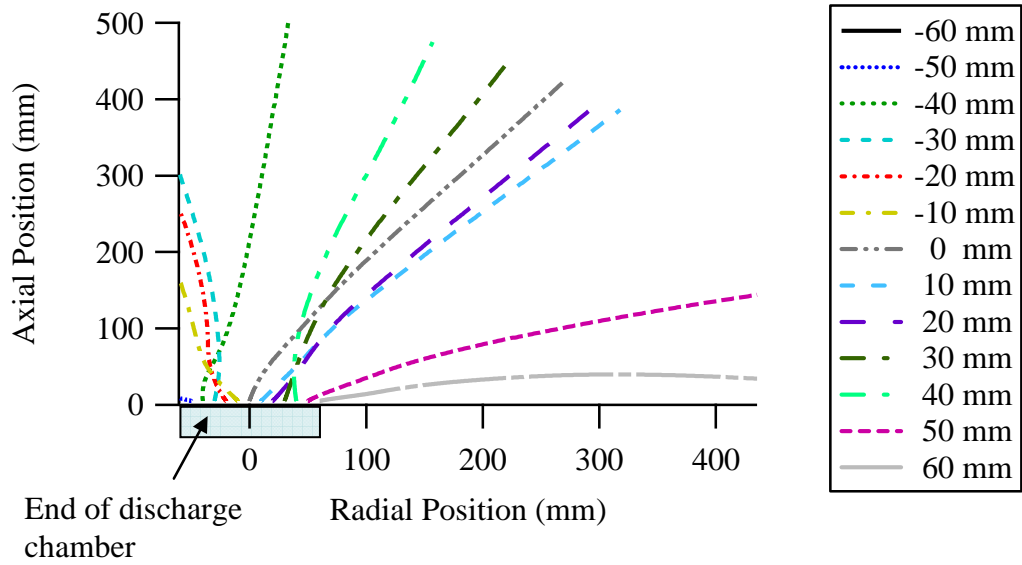
Figure 103. Simulated ion pathlines for various initial radial positions at 600 W, 50 G.
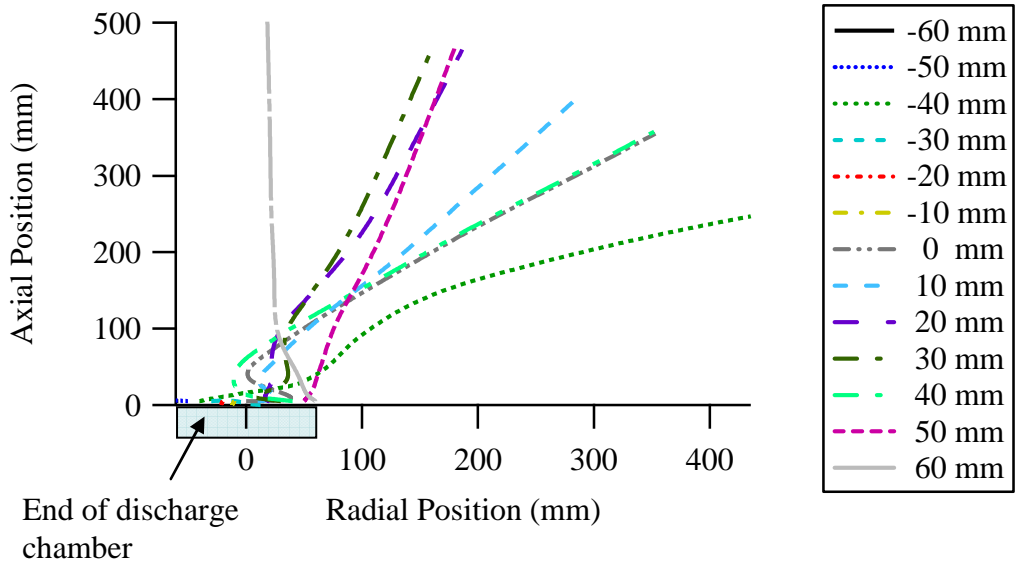
Figure 104. Simulated ion pathlines for various initial radial positions at 343 W, 150 G.
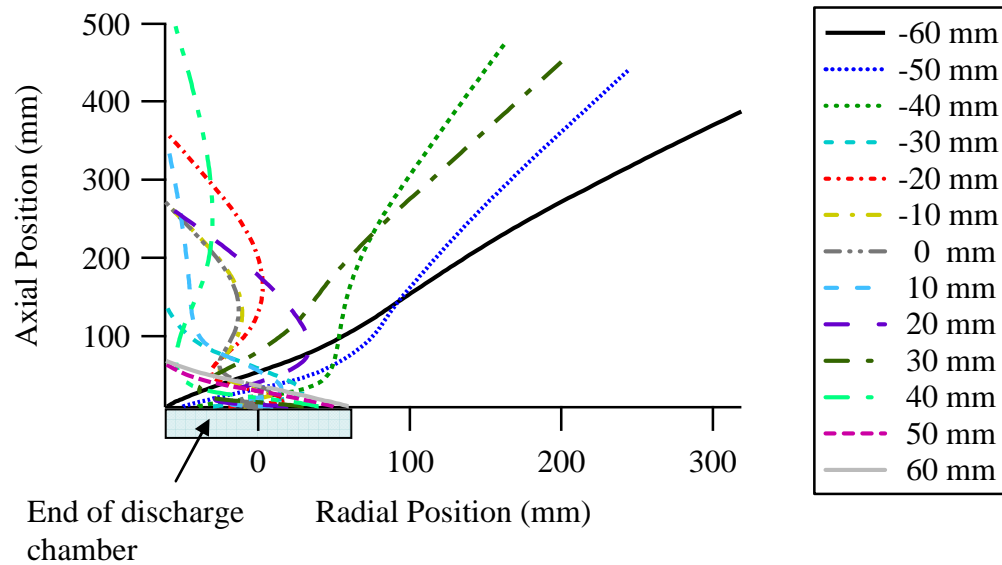
Figure 105. Simulated ion pathlines for various initial radial positions at 600 W, 350 G.

There are several noteworthy observations regarding the simulations. Firstly, the momentum equation is heavily dominated by the electric field. The temperature and density of the ions are low enough such that the pressure gradient term is smaller than the electric field term for the entire trajectory. Secondly, the effect of the magnetic field on ion trajectories explains the behavior of the current density profiles in Figure 68. At low magnetic field strength, the ions have a much more even distribution of resultant path angles. Ions at the center tend to exit at an angle, and combined with a density distribution that peaks on the centerline, this results in current density peaks at these angles. However, these current density peaks are smaller relative to the average current density compared to what is observed at other operating conditions. At higher magnetic fields the ion trajectories become much more focused on these off-center angles, which results in the formation of large peaks relative to the average.

A third observation is that the predicted trajectories are at angles less than the 60° as determined by the Faraday probe. However, this discrepancy is due to the exclusion of

ion-neutral collisions in the model. These collisions are most prevalent inside the discharge chamber and just beyond the exit plane. Using a simulation of the neutral gas expansion out of the discharge chamber,[84,85] the ion-neutral mean free path grows from approximately 50 mm at the exit plane to 150 mm at 50 mm downstream of the exit plane. After this point the mean free path rapidly increases until the plume becomes effectively collisionless. A plot of the mean free path as a function of position is shown in Figure 106.
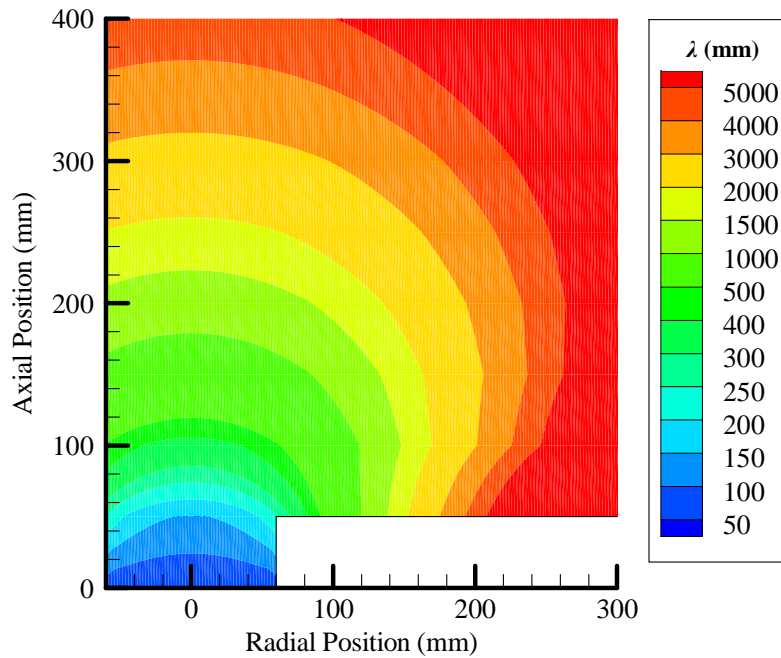
Figure 106. Simulated ion-neutral mean free path for 1.5 mg/s argon flow.

Ion-neutral collisions will dissipate ion energy, either through momentum exchange or charge-exchange, although the momentum exchange collision cross section is larger for momentum exchange.[86] As a result, the majority of collisional dissipation of ion energy will occur within the first 100 mm from the exit plane of the discharge chamber.

A closer view of this region for the three operating conditions is shown in Figure 107 through Figure 109.
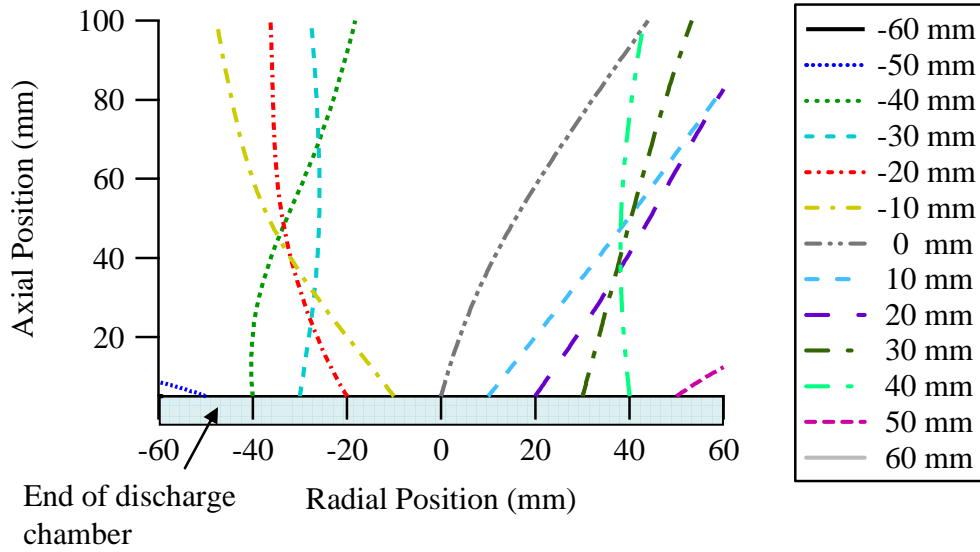
Figure 107. Simulated ion pathlines for various initial radial positions near the exit plane for 600 W, 50 G.
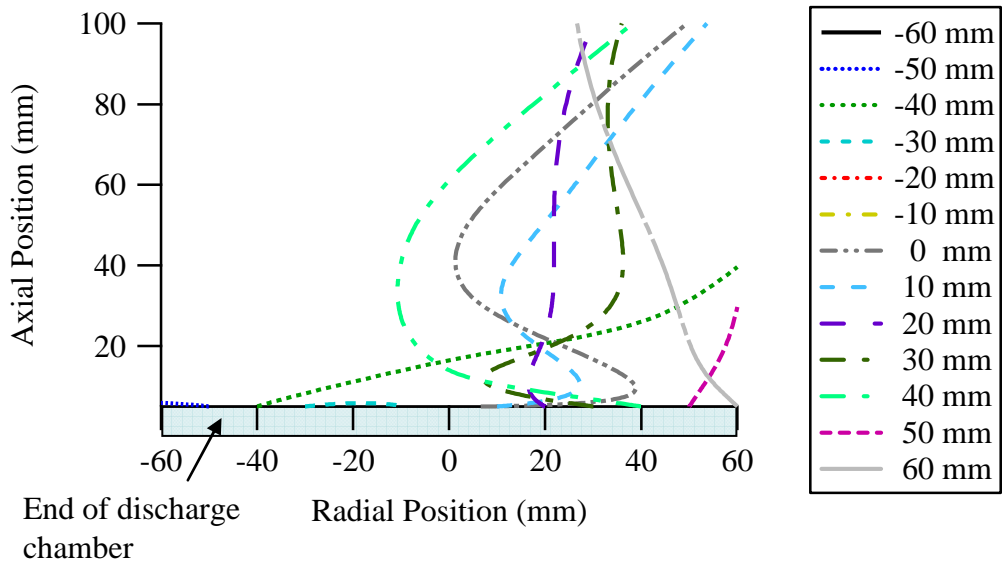
Figure 108. Simulated ion pathlines for various initial radial positions near the exit plane for 343 W, 150 G.
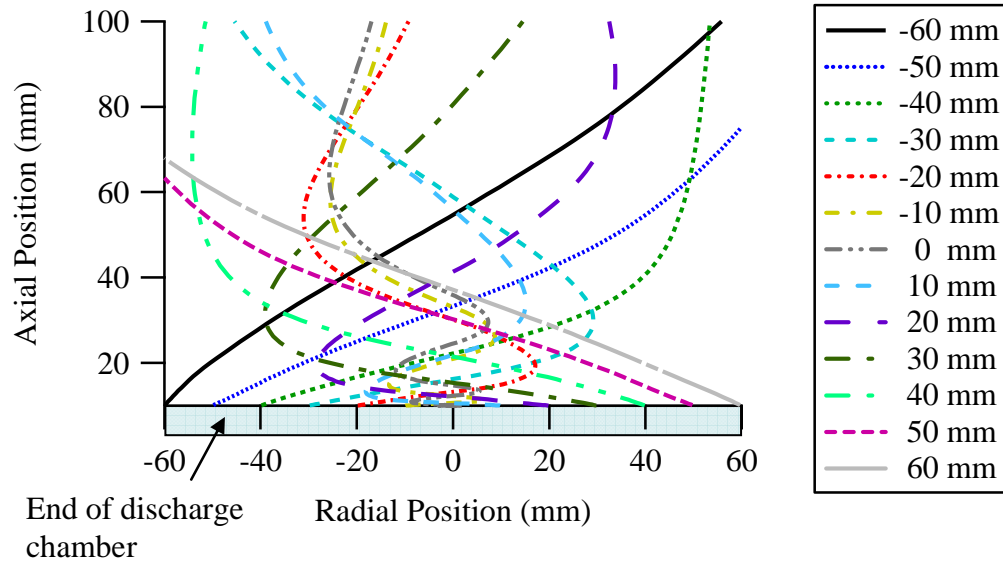
Figure 109. Simulated ion pathlines for various initial radial positions near the exit plane for 600 W, 350 G.

The region near the exit plane shows negligible net radial motion. For the 50 G case, this is a result of the electric field having negligible radial components immediately downstream of the exit plane, excluding the small regions near the walls. For the 150 G and 350 G cases, this is a result of the ions reflecting between the regions of high plasma potential that extends from the walls downstream. The 350 G case in particular subjects ions to multiple reflections. Thus ions in this region generally undergo a net axial acceleration, while any radial components are primarily added further downstream near the regions of high electron temperature that occur 100 mm downstream of the exit plane and beyond. Therefore, as ions exit the discharge chamber, collisional dissipation of ion energy primarily impacts the axial velocity of the ions. This has an impact on the ion trajectories by increasing the relative size of the radial component, which increases the trajectory divergence angle from the centerline. Therefore, the high beam divergence angle observed is most likely caused by a combination of radial electric field lines

downstream of the exit plane and collisional dissipation of axial energy close to the exit plane.

The oscillatory trajectories in the 350 G case also explain another discrepancy. Recall from Table 5 that the operating conditions that saw the greater disagreement between the beam voltage measured by the RPA and the difference in plasma potential is at 350 G. As seen in Figure 109, the 350 G is also where the greatest amount of radial ion reflection occurs near the exit plane of the discharge chamber. The electric field is a conservative force, which means the total energy gained by the ion is independent of the path taken. This is quantified by the change in plasma potential between the inside of the discharge chamber and 50 cm downstream at the RPA. However, collisional dissipation is non-conservative, which means that as the path length of the ion trajectory increases inside the region close to the exit plane, the amount of energy dissipated increases. The ions accelerated out of the discharge chamber at 350 G have a much longer path inside this collisional region than at 150 G or 50 G. Therefore, a greater amount of energy is lost, which explains why the ion that reaches the RPA has a lower energy than predicted solely by the plasma potential.

7.4 Conclusions

There are three conclusions that can be drawn about the ion acceleration capability of the EHT from the measured behavior. Firstly, the energy of the accelerated ions is equal to the change in plasma potential between the discharge chamber and the location at which the ion energy was measured. This supports the assumption that the double layer is the ion acceleration mechanism of the EHT. Additionally, ion energy can be dissipated

through ion-neutral collisions near the exit plane of the discharge chamber. This is particularly prevalent at higher magnetic fields, where radial motions of the ions increase the total path length inside this collisional region before the ions exit at large angles to the axis of the device.

The second conclusion is the gradient of the potential has a strong impact on the direction of the resulting ion velocity. The electric field in the plume structure is the primary force acting on the ions and is responsible for the large beam divergence. However, the shape of the plasma potential, and thus the electric field, is set by the magnetic field. It is the magnetic field that determines the shape of the plume structure, while RF power is observed only to impact the intensity of the plume structures.

The first two conclusions in combination yield the third conclusion: the EHT has very limited control of the ion acceleration using the available operating parameters. While each operating condition has a demonstrated effect on the ion acceleration, the set of operational parameters available do not form a basis that can clearly control each performance metric. A clear example of this is in the beam divergence half-angle, which only has a demonstrable dependence on the magnetic field. At low magnetic field strengths, the plume diverges approximately evenly across all angles. As the magnetic field strength increases, the ions are progressively deflected at large angles from the centerline. Thus while the magnetic field can impact the ion trajectory, it cannot be used to optimize the performance metric of interest, the beam divergence half-angle. Furthermore, as multiple device characteristics demonstrate a dependence on the magnetic field, there is a tradeoff between operating parameters. As an example, increasing the magnetic field strength is found to increase the ion number density, but at

the cost of decreasing ion energy and increasing beam divergence. Thus, even if one performance metric could be optimized, it would require the other two metrics to be suboptimal.

CHAPTER VIII

GHIT PERFORMANCE

While Chapters VI and VII covered the performance and ion acceleration mechanism of the EHT, the next two chapters present the performance evaluation and analysis of the GHIT. The inclusion of the grids in the device separates the ionization and ion acceleration processes, which now allows for individual evaluation of each. In addition to the selected quantitative ion acceleration metrics of ion energy, ion beam current, and beam divergence half-angle, there is considerable importance to the qualitative metric of parametric control through the device operating conditions. The design of the GHIT provides three more operating parameters that can be used to control the ion acceleration with the goal of achieving greater performance manipulation than what is observed with the EHT.

This chapter presents the performance measurements of the GHIT, both in regard to the discharge chamber and the ion plume. The behavior of the discharge chamber ionization is quantified in the first section by the average ion number density and electron temperature that is estimated using the screen grid as a planar Langmuir probe. The second section contains measurements of the individual thruster currents that are used to determine beam current and quantify behavior of the grid ion optics. In the third section, the beam divergence is measured using a Faraday probe to evaluate beam collimation and overall ion trajectory. The final section provides direct thrust measurements that are compared to the estimated thrust due to ion acceleration.

Thrust is found to be lower than predicted, primarily due to large ion losses to the grids. The relative accel grid currents and screen-to-anode current ratios demonstrate that optimal grid perveance is only achieved for one operating condition at the lowest plasma density. The under-focusing of the ions is a result of an insufficient potential drop across the grid and a spatially varying discharge plasma density. However, those ions that are successfully focused into the ion beam are found to be successfully collimated into a cohesive ion beam. The beam divergence half-angle is found to have a strong dependency on discharge voltage, which shows further increases in beam collimation can be achieved with further increases in the discharge voltage. The operating conditions also demonstrate a high degree of control over both ionization and ion acceleration.

8.1 Discharge Analysis

While a thorough examination of the performance of the helicon plasma source has already been performed in Chapter VI, the ion number density and electron temperature measurements determined are not entirely accurate for the gridded thruster configuration. This is due to the grids decreasing the effective exit area for the propellant, thereby increasing the discharge pressure and the electron-neutral ionization collision frequency. However, these two parameters describe the plasma conditions inside the discharge, and as is discussed in Chapter III, the interaction between the discharge plasma and the grid potentials determine the ion optics. Therefore, new measurements of the ion density and electron temperature are required at each thruster operating condition in order to allow for meaningful comparison of the ion optics.

8.1.1 Analysis Methodology

The most direct method is to directly measure the discharge plasma parameters using an emissive probe or Langmuir probe, though the presence of the grids greatly increases the complexity of taking such a measurement. One possible solution is to create a duplicate set of grids with a section removed to allow probe entry into the discharge. However, due to time and resource constraints, such an approach is not feasible. An alternative approach is to use the screen grid as a planar Langmuir probe to create an averaged estimate of the ion number density and the electron temperature. Using this approach, the measurement can be done during the same test as thruster performance measurements and only requires sweeping the screen grid potential and measuring the current collected by the screen grid.

As discussed in Chapter III, when an electrode is immersed in a plasma, a sheath forms. If the screen grid is biased below the discharge plasma potential, only a fraction of the electron flux incident on the sheath will have sufficient energy to traverse the adverse potential gradient and reach the screen. In contrast, Equation (3.6) shows that the ion flux is independent of the sheath potential. Thus as the screen grid potential is progressively biased below the anode potential the ion current will be constant while the electron current will decrease. Assuming a Maxwellian electron population, the electron current flux can be described as

$$j_e = j_{e,0} \exp\left(\frac{e\phi_s}{k_b T_e}\right) \qquad (8.1)$$

where $j_{e,0}$ is the electron flux when the screen grid collects zero net current, and φ_s is the screen grid sheath potential. The screen grid sheath potential is defined as

$$\phi_s = -\left(V_s - V_f\right) \tag{8.2}$$

where V_s is the bias applied on the screen grid, and V_f is the screen grid bias required to collect zero net current (called the floating potential). In Equation (8.2), the screen grid bias and the floating potential are defined as absolute values to mimic what is observed on the screen grid power supply using the thruster circuit in Figure 30. While these two potentials are treated as positive quantities for simplicity, the screen grid sheath potential is a negative quantity by definition.

As mentioned earlier, the ion flux to the sheath is invariant with the sheath potential and is equal to the Bohm current given in Equation (3.6). The total current flux collected by the screen grid is thus

$$j_s = j_i - j_{e,0} \exp\left(\frac{e\phi_s}{k_b T_e}\right) \tag{8.3}$$

The ion saturation current, I_{sat}, is the ion current collected by an electrode in the absence of an electron current and is the maximum current collected by the screen grid at the end of the I-V sweep. Since the electron flux at the floating potential must equal the ion flux in order to collect zero net current, Equation (8.3) can be rewritten using Equation (8.2) to be

$$I_s = I_{sat}\left(1 - \exp\left(\frac{-e\left(V_s - V_f\right)}{k_b T_e}\right)\right)$$ (8.4)

The electron temperature is then estimated through the use of a least-squares curve fit of the I-V sweep of the screen grid to Equation (8.4). The ion number density is then determined using Equation (3.6). Due to quasi-neutrality, this value also describes the electron number density. However, since the grid potential is much lower than at its designed point at full operation, the sheath is not a full Child-Langmuir sheath and therefore does not extend into the apertures. Instead, the discharge plasma extends past the screen grid and is present on both sides of the screen. Therefore the total collection area from the screen grid is unknown. Instead, the discharge plasma density can be estimated using the anode current and collection area at the same screen grid voltage. This is sufficient, as the current to the anode must equal the current to the grid sheath to maintain charge balance, and the anode area is known and invariant.

$$n_0 = \frac{I_a}{0.61 e A_a}\left(\frac{m_i}{k_b T_e}\right)^{1/2}$$ (8.5)

An example set of I-V sweeps at 150 G for several RF powers is shown in Figure 110. The saturation current can be clearly seen as the value asymptotically approached by each curve as the screen grid bias increases.
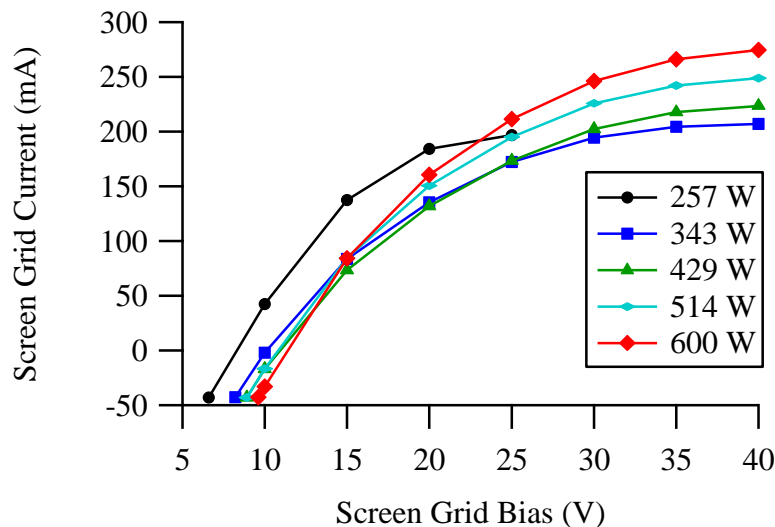
Figure 110. Screen grid current as a function of grid bias at 150 G, 1.5 mg/s. Note that the screen grid potential is below anode potential, but is defined as a positive quantity.

It is important to note that this process only generates a single value each for the electron temperature and the ion number density. However, as the results in Chapter VI show, the density and temperature are not necessarily constant along the exit plane of the discharge. Therefore this methodology only results in an estimate of an effective average of the temperature and density. There still remains the possibility that there is a finite density gradient along the plane of the grids and thus the perveance is not constant throughout the grid assembly. This effective average is still sufficient for quantifying the change in discharge performance between operating conditions, as the spatial average determines the maximum possible beam current that can be created from the discharge.

8.1.2 Discharge Results

There are four parameters that are varied to control the discharge plasma: the RF power, the axial magnetic field, the propellant flow rate, and the current through the anode coil. While not every permutation of operating conditions is tested, the sample set

includes variations of each parameter with all other conditions constant. The discharge

test is performed with the anode biased 100 V above the cathode and no potential applied

to the accel grid. Figure 111 through Figure 115 show the results of the discharge

analysis for each operating condition.
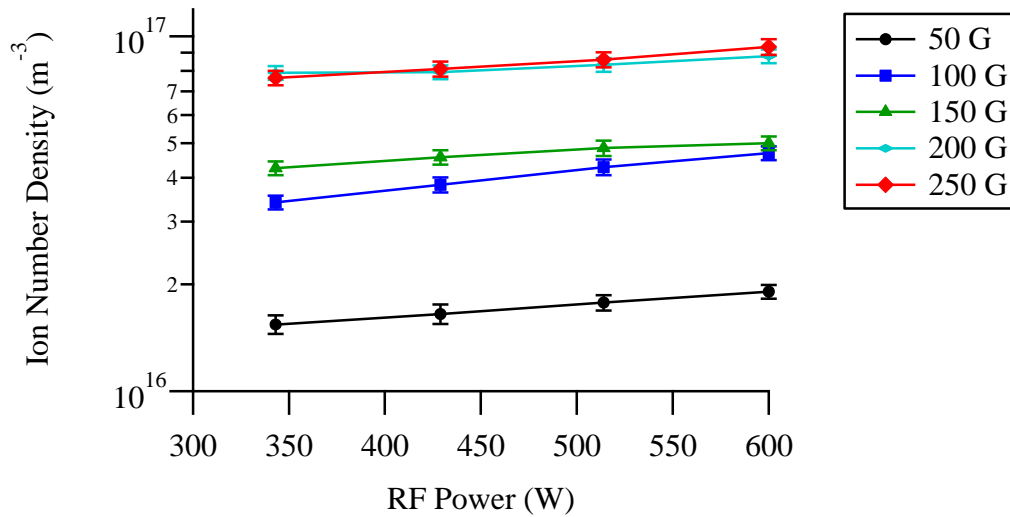
Figure 111. Discharge ion number density as a function of RF power and magnetic field. 1.5 mg/s argon, 1.6x10^{-5} Torr-Ar chamber pressure.
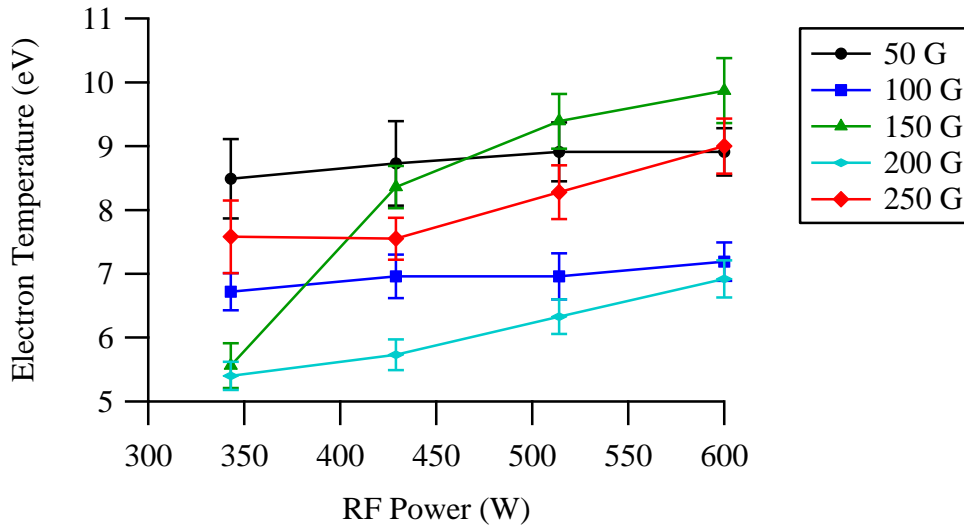
Figure 112. Discharge electron temperature as a function of RF power and magnetic field. 1.5 mg/s argon, 1.6x10^{-5} Torr-Ar chamber pressure.
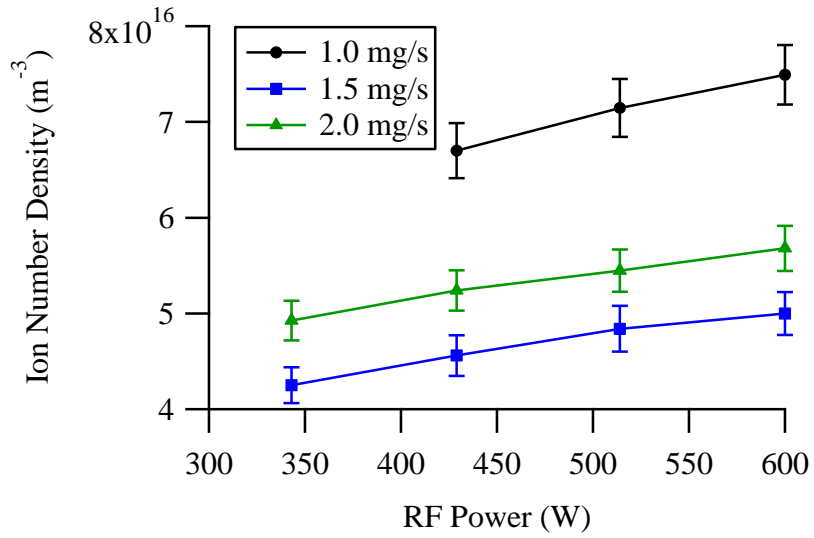
Figure 113. Discharge ion number density as a function of RF power and argon flow rate. 150 G, 1.4, 1.6, and 1.7x10^{-5} Torr-Ar chamber pressure for 1.0, 1.5, and 2.0 mg/s flow rates, respectively.
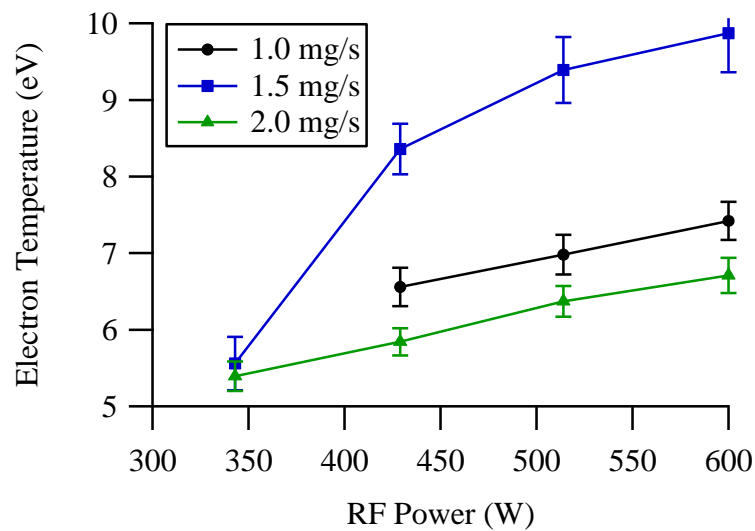
Figure 114. Discharge electron temperature as a function of RF power and argon flow rate. 150 G, 1.4, 1.6, and 1.7x10^{-5} Torr-Ar chamber pressure for 1.0, 1.5, and 2.0 mg/s flow rates, respectively.
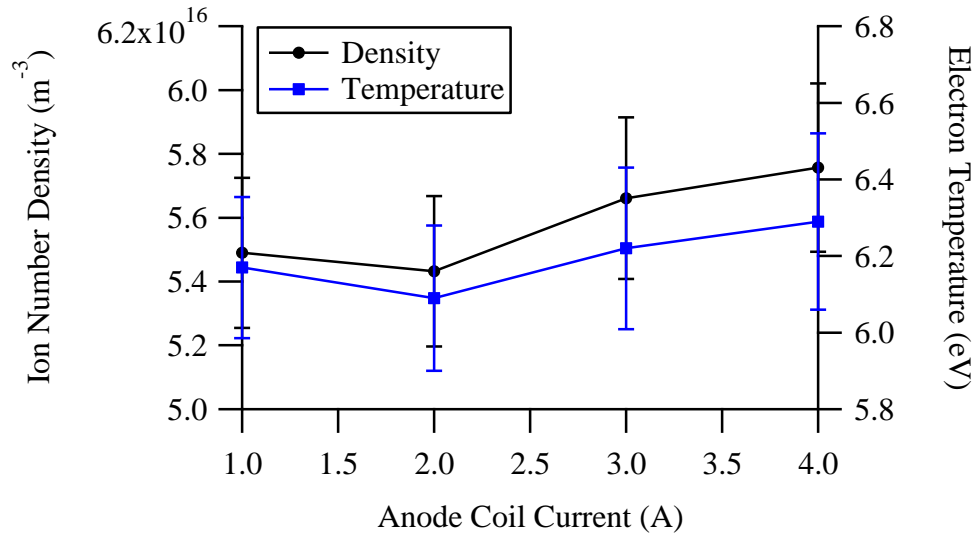
Figure 115. Discharge ion number density and electron temperature as a function of anode coil current. 500 W RF power, 150 G, 1.5 mg/s argon flow rate, 1.6×10^{-5} Torr-Ar chamber pressure.

Across the tested operating conditions, the ion number density ranges from 10^{16} to 10^{17} m^{-3} and the electron temperature varies between 5-10 eV. The magnetic field has the largest impact on the ion number density, with an approximately linear correlation. The magnetic field also has a strong effect on the electron temperature, but it is not monotonic. Increasing the RF power provides slight increases in both ion number density and electron temperature. Increasing the mass flow rate decreases the ion number density while also having a non-monotonic relationship with the electron temperature. The anode coil has the smallest effect on the discharge plasma, with a four-fold increase in magnetic field increasing the density by approximately 10%. The electron temperature is increased by a similar amount across the same range.

The observed parametric effects on discharge performance are as expected. Increasing the magnetic field has such a strong impact on the ion density for two reasons: the first is that it decreases radial electron mobility which reduces electron losses to the walls. The second reason is that confinement of the electrons to gyrations along the

magnetic field lines increases the overall path length traveled by an electron relative to axial distance traveled. This increases the probability that an electron will collide with a neutral before reaching the anode. Both of these mechanisms serve to increase ionization efficiency and the ion number density. Conversely, increasing the propellant flow rate increases neutral density and thus increases electron-neutral ionization collision frequency. However, the increased neutral density also increases ion-neutral neutralization collision frequency, as well as the frequency of electron-neutral collisions which increase radial electron mobility to the wall. Due to these competing effects, increasing the neutral pressure does not affect the discharge to the extent of a change in magnetic field.

The fact that the anode coil does not greatly increase discharge density or temperature is most likely due to the reliance on a magnetic mirror to restrict electron mobility to the anode. For a given electron confined on a magnetic field line, it has a magnetic moment, defined as

$$\mu = \frac{m_e v_{\perp}^2}{2B} \tag{8.6}$$

where $v_{\perp}$ is the velocity of the electron orthogonal to the magnetic field line. If the electron is restricted to the same magnetic field line, the magnetic moment is invariant; as the magnetic field strength increases, the orthogonal kinetic energy increases at the expense of axial velocity. The electron is repelled when the axial velocity reaches zero. At this point, the orthogonal kinetic energy is equal to the total initial kinetic energy. The invariance of the magnetic moment therefore shows

$$\frac{B}{B'} = \frac{v_{\perp}^2}{v_{\perp}'^2} = \frac{v_{\perp}^2}{v^2} = \sin^2\theta \qquad (8.7)$$

where the prime denotes values at the point of repulsion and θ is the pitch angle of the electron rotation around the magnetic field line. An electron can pass through the barrier if the pitch angle is smaller than this critical value. In velocity space, this creates a conical region of electron velocities that result in escaping the mirror, called a loss cone. The anode coil has such a small impact due to the fact collisions can alter the electron velocity and cause a confined electron to enter the loss cone. Inside the discharge, the mean free path of an electron is on the order of a centimeter, which means collisions are likely to mitigate the effectiveness of the anode coil.

One important note is that the discharge analysis is also useful for determining the ideal screen grid voltage required to prevent electron passage to the screen grid and ensure saturation. From the data collected, a screen grid potential of 35 V below the anode is sufficient across all operating conditions and is used for all further GHIT operation.

8.2 GHIT Electrical Circuit

The operation of the GHIT can be conceptualized as a circuit with currents flowing through the various sections that correspond to ion or electron collection. One advantage that ion engines have over Hall effect thrusters is during operation the beam current can be explicitly known from the currents in the thruster circuit. In a Hall thruster, the current collected by the anode is a combination of an electron current corresponding to

197

ions accelerated into the beam, and an electron current from the cathode that failed to collisionally ionize a neutral atom. This second current is recycled through the discharge circuit and returned to the cathode, creating inefficiency and preventing an accurate determination of the beam current from the discharge current. In an ion engine however, the presence of the negatively biased accel grid prevents any electrons from the neutralizer cathode from entering the discharge chamber. Therefore any electrons collected by the anode must correspond to ions exiting the discharge, either through collection at the grids, or through acceleration into the beam. Measurement of the thruster currents is therefore an accurate method to determine the beam current, which is an important metric of thruster performance.

8.2.1 Electrical Circuit Measurement and Uncertainty

The thruster circuit is a conceptualization of the schematic shown in Figure 30. The discharge plasma is treated as a conductive element that connects the grids and the anode. The grids and the anode act as direct connections from the discharge plasma to the respective power supplies that provide the component potential. The anode is assumed to collect only electrons, which results in a positive current into the discharge. The grids are assumed to collect only ions, and thus are depicted as positive currents out of the discharge. Any ion current that is not collected by either the screen or the accel grid is assumed to enter the plume as part of the ion beam. This ion current must be neutralized by an electron current of equal magnitude from the cathode, which is connected to the discharge supply. This electron current is represented as a positive current flowing to the discharge supply from the cathode. The individual currents collected by the anode and the grids are determined by measuring the voltage across three resistor shunts. The

resistances of the shunts for the anode, screen grid, and accel grid are 5.085, 5.095, and 5.079 Ω, respectively. Figure 116 shows the thruster circuit. It should be noted that while the screen and accel grids are biased below the anode and cathode, respectively, they are reported by their magnitudes.
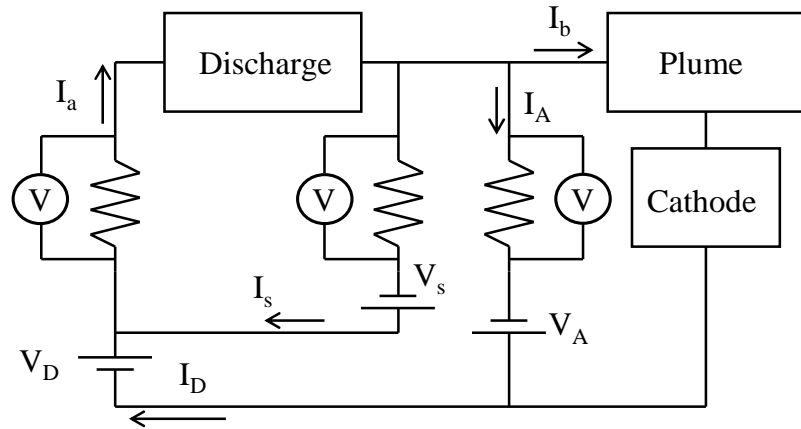
Figure 116. GHIT thruster circuit.

Using Kirchhoff's junction rule at the discharge, the beam current, I_b, can be defined from Figure 116 as

$$I_b = I_a - I_s - I_A \tag{8.8}$$

The voltage across the resistor shunts are measured using three Fluke 83 V multimeters. The Fluke 83 V has an uncertainty of $\pm 0.3\%$ of the measured value for the measurement range used. The shunt resistance is measured with an Agilent U1733C RLC meter with an accuracy of $\pm 0.7\% + 0.008\ \Omega$ for the 20 Ω range used. The total uncertainty of the current measurements is $\pm 0.9\%$.

8.2.2 Thruster Electrical Circuit Results

Figure 117 shows an example plot of the individual thruster circuit currents as a function of discharge voltage. The anode current is relatively constant throughout, increasing by only 2% across the range of the discharge voltage. This is due to the anode current consisting only of electrons that are collected to balance the drift of ions into the grid sheath. Whether the ions impact with the grids or contribute to the ion beam is irrelevant for the purposes of determining the anode current, as the electron current must equal the ion current to maintain quasi-neutrality. Since the ion flux into the sheath is independent of discharge voltage and is set only by the discharge density and temperature, the anode current is expected to be constant. The small increase is a result of the accel grid sheath progressively extending past the screen grid as the perveance decreases. Recall from Chapter III that perveance decreases as the total potential drop across the grids increases. Figure 18 through Figure 20 illustrate this small increase in sheath surface area.
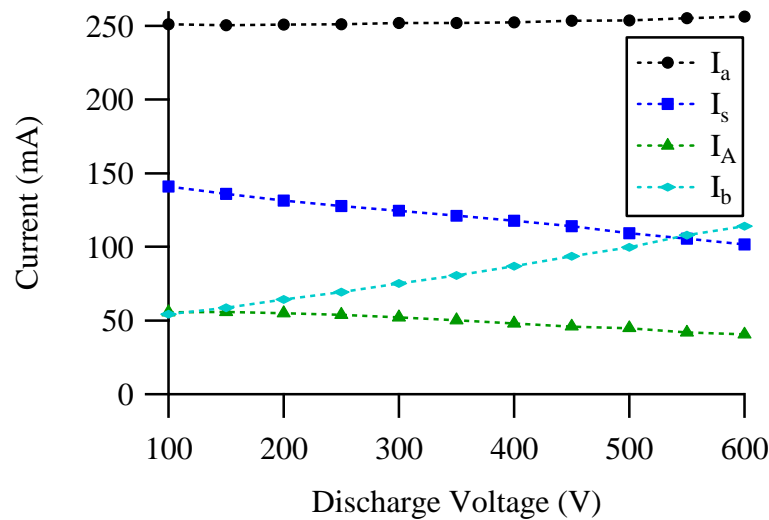
Figure 117. Thruster circuit currents as a function of discharge voltage. 600 W RF power, 100 G magnetic field, 1.5 mg/s argon, 35 V screen grid, 150 V accel grid, 1.6x10^{-5} Torr-Ar chamber pressure.

Of the information presented in Figure 117, there are two performance metrics of interest: the beam current and the relative accel grid current. The beam current is useful as it can be used to determine thrust using the equation shown below. The relative accel grid current, defined as the ratio of the accel grid current to the beam current, is an important metric that describes the performance of the ion optics. One of the goals of ion engine design is to minimize this value, as ion bombardment on the accel grid not only reduces beam current, but is also a leading cause of accel grid erosion and thruster failure. Since the relative accel grid current is dependent on the ion optics, it is plotted as a function of the normalized perveance, defined in Equation (3.15), though the only parameter varied is the discharge voltage.

For the sake of brevity, only a sample of the data is presented. Figure 118 provides an example of how the beam current varies as the discharge voltage and the RF power are changed. For all test cases, increasing either parameter increases the beam current,

though the effect does not always appear as linear as the case in Figure 118. Figure 119

shows the relative accel grid current plotted against the normalized perveance for the

same operating conditions used in Figure 118.
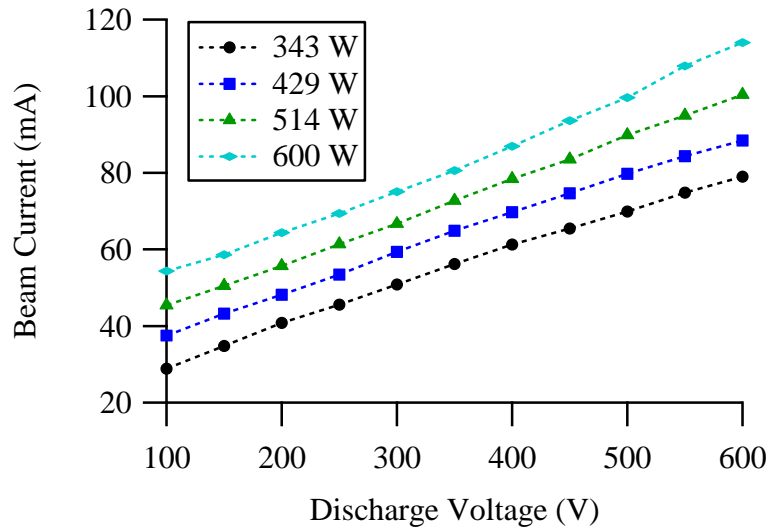
Figure 118. Beam current as a function of discharge voltage and RF power. 100 G magnetic field, 1.5 mg/s argon, 35 V screen grid bias, 150 V accel grid bias, 1.6x10^{-5} Torr-Ar chamber pressure.
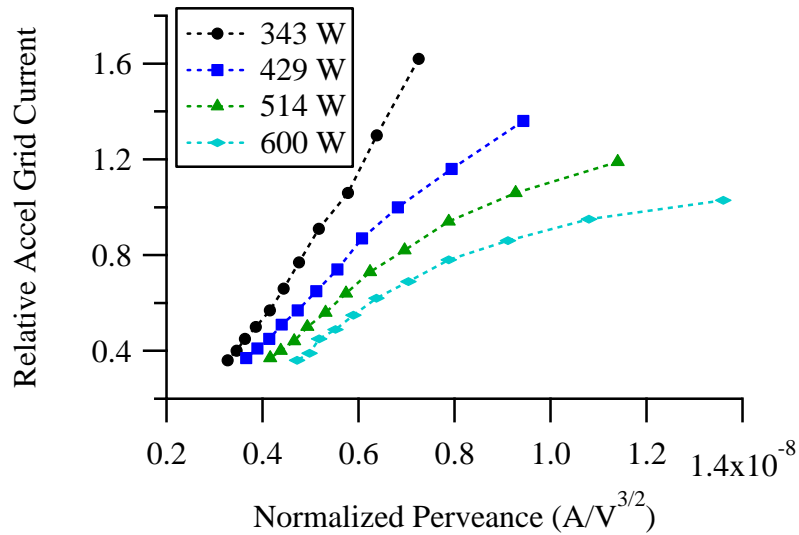
Figure 119. Relative accel grid current as a function of normalized perveance and RF power. 100 G magnetic field, 1.5 mg/s argon, 35 V screen grid bias, 150 V accel grid bias, 1.6x10^{-5} Torr-Ar chamber pressure.

The first observation of Figure 119 is the relative accel grid current is not constant for the same normalized perveance. As discussed in Chapter III, the ion optics is determined by the placement and shape of the accel grid sheath, which is set by the perveance. Even though the discharge plasma density and temperature changes with the RF power, this would be captured in the normalized perveance as a change in beam current. The expectation is that the ion optics, represented as the ratio of extracted ions striking the accel grid to beam ions, should be constant for any given normalized perveance. However, this assumes that the perveance is normalized at each aperture, or that the discharge plasma conditions are uniform across the grids. As mentioned earlier, this is unlikely to be a valid assumption since the ion number density in the helicon without grids is not constant along the radius of the exit plane and the presence of the grids is unlikely to remove that radial dependency. The most likely explanation is that as the RF power increases, the radial ion density and electron temperature distributions change, altering the distribution of local perveance at each aperture. The change in normalized perveance captured in Figure 119 reflects the change in overall ion optics as the discharge plasma changes with RF power.

An example of where this effect occurs to a much smaller extent is shown in Figure 120 and Figure 121. In this data set, there is still variation of the beam current with RF power and discharge voltage, but the relative accel grid current as a function of normalized perveance is much more consistent. Across the five magnetic fields tested, 50, 100, 150, 200, and 250 G, the degree of similarity between the relative accel grid currents at the same magnetic field strength varies. This suggests the change in the

discharge plasma density and temperature spatial distributions is a function of the magnetic field.
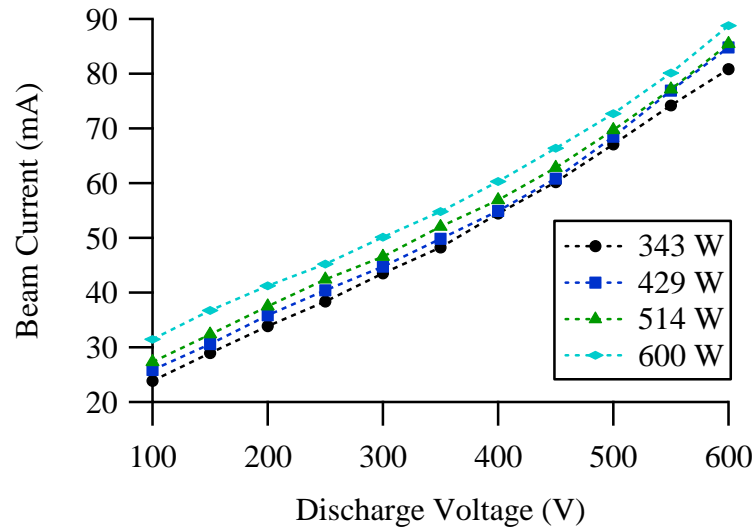
Figure 120. Beam current as a function of discharge voltage and RF power. 150 G magnetic field, 1.5 mg/s argon, 35 V screen grid bias, 150 V accel grid bias, 1.6×10^{-5} Torr-Ar chamber pressure.
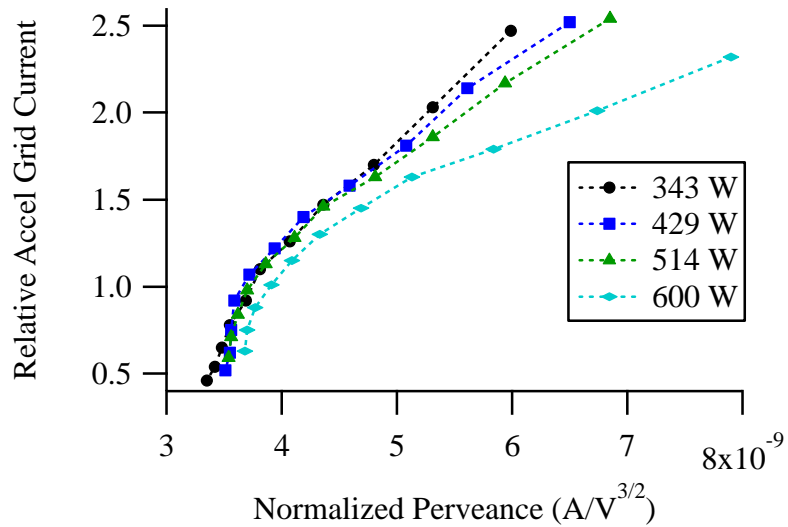
Figure 121. Relative accel grid current as a function of normalized perveance and RF power. 150 G magnetic field, 1.5 mg/s argon, 35 V screen grid bias, 150 V accel grid bias, 1.6×10^{-5} Torr-Ar chamber pressure.

Further evidence of the effect of the magnetic field on the ion optics can be seen in Figure 122, which shows the relative accel grid current for each magnetic field at 600 W. The five curves are quite disparate and show no general trend with the magnetic field. In contrast, Figure 119 and Figure 121 show either nearly identical shapes, or a distinct similarity between lines corresponding to differing RF power. The marked difference in the response of the relative accel grid current to the two parameters shows that the magnetic field has the greater impact, while the RF power only slightly alters the shape of the plot, if at all. Continuing the line of thought that variance in relative accel grid current for the same grid geometry is a result of changes in the discharge plasma spatial distribution, this suggests that the magnetic field has a greater impact on shaping the discharge plasma than does RF power.
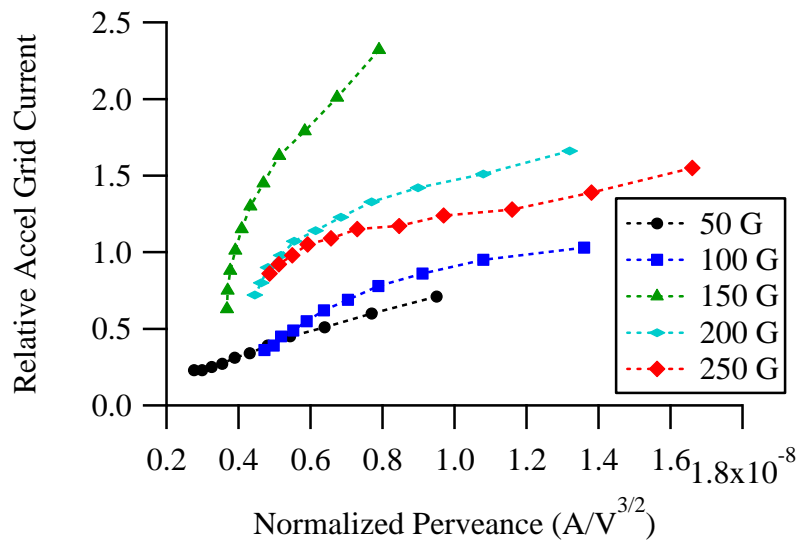
Figure 122. Relative accel grid current as a function of normalized perveance and magnetic field. 600 W RF power, 1.5 mg/s argon, 35 V screen grid bias, 150 V accel grid bias, 1.6×10^{-5} Torr-Ar chamber pressure.

The magnetic field dependency of the ion optics distorts the impact the magnetic field has on the ion beam compared to expectations based solely on the results of the discharge analysis in Section 8.1. As an example, the beam current for the same operating conditions as in Figure 122 is plotted in Figure 123. From the data in Figure 111, and since ion current into the grid sheath is linearly proportion with density and only proportional to temperature by the square root, it would be expected that beam current should be monotonic with the magnetic field. However, the data in Figure 123 shows that the beam current at 100 G is larger than the 150 G and 200 G cases. This is not due to a larger than expected impact from the electron temperature variance with the magnetic field, as the ion current extracted by the grids (whether it strikes the accel grid or enters the beam) follows expectations much more closely, as shown in Figure 124. Despite having relatively low ion extraction from the discharge plasma, the 50 and 100 G cases have a relatively larger beam current due to their low relative accel grid current compared to the other cases. Since proportionally fewer ions are lost to the accel grid compared to the higher magnetic field cases, the 50 and 100 G cases have a higher beam current than expected.
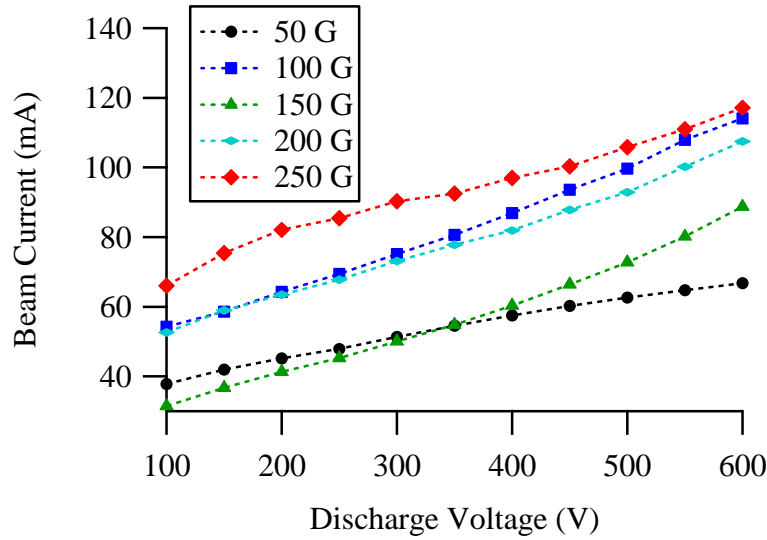
Figure 123. Beam current as a function of discharge voltage and magnetic field. 600 W RF power, 1.5 mg/s argon, 35 V screen grid bias, 150 V accel grid bias, 1.6×10^{-5} Torr-Ar chamber pressure.
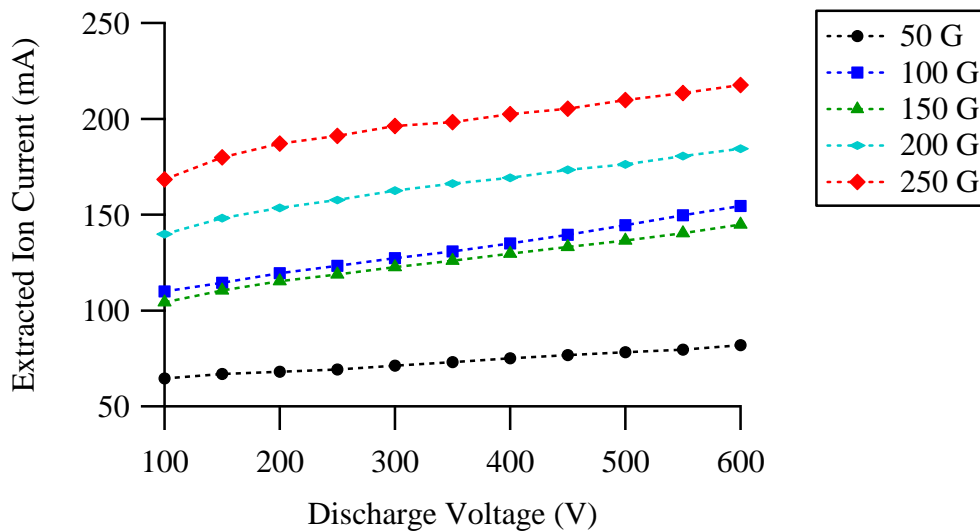
Figure 124. Extracted ion current as a function of discharge voltage and magnetic field. 600 W RF power, 1.5 mg/s argon, 35 V screen grid bias, 150 V accel grid bias, 1.6×10^{-5} Torr-Ar chamber pressure.

The impact of the propellant flow rates on the beam current and the relative accel grid current is shown below in Figure 125 and Figure 126. The beam current trend closely follows expectations based on Figure 113. The 0.73 mg/s case is performed as a test to determine if the trend of increased beam current from decreased propellant flow rate

continued, although such is not the case. This suggests that as the propellant flow rate decreases beyond a threshold, the two competing mechanisms of electron-neutral collisional ionization and electron-neutral collision-induced wall losses begin to favor the electron-neutral collisional ionization. Thus as neutral density is decreased from 1.0 mg/s to 0.73 mg/s, the ionization efficiency decreases and discharge density (and thus beam current) decreases. Considering that the 0.73, 1.5, and 2.0 mg/s cases have nearly identical ion optics and 1.0 mg/s is rather unique, it is likely that at 1.0 mg/s the ionization efficiency is high enough to transition to another coupling mode. This change in the coupling mode would alter the spatial distribution of the discharge plasma density and temperature, and therefore explain the change in overall ion optics.
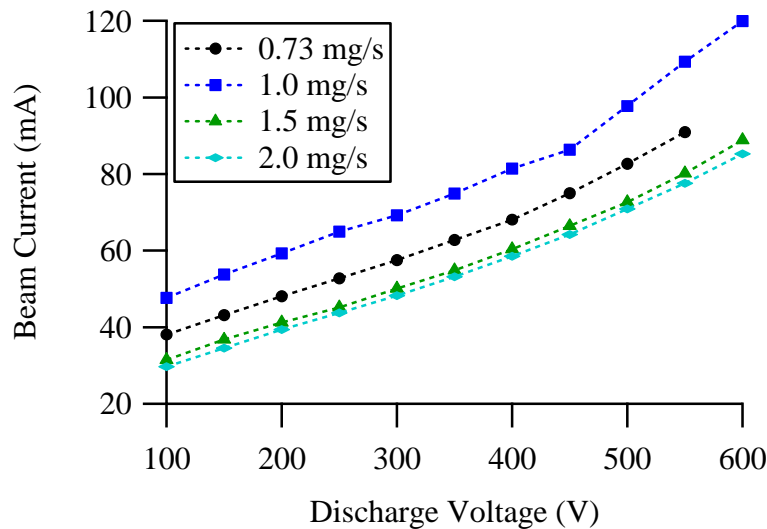
Figure 125. Beam current as a function of discharge voltage and argon flow rate. 600 W RF power, 150 G magnetic field, 35 V screen grid bias, 150 V accel grid bias, 1.4, 1.4, 1.6, and 1.7x10^{-5} Torr-Ar chamber pressure for 0.73, 1.0, 1.5, and 2.0 mg/s flow rates, respectively.
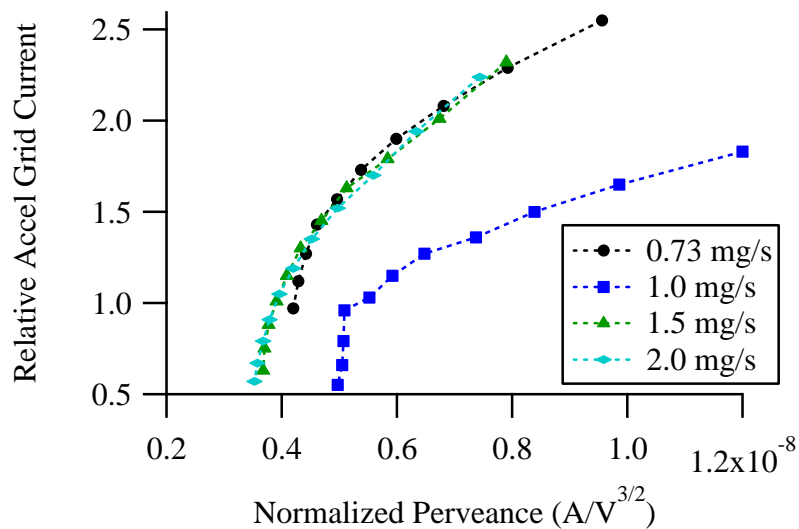
Figure 126. Relative accel grid current as a function of normalized perveance and argon flow rate. 600 W RF power, 150 G magnetic field, 35 V screen grid bias, 150 V accel grid bias, 1.4, 1.4, 1.6, and 1.7x10^{-5} Torr-Ar chamber pressure for 0.73, 1.0, 1.5, and 2.0 mg/s flow rates, respectively.

A final observation is that at all operating conditions there is a sizeable accel grid current. The minimum relative accel grid current observed is 0.23 at 600 W RF power, 50 G, 600 V discharge, and 1.5 mg/s. Figure 122 shows that for all other operating conditions the relative accel grid currents are higher. The first cause for the high relative accel grid currents for most operating conditions is the relatively low potential drop across the grids compared to the ion current from the discharge plasma. As discharge voltage increases, the total potential drop between the screen and accel grids increases, which decreases the perveance. Since the relative accel grid current decreases as perveance decreases, the thruster is clearly operating in the over-perveance condition. The expectation is as perveance is further decreased, the relative accel grid current would reach a minimum, and then increase. This minimum would mark the optimum perveance of the grids for the given discharge plasma. However, this minimum is generally not observed, which indicates that further increases in the discharge voltage are required to

reach optimum perveance. This increase in discharge voltage would reduce the relative accel grid current.

While optimal perveance is not reached in general, it is likely that optimal perveance is reached for the previously mentioned case at 600 W RF power, 50 G, 600 V discharge, and 1.5 mg/s. The last two discharge voltage points, corresponding to 550 and 600 V, have nearly equal relative accel grid currents. This suggests that optimal perveance occurs either at 600 V, or very close thereto. However, this implies that even at optimal perveance the accel grid current is 23% of the ion beam current, which is still too high for long term operation. This implies that a second cause for the high accel grid current exists, most likely the spatial variance of the discharge plasma density and temperature. The normalized perveance is an average over the entire grid assembly, which only gives the true perveance if the spatial distributions of the discharge plasma temperature and density are uniform. Since this is not the case, the normalized perveance is a spatial average of the perveance of each aperture. Thus when the relative accel grid current as a function of the normalized perveance is minimized, rather than optimizing the perveance of every aperture individually, only a majority of the perveances is optimized. The nominal optimal perveance is thus a combination of apertures at optimal perveance and others at the condition of over- and under-perveance. Therefore, uniform grids will always have a sizeable accel grid current when used with a spatially varying discharge plasma, even at the best perveance possible. The solution is to design the grids to include a spatial variance in aperture diameter to match the spatial variance in the discharge plasma temperature and density such that optimal perveance is achieved simultaneously for as many apertures as possible.

A second indication of the grids not functioning as designed can be seen in Figure 117. Despite the non-transparent portion of the screen grid only occupying 33% of the grid area, it collected 40% of the total ion flux. Ions are only extracted from the discharge through a plasma sheath from either the screen grid or the accel grid (neglecting ion losses to the discharge chamber wall). This shows that the screen grid sheath surface area accounts for 40% of the total sheath surface area, which is larger than the non-transparent grid area. This suggests that the accel grid sheath does not fully extend to the screen grid, which enables the screen grid sheath in the apertures to collect additional ions that would have passed through to the accel grid sheath. Figure 127 illustrates conceptually why severe over-perveance would cause excessive screen grid ion collection.
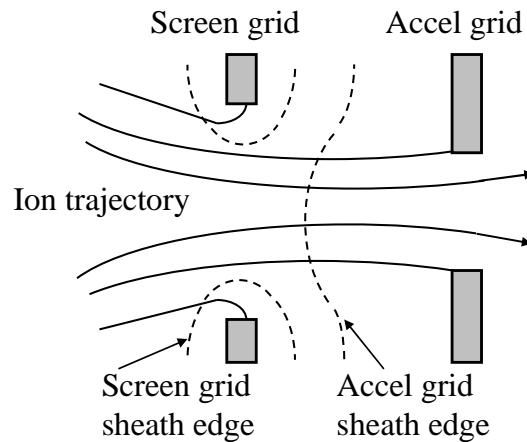
Figure 127. Conceptualization of severe over-perveance.

This problem of screen grid over-collection is a result of increased perveance. In terms of operating parameters, as the discharge density increases, the discharge voltage must be increased simply to maintain perveance. As the discharge density increases at

constant grid voltage, the accel grid sheath length decreases and the accel grid sheath withdraws from the screen grid aperture. If the discharge density is progressively increased, the surface area of the accel grid sheath continues to decrease and the ratio of the screen grid current to the anode current increases. This effect is countered by an increase in the discharge voltage, which increases the sheath potential between the accel grid and the discharge plasma, thus increasing the sheath length and extending the accel grid sheath towards the screen grid. Figure 128 shows that these parametric effects hold: as discharge voltage is increased, the screen grid to anode current ratio decreases, representing a decrease in screen grid collection and by extension, an increase in accel grid sheath surface area. Increasing the magnetic field, which has already been found to increase discharge plasma density, increases the screen grid current collection relative to the anode. Furthermore, this data shows that only the 50 G cases at higher discharge voltages came close to reaching optimal perveance, where the screen grid collected only about a third of the total ion flux. This demonstrates that future optimization of the GHIT will require higher discharge voltages at magnetic fields higher than 50 G to ensure proper accel grid sheath formation and optimal perveance.
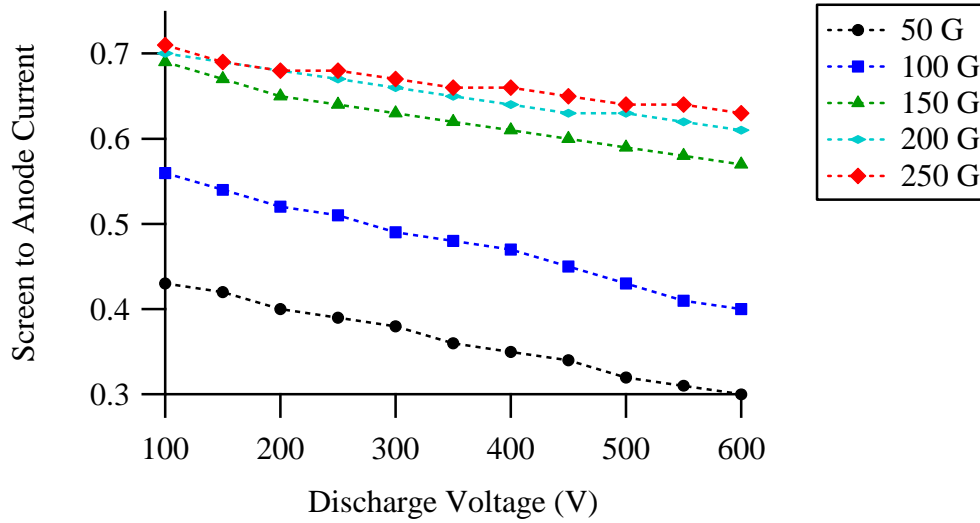
Figure 128. Screen grid to anode current ratio as a function of discharge voltage and magnetic field. 600 W RF power, 1.5 mg/s argon, 35 V screen grid bias, 150 V accel grid bias, 1.6x10^{-5} Torr-Ar chamber pressure.

8.3 Plume Divergence

Thus far two performance metrics of the thruster have been discussed: beam current and the relative accel grid current. The former is a measure of the ion production of the discharge plasma and how effectively the grid assembly extracts ions, while the latter quantifies how accurately the ion optics focuses the ions through the grids. Equation (4.10) contains another parameter that, while it is of less relative importance, must still be considered, the beam divergence factor.

There are two operational parameters that are varied to determine their effects on the beam divergence: the discharge voltage and the axial magnetic field. The discharge voltage impacts the beam divergence by setting the axial kinetic energy and by altering the value of the voltage ratio R, introduced in Section 3.2.2. As the discharge voltage increases, the total potential drop experienced by the ion increases, which increases the axial velocity component relative to the radial velocity imparted by the plume jet

213

expansion. Increasing the discharge voltage also increases R, which is the ratio of the net beam voltage to the total potential drop across the grids. Since the accel grid is biased below the cathode, as an ion exits the grids it encounters an adverse potential gradient. While the ions have sufficient energy to cross the gradient, the passage imparts a small radial velocity component. This effect is generally smaller than the impact of the axial kinetic energy, but still adds to divergence if not taken into account.

The other parameter of interest is the axial magnetic field. While the magnetic field is far too low to magnetize the ions, near the grids it is still high enough to magnetize the electrons. If electrons are confined, an ambipolar electric field arises to accelerate the electrons to the ions and slow the ions. If the electrons are bound to magnetic field lines that rapidly diverge out along the radial axis, this could lead to an electric field with a radial component, which could impart a radial velocity on the ions in the plume. Therefore a comparison of the beam divergence at differing magnetic fields is required.

Since the primary area of interest is the parametric effects of the discharge voltage and the magnetic field, current density is measured only for variations in these parameters. The current density distributions for three magnetic fields at varying discharge voltages are shown from Figure 129 to Figure 131. The first trait that all three plots share is as the discharge voltage increases, the intensity of the central peak increases. This reflects both an increase in overall beam current and a decrease in beam divergence. The increase in beam current is due to the combination of previously observed effects: increased extraction of ions into the accel grid sheath rather than the screen grid sheath, and increased ion focusing resulting in decreased ion collisions with the accel grid. As mentioned earlier, the increased ion focusing is caused by the

increased discharge voltage imparting greater axial kinetic energy into the ions and decreasing the radial velocity component relative to the total velocity. This results in a reduction of ions on the wings and an increase of ions in the center. This is more clearly illustrated in a semi-log plot of the data from Figure 130, shown in Figure 132.
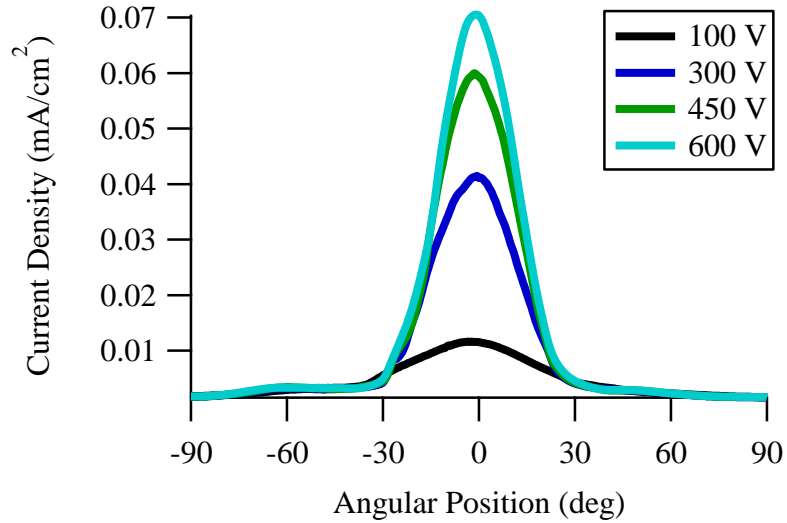
Figure 129. Plume current density as a function of discharge voltage 50 cm from the grids. 429 W RF power, 50 G magnetic field, 1.5 mg/s argon, 35 V screen grid bias, 150 V accel grid bias, 1.6x10^{-5} Torr-Ar chamber pressure.
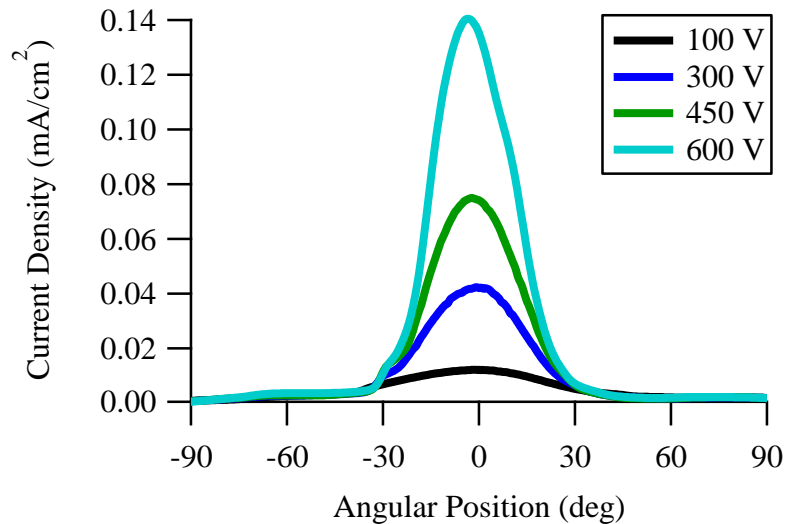
Figure 130. Plume current density as a function of discharge voltage 50 cm from the grids. 429 W RF power, 150 G magnetic field, 1.5 mg/s argon, 35 V screen grid bias, 150 V accel grid bias, 1.6x10^{-5} Torr-Ar chamber pressure.
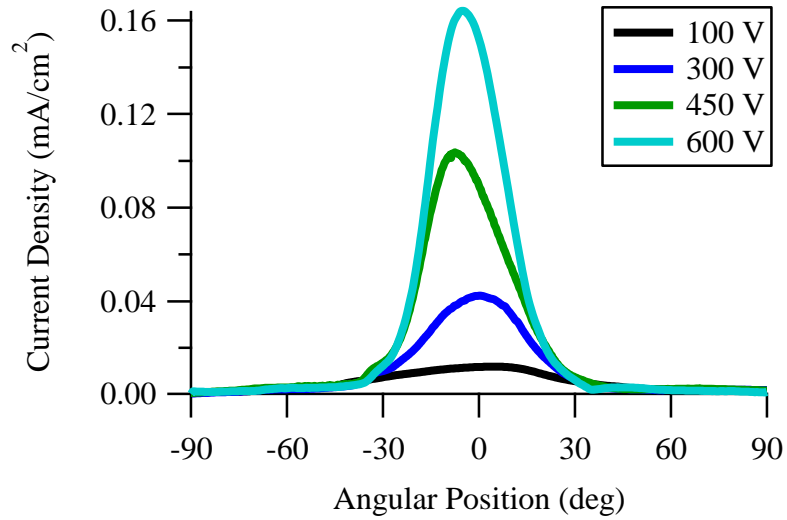
Figure 131. Plume current density as a function of discharge voltage 50 cm from the grids. 429 W RF power, 200 G magnetic field, 1.5 mg/s argon, 35 V screen grid bias, 150 V accel grid bias, 1.6x10^{-5} Torr-Ar chamber pressure.
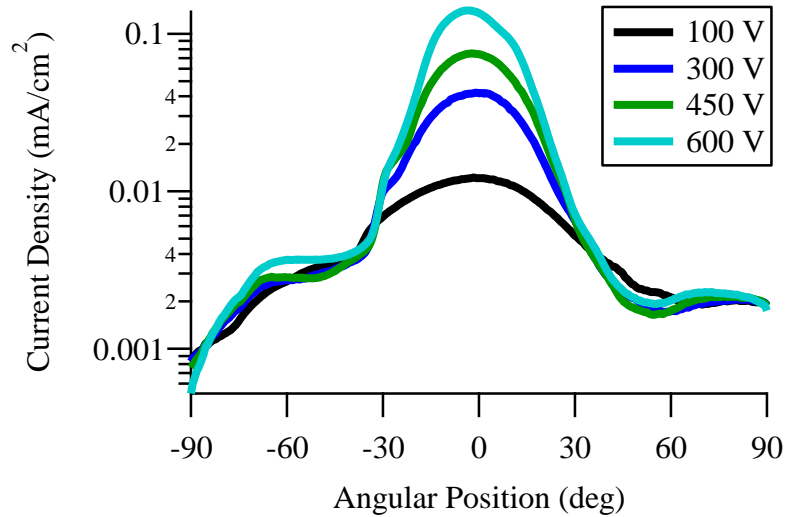
Figure 132. Plume current density as a function of discharge voltage 50 cm from the grids. 429 W RF power, 150 G magnetic field, 1.5 mg/s argon, 35 V screen grid bias, 150 V accel grid bias, 1.6x10^{-5} Torr-Ar chamber pressure.

The overall effect on the beam divergence is best quantified by calculating the beam half angle, defined in Equation (5.5) and plotted in Figure 133. Increasing the discharge voltage decreases the beam half angle as expected, but increasing the magnetic field also

decreases the beam half angle. This suggests that the proposed mechanism of ambipolar electric fields creating a radial velocity component on the ion is either nonexistent, or the effect is negligible compared to another effect caused by increasing the magnetic field. One of the effects of increasing the magnetic field is increasing the discharge plasma density. As has been discussed in the previous section, this increases the perveance for an ion optics system that is already in over-perveance. Increasing the perveance further would increase beam divergence, not reduce it.[1] As a result, whatever mechanism is reducing the beam divergence does so in spite of competing phenomena.
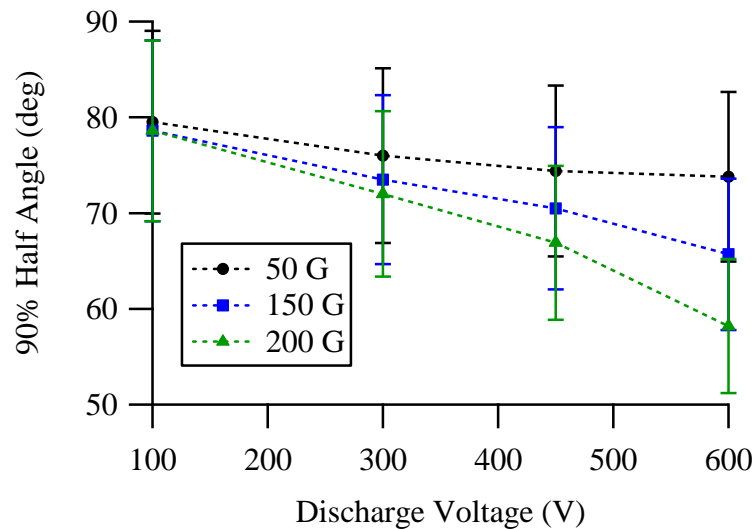
Figure 133. Beam divergence half angle as a function of discharge voltage and magnetic field 50 cm from the grids. 429 W RF power, 1.5 mg/s argon, 35 V screen grid bias, 150 V accel grid bias, 1.6x10^{-5} Torr-Ar chamber pressure.

Another observation from Figure 133 is that the impact of changing the magnetic field varies with the discharge voltage. Figure 134 through Figure 137 shows a progression of the current density profiles for each magnetic field as the discharge voltage is increased from 100 V in Figure 134 to 600 V in Figure 137. At 100 and 300 V,

the profiles at the three magnetic fields are largely identical. The current density at the wings is still reduced at higher magnetic fields, with only a broadening of the center peak. The maximum current density at each peak is still approximately the same value. At 450 and 600 V the profiles are much more differentiated, with a noticeable increase in the center peak to complement the decrease in the wings as the magnetic field strength is increased.
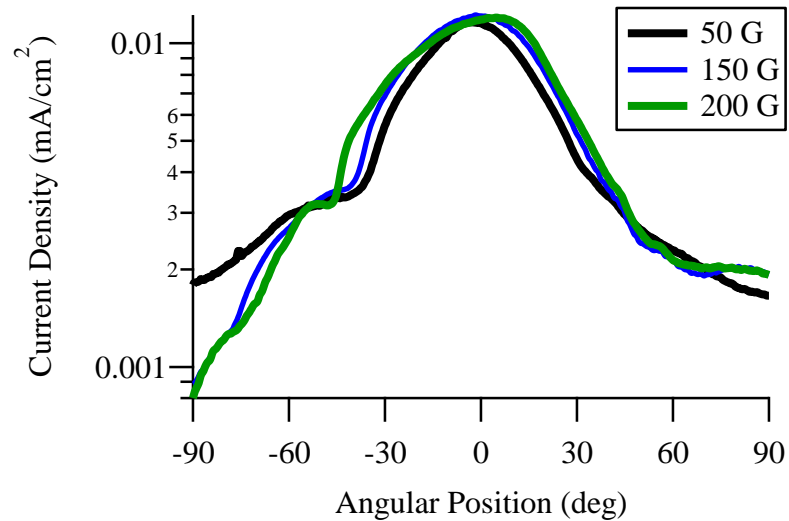
Figure 134. Plume current density as a function of magnetic field 50 cm from the grids. 429 W RF power, 100 V discharge, 1.5 mg/s argon, 35 V screen grid bias, 150 V accel grid bias, 1.6x10^{-5} Torr-Ar chamber pressure.
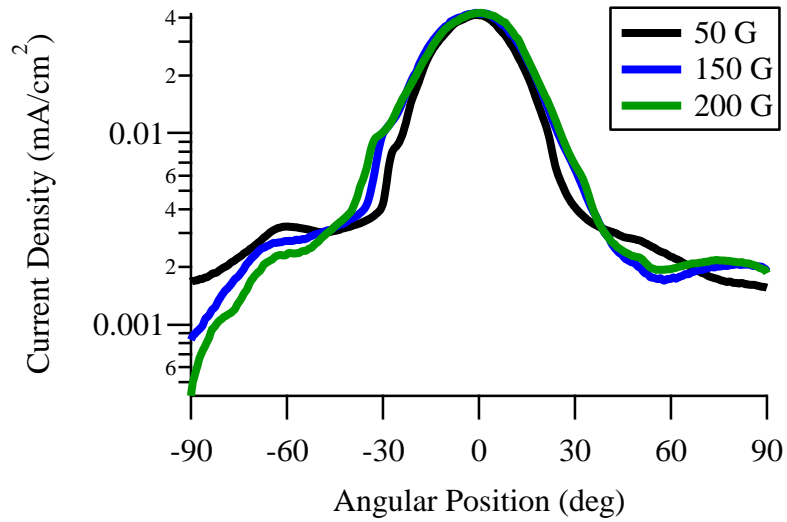
Figure 135. Plume current density as a function of magnetic field 50 cm from the grids. 429 W RF power, 300 V discharge, 1.5 mg/s argon, 35 V screen grid bias, 150 V accel grid bias, 1.6x10^{-5} Torr-Ar chamber pressure.
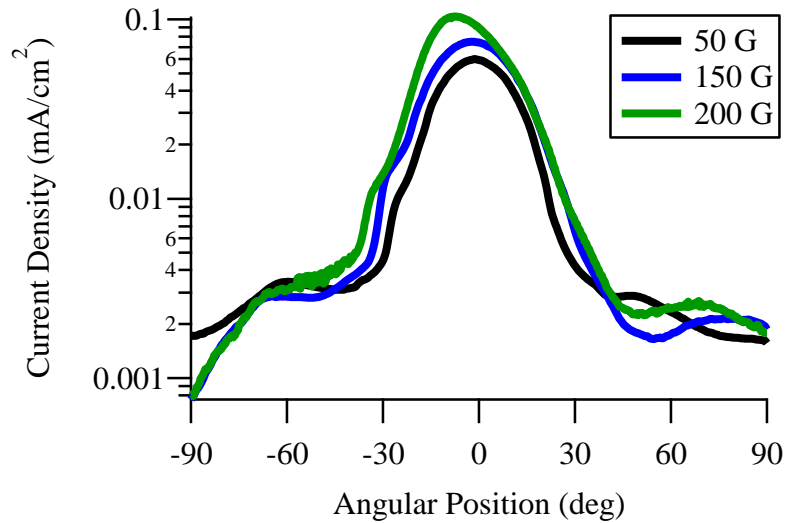
Figure 136. Plume current density as a function of magnetic field 50 cm from the grids. 429 W RF power, 450 V discharge, 1.5 mg/s argon, 35 V screen grid bias, 150 V accel grid bias, 1.6x10^{-5} Torr-Ar chamber pressure.
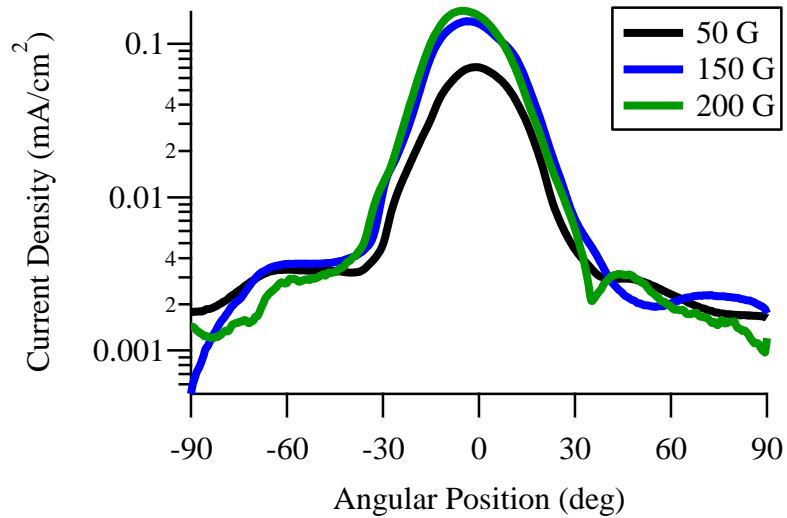
Figure 137. Plume current density as a function of magnetic field 50 cm from the grids. 429 W RF power, 600 V discharge, 1.5 mg/s argon, 35 V screen grid bias, 150 V accel grid bias, 1.6x10^{-5} Torr-Ar chamber pressure.

The reason for this dependency on the discharge voltage is that at low discharge voltages and higher plasma densities, the grids become space-charge limited. As the magnetic field increases from 50 G to 200 G, the discharge density increases, which increases the Bohm current density into the grid sheath, up to 28.6 A/m^2 at 200 G. However, with a 100 V discharge and grid voltages used, the GHIT performance model outlined in Section 4.2.5 predicts a maximum allowable current density of 9.32 A/m^2. Therefore despite the increased discharge plasma density at 150 and 200 G, the grids limit the size of the ion beam. As the discharge voltage is increased to 300 V the maximum current density allowable reaches 24.6 A/m^2, which allows for some variation between the lower magnetic fields, but still limits the 200 G case. Once the discharge voltage reaches 450 V the maximum allowable current density increases beyond 28.6 A/m^2 and the maximum possible ion beam from the 200 G case can be achieved. With the space charge limitation removed, the 200 and 150 G cases are more distinguishable

from the 50 G case, which is now limited by the ion flux into the grid sheath from the discharge plasma.

8.4 Thrust Measurement

The remaining unknown term from Equation (4.10) is the beam voltage. This term is the change in potential from the discharge plasma to the plume, and can be related to the discharge voltage by

$$V_b = V_D - V_{space} \tag{8.9}$$

where V_{space} is the space potential, which is the plasma potential far downstream of the thruster. While the space potential is not measured directly, a reasonable estimate is 20 V based on the space potential for a Hall effect thruster.[64] Estimates of the thrust using Equation (4.10) and the data already presented are shown in Figure 138. Since each parameter of Equation (4.10) is sensitive to the discharge voltage and magnetic field, it is expected that the thrust should be likewise. All three terms, beam current, beam divergence factor, and beam voltage, are strongly dependent on the discharge voltage; as a result, the thrust is most affected by the discharge voltage.
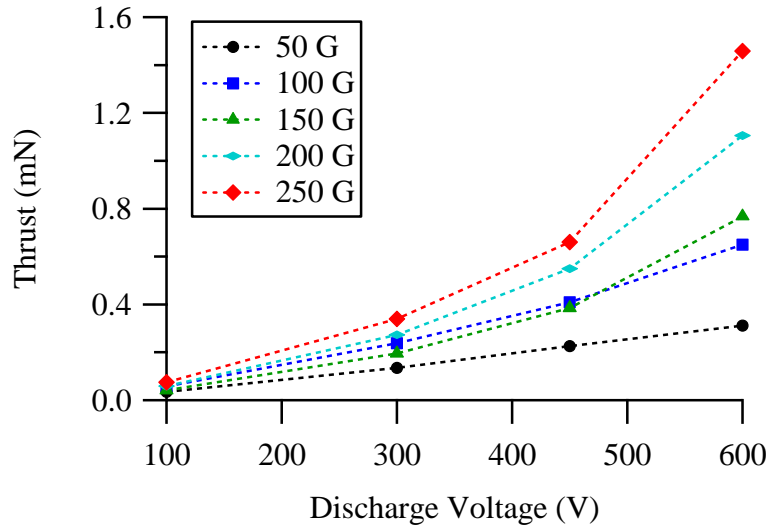
Figure 138. Estimated thrust as a function of discharge voltage and magnetic field. 429 W RF power, 1.5 mg/s argon, 35 V screen grid bias, 150 V accel grid bias, 1.6x10^{-5} Torr-Ar chamber pressure.

Since the estimated thrust is low compared to the thrust stand noise seen in Chapter VI, a full set of thrust measurements would not be worthwhile. Instead, a sampling of various operating conditions is sufficient to validate the estimation in Figure 138. The measured thrust sample is shown in Table 6 at the given operating conditions; parameters not listed in the table are constant between all tests: 600 V discharge, 35 V screen grid, and 150 V accel grid voltages. The measured thrust is slightly higher than the estimated thrust, as estimated thrust only considered thrust contributions from accelerated ions and does not include thrust from neutral gas expansion. Assuming a discharge pressure of 2 mTorr, thrust due to pressure is approximately 1.4 mN, which is approximately equal to the thrust discrepancy between the predicted and measured thrust.

Table 6. Measured GHIT thrust.

P_{RF} (W)	B (G)	$\dot{m}_p$ (mg/s)	T (mN)	Uncertainty (mN)
429	50	1.5	-0.13	±5.01
600	150	1.5	2.75	±2.00
429	200	1.5	2.77	±3.61
429	150	1.0	1.47	±2.19
429	150	2.0	2.28	±2.60
429	150	3.0	1.51	±2.35

Ultimately the low thrust can be increased by increasing the beam current and the discharge voltage. Since thrust increases linearly with beam current and only with the square root of the discharge voltage (assuming that the grids are not space-charge limited), it is more effective to increase beam current. Therefore, while the GHIT in the current form is a less-than-ideal thruster, there is an identifiable path for improvement by identifying all ion losses from the discharge and determining the most effective means to reduce these losses.

8.5 Conclusions

There are two primary conclusions that can be drawn from the measured data. Firstly, there are two causes for lower than expected beam current: over-perveance of the grids, and spatial variance in the discharge plasma density at the grids. These limit performance, as they cause the grids to under-focus the ions, which leads to ion impingement on the grids and beam divergence. The over-perveance is primarily a result of low grid voltages relative to the ion number density, which reduces the accel grid sheath length and retracts the accel grid sheath behind the screen grid. The spatial variation of the ion number density is another factor, as it creates a spatial dependency of

the perveance. As a result, optimal perveance cannot be achieved over the entirety of the grids unless there is a similar variation of the grid aperture diameters.

The second conclusion drawn is that the GHIT displays a high degree of control over the three ion acceleration performance metrics. Despite the aforementioned issues with over-perveance, the grid voltages demonstrated a significant effect on the ion optics and the ion impingement on the grids. Rather than indicating that the grid assembly is ineffective, the observed performance indicates only that the GHIT operating conditions are not optimized. Additionally, the expanded number of operating parameters allows for individual manipulation of each ion acceleration performance metric without adversely impacting another. As a specific example, an increase in the ion beam current can be achieved by increasing the discharge ion density. This would in turn cause the perveance to increase, which would increase beam divergence, but this can be offset by increasing the grid voltages. Thus one metric can be increased without affecting the other.

Due to the observed degree of control, the evaluation of the GHIT would benefit from an examination of potential modifications that would improve performance. Such an exercise would allow for a more accurate measure of the ion acceleration capability of the GHIT and of two-stage ion acceleration. Another goal is to utilize the combination of the data presented in this chapter with the helicon plasma structure measured in Chapter VI to determine the ion production cost of the helicon plasma source. These two tasks are accomplished in the next chapter.

CHAPTER IX

GHIT DESIGN OPTIMIZATION

In the previous chapter, the GHIT is found to have ineffective ion optics that result in a lower beam current and a higher beam divergence angle than expected for the given operating conditions. However, the GHIT displays a high degree of control over the performance metrics through the device operational parameters. Thus, it is clear that a higher ion beam current and a lower plume divergence angle are possible with further device optimization. There are two categories of modifications that are possible: alterations to the device hardware and changes to the device operating conditions. While the former can offer clear benefits it is difficult to accurately model the affects using the existing data. Therefore, while there are several suggestions for modifying the GHIT architecture, the primary approach in this chapter is modeling the ion acceleration and resultant GHIT performance using through parametric optimization of the operating conditions. This is conducted using extrapolation of the measurements in Chapter VIII.

The second goal of this chapter is to determine the ion production cost of the helicon plasma source. The ion currents through the grids and anode are known and allows for a more accurate determination of the ion production rate of the helicon plasma source. A combination of this and the helicon plasma structure measured in Chapter VI is used in the discharge efficiency model in Chapter III to calculate the ion production cost of the helicon plasma source. The model also enables identification of the primary power

expenditures and parametric analysis of the ion production cost to assist in determining optimal operating conditions.

Ion production cost is found to be in the range of 132-212 eV/ion. The primary losses in the discharge chamber are due to ion loss to the discharge chamber wall and high sheath potentials at the plasma boundaries. The proposed solution to increase discharge efficiency is to increase the magnetic field strength to decrease ion diffusion to the walls and decrease the electron temperature of the discharge plasma by manipulating the electron energy distribution using the helicon plasma source. The final source of inefficiency is approximately only 15% of the transmitted RF power couples to the plasma. The remaining power is likely coupled to the solenoid mounts to create eddy currents, capacitively coupled to the thrust stand and grounded, or is coupled to the plasma through RF excitation of photon emission that is not included in the discharge model. Reduction of this RF power loss would increase the device efficiency and potentially increase the ionization fraction of the discharge plasma.

9.1 Component Optimization

The primary cause for the low thrust observed in Chapter VIII is the low beam current extracted from the discharge. The beam current is the numbers of ions extracted from the discharge and accelerated per unit time. Therefore if the beam current is low, the amount of propellant accelerated is low, resulting in low thrust. Increasing the beam voltage is an alternative method to increasing thrust, but there are two disadvantages to substatially increasing beam voltage. The first is seen in Equation (4.10), where thrust is only proportional to the square root of the beam voltage, compared to the linear

proportionality to beam current. Hence, it would take a much larger increase in beam voltage than beam current to generate the same increase in thrust. The second disadvantage to the beam voltage approach is that the beam power required is linear with the beam voltage, but as already mentioned thrust increases with the square root. The thrust-to-power ratio would then decrease with the square root of the beam voltage. Therefore it is more advantageous to focus on increasing the beam current.

There are two areas of the GHIT that can be improved to increase beam current: the discharge plasma source and the grid assembly. Improvements to the helicon discharge focus on increasing ion density and mass utilization while decreasing ion losses. For the grid assembly, suggested modifications are meant to decrease ion beam impingement on the accel grid and to match the aperture geometry to the spatial variations of the discharge plasma density and temperature.

9.1.1 Grid Assembly

Based on the results of the relative accel grid current as a function of normalized perveance, it is clear that discharge plasma characteristics are not uniform across the exit plane of the discharge. The first modification to the grid assembly would be to spatially match the aperture geometry to the discharge plasma characteristics. Assuming the grids enforce a radial symmetry to the discharge plasma, the screen and accel grid aperture diameters would be a function of radial position.

The second modification to the ion optics is to increase the electric field between the grids. The previous chapter demonstrates testing of the GHIT almost completely occurs in the over-perveance condition. Over-perveance leads to excessive ion collection by the screen and accel grids and degrades both thruster lifetime and performance. The two

options to decrease the perveance are to either decrease the ion flux through the grids or increase the potential drop across the grids. Since the stated goal is to increase the beam current, the first option is not feasible. Furthermore, the sought increase in beam current will require even higher grid voltages in order to attain optimum perveance. An alternative to increasing the potential drop across the grids is to decrease the grid spacing, as this will increase the electric field for a constant grid gap. The primary drawback to decreasing the grid spacing is it increases the likelihood of the grids shorting.

Now that the second modification has been specified as an increase in the potential drop across the grids, there are two potentials that can be varied. The screen grid potential is determined by what is sufficient to ensure ion saturation of the grids, and is therefore not available for modification. The first option is the accel grid, as biasing it below cathode will increase the potential drop across the grids without an increase in specific impulse and decrease in the thrust-to-power ratio. However, the accel grid cannot have a large portion of the total voltage drop, as this would drop the voltage ratio R below the design goal of 0.8. This requires the discharge voltage to be increased. While this does decrease the thrust-to-power ratio, it can be offset slightly by also increasing the accel grid voltage to maintain R.

9.1.2 Helicon Discharge

There are two ways to increase the beam current: increase the ion flux to the grid sheath and increase total grid area. The most direct method to increase the grid area is to increase the diameter of the discharge chamber. This approach has multiple effects, as the discharge chamber geometry impacts several parameters. The intended effect is to increase the grid area by which to extract ions. However, this also increases the volume

of the discharge chamber, which would decrease the power density of the discharge, neglecting all other effects. The power density could be increased by decreasing the length of the discharge chamber. One potential concern is if there is a minimum length required for adequate ionization, as the discharge plasma data in Chapter VI did demonstrate an axial dependency. Another advantage would be a decrease in the discharge surface-area-to-volume ratio and the resulting decrease ion loss to the walls.

The other method to increase beam current is to increase the ion flux to the grid sheath. In essence, this requires increasing the discharge plasma density and temperature, as increasing either characteristic increases the Bohm current. The results of the discharge analysis show that increasing the magnetic field beyond 250 G offers the most effective means to increase the density. Likewise, data shows that decreasing the neutral propellant flow rate to 1.0 mg/s would increase the number density. Before a set of new design operating conditions can be defined, an analysis of the GHIT discharge in conjunction with the helicon plasma measurements is needed to identify any other sources of potential losses.

9.2 GHIT Discharge Efficiency

There are three functions that the GHIT performs that can be optimized: ion production in the discharge chamber, extraction of ions from the discharge chamber into the grids, and collimation of the ions into a coherent beam. In Chapter VIII both beam collimation and ion extraction are discussed. Beam collimation is found to be as designed, while ion extraction suffers from severe over-perveance caused by low grid voltages. What remains is an analysis of the efficiency of the helicon plasma source as

an ion source. This can be determined by calculating the discharge efficiency using the average ion number density and electron temperature, along with the thruster currents during operation.

9.2.1 Discharge Model

The discharge model used is outlined in Section 3.3.3. The helicon and GHIT operating conditions overlap at 150 G, thus the model is calculated using data from both thrusters at 343 W and 600 W at 150 G and a discharge voltage of 600 V. Ambipolar diffusion into the walls is assumed; ions diffuse radially into the discharge chamber wall at the same rate as electrons. For simplicity of calculations, the plasma is assumed to have averaged characteristics represented by a single value each for density, temperature, etc. The ion number density and electron temperature are taken from the discharge analysis performed in Chapter VIII, and likewise thruster currents use the measured values presented earlier. Gradients of the discharge plasma characteristics are calculated from the measurements of the helicon discharge plasma without grids taken in Chapter VI. While there is a difference in the plasma characteristics between the helicon with and without the grids, it is assumed that the shape of the plasma contour for each characteristic is constant. This assumption, while not ideal, is sufficient for a first order approximation of the power expended in the discharge and for the estimation of wall losses. Additionally, an ion temperature of 0.2 eV is assumed.

Since the model uses measurements of both the EHT and the GHIT, there are only two cases where the operating conditions overlap. The results of the model for these two cases are shown in Table 7. The discharge efficiency is modified to use the total ion flux

to the grids as the beam current in Equation (3.17), as otherwise the inefficiency of the ion optics in over-perveance would be included in the discharge efficiency calculation.

$$\eta_d = \frac{P_{abs}}{I_b + I_s + I_A}$$

(9.1)

Therefore, the discharge efficiency represents the energy cost to create and transport an ion to the grid sheath. The discharge efficiency is higher than what is common, as a standard DC discharge chamber using argon has a discharge efficiency of approximately 150 eV. The reader should recall that discharge efficiency can be considered as an ion production cost, thus a high discharge efficiency is not desirable. For the sake of clarity, all further comparative discussion on the discharge efficiency will use the alternate nomenclature of ion production cost.

Table 7. Estimated discharge performance parameters at 150 G, 600 V discharge, 1.5 mg/s Ar.

P_{RF} (W)	I_b (mA)	I_w (mA)	P_{abs} (W)	η_d (eV)
343	80.8	201	46.3	185
600	88.8	225	67.3	201

One consideration is there is no magnetic shielding of the anode from ions for most of the data collected. Standard ion engine discharges provide a magnetic shield of the anode to reduce ion collection and reduce power losses. A design concern for future work would be to incorporate an improved magnetic shield at the anode, either through improving the current magnetic mirror concept or utilizing an alternate design that creates radial magnetic field lines near the anode.

The ion loss rate to the walls is found to be considerably larger than the beam current, which demonstrates that wall losses are a significant fraction of the ions created, approximately 27%. This is a consequence of the discharge chamber geometry that had a large surface-area-to-volume ratio. Ion losses can be reduced by increasing the discharge chamber diameter and decreasing the length, as this decreases the area the plasma can contact. However, further analysis will assume constant discharge chamber geometry of allow use of the previously measured plasma characteristics in subsequent analysis. Discussion of the effects of varying discharge chamber geometry is presented in Section 9.1. Instead, discussion will proceed to two parameters of the discharge plasma that have a strong impact on the ion production cost: the magnetic field strength and the electron temperature.

9.2.2 Magnetic Field Effects

The first effect of the magnetic field is to increase the ion number density of the discharge plasma, as has been observed previously. This leads to increased ion extraction and the resulting thruster currents, as well as increased power absorption by the discharge plasma. While this has some impact on the ion production cost, ignoring any changes to the spatial distribution of the density and resulting changes to the perveance and ion optics, the magnetic field has a greater effect on ion loss to the walls. The radial ion velocity can be reduced by increasing the magnetic field, which reduces radial ion mobility to the wall by Equation (3.27). A reduction of the radial ion velocity leads to decreased ion losses to the walls, which decreases the ion production cost. Figure 139 shows that increasing the magnetic field from 150 G to 250 G greatly decreases the radial ion velocity and the ion wall current. These calculations involve interpolating some of

the data from the EHT measurements, as such data at 250 G or at RF power other than

343 or 600 W is not available.
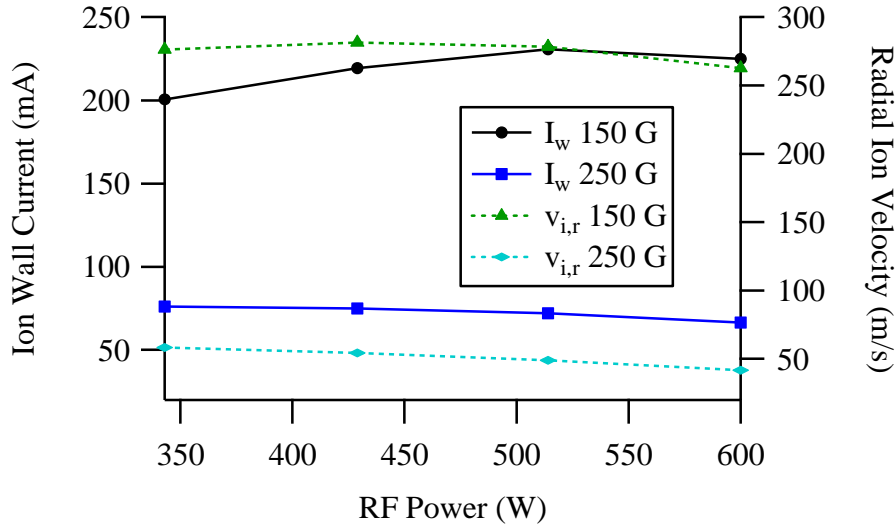
Figure 139. Ion current and radial ion velocity as a function of RF power and magnetic field.

Since each ion lost to the wall is an expenditure of energy that does not produce an

ion for extraction and acceleration, decreasing the ion-wall loss also decreases the ion

production cost. At 200 and 250 G the ion production cost is much closer to what is

generally seen in DC discharges, as seen in Figure 140. Further increases of the magnetic

field would decrease the discharge efficiency below 150 eV, but the ion loss rate to the

walls becomes too small to have a discernible effect. That is not to say this is a clear case

of diminishing returns, as thus far increasing the magnetic field demonstrates only

positive enhancements to performance: increased ion density, decreased beam

divergence, and decreased ion production cost. However, if further decreases in ion

production cost are desired, there is another source of energy loss that must be examined,

one which also explains why the 200 G cases have a lower ion production cost than the 250 G cases – the discharge chamber sheaths.
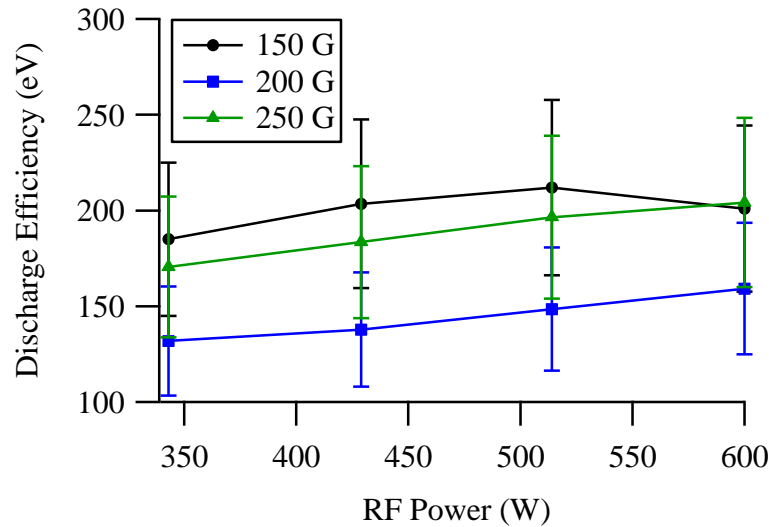
Figure 140. Discharge efficiency (ion cost) as a function of RF power and magnetic field for 1.5 mg/s argon.

9.2.3 Electron Temperature Effects

The two largest expenditures of power in the discharge are ionization of neutrals, and acceleration of ions and electrons through the boundary plasma sheaths. The first consists of the cost to create the ions that are extracted by the grids, plus an additional amount of power spent creating ions that are lost to wall neutralizations. The previous section has demonstrated that while considerable decreases in the ion production cost can be attained by decreasing wall losses, it is insufficient to decrease the ion production cost below that of standard DC discharges. The second major power expenditure occurs when ions and electrons pass through the sheaths at the boundaries of the discharge chamber. Across each sheath exists a potential drop that repels a sufficient number of electrons to balance the ion flux incident on the sheath. Each ion or electron that passes through the

sheath has electric work done on it, which expends energy from the discharge plasma. Therefore, decreasing the sheath potentials will yield a further decrease in the ion production cost.

Equation (3.39) shows that the sheath potential has a linear dependency on the electron temperature. This arises from the fact that the sheath potential must repel a certain amount of electrons, and the repulsion force opposes the thermal kinetic energy of the electron. Higher temperature electrons have a higher kinetic energy than lower temperature electrons, and thus require a larger sheath potential. Therefore, decreasing the electron temperature of the discharge plasma decreases the anode sheath potential as well as the ion production cost. This is the cause for the 200 G cases having a lower ion production cost than the 250 G cases, as the 200 G cases have lower electron temperatures (5-7 eV compared to 7-9 eV) despite having a higher ion loss rate to the walls. Figure 141 shows an example of this effect where the 600 W condition at 150 is modeled assuming arbitrary electron temperatures. While the electron temperature is not a free variable that can be altered without other effects, it demonstrates the impact of the electron temperature of the discharge efficiency.
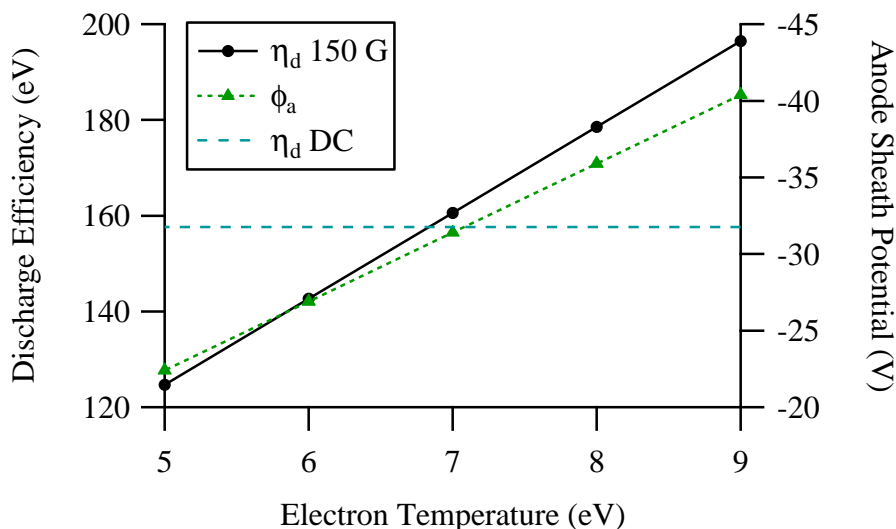
Figure 141. Discharge efficiency (ion cost) and anode sheath potential as a function of electron temperature. The average discharge efficiency of a DC discharge chamber is shown for comparison.

The results of the discharge model show that while most of these initial experiments show a higher ion production cost compared to DC discharges, a lower ion production cost is possible at certain operating conditions. The 200 G demonstrate a discharge efficiency of 132-159 eV, which shows that such operating conditions are possible. These values are still higher than observed with other work using helicon plasma sources,[30,31] but such experiments were performed at a higher magnetic field strength. The primary impact of such operating conditions is the increased confinement of the ions, which would not only reduce wall losses, but also restrict radial and azimuthal velocity and reduce ion collisions and the associated losses. Additionally, the total beam current in the other work was determined using planar Langmuir probes, which can overestimate the ion current in the same manner of Faraday probes. The results of this study demonstrate that even without magnetization of the ions, the helicon plasma source is capable of a superior discharge efficiency compared with DC discharges. Further improvements to the discharge efficiency should involve examining how to use the

helicon plasma source to tailor the electron energy distribution function to favor lower energy electrons that are still sufficient to ionize the propellant.

9.2.4 RF Power Losses

A greater concern with the results of the discharge model is that the predicted power absorbed by the plasma is only approximately 15% of the RF power transmitted to the antenna. While this model is only a first order approximation, it demonstrates that a significant amount of power does not couple to the plasma. Another way to quantify the problem is comparing total ion current to the propellant mass flow rate. For the 600 W case, total ion production is estimated to be 440 mA, which is equal to 2.8×10^{18} ions per second. The mass flow rate of 1.5 mg/s yields a neutral rate of 2.3×10^{19}, which yields an ionization rate of about 12%. The amount of power needed to ionize all the propellant at the same discharge efficiency is approximately 490 W, which again demonstrates that sufficient power is available yet is not absorbed by the plasma.

If only a fraction of the RF power is absorbed by the plasma, it is likely that the RF power is coupling to something else in addition to the plasma. Several possibilities include capacitive coupling with the thrust stand through the solenoids mounts, inductively creating eddy currents within the solenoid mounts, or coupling to the chamber at the feedthrough. In the 600 W, 150 G case, the skin depth according to Equation (2.14) is approximately 5 cm, so it is not the case that the plasma is insufficiently opaque to the RF wave. One method to investigate this further is to attempt to measure the directionality of the double saddle antenna. The solenoid mounts are a likely object for the antenna to couple to, as they are very close to the antenna and the aluminum cylinder that the wire is wrapped around provides a continuous loop radially

around the antenna. This loop provides a pathway for the antenna to induce a circular eddy current that can resistively dissipate the RF energy. The solenoid mount also is only separated from the thrust stand mount by four 0.6 cm thick PEEK spacers. This gap creates a small capacitance, which allows the RF in the solenoid mount to capacitively couple to the thrust stand mount, and from there to ground.

One method to test this is to replace the solenoid mounts with ones fabricated from insulating materials. This should both eliminate the circular path with which to induce an eddy current, and remove the capacitive path to ground. Another method to reduce RF losses is to use the in-vacuum matching network RF system configuration from Appendix D. This would reduce any potential coupling between the RF system and the feedthrough that might arise due to the feedthrough being a part of the matching circuit. If the matching network is relocated inside of the vacuum chamber, this is less likely to occur. This would also reduce the length of transmission line that is a component of the matching circuit, which might eliminate RF coupling between the transmission line and vacuum chamber surfaces.

Another consideration is that it is unknown how much power is spent in RF excitation of neutrals and ions. The discharge efficiency model includes a term for collisional excitation, but this term is too small (on average 72 mW) to justify the visual intensity of the light emitted by the plasma. Therefore it is highly likely that additional power is expended in RF excitation of photon emission from the argon species in the discharge chamber.

9.3 Proposed GHIT Operation

With the primary causes for the observed GHIT performance identified, a proposed set of operating conditions can be determined from extrapolation of the measured data. While increasing the discharge chamber diameter would have several benefits that have already been outlined, such changes will be neglected in order to maintain use of the measured data. For the same reason, the effects of different propellants will not be considered. The following modifications to GHIT operation are proposed and the resulting performance is modeled using the ion engine and discharge efficiency models outlined in Chapter III.

The first modification is to correct the grid aperture diameters to match the spatial variation of the plasma density. The aperture diameters were designed with a plasma density of 2×10^{16} m^{-3}, which is accurate only for the 50 G cases. Since higher magnetic field operation is desired, the aperture diameters should be decreased for regions of higher ion density. The spatially varying grid apertures should reduce the relative accel grid current to a goal of 0.05.

The second modification is to the discharge plasma: an increase in the magnetic field to 350 G and decrease electron temperature to 6 eV, as this increases ion density and decreases ion production cost. This assumes that the helicon plasma source operating conditions are altered in such a way to enable this decrease in temperature, which still must be explored. The data for the 600 W, 350 G helicon plasma is used to determine the gradients, and extrapolation the GHIT discharge analysis yields the average ion number density.

The third modification is to increase the grid voltages in order to decrease the perveance. There are two reasons: first, increasing the potential drop between the grids is required to maintain perveance as the density increases, along with increasing perveance to reach the optimum condition at all. The second reason for increasing the grid voltages is to extend the accel grid sheath fully into the screen grid aperture and reduce the screen-to-anode current ratio and ensure that the ion transparency of the screen is not less than the physical transparency. To that end, the discharge voltage is increased to 1500 V, and the accel grid potential to -300 V relative to common. This value is extrapolated from the screen-to-anode current ratios measured in Chapter VIII to ensure a ratio of 0.33. Likewise, the beam divergence half-angle is extrapolated from the data as a function of discharge voltage. A summary of the proposed GHIT operating conditions and estimated performance parameters is shown in Table 8. The efficiency calculation still assumes a total RF power of 600 W, which can probably be decreased by eliminating sources of extraneous RF coupling.

Table 8. Proposed GHIT operating conditions and predicted performance.

$P_{nominal}$	1160 W
P_{RF}	600 W
B	350 G
V_D	1500 V
V_s	35 V
V_A	-300 V
T	12.3 mN
I_{sp}	8670 s
η	48.6%
α	23.5°
I_a	599 mA
I_s	203 mA
I_A	18.8 mA
I_b	376 mA
I_w	35.8 mA
η_d	159 eV

The performance listed above is much more in line with commercially available EP thrusters. Even further performance improvements can be made using the two modifications not modeled: discharge chamber geometry and a change of propellant. A larger discharge chamber diameter and a shorter length would decrease ion-wall losses, as well as allow for larger grid areas and higher thrust. Using a higher-mass noble gas as a propellant would also increase the thrust-to-power ratio as well as decrease the ion production cost due to the reduced ionization energy. This confirms the GHIT is still a valid concept as a propulsive unit, despite initial thrust and efficiency that are lower than contemporary thrusters.

9.4 Conclusions

In the preceding chapter, the GHIT demonstrated lower than expected beam current and higher than expected beam divergence. However, unlike the EHT, the performance of the GHIT can be clearly modified through operating parameter manipulation. Using the performance models developed in Chapters III and IV and extrapolating the data from Chapter VIII, the above modifications to the operating conditions and grid assembly are estimated to improve the performance of the GHIT to similar levels of commercially available ion engines. Further improvements can be made by changing the propellant to xenon for decreased ionization cost and a higher thrust-to-power ratio. Likewise, the thrust of the device can be further increased by scaling up the diameter of the discharge chamber to increase grid area and ion extraction, though this would require an increase in power to accommodate the larger discharge plasma. Therefore, while initial performance of the GHIT is less than optimal, there is a clearly identified path to improvement.

241

Additionally, analysis of the helicon discharge plasma reveals that the helicon plasma source is capable of exceeding DC discharges in terms of reducing the ion production cost. The two key operating parameters in this optimization are the magnetic field, which controls ion loss to the walls, and the electron temperature, which sets the sheath potentials at the discharge chamber boundaries. Another concern is that only 15% of RF power that is transmitted to the antenna is accounted for in the discharge model. While some of the power must be spent in RF excitation of neutrals and ions, as collisional excitation is insufficient for the given luminosity, there is still a large amount that remains unaccounted for. It is likely that this energy is coupling to other conductive surfaces near the thruster and transmitted to ground. Thus two key areas for future work are determining how to set the electron temperature of the discharge chamber plasma through manipulation of the electron energy distribution produced by the helicon plasma source, and elimination of external RF coupling. This will further increase the discharge efficiency of the helicon plasma source and decrease the ion production cost.

CHAPTER X

CONCLUSIONS

The goal of this dissertation is to comparatively evaluate the ion acceleration capability of a single-stage and a two-stage helicon thruster. The two-stage device also serves to separate the ionization and acceleration stages and permit individual evaluation of each process. Chapters VI and VII presented the ion acceleration performance of the single-stage EHT, which is characterized by low ion energy, low ion beam current, and high beam divergence. Chapters VIII and IX covered the performance of the two-stage GHIT, which demonstrated higher ion energy, higher beam current, and a more collimated beam despite suboptimal operating conditions. The ion production cost was also determined using a discharge efficiency model and a combination of measurements of the EHT and the GHIT.

There are two primary conclusions that can be drawn from this work. The first is that a helicon plasma source functions as an ion source, not an ion accelerator. The second conclusion is that the ion production cost of a helicon plasma source integrated into a thruster can match that of DC discharges, and even be reduced further. From these two conclusions it is seen that a helicon plasma source has great potential in electric propulsion devices, but as an ion source integrated into a larger device and not as a single-stage ion accelerator. Future work is also suggested that can further improve the use of a helicon plasma source in an integrated component in a propulsion system.

10.1 Comparison of Ion Acceleration

A helicon plasma source functions essentially as an ion source and not an ion accelerator, for the purposes of propulsion application. There are three performance metrics used to evaluate ion acceleration: ion energy, beam current, and the beam divergence half-angle. The EHT demonstrated sub-standard ion acceleration according to all three metrics. The ion energies observed are presumed to be a result of a current-free double layer caused by plasma expansion from a high-density region in the discharge chamber to a low-density region in the plume. This only results in a beam voltage in the range of 20-40 V. Assuming an average ion production cost of approximately 150 eV, this results in an inherently inefficient thruster where the majority of the power is spent creating ions rather than in acceleration. The beam current is also very low, as the double layer allows only a limited number of ions to exit the discharge chamber.

Likewise, the plume structure creates a highly divergent ion beam. At low magnetic field strengths, the electric field disperses from the discharge chamber in a broad pattern that imparts large radial velocities to much of the ions. This leads to a relatively symmetric plasma expansion and a diffuse plume with an even distribution of ion trajectories. At higher magnetic field strengths, the electric field lines are concentrated through regions of high electron temperature that form off the discharge chamber wall. This creates a distribution of electric field lines that are much more focused at large angles, rather than towards the centerline or a broad range of trajectories, which cause the ions to be deflected off centerline at these large angles.

Beyond the fact that all three performance metrics show the EHT to be ineffective at ion acceleration, there was negligible performance increase from varying the operating

conditions. The second figure of merit for an ion accelerator is the ability to control the acceleration process through the variance of the operating conditions. None of the performance metrics could clearly be manipulated using the operating parameters. One example is the beam half-angle, where the magnetic field could affect the current distribution but not decrease overall beam divergence. This demonstrates the inherent weakness of indirect ion acceleration, as there is no definitive method to set the plasma potential contours to dictate ion energy or trajectory. The ion acceleration is heavily dependent on the presence of downstream plume structures of high plasma potential or high electron temperature. These plume structures form as a result of the plasma expansion, the size and intensity of which are determined by the magnetic field. Despite this dependency on the magnetic field, there is little demonstrable control over the shape of these regions using only the magnetic field strength, and thus negligible control over ion acceleration.

An additional factor is the shape of the magnetic field. The regions of high electron temperature are created by the separation of hot and cold portions of the electron population due to confinement on the magnetic field lines. Therefore the location of these regions can be adjusted by altering the shape of the magnetic field divergence downstream of the discharge chamber. One possibility would be to extend the magnetic field lines so they remain axial further downstream of the exit plane of the discharge chamber. This should prevent the regions of high electron temperature from forming near the walls of the discharge chamber. Additionally, if the magnetic field lines diverge more gradually, then separation of the higher energy electrons should be less pronounced and the formation of these regions of high electron temperature should be reduced. This

should lead to fewer radial electric field lines and less radial divergence of ions. Alternatively, if the magnetic field shape could be manipulated such that a region of higher electron temperature can be formed only along the centerline, then potentially the electric field lines will be focused axially, leading to a more collimated beam.

This is contrasted by the GHIT, where the grid geometry and operating conditions can directly control the grid sheath structure, the intervening potential, and the resulting ion energies and trajectories. The comparison between thruster configurations can be made even clearer using the calculated thrust contribution from the ions. The GHIT, despite the severe under-perveance of the grids, still provided 2 mN of thrust compared to the 12 μN of thrust from the EHT. Furthermore, the GHIT demonstrated a high degree of control over the performance metrics, as the beam divergence angle, ion energy, and beam current could be directly manipulated using the operating conditions. While variance of an operating parameter does affect multiple performance metrics, there are multiple methods to alter each parameter, granting a large degree of control over the thruster performance.

It can thus be concluded that the application of a helicon plasma source in propulsion requires the use of a second stage for the acceleration of ions. A helicon plasma source alone demonstrates limited ion acceleration and negligible control thereof. However, the helicon plasma source can clearly be integrated as part of a thruster system to replace the DC plasma discharge system.

10.2 Helicon Discharge Efficiency

The helicon plasma source demonstrates an ion production cost in the range of 132-212 eV/ion, which at the lower bound confirms that it is capable of meeting and exceeding the discharge efficiency of DC discharges. The primary parameters that determine the discharge efficiency are the magnetic field and the discharge plasma electron temperature. This dependency on the electron temperature yields an additional strength of the helicon plasma source, as it is capable of adapting the electron energy distribution to alter the electron temperature. This feature should be the focus of further work, as reduction of the electron temperature will further reduce the ion production cost. Further gains can be attained by adapting the helicon plasma source into a geometry more suited to use with an ion engine, such as decreasing the discharge chamber length and increasing the diameter. As a result, it can be concluded that helicon plasma sources can be used to replace DC plasma discharges given sufficient optimization to bring it to the same level of development.

10.3 Future Work

There are two primary areas that are recommended for future work. The first is to identify and correct the cause for the low RF coupling to the plasma, as this is the most likely cause for the low ionization rate. A direct approach to determine the cause would be to replace the solenoids with ones wrapped around a non-conductive material, as this would avoid creating a pathway for eddy currents to form. Likewise, it would remove a capacitive pathway to ground through the thrust stand. Another modification is to

reconfigure the RF system to the in-vacuum matching network configuration. While this increases the probability of matching network component failure, it should reduce coupling to the vacuum chamber through the feedthrough or transmission from the coax cable to the ambient plasma.

The second area for future work encompasses modifications to the GHIT in order to improve performance. The first is to vary the grid aperture diameters as a function of radial position to match the grid geometry to the ion number density variations in the discharge chamber. The second is to reduce the discharge chamber length and increase the diameter. This serves to decrease the wall area and reduce ion losses to the wall, as well as allow for a larger grid area to enable higher beam current extraction. Another suggestion is to examine GHIT operation at higher magnetic fields and discharge voltages, both to increase plasma density and decrease perveance. These two changes in operating parameters should increase the ion current by both increasing discharge plasma density and decreasing ion collection by the screen and accel grids. Exploration of these areas should lead to improved performance of the GHIT to the point where it can produce easily discernible thrust.

APPENDIX A

UNIFORM DENSITY, COLLISIONLESS PLASMA DISPERSION RELATION

This derivation is included as it contains the full derivation of the dispersion relation with all intervening steps shown. It serves not only as an educational tool to explain the origin and assumptions of the dispersion relation, but also as a stepping stone for future adaptation. The derivation begins with Maxwell's equations,[3]

$$\nabla \times \vec{E} = -\frac{\partial \vec{B}}{\partial t} \tag{A.1}$$

$$\nabla \times \vec{B} = \mu_0 \vec{j} + \mu_0 \varepsilon_0 \frac{\partial \vec{E}}{\partial t} \tag{A.2}$$

$$\vec{E} = \vec{j} \times \frac{\vec{B}_0}{e n_0} \tag{A.3}$$

$$\nabla \bullet \vec{B} = 0 \tag{A.4}$$

where B_0 is the equilibrium magnetic field and B is the perturbed magnetic field. These magnetic parameters are defined as

$$\vec{B}_0 = B_0 \hat{z}$$

$$\vec{B} = B \exp[i(m\theta + kz - \omega t)]$$

With this definition, B rotates clockwise along k for positive m. Several assumptions are made: displacement current is negligible, plasma current is carried only by the ExB drift of the electrons, and that the plasma has zero resistivity. Quantitatively, this means that

$$\mu_0 \varepsilon_0 \frac{\partial \vec{E}}{\partial t} = 0$$

$$\omega_{lh} \ll \omega \ll \omega_{ce}$$

$$E_z = 0$$

Taking the divergence of Equation (A.2) and substituting the above assumptions,

$$\nabla \bullet \nabla \times \vec{B} = \nabla \bullet \left(\mu_0 \vec{j} \right)$$

$$\mu_0 \nabla \bullet \vec{j} = \nabla \bullet \left[\left(\frac{1}{r} \frac{\partial B_z}{\partial \theta} - \frac{\partial B_z}{\partial z} \right) \hat{r} + \left(\frac{\partial B_r}{\partial z} - \frac{\partial B_z}{\partial r} \right) \hat{\theta} + \frac{1}{r} \left(\frac{\partial}{\partial r} r B_\theta - \frac{\partial B_r}{\partial \theta} \right) \hat{z} \right]$$

$$\mu_0 \nabla \bullet \vec{j} = \frac{1}{r} \frac{\partial}{\partial r} \left(\frac{\partial B_z}{\partial \theta} - r \frac{\partial B_\theta}{\partial z} \right) + \frac{1}{r} \frac{\partial}{\partial \theta} \left(\frac{\partial B_r}{\partial z} - \frac{\partial B_z}{\partial r} \right) + \frac{\partial}{\partial z} \left(\frac{1}{r} \left(\frac{\partial}{\partial r} r B_\theta - \frac{\partial B_r}{\partial \theta} \right) \right)$$

$$\mu_0 \nabla \bullet \vec{j} = \frac{1}{r} \left(\frac{\partial^2 B_z}{\partial r \partial \theta} - \frac{\partial B_\theta}{\partial z} - r \frac{\partial^2 B_\theta}{\partial z \partial r} \right) + \frac{1}{r} \frac{\partial^2 B_r}{\partial \theta \partial z} + \frac{1}{r} \frac{\partial^2 B_z}{\partial r \partial \theta} + \frac{1}{r} \frac{\partial B_\theta}{\partial z} + \frac{1}{r} \frac{\partial^2 B_\theta}{\partial r \partial z} - \frac{1}{r} \frac{\partial^2 B_r}{\partial z \partial \theta}$$

$$\nabla \bullet \vec{j} = 0 \qquad\qquad (A.5)$$

Substituting the form of B into Equation (A.1),

$$\nabla \times \vec{E} = -\frac{\partial \vec{B}}{\partial t}$$

$$\nabla \times \vec{E} = i\omega\vec{B}$$

Substituting Equation (A.3) in for *E*,

$$i\omega\vec{B} = \nabla \times \left(\vec{j} \times \frac{\vec{B}_0}{en_0} \right)$$

$$i\omega\vec{B} = \frac{1}{en_0}\left[\vec{j}\left(\nabla \bullet \vec{B}_0\right) - \vec{B}_0\left(\nabla \bullet \vec{j}\right)\right]$$

Using the results of Equation (A.5),

$$i\omega\vec{B} = \frac{\left(\nabla \bullet \vec{B}_0\right)\vec{j}}{en_0}$$

$$\vec{B} = \frac{\vec{j}}{i\omega en_0}\frac{\partial\vec{B}_0}{\partial z}$$

$$\vec{B} = \frac{\vec{j}}{i\omega en_0}ikB_0$$

$$\vec{B} = \frac{k}{\omega}\frac{B_0\vec{j}}{en_0} \qquad\qquad (A.7)$$

Substituting Equation (A.2) into (A.7),

$$\vec{B} = \frac{k}{\omega}\frac{B_0}{en_0}\frac{1}{\mu_0}\left(\nabla \times \vec{B}\right)$$

251

$$\vec{B} = \frac{1}{\alpha}\left(\nabla \times \vec{B}\right)$$

where

$$\alpha = \frac{\omega}{k}\frac{\mu_0 e n_0}{B_0} \qquad (A.8)$$

This yields

$$\alpha\vec{B} = \nabla \times \vec{B} \qquad (A.9)$$

Taking the curl of Equation (A.9),

$$\nabla \times \alpha\vec{B} = \nabla \times \nabla \times \vec{B}$$

$$\alpha\left(\nabla \times \vec{B}\right) = \nabla\left(\nabla \bullet \vec{B}\right) - \left(\nabla \bullet \nabla\right)\vec{B}$$

Substituting in Equations (4) and (9),

$$\nabla^2 \vec{B} + \alpha^2 \vec{B} = 0 \qquad (A.10)$$

Expanding the Laplacian in Equation (A.10) for the z-component,

$$\frac{\partial^2 B_z}{\partial r^2} + \frac{1}{r}\frac{\partial B_z}{\partial r} + \frac{1}{r^2}\frac{\partial^2 B_z}{\partial \theta^2} + \frac{\partial^2 B_z}{\partial z^2} + \alpha^2 B_z = 0 \tag{A.11}$$

From the definition of *B*,

$$\frac{\partial^2 B_z}{\partial \theta^2} = -m^2 B_z$$

$$\frac{\partial^2 B_z}{\partial z^2} = -k^2 B_z$$

Substituting this into Equation (A.11) and denoting all radial derivatives of *B* with a prime,

$$B_z'' + \frac{1}{r}B_z' + \left(-\frac{m^2}{r^2} + \alpha^2 - k^2\right)B_z = 0$$

$$B_z'' + \frac{1}{r}B_z' + \left(T^2 - \frac{m^2}{r^2}\right)B_z = 0 \tag{A.12}$$

where *T* is the transverse wavenumber, defined as

$$T^2 \equiv \alpha^2 - k^2$$

Equation (A.12) is in the form of Bessel's equation. In order to solve (A.12), the Frobenius Method is used. Therefore let the solution take the form of

253

$$B_z = \sum_{k=0}^{\infty} a_k r^{k+n}$$

$$B_z' = \sum_{k=0}^{\infty} a_k (k+n) r^{k+n-1}$$

$$B_z'' = \sum_{k=0}^{\infty} a_k (k+n)(k+n-1) r^{k+n-2}$$

Substituting these quantities into Equation (A.12),

$$\sum_{k=0}^{\infty} a_k (k+n)(k+n-1) r^{k+n-2} + \sum_{k=0}^{\infty} a_k (k+n) r^{k+n-2} + \sum_{k=0}^{\infty} a_k T^2 r^{k+n} - \sum_{k=0}^{\infty} a_k m^2 r^{k+n-2} = 0$$

Rewriting the third series so that r has the exponent of $(k+n-2)$,

$$\sum_{k=0}^{\infty} a_k (k+n)(k+n-1) r^{k+n-2} + \sum_{k=0}^{\infty} a_k (k+n) r^{k+n-2} + \sum_{k=2}^{\infty} a_{k-2} T^2 r^{k+n-2} - \sum_{k=0}^{\infty} a_k m^2 r^{k+n-2} = 0$$

For $k = 0$,

$$n(n-1)a_0 r^{n-2} + na_0 r^{n-2} - m^2 a_0 r^{n-2} = 0$$

$$a_0 \left(n(n-1) + n - m^2 \right) = 0$$

$$a_0 \left(n^2 - m^2 \right) = 0$$

$$n = \pm m$$

254

If n = m,

$$\sum_{k=0}^{\infty}\left[(k+m)(k+m-1)+(k+m)-m^2\right]a_k r^{k+m-2}+\sum_{k=2}^{\infty}T^2 a_{k-2}r^{k+m-2}=0$$

$$\sum_{k=0}^{\infty}k\left[(k+2m)\right]a_k r^{k+m-2}+\sum_{k=2}^{\infty}T^2 a_{k-2}r^{k+m-2}=0$$

$$(1+2m)a_1 r^{m-1}+\sum_{k=2}^{\infty}\left(k\left[(k+2m)\right]a_k r^{k+m-2}+T^2 a_{k-2}r^{k+m-2}\right)=0$$

If m is not equal to -½ then,

$$a_1=0$$

$$a_k=\frac{-T^2}{k(k+2m)}a_{k-2}\ \text{ for } k=2,\ 3,\ \dots$$

Thus all odd indexed a coefficients are zero. Therefore, for even indices of a,

$$a_{2l}=\frac{-T^2}{4l(l+m)}a_{2l-2}$$

Substituting in the first few values of l (1, 2, 3) to look for a pattern,

$$a_2=\frac{-T^2}{4(m+1)}a_0$$

$$a_4 = \frac{T^4}{4 \cdot 8(m+1)(m+2)} a_0$$

$$a_6 = \frac{(-1)^3 (T^2)^3}{4^3 (1 \cdot 2 \cdot 3)(m+1)(m+2)(m+3)} a_0$$

$$a_k = \frac{(-1)^k (T^2)^k}{2^{2k} (k!)(m+k)!} a_0$$

Substituting into the equation for B_z,

$$B_z = a_0 \sum_{k=0}^{\infty} \frac{(-1)^k T^{2k}}{2^{2k} (k!)(m+k)!} r^{2k+m}$$

$$B_z = \frac{a_0}{T^m} \sum_{k=0}^{\infty} \frac{(-1)^k (Tr)^{2k+m}}{2^{2k} k!(m+k)!}$$

$$B_z = C_3 J_m (Tr) \tag{A.13}$$

where C_3 is a constant, and $J_m(Tr)$ is Bessel's function of the first kind of the mth order.

To find the r and θ components of Equation (A.9),

$$\alpha \vec{B} = \nabla \times \vec{B}$$

$$\alpha B_r = \frac{1}{r} \frac{\partial B_z}{\partial \theta} - \frac{\partial B_\theta}{\partial z}$$

$$\alpha B_r = \frac{1}{r} im B_z - ik B_\theta \tag{A.14}$$

$$\alpha B_\theta = \frac{\partial B_r}{\partial z} - \frac{\partial B_z}{\partial r}$$

$$\alpha B_\theta = ikB_r - \frac{\partial B_z}{\partial r} \tag{A.15}$$

Substituting Equation (A.15) into (A.14),

$$\alpha B_r = \frac{1}{r}imB_z - ik\left(\frac{ikB_r}{\alpha} - \frac{1}{\alpha}\frac{\partial B_z}{\partial r}\right)$$

$$\alpha^2 B_r = \frac{\alpha}{r}imB_z + k^2 B_r + ik\frac{\partial B_z}{\partial r}$$

$$\left(\alpha^2 - k^2\right)B_r = \frac{\alpha}{r}imB_z + ik\frac{\partial B_z}{\partial r}$$

$$T^2 B_r = \frac{\alpha}{r}imB_z + ik\frac{\partial B_z}{\partial r} \tag{A.16}$$

Conversely by substituting (A.14) into (A.15),

$$\alpha B_\theta = ik\left(\frac{imB_z}{r\alpha} - \frac{ikB_\theta}{\alpha}\right) - \frac{\partial B_z}{\partial r}$$

$$\alpha^2 B_\theta = -\frac{mkB_z}{r} + k^2 B_\theta - \alpha\frac{\partial B_z}{\partial r}$$

$$\left(\alpha^2 - k^2\right)B_\theta = -\frac{mkB_z}{r} - \alpha\frac{\partial B_z}{\partial r}$$

$$T^2 B_\theta = -\frac{mkB_z}{r} - \alpha\frac{\partial B_z}{\partial r} \tag{A.17}$$

Taking Equations (A.16) and (A.17) and substituting in (A.13) for B_z and letting radial derivatives of Bessel's function be denoted with a prime,

$$B_r = \frac{iC_3}{T^2}\left(\frac{\alpha m}{r} J_m(Tr) + kJ'_m(Tr)\right) \qquad \text{(A.18)}$$

$$B_\theta = \frac{-C_3}{T^2}\left(\frac{km}{r} J_m(Tr) + \alpha J'_m(Tr)\right) \qquad \text{(A.19)}$$

The recurrent relations for Bessel's function are

$$J'_m(Tr) = \frac{T}{2}\left(J_{m-1}(Tr) - J_{m+1}(Tr)\right)$$

$$J_m(Tr) = \frac{Tr}{2m}\left(J_{m-1}(Tr) + J_{m+1}(Tr)\right)$$

Using these relations B_r and B_θ can be written as

$$B_r = \frac{iC_3}{T^2}\left(\frac{\alpha T}{2}\left(J_{m-1}(Tr) + J_{m+1}(Tr)\right) + \frac{Tk}{2}\left(J_{m-1}(Tr) - J_{m+1}(Tr)\right)\right)$$

$$B_r = \frac{iC_3}{2T}\left((\alpha + k)J_{m-1}(Tr) + (\alpha - k)J_{m+1}(Tr)\right) \qquad \text{(A.20)}$$

$$B_\theta = \frac{-C_3}{T^2}\left(\frac{kT}{2}\left(J_{m-1}(Tr) + J_{m+1}(Tr)\right) - \frac{\alpha T}{2}\left(J_{m-1}(Tr) - J_{m+1}(Tr)\right)\right)$$

$$B_\theta = \frac{-C_3}{2T}\left((\alpha + k)J_{m-1}(Tr) - (\alpha - k)J_{m+1}(Tr)\right) \qquad \text{(A.21)}$$

Now let the amplitude, A, be defined as

$$A \equiv \frac{iC_3}{2T}$$

Substituting the amplitude into Equations (A.20) and (A.21), and rewriting (A.13) for the sake of completeness,

$$B_z = C_3 J_m(Tr)$$

$$B_r = C_1 J_{m-1}(Tr) + C_2 J_{m+1}(Tr) \qquad (\text{A.22})$$

$$B_\theta = iC_1 J_{m-1}(Tr) - iC_2 J_{m+1}(Tr) \qquad (\text{A.23})$$

where,

$$C_1 = (\alpha + k)A$$

$$C_2 = (\alpha - k)A$$

$$C_3 = -2iTA$$

To get the components of the electric field, start with Equation (A.7) and rewrite,

$$\vec{B} = \frac{k}{\omega} \frac{B_0 \vec{j}}{e n_0}$$

$$\vec{j} = \frac{\omega}{k}\frac{en_0}{B_0}\vec{B}$$

$$\vec{j} \times \frac{\vec{B}}{en_0} = \frac{\omega}{k}\frac{en_0}{B_0}\vec{B} \times \frac{\vec{B}}{en_0}$$

$$\vec{E} = \frac{\omega}{k}\vec{B} \times \frac{\vec{B}_0}{B_0}$$

Substituting the definition of B_0,

$$\vec{E} = \frac{\omega}{k}\left[\left(B_r\hat{r} \times \hat{z}\right) + \left(B_\theta\hat{\theta} \times \hat{z}\right) + \left(B_z\hat{z} \times \hat{z}\right)\right]$$

$$\vec{E} = \frac{\omega}{k}B_\theta\hat{r} - \frac{\omega}{k}B_r\hat{\theta}$$

Thus,

$$E_r = \frac{\omega}{k}B_\theta \tag{A.24}$$

$$E_\theta = -\frac{\omega}{k}B_r \tag{A.25}$$

$$E_z = 0$$

Substituting Equations (A.22) and (A.23) into (A.24) and (A.25),

$$E_r = \frac{i\omega}{k}\left(C_1 J_{m-1}(Tr) - C_2 J_{m+1}(Tr)\right) \tag{A.26}$$

$$E_{\theta} = -\frac{\omega}{k}\left(C_1 J_{m-1}(Tr) + C_2 J_{m+1}(Tr)\right) \tag{A.27}$$

The boundary conditions for the wall can either be insulating or conducting. For an insulating boundary, $j_r = 0$ at $r = a$, where a is the radius of the discharge chamber. From Equation (A.7), this leads to $B_r = 0$ at $r = a$. For a conducting boundary, $E_{\theta} = 0$ at $r = a$, which also leads to $B_r = 0$ at $r = a$. Thus for a simple helicon the choice of boundary conditions is irrelevant. However, it is unknown whether the solenoids surrounding the discharge chamber (a conductive boundary) dominates over the Pyrex discharge vessel (an insulating boundary). Therefore the effective value of a changes depending on the nature of the boundary condition, but the form of the equations remains the same. Figure 142 shows the two possible boundary conditions.
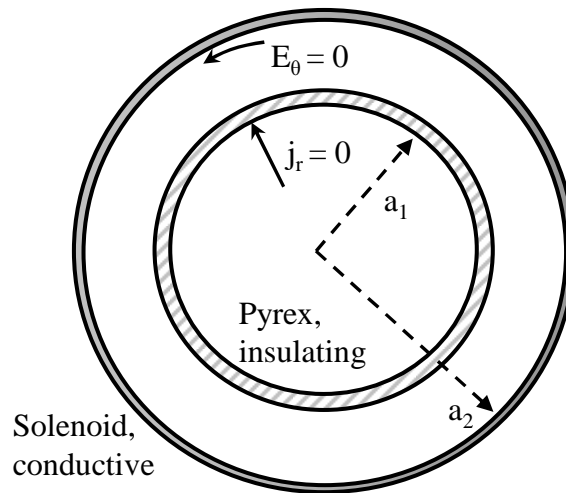
Figure 142. Possible helicon wave radial boundary conditions.

Substituting this boundary condition into Equation (A.18),

$$B_r = \frac{iC_3}{T^2}\left(\frac{\alpha m}{r}J_m(Tr) + kJ'_m(Tr)\right)$$

$$0 = \frac{\alpha m}{a}J_m(Ta) + kJ'_m(Ta) \tag{A.28}$$

Let the following variables be defined as,

$$Z = Ta$$

$$\kappa = ka$$

Equation (A.28) can be rewritten as

$$J_m(Z) = \frac{\kappa}{\alpha m}J'_m(Z) \tag{A.29}$$

Taking a Taylor expansion of $J_m(Z)$ about Z_m,

$$J_m(Z) \approx J_m(Z_m) + (Z - Z_m)J'_m(Z_m)$$

where Z_m is the solution to the equation

$$J_m(Z_m) = 0$$

Thus,

$$J_m(Z) \approx (Z - Z_m) J'_m(Z_m) \qquad \text{(A.30)}$$

Now assume that a variable α_m can be defined from an approximation of Equation (A.29),

$$J_m(Z) \approx \frac{\kappa}{\alpha_m m} J'_m(Z_m)$$

Substituting this into Equation (A.30),

$$\frac{\kappa}{\alpha_m m} J'_m(Z_m) = (Z - Z_m) J'_m(Z_m)$$

$$Z \approx \frac{\kappa}{\alpha_m m} + Z_m$$

where

$$\alpha_m = \frac{1}{a}\left(Z_m^2 + \kappa^2\right)^{1/2} \qquad \text{(A.32)}$$

$$\alpha = \frac{1}{a}\left(Z^2 + \kappa^2\right)^{1/2} \qquad \text{(A.33)}$$

Using Equation (A.8) and substituting in for α results in the plasma dispersion relation.

$$\frac{\omega}{k}\frac{\mu_0 e n_0}{B_0} = \frac{1}{a}\left[\left(\frac{ka}{\alpha_m m} + Z_m\right)^2 + k^2 a^2\right]^{1/2} \qquad \text{(A.34)}$$

263

APPENDIX B

UNIFORM COLLISIONAL PLASMA DISPERSION RELATION DERIVATION

Like Appendix A, this derivation is included so that a full derivation of the problem. A full solution is not included, as it requires numerical integration using the boundary conditions. However, a full definition of the problem and constants are presented.

B.1 Derivation of the Modified Ohm's Law

The derivation starts with Faraday's Law,[3]

$$m\frac{\partial \vec{v}}{\partial t} = -e\left(\vec{E} + \vec{v} \times \vec{B}_0\right) - m\vec{v}\,\nu \tag{B.1}$$

where m and v is the mass and velocity of an electron, respectively, e is the charge of an electron, E is the electric field, B is the magnetic field, and ν is the electron collision frequency. Since the speed of the electrons is much greater than that of the ions, the contribution to current flow via ion motion can be neglected, resulting in a current density, j, of

$$\vec{j} = -n_0 e\vec{v} \tag{B.2}$$

The resistivity, η, is defined as

$$\eta = \frac{mv}{n_0 e^2} \tag{B.3}$$

Substituting Equations (B.2) and (B.3) into Equation (B.1),

$$m\frac{\partial \vec{v}}{\partial t} = -e\left(\vec{E} + \frac{-\vec{j}\times\vec{B}_0}{n_0 e}\right) - n_0 e^2 \eta \vec{v} \tag{B.4}$$

Assuming the velocity oscillates as a complex exponential such that

$$v = v\exp(-i\omega t)$$

Equation (B.4) can be written as

$$-i\omega m\vec{v} = -e\left(\vec{E} + \frac{-\vec{j}\times\vec{B}_0}{n_0 e}\right) - n_0 e^2 \eta \vec{v}$$

$$0 = -e\left(\vec{E} - \frac{\vec{j}\times\vec{B}_0}{n_0 e}\right) - n_0 e^2 \eta \vec{v} + i\omega m\vec{v}$$

Substituting Equations (B.2) and (B.3) in place of v and m, respectively

$$0 = -e\left(\vec{E} - \frac{\vec{j}\times\vec{B}_0}{n_0 e}\right) + n_0 e^2 \eta \frac{\vec{j}}{n_0 e} - i\omega \frac{n_0 e^2 \eta}{v} \frac{\vec{j}}{n_0 e}$$

$$0 = -\left(\vec{E} - \frac{\vec{j} \times \vec{B}_0}{n_0 e} \right) + \eta \left(1 - \frac{i\omega}{\nu} \right) \vec{j}$$

$$\vec{E} = \frac{\vec{j} \times \vec{B}_0}{n_0 e} + \eta \left(1 - \frac{i\omega}{\nu} \right) \vec{j} \tag{B.5}$$

Note that if m goes to zero, η goes to zero and Equation (B.5) becomes identical to (A.3).

B.2 Problem Definition

Begin with Maxwell's Equations like before, but using the modified Ohm's law in Equation (B.5).

$$\nabla \times \vec{E} = -\frac{\partial \vec{B}}{\partial t} \tag{B.6}$$

$$\nabla \times \vec{B} = \mu_0 \vec{j} + \mu_0 \varepsilon_0 \frac{\partial \vec{E}}{\partial t} \tag{B.7}$$

$$\vec{E} = \frac{\vec{j} \times \vec{B}_0}{n_0 e} + \eta \left(1 - \frac{i\omega}{\nu} \right) \vec{j} \tag{B.8}$$

$$\nabla \bullet \vec{B} = 0 \tag{B.9}$$

Again, neglect the displacement current and let all perturbations be complex exponentials of the form

$$f = f \exp(i(m\theta + kz - \omega t))$$

Taking the curl of Equation (B.8),

$$\nabla \times \vec{E} = \frac{1}{n_0 e} \nabla \times \vec{j} \times \vec{B}_0 + \eta \left(1 - \frac{i\omega}{\nu} \right) \nabla \times \vec{j}$$

Substituting Equations (B.6) and (B.7),

$$\frac{1}{n_0 e} \nabla \times \vec{j} \times \vec{B}_0 + \eta \left(1 - \frac{i\omega}{\nu} \right) \nabla \times \nabla \times \vec{B} = i\omega \vec{B} \qquad (B.8)$$

Note that the cross products of the first term can be written as

$$\nabla \times \vec{j} \times \vec{B}_0 = \vec{j} \left(\nabla \bullet \vec{B}_0 \right) - \vec{B}_0 \left(\nabla \bullet \vec{j} \right)$$

$$\nabla \times \vec{j} \times \vec{B}_0 = \vec{j} \left(ikB_0 \right) - \vec{B}_0 \left(\frac{\nabla \bullet \nabla \times \vec{B}}{\mu_0} \right)$$

$$\nabla \times \vec{j} \times \vec{B}_0 = \vec{j} \left(ikB_0 \right)$$

$$\nabla \times \vec{j} \times \vec{B}_0 = ikB_0 \frac{\nabla \times \vec{B}}{\mu_0} \qquad (B.9)$$

Substituting Equation (B.9) into (B.8),

$$\frac{ikB_0}{\mu_0 n_0 e} \nabla \times \vec{B} + \eta \left(1 - \frac{i\omega}{\nu} \right) \frac{\nabla \times \nabla \times \vec{B}}{\mu_0} - i\omega \vec{B} = 0$$

$$\frac{\eta}{\mu_0} (\omega + i\nu) \nabla \times \nabla \times \vec{B} - \frac{kB_0 \nu}{\mu_0 n_0 e} \nabla \times \vec{B} + \nu \omega \vec{B} = 0$$

Substituting Equation (B.3) for the resistivity,

$$\frac{m\nu}{\mu_0 n_0 e^2}(\omega + i\nu)\nabla \times \nabla \times \vec{B} - \frac{kB_0\nu}{\mu_0 n_0 e}\nabla \times \vec{B} + \nu\omega\vec{B} = 0$$

$$(\omega + i\nu)\nabla \times \nabla \times \vec{B} - \frac{kB_0 e}{m}\nabla \times \vec{B} + \frac{n_0 e^2 \mu_0 \omega}{m}\vec{B} = 0 \qquad (B.10)$$

Repeating the definition of α from Appendix A for convenience,

$$\alpha = \frac{\omega}{k}\frac{\mu_0 e n_0}{B_0} \qquad (A.8)$$

α can also be written in terms of the plasma frequency, ω_p, and electron cyclotron frequency, ω_c, and the speed of the wave, c.

$$\alpha = \frac{\omega}{k}\frac{\omega_p^2}{\omega_c c^2} \qquad (B.11)$$

For convenience, the definitions of the plasma frequency and the cyclotron frequency are repeated below.

$$\omega_c = \frac{eB_0}{m} \qquad \qquad \omega_p = \left(\frac{n_0 e^2}{\varepsilon_0 m}\right)$$

Substituting (B.11) into (B.10),

$$(\omega + i\nu)\nabla \times \nabla \times \vec{B} - k\omega_c \nabla \times \vec{B} + \alpha k\omega_c \vec{B} = 0 \qquad (\text{B.12})$$

Now let Equation (B.12) be factorable into the form

$$(\beta_1 - \nabla \times)(\beta_2 - \nabla \times)\vec{B} = 0 \qquad (\text{B.13})$$

where

$$\beta_1 \beta_2 = \frac{\alpha k\omega_c}{\omega + i\nu} \qquad (\text{B.14})$$

The general solution to Equation (B.13) is

$$\vec{B} = \vec{B}_1 + \vec{B}_2$$

where

$$\nabla \times \vec{B}_1 = \beta_1 \vec{B}_1 \qquad\qquad \nabla \times \vec{B}_2 = \beta_2 \vec{B}_2 \qquad (\text{B.15})$$

This means that the solution is the composition of two different waves, each with a distinct total wave number β. Note that the general solution to Equation (B.13) when substituted into Equation (B.13) results in the following.

$$(\beta_1 - \nabla \times)(\beta_2 - \nabla \times)\vec{B}_1 + (\beta_1 - \nabla \times)(\beta_2 - \nabla \times)\vec{B}_2 = 0$$

Taking the curl of Equations (B.15),

$$\nabla \times \nabla \times \vec{B}_1 = \nabla \times \beta_1 \vec{B}_1 \qquad \nabla \times \nabla \times \vec{B}_2 = \nabla \times \beta_2 \vec{B}_2$$

$$\nabla \left(\nabla \bullet \vec{B}_1 \right) - \nabla^2 \vec{B}_1 = \beta_1^2 \vec{B}_1 \qquad \nabla \left(\nabla \bullet \vec{B}_2 \right) - \nabla^2 \vec{B}_2 = \beta_2^2 \vec{B}_2$$

Adding the two equations together yields

$$\nabla \left(\nabla \bullet \vec{B}_1 \right) - \nabla^2 \vec{B}_1 + \nabla \left(\nabla \bullet \vec{B}_2 \right) - \nabla^2 \vec{B}_2 = \beta_1^2 \vec{B}_1 + \beta_2^2 \vec{B}_2$$

$$\nabla \left[\left(\nabla \bullet \vec{B}_1 \right) + \left(\nabla \bullet \vec{B}_2 \right) \right] - \nabla^2 \vec{B}_1 - \beta_1^2 \vec{B}_1 = \nabla^2 \vec{B}_2 + \beta_2^2 \vec{B}_2$$

$$\nabla \left[\nabla \bullet \left(\vec{B}_1 + \vec{B}_2 \right) \right] - \nabla^2 \vec{B}_1 - \beta_1^2 \vec{B}_1 = \nabla^2 \vec{B}_2 + \beta_2^2 \vec{B}_2$$

$$-\nabla \left[\nabla \bullet \left(\vec{B}_1 + \vec{B}_2 \right) \right] + \nabla^2 \vec{B}_1 + \beta_1^2 \vec{B}_1 = -\left(\nabla^2 \vec{B}_2 + \beta_2^2 \vec{B}_2 \right)$$

$$\nabla^2 \vec{B}_1 + \beta_1^2 \vec{B}_1 = -\left(\nabla^2 \vec{B}_2 + \beta_2^2 \vec{B}_2 \right)$$

Since B_1 and B_2 are different functions they must vanish individually. Therefore,

$$\nabla^2 \vec{B}_1 + \beta_1^2 \vec{B}_1 = 0 \qquad \nabla^2 \vec{B}_2 + \beta_2^2 \vec{B}_2 = 0 \qquad \text{(B.16)}$$

In order to determine the value of β_1 and β_2, use Equation (B.14) to give β_1 in terms of β_2.

$$\beta_1 = \frac{\alpha k \omega_c}{\beta_2 (\omega + i\nu)} \tag{B.17}$$

Comparing Equations (B.12) and (B.13), it can be seen that when Equation (B.13) is expanded and set equal to Equation (B.12) it leads to the relation

$$\beta_1 + \beta_2 = \frac{k \omega_c}{(\omega + i\nu)} \tag{B.18}$$

Substituting Equation (B.17) into (B.18),

$$\beta_2 = \frac{k \omega_c}{(\omega + i\nu)} - \frac{\alpha k \omega_c}{\beta_2 (\omega + i\nu)}$$

$$\beta_2^2 = \frac{\beta_2 k \omega_c}{(\omega + i\nu)} - \frac{\alpha k \omega_c}{(\omega + i\nu)}$$

$$(\omega + i\nu)\beta_2^2 = \beta_2 k \omega_c - \alpha k \omega_c$$

$$0 = (\omega + i\nu)\beta_2^2 - \beta_2 k \omega_c + \alpha k \omega_c$$

$$\beta_2 = \frac{k \omega_c \pm \sqrt{k^2 \omega_c^2 - 4\alpha k \omega_c (\omega + i\nu)}}{2(\omega + i\nu)}$$

For convenience, let

271

$$\gamma = \frac{\omega + i\nu}{k\omega_c} \tag{B.19}$$

Substituting this into the equation of the solution of the quadratic yields

$$\beta_{2,1} = \frac{1 \pm \sqrt{1 - 4\alpha\gamma}}{2\gamma} \tag{B.20}$$

Applying a second-order Taylor expansion to the discriminant yields

$$\beta_{1,2} = \frac{1 \mp \left(1 - 2\alpha\gamma - 2\alpha^2\gamma^2\right)}{2\gamma} \tag{B.21}$$

Note the similarity between Equations (A.9) and (B.15). The equations are of the same form and can be solved in a similar manner; this means that α and β are analogous parameters. From this it can be seen that Equation (B.15) thus describes two different waves, each one related to a corresponding β term. To further examine these two waves, a closer look at β_1 is illuminating.

$$\beta_1 = \alpha + \alpha^2\gamma \tag{B.22}$$

Now suppose that the assumption that the electron mass can be neglected is brought back into use. If m_e goes to zero, the cyclotron frequency becomes infinite, which makes γ approach zero by Equation (B.19). This would create the identity of $\beta_1 = \alpha$, which would

make the first portion of Equation (B.15) identical to Equation (A.9). Therefore, β_1 corresponds to a helicon wave. Examining β_2 now yields

$$\beta_2 = \frac{1}{\gamma} - \alpha - \alpha^2 \gamma \qquad (B.23)$$

For small magnetic fields, the following inequality is true.

$$4\alpha\gamma << 1$$

This means that

$$\beta_2 \cong \frac{1}{\gamma} = \frac{k\omega_c}{\omega + i\nu}$$

Assume for a moment that collisions are neglected. Thus,

$$\beta_2 = \frac{k\omega_c}{\omega}$$

$$\omega = \frac{k}{\beta_2}\omega_c$$

Now recall that β, like α, is the total wave number of the wave, and k is the longitudinal (or axial) wave number. This means

$$\omega = \frac{k_\parallel}{k_{tot}} \omega_c = \omega_c \cos\theta$$

Verbally, this means that β_2 corresponds to an electron cyclotron wave, which is identified as the Trivelpiece-Gould wave.

Since Equations (A.9) and (B.15) are of the same form they can be solved in the same fashion, which means that their solutions are of a similar form. The two differences are: α is replaced with β, and there are now two waves and solutions for β and T. These observations combined with Equations (A.13), (A.18) and (A.19) result in the components of the magnetic field of both B_1 and B_2,

$$B_{z,j} = C_{3,j} J_m (T_j r) \tag{B.24}$$

$$B_{r,j} = \frac{iC_{3,j}}{T_j^2} \left(\frac{\beta_j m}{r} J_m (T_j r) + k J_m' (T_j r) \right) \tag{B.25}$$

$$B_{\theta,j} = \frac{-C_{3,j}}{T_j^2} \left(\frac{km}{r} J_m (T_j r) + \beta_j J_m' (T_j r) \right) \tag{B.26}$$

where j indexes the solution considered and takes the value of one or two, for the helicon wave or TG wave, respectively. The transverse wave number, T_j, is defined as

$$T_j^2 \equiv \beta_j^2 - k^2 \tag{B.27}$$

Equations (B.25) and (B.26) can also be expressed similarly to Equations (A.20) and A.21) using the recurrent relations.

$$B_r = \frac{iC_{3,j}}{2T_j}\left(\left(\beta_j + k\right)J_{m-1}\left(T_j r\right) + \left(\beta_j - k\right)J_{m+1}\left(T_j r\right)\right) \tag{B.28}$$

$$B_\theta = \frac{-C_{3,j}}{2T_j}\left(\left(\beta_j + k\right)J_{m-1}\left(T_j r\right) - \left(\beta_j - k\right)J_{m+1}\left(T_j r\right)\right) \tag{B.29}$$

At this point it should be noted that since there are two waves to solve, there are too many degrees of freedom for the single boundary condition used in Appendix A to be sufficient. Additional boundary conditions require examining the behavior of the wave beyond the insulating boundary. Generally there is a gap between the insulating boundary of the discharge chamber and the conducting surface of the magnetic solenoids where there is no plasma, yet the RF waves can still propagate. This region is called the vacuum gap and requires an additional solution of Maxwell's equations.

B.3 Vacuum Gap

Starting with Maxwell's equations,

$$\nabla \bullet \vec{E} = 0 \tag{B.30}$$

$$\nabla \bullet \vec{B} = 0 \tag{B.31}$$

$$\nabla \times \vec{E} = -\frac{\partial \vec{B}}{\partial t} \tag{B.32}$$

$$\nabla \times \vec{B} = \mu_0 \vec{j} + \mu_0 \varepsilon_0 \frac{\partial \vec{E}}{\partial t} \qquad (B.33)$$

The one major change in the vacuum gap is that with no plasma there can be no current, forcing j to be zero and the curl of B to be entirely drift current. As before, let the magnetic field be of the form

$$\vec{B} = B \exp[i(m\theta + kz - \omega t)]$$

Substituting this into Equations (B.32) and (B.33) yields

$$\nabla \times \vec{E} = i\omega \vec{B} \qquad (B.34)$$

$$\nabla \times \vec{B} = -i\omega \mu_0 \varepsilon_0 \vec{E} \qquad (B.35)$$

Taking the curl of Equation (B.35) results in

$$\nabla \times \nabla \times \vec{B} = -i\omega \mu_0 \varepsilon_0 \nabla \times \vec{E}$$

Substituting in Equation (B.34) for the curl of E,

$$-\nabla^2 \vec{B} = \omega^2 \mu_0 \varepsilon_0 \vec{B}$$

$$\nabla^2 \vec{B} + \frac{\omega^2}{c^2} \vec{B} = 0$$

$$\nabla^2\vec{B} + k_0^2\vec{B} = 0 \tag{B.36}$$

where k_0 is defined as

$$k_0 = \frac{\omega}{c} \tag{B.37}$$

It can be seen that Equation (B.36) looks very similar to Equation (A.10) except for the difference between k_0 and α. In this case, k_0 is the total wave number inside the vacuum gap. One can then make the assumption that an equivalent equation exists that is a counterpart to Equation (A.9). To determine this, assume that such an equation exists as

$$k_0\vec{B} = \nabla \times \vec{B} \tag{B.38}$$

Taking the curl of both sides yields

$$\nabla \times k_0\vec{B} = \nabla \times \nabla \times \vec{B}$$

$$k_0\nabla \times \vec{B} = -\nabla^2\vec{B}$$

$$\nabla^2\vec{B} + k_0^2\vec{B} = 0$$

which matches Equation (B.36) and confirms the assumption of Equation (B.38). Expanding the Laplacian in Equation (B.36) for the z-component,

$$\frac{\partial^2 B_z}{\partial r^2} + \frac{1}{r}\frac{\partial B_z}{\partial r} + \frac{1}{r^2}\frac{\partial^2 B_z}{\partial \theta^2} + \frac{\partial^2 B_z}{\partial z^2} + k_0^2 B_z = 0 \qquad \text{(B.39)}$$

From the definition of B,

$$\frac{\partial^2 B_z}{\partial \theta^2} = -m^2 B_z$$

$$\frac{\partial^2 B_z}{\partial z^2} = -k^2 B_z$$

Substituting this into Equation (B.39) and denoting all radial derivatives of B with a prime,

$$B_z'' + \frac{1}{r}B_z' + \left(-\frac{m^2}{r^2} + \alpha^2 - k^2\right)B_z = 0$$

$$B_z'' + \frac{1}{r}B_z' + \left(T^2 - \frac{m^2}{r^2}\right)B_z = 0 \qquad \text{(B.40)}$$

where T is the transverse wavenumber defined as

$$T^2 \equiv k_0^2 - k^2$$

Equation (B.40) is identical to Equation (A.12) solved earlier. What has changed is that k is much larger than k_0 which makes the transverse wave number imaginary.

$$T^2 \equiv k_0^2 - k^2 = -T_3^2$$

$$T_3 \equiv \sqrt{k^2 - k_0^2}$$

$$T = iT_3$$

Here the subscript of three to refers to the vacuum gap, while one and two still refer to the helicon and TG wave solutions, respectively. Equation (B.40) is thus Bessel's equation with an imaginary argument, the solution of which is

$$B_z = C_1 I_m(T_3 r) + C_2 K_m(T_3 r)$$

For the vacuum gap case, we need a solution that is finite (specifically zero) as r goes to infinity, in which case only the second term is applicable. This results in the solution

$$B_z = C_3 K_m(T_3 r) \tag{B.41}$$

where K_m is the modified Bessel function of the second kind of order m. This solution is similar to the ones already seen for B_z with a slight change due to the nature of the transverse wavenumber. Expanding the curl of B in Equation (B.38) yields

$$k_0 \vec{B} = \nabla \times \vec{B}$$

$$k_0 B_r = \frac{1}{r} \frac{\partial B_z}{\partial \theta} - \frac{\partial B_\theta}{\partial z}$$

$$k_0 B_r = \frac{1}{r} im B_z - ik B_\theta \tag{B.42}$$

$$k_0 B_\theta = \frac{\partial B_r}{\partial z} - \frac{\partial B_z}{\partial r}$$

$$k_0 B_\theta = ik B_r - \frac{\partial B_z}{\partial r} \tag{B.43}$$

Substituting (B.43) into (B.42) gives the following.

$$k_0 B_r = \frac{1}{r} im B_z - \frac{ik}{k_0}\left(ik B_r - \frac{\partial B_z}{\partial r} \right)$$

$$k_0^2 B_r = \frac{k_0}{r} im B_z + k^2 B_r + ik \frac{\partial B_z}{\partial r}$$

$$\left(k_0^2 - k^2\right) B_r = i\left(\frac{k_0 m}{r} B_z + k \frac{\partial B_z}{\partial r} \right)$$

$$-T_3^2 B_r = i\left(\frac{k_0 m}{r} B_z + k \frac{\partial B_z}{\partial r} \right)$$

$$B_r = -\frac{iC_{3,3}}{T_3^2}\left(\frac{k_0 m}{r} K_m(T_3 r) + k K_m'(T_3 r) \right) \tag{B.44}$$

Substituting (B.42) into (B.43) results in

$$k_0 B_\theta = \frac{ik}{k_0}\left(\frac{1}{r} im B_z - ik B_\theta \right) - \frac{\partial B_z}{\partial r}$$

$$k_0^2 B_\theta = -\frac{mk}{r} B_z + k^2 B_\theta - k_0 \frac{\partial B_z}{\partial r}$$

$$\left(k_0^2 - k^2\right) B_\theta = -\left(\frac{mk}{r} B_z + k_0 \frac{\partial B_z}{\partial r}\right)$$

$$B_\theta = \frac{C_{3,3}}{T_3^2}\left(\frac{mk}{r} K_m\left(T_3 r\right) + k_0 K_m'\left(T_3 r\right)\right) \tag{B.45}$$

A distinction to note between Equations (B.25) and (B.26) and those above is the presence of an additional negative due to the definition of T_3. The recurrence relations for the modified Bessel function of the second kind are

$$\zeta_m K_m'\left(T_3 r\right) = \frac{T_3}{2}\left(\zeta_{m-1} K_{m-1}\left(T_3 r\right) - \zeta_{m+1} K_{m+1}\left(T_3 r\right)\right)$$

$$\zeta_m K_m\left(T_3 r\right) = \frac{T_3 r}{2m}\left(\zeta_{m-1} K_{m-1}\left(T_3 r\right) - \zeta_{m+1} K_{m+1}\left(T_3 r\right)\right)$$

where

$$\zeta_m = e^{m\pi i} = \left(-1\right)^m$$

Simplifying the above results in

$$K_m'\left(T_3 r\right) = -\frac{T_3}{2}\left(K_{m-1}\left(T_3 r\right) + K_{m+1}\left(T_3 r\right)\right) \tag{B.46}$$

$$K_m(T_3 r) = -\frac{T_3 r}{2m}(K_{m-1}(T_3 r) - K_{m+1}(T_3 r)) \tag{B.47}$$

Substituting Equations (B.46) and (B.47) into (B.44) and (B.45),

$$B_{r,3} = -\frac{iC_{3,3}}{T_3^2}\left[-\frac{k_0 m}{r}\frac{T_3 r}{2m}(K_{m-1}(T_3 r) - K_{m+1}(T_3 r)) - \frac{T_3 k}{2}(K_{m-1}(T_3 r) + K_{m+1}(T_3 r))\right]$$

$$B_{r,3} = \frac{iC_{3,3}}{2T_3}\left[k_0(K_{m-1}(T_3 r) - K_{m+1}(T_3 r)) + k(K_{m-1}(T_3 r) + K_{m+1}(T_3 r))\right]$$

$$B_{r,3} = \frac{iC_{3,3}}{2T_3}\left[(k_0 + k)K_{m-1}(T_3 r) - (k_0 - k)K_{m+1}(T_3 r)\right] \tag{B.48}$$

$$B_{\theta,3} = \frac{C_{3,3}}{T_3^2}\left[-\frac{mk}{r}\frac{T_3 r}{2m}(K_{m-1}(T_3 r) - K_{m+1}(T_3 r)) - k_0\frac{T_3}{2}(K_{m-1}(T_3 r) + K_{m+1}(T_3 r))\right]$$

$$B_{\theta,3} = -\frac{C_{3,3}}{2T_3}\left[k(K_{m-1}(T_3 r) - K_{m+1}(T_3 r)) + k_0(K_{m-1}(T_3 r) + K_{m+1}(T_3 r))\right]$$

$$B_{\theta,3} = -\frac{C_{3,3}}{2T_3}\left[(k_0 + k)K_{m-1}(T_3 r) + (k_0 - k)K_{m+1}(T_3 r)\right] \tag{B.49}$$

B.4 Boundary Conditions

To summarize the above findings, there are two regions of interest: the discharge chamber ($r < a$) that contains the plasma and the vacuum gap ($r > a$) where it is assumed that no plasma exists. In the discharge chamber there are two possible solutions that correspond to the helicon wave and the TG wave, while the vacuum gap contains only

one possible solution for the RF wave. These three solutions are given the indices of one, two, and three respectively. The two quantities of interest are β_1 and β_2, which can be used in Equation (B.20) to relate the plasma properties to device parameters and operating conditions. Reintroducing the definition of the amplitude of the wave as

$$A_j = \frac{iC_{3,j}}{2T_j} \tag{B.50}$$

the unknown quantities at this point are β_1, β_2, and the three A_j values.

To solve for the above quantities, boundary conditions must be introduced. The insulating boundary condition for the wall of the discharge chamber still applies, but the presence of multiple waves requires additional boundary conditions. Three additional boundary conditions are set by the continuity of the radial, azimuthal, and axial magnetic fields through the insulating boundary. The insulating boundary condition requires that

$$j_r \mid_{r=a} = 0 \tag{B.51}$$

Substituting the definition of the current density into Equation (B.51) and taking into account the presence of two possible waves yields

$$\left(j_{r,1} + j_{r,2} \right)\mid_{r=a} = 0$$

$$\frac{\beta_1}{\mu_0} B_{r,1} + \frac{\beta_2}{\mu_0} B_{r,2} = 0$$

$$\beta_1 B_{r,1} + \beta_2 B_{r,2} = 0 \tag{B.52}$$

Together the four boundary conditions require that

$$\left(\beta_1 B_{r,1} + \beta_2 B_{r,2}\right)\big|_{r=a} = 0 \tag{B.52}$$

$$\left(B_{r,1} + B_{r,2}\right)\big|_{r=a} = B_{r,3}\big|_{r=a} \tag{B.53}$$

$$\left(B_{\theta,1} + B_{\theta,2}\right)\big|_{r=a} = B_{\theta,3}\big|_{r=a} \tag{B.54}$$

$$\left(B_{z,1} + B_{z,2}\right)\big|_{r=a} = B_{z,3}\big|_{r=a} \tag{B.55}$$

Substituting Equations (B.24), (B.28), (B.29), (B.41), (B.48), and (B.49) into the above four boundary conditions results in

$$\beta_1 A_1 Z_1^+ + \beta_2 A_2 Z_2^+ = 0 \tag{B.56}$$

$$A_1 Z_1^+ + A_2 Z_2^+ = A_3 Z_3^- \tag{B.57}$$

$$A_1 Z_1^- + A_2 Z_2^- = A_3 Z_3^+ \tag{B.58}$$

$$T_1 A_1 J_m\left(T_1 a\right) + T_2 A_2 J_m\left(T_2 a\right) = T_3 A_3 K_m\left(T_3 a\right) \tag{B.59}$$

where

$$Z_j^{\pm} = \left(\beta_j + k\right)J_{m-1}\left(T_j a\right) \pm \left(\beta_j - k\right)J_{m+1}\left(T_j a\right) \tag{B.60}$$

For $j = 3$, β goes to k_0 and J goes to K. From Equation (B.56),

$$A_2 = -A_1 \frac{\beta_1 Z_1^+}{\beta_2 Z_2^+} \tag{B.61}$$

Substituting Equation (B.61) into (B.57),

$$A_3 Z_3^- = A_1 Z_1^+ + A_2 Z_2^+$$

$$A_3 Z_3^- = A_1 Z_1^+ - A_1 \frac{\beta_1 Z_1^+}{\beta_2}$$

$$A_3 = A_1 \frac{Z_1^+}{Z_3^-} \left(1 - \frac{\beta_1}{\beta_2}\right) \tag{B.62}$$

Substituting Equations (B.61) and (B.62) into (B.58),

$$A_1 Z_1^- + A_2 Z_2^- = A_3 Z_3^+$$

$$A_1 Z_1^- - A_1 \frac{\beta_1 Z_1^+}{\beta_2 Z_2^+} Z_2^- = A_1 \frac{Z_1^+}{Z_3^-}\left(1 - \frac{\beta_1}{\beta_2}\right) Z_3^+$$

$$Z_1^- - \frac{\beta_1 Z_1^+ Z_2^-}{\beta_2 Z_2^+} = \frac{Z_1^+ Z_3^+}{Z_3^-}\left(1 - \frac{\beta_1}{\beta_2}\right) \tag{B.63}$$

Similarly, substituting Equations (B.61) and (B.62) into (B.59) yields

$$T_1 A_1 J_m(T_1 a) + T_2 A_2 J_m(T_2 a) = T_3 A_3 K_m(T_3 a)$$

$$T_1 A_1 J_m(T_1 a) - T_2 A_1 \frac{\beta_1 Z_1^+}{\beta_2 Z_2^+} J_m(T_2 a) = T_3 A_1 \frac{Z_1^+}{Z_3^-}\left(1 - \frac{\beta_1}{\beta_2}\right) K_m(T_3 a)$$

$$T_1 J_m(T_1 a) - T_2 \frac{\beta_1 Z_1^+}{\beta_2 Z_2^+} J_m(T_2 a) = T_3 \frac{Z_1^+}{Z_3^-}\left(1 - \frac{\beta_1}{\beta_2}\right) K_m(T_3 a) \qquad (B.64)$$

Equations (B.63) and (B.64) combined with Equation (B.60) and the definition of T thus define the value of β_1 and β_2 in terms of the device geometry. The two equations are nonlinear equations that cannot be solved analytically but instead must be solved numerically for a given device configuration. Once these values are calculated they can be substituted into Equation (B.20) to generate the plasma dispersion relation for both the helicon and the TG waves.

APPENDIX C

DERIVATION OF GENERAL SHEATH EQUATION

The convention for potential, φ, used is that in the bulk plasma the plasma potential is the zero point. Quantitatively, at $x = 0$, $\varphi = 0$. Beginning with Poisson's equation,

$$\frac{d^2\phi}{dx^2} = -\frac{e}{\varepsilon_0}\left(n_i - n_e\right) \tag{C.1}$$

where ε_0 is the permittivity of free space, e is the charge of an electron, n_i is the ion number density, and n_e is the electron number density. The electron number density is proportional to the exponential of the potential, given as

$$n_e = n_0 \exp\left(\frac{e\phi}{k_b T_e}\right) \tag{C.2}$$

where k_b is Boltzmann's constant, and n_0 and T_e is the electron number density and the electron temperature of the bulk plasma, respectively. The ion number density at a certain potential in the sheath is determined by ion continuity from the sheath boundary ion flux.

$$n_s v_{Bohm} = n_i(\phi) v_i(\phi) \tag{C.3}$$

The sheath boundary values are

$$n_s = n_0 \exp\left(\frac{e\phi_{Bohm}}{k_b T_e}\right) \tag{C.4}$$

$$v_{Bohm} = \left(-\frac{2e\phi_{Bohm}}{m_i}\right)^{\frac{1}{2}} \tag{C.5}$$

$$\phi_{Bohm} = -\frac{kT_e}{2e} \tag{C.6}$$

Assuming that the ions in the bulk plasma have negligible thermal velocity, the velocity of the ions at a given potential is found using conservation of energy,

$$\frac{1}{2}m_i v_i^2 = -e\phi \tag{C.7}$$

which when substituted into Equation (C.3) results in

$$n_i = 0.61n_0\left(\frac{\phi_{Bohm}}{\phi}\right)^{\frac{1}{2}} \tag{C.8}$$

Substitution of Equations (C.2) and (C.8) into (C.1) yields the second differential of the sheath equation.

$$\frac{d^2\phi}{dx^2} = -\frac{en_0}{\varepsilon_0}\left[0.61\left(\frac{\phi_{Bohm}}{\phi}\right)^{1/2} - \exp\left(\frac{e\phi}{k_bT_e}\right)\right] \tag{C.9}$$

Equation (C.9) can be non-dimensionalized by using the following substitutions.

$$\chi \equiv \frac{-e\phi}{k_bT_e} \tag{C.10}$$

$$\chi_{Bohm} \equiv \frac{-e\phi_{Bohm}}{k_bT_e} \tag{C.11}$$

$$\xi \equiv \frac{x}{\lambda_D} = x\left(\frac{n_0e^2}{\varepsilon_0 k_bT_e}\right)^{1/2} \tag{C.12}$$

The substitution of the second derivative of the potential is done using the Chain Rule.

$$\frac{\partial\phi}{\partial x} = \frac{\partial\phi}{\partial\chi}\frac{\partial\chi}{\partial\xi}\frac{\partial\xi}{\partial x}$$

$$\frac{\partial^2\phi}{\partial x^2} = \left(\frac{\partial}{\partial x}\frac{\partial\phi}{\partial\chi}\right)\frac{\partial\chi}{\partial\xi}\frac{\partial\xi}{\partial x} + \left(\frac{\partial}{\partial x}\frac{\partial\chi}{\partial\xi}\right)\frac{\partial\phi}{\partial\chi}\frac{\partial\xi}{\partial x} + \left(\frac{\partial}{\partial x}\frac{\partial\xi}{\partial x}\right)\frac{\partial\phi}{\partial\chi}\frac{\partial\chi}{\partial\xi}$$

$$\frac{\partial^2\phi}{\partial x^2} = \left(\frac{\partial}{\partial x}\frac{-k_bT_e}{e}\right)\frac{\partial\chi}{\partial\xi}\frac{\partial\xi}{\partial x} + \left(\frac{\partial\xi}{\partial x}\frac{\partial}{\partial\xi}\frac{\partial\chi}{\partial\xi}\right)\frac{\partial\phi}{\partial\chi}\frac{\partial\xi}{\partial x} + \left(\frac{\partial}{\partial x}\frac{1}{\lambda_D}\right)\frac{\partial\phi}{\partial\chi}\frac{\partial\chi}{\partial\xi}$$

$$\frac{\partial^2\phi}{\partial x^2} = \left(\frac{\partial\xi}{\partial x}\frac{\partial}{\partial\xi}\frac{\partial\chi}{\partial\xi}\right)\frac{\partial\phi}{\partial\chi}\frac{\partial\xi}{\partial x}$$

$$\frac{\partial^2\phi}{\partial x^2} = -\left(\frac{1}{\lambda_D}\frac{\partial^2\chi}{\partial\xi^2}\right)\frac{k_bT_e}{e}\frac{1}{\lambda_D} \tag{C.13}$$

Substituting Equations (C.10) through (C.13) into (C.9) yields

$$-\frac{k_b T_e}{e\lambda_D^2}\frac{d^2\chi}{d\xi^2} = -\frac{en_0}{\varepsilon_0}\left(0.61\left(\frac{\chi_{Bohm}}{\chi}\right)^{1/2} - \exp(-\chi)\right)$$

$$\frac{\partial^2\chi}{\partial\xi^2} = \left(0.61\left(\frac{\chi_{Bohm}}{\chi}\right)^{1/2} - \exp(-\chi)\right) \qquad\qquad (C.14)$$

Multiplying both sides by the first derivative of χ and integrating yields

$$\frac{\partial\chi}{\partial\xi}\frac{\partial^2\chi}{\partial\xi^2} = \left(0.61\frac{\partial\chi}{\partial\xi}\left(\frac{\chi_{Bohm}}{\chi}\right)^{1/2} - \frac{\partial\chi}{\partial\xi}\exp(-\chi)\right)$$

$$\frac{1}{2}\frac{\partial}{\partial\xi}\left(\frac{\partial\chi}{\partial\xi}\right)^2 = \left(1.21\frac{\partial}{\partial\xi}\sqrt{\chi\chi_{Bohm}} + \frac{\partial}{\partial\xi}\exp(-\chi)\right)$$

$$\int_0^\xi\frac{1}{2}\frac{\partial}{\partial\xi}\left(\frac{\partial\chi}{\partial\xi}\right)^2 = \int_0^\xi\left(1.21\frac{\partial}{\partial\xi}\sqrt{\chi\chi_{Bohm}} + \frac{\partial}{\partial\xi}\exp(-\chi)\right)$$

$$\frac{1}{2}\left(\frac{\partial\chi}{\partial\xi}\right)^2\bigg|_0^\xi = 1.21\sqrt{\chi\chi_{Bohm}}\bigg|_0^\xi + \exp(-\chi)\big|_0^\xi$$

The bulk plasma has no electric fields, which makes the first derivative of the potential zero at $x = 0$. Furthermore, by convention φ, and thus χ, is zero at $x = 0$.

$$\left(\frac{\partial\chi}{\partial\xi}\right)^2 = 2.42\sqrt{\chi\chi_{Bohm}} + 2\exp(-\chi) - 2$$

$$\frac{\partial \chi}{\partial \xi} = \left(2.42\sqrt{\chi\chi_{Bohm}} + 2\exp(-\chi) - 2\right)^{\frac{1}{2}} \qquad (C.15)$$

Further integration must be done numerically to resolve the potential.

APPENDIX D

RF SYSTEM DESIGN

The purpose of the RF system is to generate an alternating voltage across the antenna that will propagate RF waves into the helicon discharge chamber. The RF system consists of a Yaesu FT-540 high frequency transceiver to produce the RF signal, an ACOM 2000a linear amplifier to increase the signal power, an LP-100 power meter to monitor the output power, a pi-type matching network for tuning the system, the antenna to transmit the signal into the plasma, and the RF transmission line to connect the components. The transceiver and amplifier are selected to provide the desired frequency and power of the RF signal, while the antenna design is set by the size of the discharge chamber and the frequency of the RF wave to be propagated. The matching network and the transmission line both require additional design, as the former must account for the interaction of the latter with the rest of the system.

D.1 Transmission Lines

Generally speaking, a transmission line is a device designed to transfer energy from one point to another. Specifically, for RF applications a transmission line is a device to propagate an electromagnetic wave within a controlled medium. One of the key design requirements of RF systems is the transfer of an RF signal from the source to the load without contaminating other devices. Therefore, one of the requirements of a transmission line is to contain the RF signal such that there is negligible far-field

radiation. Another desired attribute of a transmission line is to minimize thermal losses that could decrease transmission efficiency.

D.1.1 Overview of Transmission Lines

From a general perspective, there are two categories of transmission lines: those capable of transmitting transverse electromagnetic (TEM) waves and those that transmit only higher-order wave modes. TEM waves are characterized by the electric and magnetic fields being orthogonal to the direction of propagation; in the higher-order propagation one or both of the components of the wave is in the direction of propagation. In the vernacular of RF system design, "transmission line" usually refers to the propagation of TEM waves, while the higher order modes are propagated by devices called waveguides. Waveguides are outside the scope of this work and are neglected for the sake of brevity; therefore, the use of "transmission line" will refer only to those devices capable of transmitting TEM waves and not to waveguides.

The most basic theoretical transmission line is a system of two infinite parallel plates, shown in Figure 143. When viewed along the axis of propagation, the electric field lines are orthogonal to the plates, while the magnetic field lines are parallel to the plates. In this configuration the wave propagates in part through the medium between the plates, be it vacuum or some dielectric material. Since TEM waves are a subset of plane waves, the components of the wave will extend into the plates and propagate through a portion of the plates adjacent to the intervening medium. As the field penetrates a distance x, it is attenuated by the conductive material according to Equation (D.1).

E lines

B lines
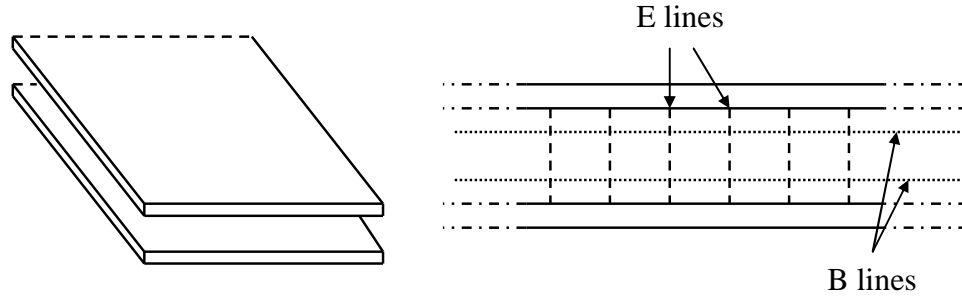
Figure 143. Infinite parallel-plate transmission line.

$$E(x) = E_0 \exp\left(-\sqrt{\frac{\omega\mu\sigma}{2}}\,x\right)\exp\left(-i\sqrt{\frac{\omega\mu\sigma}{2}}\,x\right) \qquad \text{(D.1)}$$

In the above equation, ω is the angular frequency of the signal, μ is the permeability of the conductor, and σ is the conductivity of the conductor. Furthermore, x is defined such that x is zero at the surface of the conductor with a field strength of E_0. The skin depth is defined as

$$\delta = \sqrt{\frac{2}{\omega\mu\sigma}} = \frac{1}{\sqrt{f\pi\mu\sigma}} \qquad \text{(D.2)}$$

Substituting Equation (D.2) into (D.1) yields

$$E(x) = E_0 \exp\left(-\frac{x}{\delta}\right)\exp\left(-i\frac{x}{\delta}\right) \qquad \text{(D.3)}$$

Thus when the wave has propagated a distance of δ, the amplitude of the field has decreased by a factor of 1/e. Since the current density is related to the electric field,

$$J = \sigma E$$

$$J(x) = J_0 \exp\left(-\frac{x}{\delta}\right) \exp\left(-i\frac{x}{\delta}\right) \tag{D.4}$$

The current per unit width, I', of the transmission line can be calculated as

$$I' = \int_0^\infty |J(x)| dx$$

$$I' = J_0 \int_0^\infty \exp\left(-\frac{x}{\delta}\right) dx$$

$$I' = J_0 \delta \tag{D.5}$$

While the field will penetrate into the conductor beyond the skin depth, the effective area for conducting current is a layer of material with thickness δ. Since the skin depth is inversely proportional to the frequency, at higher frequencies a smaller portion of the conductor is used to carry the current. This effect causes the resistance to be larger compared to the DC resistance. For example, a square sheet of conducting material has a resistance of

$$R_{AC} = \frac{1}{\sigma\delta} \tag{D.6}$$

D.1.2 Characteristic Impedance

The transmission line in Figure 143 is an idealized abstraction, but every transmission line contains two conductors to propagate the signal. The interaction between the two conductors gives rise to a capacitance and inductance between them. If the line is not lossless, it will also have a resistance along each conductor and a shunt conductance between the two that must be considered. The net effect of these components is to create an impedance through the line. Assuming the characteristics of the transmission line do not change along the length of the line, this impedance can be represented by a characteristic impedance of the line. To demonstrate this, suppose one examines an infinitesimal segment of the transmission line from Figure 143 that is carrying a harmonically varying wave. As a current I passes through a small segment of the line dx, a small voltage drop of dV will exist across the segment. At the same time a, voltage drop V exists between the two conductors that drives the signal. Figure 144 shows an illustration of the transmission line segment.
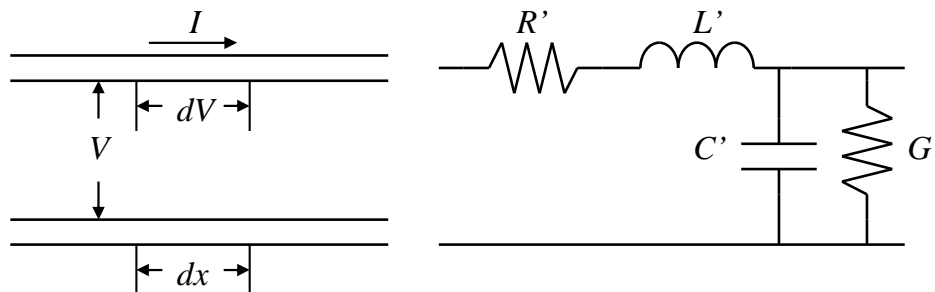
Figure 144. Differential element of a two-conductor transmission line (*left*), and corresponding circuit diagram (*right*).

The series impedance per unit length of the segment is determined by the line resistance, R', and the inductance, L', expressed as

$$Z' = R' + i\omega L' \tag{D.7}$$

The shunt conductance, *G'*, and the capacitance, *C'*, determine the shunt admittance, defined as

$$Y' = G' + i\omega C' \tag{D.8}$$

In both Equation (D.7) and (D.8) the transmission line characteristics are per unit length. The voltage drop *dV* across the segment is then

$$dV = IZ'dx$$

$$\frac{dV}{dx} = IZ' \tag{D.9}$$

Likewise, the current *dI* passed between the two conductors is

$$dI = VY'dx$$

$$\frac{dI}{dx} = VY' \tag{D.10}$$

Differentiating both Equation (D.9) and (D.10) with respect to *x* yields

$$\frac{d^2V}{dx^2} = I\frac{dZ'}{dx} + Z'\frac{dI}{dx}$$

$$\frac{d^2V}{dx^2} = I\frac{dZ'}{dx} + Z'VY' \qquad (D.11)$$

$$\frac{d^2I}{dx^2} = V\frac{dY'}{dx} + Y'\frac{dV}{dx}$$

$$\frac{d^2I}{dx^2} = V\frac{dY'}{dx} + Y'IZ' \qquad (D.12)$$

Since the transmission line is assumed to be uniform across its length, the derivatives of Y' and Z' with respect to x are zero. Equations (D.11) and (D.12) then reduce to

$$0 = \frac{d^2V}{dx^2} - Z'VY' \qquad (D.13)$$

$$0 = \frac{d^2I}{dx^2} - Y'IZ' \qquad (D.14)$$

Equations (D.13) and (D.14) are the basic wave equations for a transmission line, which form a system of two second-order ordinary differential equations. Assuming a solution for Equation (D.13) of the form

$$V = e^{\gamma x} \qquad (D.15)$$

Substituting Equation (D.15) into (D.13) yields

$$0 = \gamma^2 e^{\gamma x} - Z'Y'e^{\gamma x}$$

$$0 = \left(\gamma^2 - Z'Y'\right)e^{\gamma x}$$

$$0 = \gamma^2 - Z'Y'$$

$$\gamma = \pm\sqrt{Z'Y'} \tag{D.16}$$

Since there are two roots, the general form of the solution is

$$V = C_1 \exp\left(\sqrt{Z'Y'}x\right) + C_2 \exp\left(-\sqrt{Z'Y'}x\right) \tag{D.17}$$

Equation (D.14) could be solved in a similar fashion, but this would result in two additional constants. Instead, Equation (D.17) can be differentiated with respect to x and substituted into Equation (D.9)

$$I = \frac{1}{Z'}\frac{dV}{dx}$$

$$I = \frac{C_1}{\sqrt{Z'/Y'}}\exp\left(\sqrt{Z'Y'}x\right) - \frac{C_2}{\sqrt{Z'/Y'}}\exp\left(-\sqrt{Z'Y'}x\right) \tag{D.18}$$

In order to determine the constants C_1 and C_2, Equation (D.17) is evaluated at the boundary condition of $x = 0$, yielding

$$V\mid_{x=0} = C_1 + C_2 \tag{D.19}$$

In general, the voltage on the line is actually the sum of two harmonically varying voltages of unequal amplitudes, V_1 and V_2. Thus the constants C_1 and C_2 can be considered as corresponding to the voltages V_1 and V_2. Since the constants are independent of x, but are harmonically varying with respect to time, they can be written as

$$C_k = V_k e^{i\omega t} \tag{D.20}$$

where k is either 1 or 2. Substituting (D.20) into Equations (D.17) and (D.18) yields

$$V = V_1 e^{i\omega t} \exp\left(\sqrt{Z'Y'}\,x\right) + V_2 e^{i\omega t} \exp\left(-\sqrt{Z'Y'}\,x\right) \tag{D.21}$$

$$I = \frac{V_1 e^{i\omega t}}{\sqrt{Z'/Y'}} \exp\left(\sqrt{Z'Y'}\,x\right) - \frac{V_2 e^{i\omega t}}{\sqrt{Z'/Y'}} \exp\left(-\sqrt{Z'Y'}\,x\right) \tag{D.22}$$

Revisiting Equation (D.16), γ is the propagation constant and is a complex quantity. The real part is called the attenuation constant, α, and the imaginary part is called the phase constant, β. The propagation constant can thus be written as

$$\gamma = \sqrt{Z'Y'} = \alpha + i\beta \tag{D.23}$$

Substituting α and β into Equations (D.21) and (D.22) yields

$$V = V_1 e^{\alpha x} e^{i(\omega t + \beta x)} + V_2 e^{-\alpha x} e^{i(\omega t - \beta x)} \tag{D.24}$$

$$I = \frac{V_1}{\sqrt{Z'/Y'}} e^{\alpha x} e^{i(\omega t + \beta x)} - \frac{V_2}{\sqrt{Z'/Y'}} e^{-\alpha x} e^{i(\omega t - \beta x)} \tag{D.25}$$

From Equations (D.24) and (D.25) it can be seen that the voltage and current are set by two waves propagating through the transmission line. The difference in sign of the $e^{\alpha + i\beta}$ terms between the two waves signifies that the waves propagate in opposite directions along x. The first term in both equations corresponds to a wave propagating in the negative x direction, while the second term corresponds to a wave propagating in the positive x direction. Additionally, each wave has two exponential factors, one corresponding to the attenuation constant, and the other corresponding to the phase constant. The different sign of the attenuation constant between the two waves means that the first wave decreases in amplitude as it propagates in the negative x direction, and the second wave increases in amplitude as it propagates in the positive x direction.

To return to the original intent, the characteristic impedance is the ratio of the voltage across the line to the current passed for a single wave. Taking the first wave of Equations (D.24) and (D.25) this results in

$$Z_0 = \frac{V}{I} = \sqrt{\frac{Z'}{Y'}} \tag{D.26}$$

Recalling Equations (D.7) and (D.8), the definitions of Z' and Y' can be substituted into Equation (D.26).

$$Z_0 = \sqrt{\frac{R' + i\omega L'}{G' + i\omega C'}} \qquad \text{(D.27)}$$

In general the characteristic impedance is complex. If *R'* and *G'* are small, or if the frequency is large such that *ωL' >> R'* and *ωC' >> G'* then Equation (D.27) reduces to

$$Z_0 = \sqrt{\frac{L'}{C'}} \qquad \text{(D.28)}$$

In this case, the characteristic impedance is real and can be thought of as a characteristic resistance, but in general it is still referred to as an impedance. When the characteristic impedance is real, the line is considered lossless. If *R'* and *G'* are small but not negligible, Equation (D.27) can be approximated as

$$Z_0 = \sqrt{\frac{L'}{C'}} \left[1 + i \left(\frac{G'}{2\omega C'} - \frac{R'}{2\omega L'} \right) \right] \qquad \text{(D.29)}$$

This reveals that there is a special case in which the line can still be considered lossless, which is called Heaviside's condition for a distortionless line.

$$\frac{G'}{C'} = \frac{R'}{L'}$$

The phase velocity of the wave through the transmission line is defined as

$$v_\phi = \frac{\omega}{\beta}$$ (D.30)

For a lossless line this simplifies to

$$v_\phi = \frac{1}{\sqrt{L'C'}}$$ (D.31)

The above derivation applies to any given transmission line, but the exact values for *L'* and *C'* are dependent on the geometry and material of the transmission line. While the infinite parallel plate transmission line is convenient for calculations, it is impractical for actual applications. Therefore, more realistic transmission line configurations will have to be considered.

D.1.3 Types of Transmission Lines

There are two primary geometric configurations for transmission lines that are derived from the parallel plates. Consider a transmission line made from finite parallel plates, shown in Figure 145 (a). Supposing one wished to change the geometry by bending the plates, there are two options: deflecting the plates in opposing or matching directions, shown in Figure 145 (b) and (c), respectively. Continuing until the boundaries of each plate closes, this results in either a two wire transmission line, Figure 145 (d), or a coaxial transmission line, Figure 145 (e). The two-wire line is commonly referred to as a "balanced line," as the configuration lends itself to having both lines carrying a voltage with respect to ground that is equal in magnitude, but opposite in polarity. The coaxial

line is referred to as an "unbalanced line," as the voltage drop between the center conductor and ground is equal to the voltage signal of the line, while the outer conductor is at approximately ground potential.
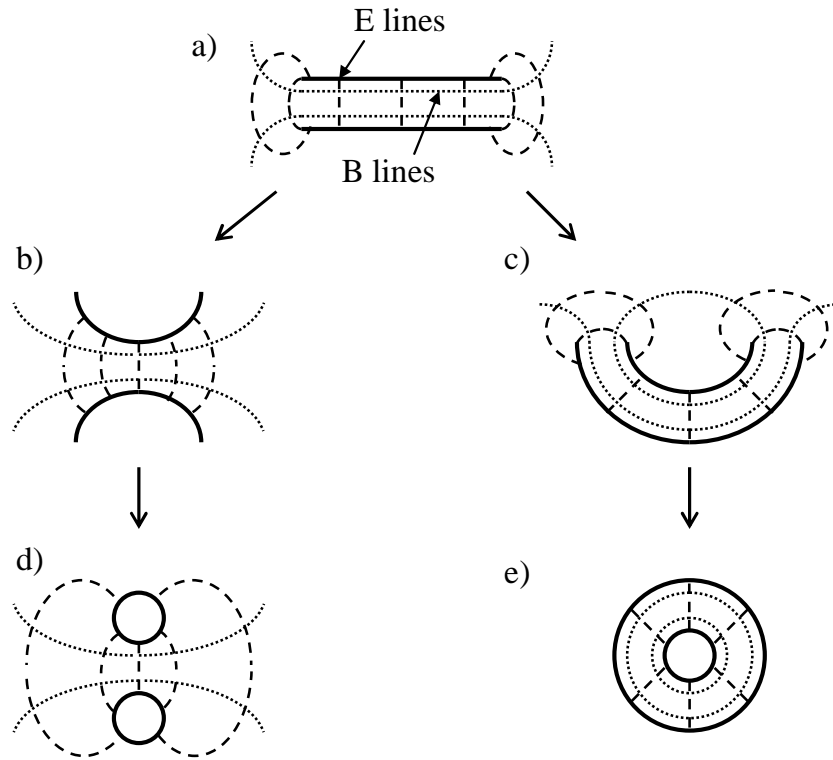
Figure 145. Transmission line evolution. a) parallel plate, b) plates deflected in opposing directions, c) plates deflected in the same direction, d) two wire line, e) coaxial line.

D.1.3.1 Balanced Transmission Lines

Recalling Equation (D.28), the characteristic impedance, for a lossless line, is a function of the series inductance and the shunt capacitance between the two inductors. With a specific geometry and line material this can be rewritten as

$$Z_0 = \frac{1}{\pi}\sqrt{\frac{\mu}{\varepsilon}}\ln\left(\frac{D}{2a}+\sqrt{\left(\frac{D}{2a}\right)^2-1}\right)$$

(D.32)

where D is the distance between the centers of the two conductors, a is the radius of the conductors, and μ and ε are the permeability and permittivity of the surrounding medium, respectively. This expression assumes that the line is lossless, or that the frequency is high enough such that the line can be considered lossless. A simplification can be made if the distance between the conductors is much larger than the radius of the conductors.

$$Z_0 = \frac{1}{\pi}\sqrt{\frac{\mu}{\varepsilon}}\ln\frac{D}{a} \qquad (D.33)$$
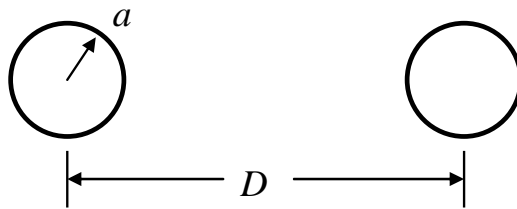
Figure 146. Balanced line geometry.

A key fact of RF system design, which will be explained in further detail in the next section, is that changes in impedance must be avoided to ensure optimal system performance. From Equation (D.33) it is seen that balanced lines are sensitive to the separation distance between the conductors. Should a section of the line undergo some geometric distortion, the impedance of that section would change and lead to an impedance mismatch and a corresponding loss of power. A common solution is to attach non-conducting supports between the two elements at an interval to constrain the separation distance. This configuration is referred to as a ladder line, although the support structure does not necessarily have to be confined to that shape. Some smaller ladder lines are constructed with an insulating plastic ribbon that connects along an

insulating sleeve covering each conductor. Another concern with balanced lines is that while for the far-field condition the line has negligible exterior power radiation, for the near-field this is not necessarily the case. This means that either the line must be placed away from other conductors and signal lines, or a grounded shield must be placed around the line.

D.1.3.2 Unbalanced Transmission Lines

The characteristic impedance of an unbalanced line is given by

$$Z_0 = \frac{1}{2\pi}\sqrt{\frac{\mu}{\varepsilon}}\ln\frac{b}{a} \qquad\qquad (D.34)$$

where a is the radius of the inner conductor, and b is the inner radius of the outer conductor. Again, μ and ε are the permeability and permittivity of the intervening medium between the conductors.
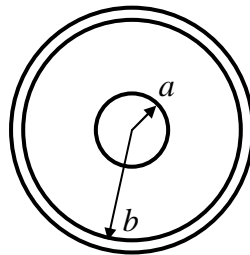
Figure 147. Unbalanced line geometry.

Like balanced lines, the impedance of the unbalanced line is sensitive to the separation distance between the inner and outer conductors. While it is possible to use a truss frame to constrain the geometry if a vacuum gap is desired, it is much more

common to fill the region with an insulating material such as nylon or Teflon. One practical consideration when using unbalanced lines is that the line is not bent through a small radius of curvature, as this would distort the shape of the line and lead to a change in impedance. Coaxial lines avoid the near-field radiation concerns by completely internalizing the interaction between the two conductors. Since a wave can only propagate into a medium an effective distance of the skin depth, only the inner region of the outer conductor passes the signal; the outer surface of the outer conductor carries no signal and acts as a shield.

D.1.4 Transmission Line Termination

In the discussion thus far, the transmission line has been treated as effectively infinite with no termination. Since the goal of a transmission line is to deliver an RF signal from the source to some load, the effects of connecting to this load must be considered. As has already been discussed, a signal propagating on a transmission line can be thought of as the sum of two travelling waves moving in opposite directions. The first is a forward, or incident, wave on the load and the other is a reflected wave towards the source, as shown in Figure 148.
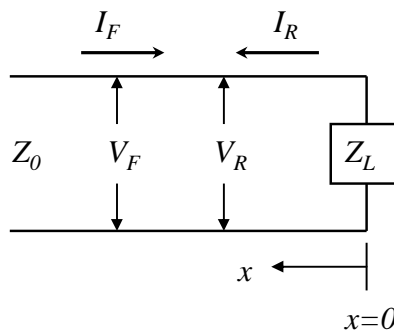
Figure 148. Transmission line termination.

Using Equation (D.24), the expressions for the waves can be written as

$$V_F = V_{F,0} e^{\gamma x} e^{i\omega t} \tag{D.35}$$

$$V_R = V_{R,0} e^{-\gamma x + i\zeta} e^{i\omega t} \tag{D.36}$$

where V_F is the voltage of the forward wave, V_R is the voltage of the reflected wave, and ζ is the phase shift between the two waves that occurs at the load. The reflection coefficient for voltage, ρ_v, is defined as

$$\rho_v = \left. \frac{V_R}{V_F} \right|_{x=0}$$

$$\rho_v = \frac{V_{R,0}}{V_{F,0}} e^{i\zeta} = \frac{V_{R,0}}{V_{F,0}} \angle \zeta \tag{D.37}$$

The net voltage at a point is thus

$$V = V_{F,0} \left(e^{\gamma x} + \rho_v e^{-\gamma x} \right) \tag{D.38}$$

Similarly, the current carried in the two component waves are defined as

$$I_F = I_{F,0} e^{\gamma x - i\varphi} e^{i\omega t} \tag{D.39}$$

$$I_R = I_{R,0} e^{-\gamma x + i(\zeta - \phi)} e^{i\omega t} \tag{D.40}$$

308

where φ is the phase difference between the current and the voltage. The reflection coefficient for the current, ρ_i, is

$$\rho_i = \frac{I_F}{I_R}\bigg|_{x=0}$$

$$\rho_i = \frac{I_{R,0}}{I_{F,0}} e^{i\zeta} = \frac{I_{R,0}}{I_{F,0}} \angle \zeta \tag{D.41}$$

The net current can then be expressed as

$$I = I_{F,0} e^{-i\varphi} \left(e^{\gamma x} - \rho_i e^{-\gamma x} \right) \tag{D.42}$$

The goal of this examination is to determine how the behavior of the wave changes with respect to the impedance of the line and the load. For any point on the transmission line

$$Z_0 = \frac{V_F}{I_F} = \frac{V_R}{I_R} \tag{D.43}$$

while at the load

$$Z_L = \frac{V}{I} \tag{D.44}$$

Separating the current into the two component waves,

309

$$\frac{V}{Z_L} = I$$

$$\frac{V}{Z_L} = I_F - I_R$$

$$\frac{V}{Z_L} = \frac{V_F}{Z_0} - \frac{V_R}{Z_0}$$

However, the net wave voltage is the sum of the two components, which leads to

$$\frac{V_R + V_F}{Z_L} = \frac{V_F - V_R}{Z_0}$$

Rearranging, this yields

$$\frac{V_R}{V_F} = \frac{Z_L - Z_0}{Z_L + Z_0} = \rho_v \qquad (D.45)$$

The above equation reveals a special case where the reflected wave is zero when the impedance of the load is the same as the impedance of the transmission line. It also shows that the reflection coefficient can range from -1 to 1 in value. Another parameter used to describe wave propagation through a transmission line is the voltage standing-wave ratio (VSWR, also referred to as simply the SWR).

$$SWR = \frac{V_{max}}{V_{min}}$$

$$SWR = \frac{V_{F,0} + V_{R,0}}{V_{F,0} - V_{R,0}} \tag{D.46}$$

The SWR can also be expressed in terms of the voltage reflection coefficient,

$$SWR = \frac{1 + \left(V_{R,0}/V_{F,0}\right)}{1 - \left(V_{R,0}/V_{F,0}\right)}$$

$$SWR = \frac{1 + |\rho_v|}{1 - |\rho_v|} \tag{D.47}$$

The SWR varies in value from one to infinity, where one corresponds to no reflection, and infinity corresponds to complete reflection. A large SWR can be problematic for two reasons. The first is that the reflected wave propagates back through the transmission line and is attenuated by the line impedance, which is dissipated as heat into the line. The second reason is a large voltage signal reflected back at the source could damage the equipment. Therefore it is highly advantageous to have the load impedance equal to the line impedance. However, in this particular application the load is often an antenna coupling to a plasma. Due to the potential for the plasma impedance to change as a function of the input power and other operational parameters, a fixed load impedance is not guaranteed. Therefore an additional device, called a matching network, must be included that can provide a variable impedance to ensure the load impedance matches the transmission line impedance.

D.1.5 Power Attenuation

While much of the discussion on transmission lines has assumed negligible power loss, in practice there is always some loss across a transmission line that should be taken into account. Line loss, sometimes referred to as cable loss, is the ratio of the power received at one end of the line to the power transmitted at the other end. The cable loss for a matched line, L_{ML}, is defined as

$$L_{ML} = \frac{P_{Rx}}{P_{Tx}}$$
(D.48)

where P_{Rx} is the received power and P_{Tx} is the transmitted power. It is most common to see the cable loss given in decibels.

$$L_{ML,dB} = 10\log\left(\frac{P_{Tx}}{P_{Rx}}\right)$$
(D.49)

This form of the cable loss is called the matched-line loss and assumes no reflected signal. If the SWR is greater than 1, the signal is further attenuated by a portion of the wave reflecting back towards the source before it returns. The mismatched-line loss is

$$L_{MML,dB} = 10\log\left(\frac{a^2 - \rho_v^2}{a - a\rho_v^2}\right)$$
(D.50)

where a is the matched line ratio, defined as

$$a = 10^{L_{ML,dB}/10} \tag{D.51}$$

One consideration to remember is that in Equation (D.47) the reflection coefficient is at the load. If a directional coupler is used to measure the SWR and is placed near the source, it will give an inaccurate reading because part of the reflected wave will be attenuated by the transmission line. In that situation the reflection coefficient at the source is given by

$$\rho_v = a \left| \frac{1 + SWR_s}{1 - SWR_s} \right| \tag{D.52}$$

where SWR_s is the SWR measured at the source.

D.2 Matching Networks

D.2.1 Impedance Matching

A key note from the previous section is maximum power transfer is achieved when the impedance of the source and the load are equal. When a change of impedance occurs, part of the signal is reflected back towards the source. Once at the source this signal is reflected again towards the load, eventually setting up a standing wave between the source and the load. This situation is undesirable for two reasons: a signal reflected repeatedly through the system passes through a longer distance of the transmission line which leads to increased power dissipation into the transmission line. The second reason is signals reflected back at the source can damage the amplifier or the transceiver. The

solution to this is to ensure that every component of the RF system has the same impedance. Most commercially available components, such as the transceiver, the amplifier, and the power meter, have impedances of 50 Ω. Transmission lines and associated fittings and feedthroughs also are available in various characteristic impedances, including 50 Ω. The one component that does not have a 50 Ω impedance is the antenna.

There are two approaches to designing an RF system that includes an antenna. The first is to design an antenna with a set impedance at a specific frequency of interest that matches the impedance of commercially available equipment. Since the impedance of the antenna changes as a function of frequency, this essentially limits the system to a single frequency, but ensures that there is no impedance mismatch. The second approach is to design a circuit network consisting of inductors and capacitors that, when connected in series with the antenna, creates an equivalent impedance that matches the rest of the system. If the components of this circuit network are tunable, this allows for a variable frequency system since the impedance of the circuit can be tuned as the impedance of the antenna changes with frequency.

As an example, suppose one wishes to match a 50 Ω source to a 2 Ω antenna, as shown in Figure 149. The simplest impedance matching circuit consists of a variable inductor in series with the antenna and a parallel variable capacitor shunt to ground. The placement of the shunt capacitor depends on the relative impedances of the source and the load, as the capacitor is always placed on the side of the inductor that has the higher impedance. In this example the shunt capacitor is placed on the source side of the inductor, as it has a higher impedance than the antenna.
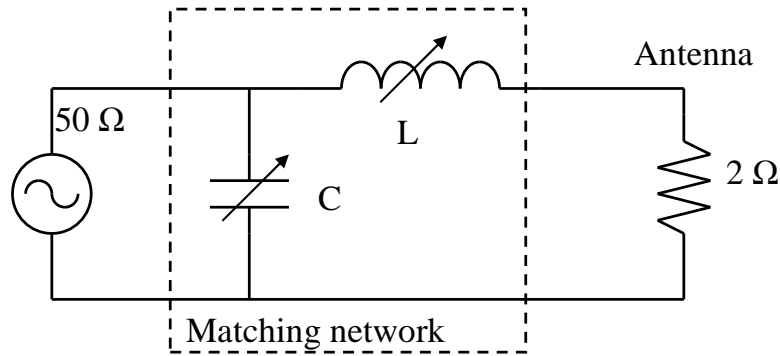
Figure 149. Example impedance matching.

The addition of the matching network serves to increase the equivalent impedance downstream of the source up to 50 Ω. The values of the capacitor and inductor needed to reach 50 Ω can be determined by summing the series impedance of the inductor and the antenna and combining it with the parallel impedance of the capacitor, shown below.

$$\frac{1}{Z_{eq}} = \frac{1}{Z_C} + \frac{1}{Z_A + Z_L}$$ (D.53)

Here Z denotes impedance, which can be complex. The impedance of the capacitor and inductor are

$$Z_C = \frac{-i}{\omega C}$$ (D.54)

$$Z_L = i\omega L$$ (D.55)

Note that since j is used to denote current density, the standard electrical engineering convention of denoting the imaginary component with j will be replaced with the mathematical convention of using i. Substituting these definitions into Equation (D.53),

$$\frac{1}{Z_{eq}} = i\omega C + \frac{1}{2 + i\omega L}$$

$$Z_{eq} = \frac{2 + i\omega L}{\left(1 - \omega^2 LC\right) + i\left(2\omega C\right)} \tag{D.56}$$

To solve the complex division, the numerator and denominator of Equation (D.56) are multiplied by the complex conjugate of the denominator.

$$Z_{eq} = \frac{2 + i\left(\omega L - \omega^3 L^2 C - 4\omega C\right)}{1 - 2\omega^2 LC + \omega^4 L^2 C^2 + 4\omega^2 C^2} \tag{D.57}$$

The goal of the matching network is to transform the load into a purely resistive impedance of 50 Ω. For complex impedances, the real component denotes resistive impedance, and the imaginary component denotes reactive impedance. For optimal performance, the imaginary component of Equation (D.57) must be zero, yielding

$$C = \frac{L}{\omega^2 L^2 + 4} \tag{D.58}$$

Substituting Equation (D.58) into (D.57) and the desired value of 50 for Z_{eq}, the value of L is found to be 0.115 µH. Substituting L into Equation (D.58), the value of C is 1,150 pF. Thus a 2 Ω load is matched to a 50 Ω source and power transfer efficiency is maximized.

D.2.2 Matching Network Types

There are many different configurations of impedance matching circuits, with the application of each one depending on relative impedances between the source and the load. The three outlined below are the ones most commonly seen in RF applications.

D.2.2.1 L-type:

The network depicted in Figure 149 is a simplified version of an L-type matching network with an idealized load. In a real application the antenna is not solely resistive, but instead consists of resistive, inductive, and capacitive components. The resistive load is caused by the finite length of the transmission line and the antenna, while the inductive load arises from the shape of the antenna. The capacitive component of the load is partially the stray capacitance between system elements, but also includes parasitic capacitance between the system and the surroundings. Furthermore, as had been mentioned in the example, there are two configurations for the network, depending on the relative impedances of the source and the load. A more complete representation of an L-type matching network is shown below in Figure 150 and Figure 151.
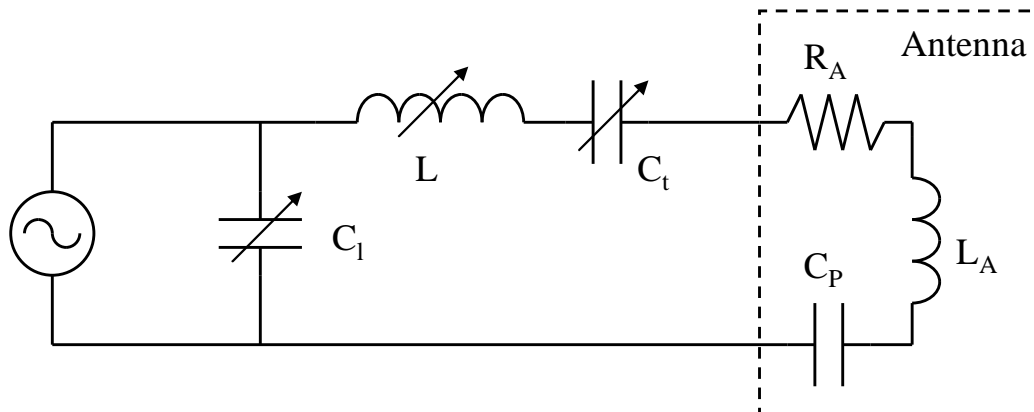
Figure 150. L-type matching network, $Z_A < Z_s$
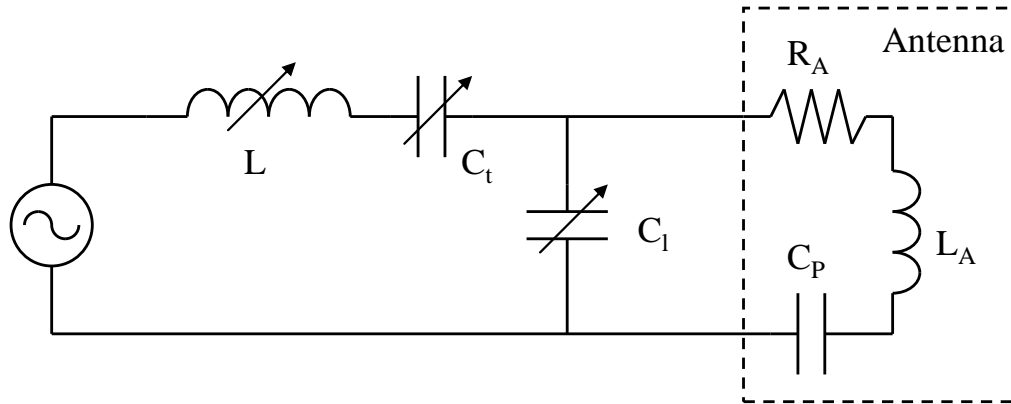
Figure 151. L-type matching network, $Z_A > Z_s$

In general L-type networks consist of an inductor and capacitor in series with the antenna and an additional shunt capacitor in parallel. The shunt capacitor is called the load capacitor, while the series capacitor is called the tuning capacitor. The origin of these names can be found by repeating the example from the previous section, but with the expanded L-type network. For the sake of simplicity, assume that L_A and C_p are both zero, and R_A is still 2 Ω. Additionally, instead of considering the load being tuned to the source impedance, it is the source that is tuned to the load impedance. Thus the circuit becomes as shown in Figure 152.
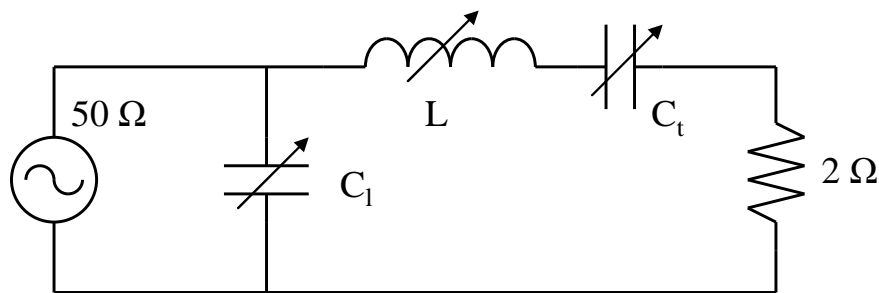
Figure 152. Example L-network revisited.

From the perspective that the 50 Ω source is being matched to the 2 Ω load, the circuit becomes the source in parallel with the load capacitor, with the combination of the

318

two in series with the inductor and the tuning capacitor. Hence, the equivalent impedance of the source and the matching network is given as

$$Z_{eq} = \frac{Z_s Z_{C,l}}{Z_s + Z_{C,l}} + Z_L + Z_{C,t} \qquad \text{(D.59)}$$

Here it is useful to consider the impedance as the sum of the resistive (real) and reactive (imaginary) components,

$$Z = R + iX$$

The inductive reactance and capacitive reactance are defined as

$$X_C = \frac{-1}{\omega C} \qquad \text{(D.60)}$$

$$X_L = \omega L \qquad \text{(D.61)}$$

Rewriting Equation (D.53) in terms of resistance and reactance yields

$$Z_{eq} = \frac{R_s i X_{C,l}}{R_s + i X_{C,l}} + iX_L + iX_{C,t}$$

$$Z_{eq} = \frac{R_s X_{C,l}^2}{R_s^2 + X_{C,l}^2} + i\left(\frac{R_s^2 X_{C,l}}{R_s^2 + X_{C,l}^2} + X_L + X_{C,t} \right) \qquad \text{(D.62)}$$

The important point to take from Equation (D.56) is that the only real component is the first term. Since from this perspective the equivalent impedance is being matched to 2 Ω of pure resistance, this results in a system of two equations:

$$R_A = \frac{R_s X_{C,l}^2}{R_s^2 + X_{C,l}^2} \tag{D.63}$$

$$0 = \frac{R_s^2 X_{C,l}}{R_s^2 + X_{C,l}^2} + X_L + X_{C,t} \tag{D.64}$$

Substituting the values for R_s and R_A into Equation (D.57) yields a load capacitance of 1,150 pF, which is the same value found previously. Thus for this perspective (matching to the load, rather than the source) the shunt capacitor sets the real component of the equivalent impedance to match the load, hence the name "load" capacitor. The tuning capacitor gets its name from the fact that it tunes the imaginary component of the equivalent impedance in conjunction with the inductor. Mathematically, Equation (D.64) cannot be solved, as there are two unknown variables. Since this kind of L network is over-controlled, only one component is theoretically needed. In practice the load is rarely purely resistive. Since inductive and capacitive elements have positive and negative reactances, respectively, a capacitor and an inductor are used to compensate for potential presence of capacitive and inductive loads, respectively.

D.2.2.2. π-type:

The primary limitation of the L-type network is that it can only tune in one direction, for either a higher load impedance than the source, or a lower load impedance. The π

network solves this problem by joining two L networks together, overlapping at the inductor. This allows for matching the impedance of the load to the source regardless of whether the load impedance is greater or less than the source impedance. In this configuration the capacitors are called "input" and "output," where the input capacitor is placed on the source side of the inductor, and the output capacitor is placed on the load side. A schematic of a π network is shown below in Figure 153.
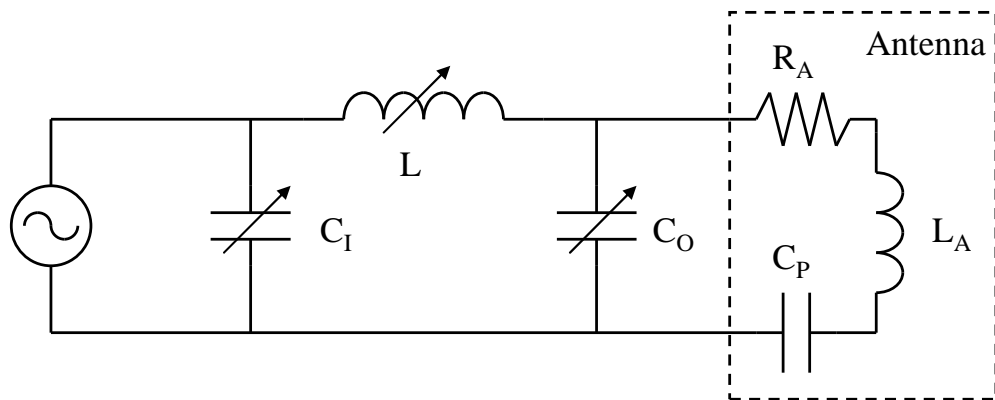
Figure 153. π-type matching network.

The flexibility of the π network can be seen by comparing it to an L network. While the L network matches the load to the source or vice versa, the π network tunes both impedances to some common point. Consider the π network circuit redrawn below in Figure 154 with the input and output capacitors grouped with the source and load, respectively, in parallel. This results in a series of three impedances: the equivalent impedance of the source, the impedance of the inductor, and the equivalent impedance of the load (in this case the antenna).
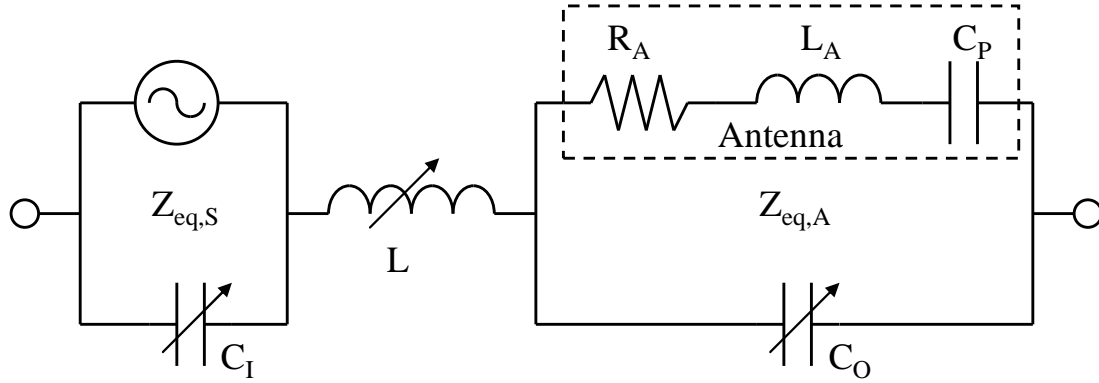
Figure 154. π network with equivalent impedances.

For convenience, the impedance of the antenna and the source can be written as

$$Z_A = R_A + iX_A$$

$$Z_S = R_S$$

The equivalent impedance can then be written as

$$\frac{1}{Z_{eq,S}} = \frac{1}{R_s} + \frac{1}{iX_{C,I}}$$

$$Z_{eq,S} = \frac{R_s X_{C,I}^2}{R_s^2 + X_{C,I}^2} + i\frac{R_s X_{C,I}^2}{R_s^2 + X_{C,I}^2} \qquad (D.65)$$

$$\frac{1}{Z_{eq,A}} = \frac{1}{R_A + iX_A} + \frac{1}{iX_{C,O}}$$

$$Z_{eq,A} = \frac{R_A X_{C,O}(X_A + X_{C,O}) - R_A X_A X_{C,O}}{R_A^2 + (X_A + X_{C,O})^2} + i\frac{R_A^2 X_{C,O} + X_A X_{C,O}(X_A + X_{C,O})}{R_A^2 + (X_A + X_{C,O})^2} \qquad (D.66)$$

The impedance matching requirement can be written as

$$Z_{eq,S} = Z_L + Z_{eq,A} \qquad \text{(D.67)}$$

Separating Equation (D.67) into the real and imaginary terms and substituting Equations (D.65) and (D.66),

$$\frac{R_s X_{C,I}^2}{R_s^2 + X_{C,I}^2} = \frac{R_A X_{C,O}(X_A + X_{C,O}) - R_A X_A X_{C,O}}{R_A^2 + (X_A + X_{C,O})^2} \qquad \text{(D.68)}$$

$$\frac{R_s X_{C,I}^2}{R_s^2 + X_{C,I}^2} = X_L + \frac{R_A^2 X_{C,O} + X_A X_{C,O}(X_A + X_{C,O})}{R_A^2 + (X_A + X_{C,O})^2} \qquad \text{(D.69)}$$

Thus the two capacitors tune the real component of the impedance of source and the antenna to each other, while the inductor serves to balance the imaginary component.

D.2.2.3. T-type:

While a π network can be thought of as two L networks joined at a common series inductor, a T network is analogous to two L networks sharing a common shunt capacitor. The goal of this configuration is similar to the π network, as it is capable of matching to either a higher or lower load impedance compared to the source. Figure 155 shows a circuit diagram of a T network.
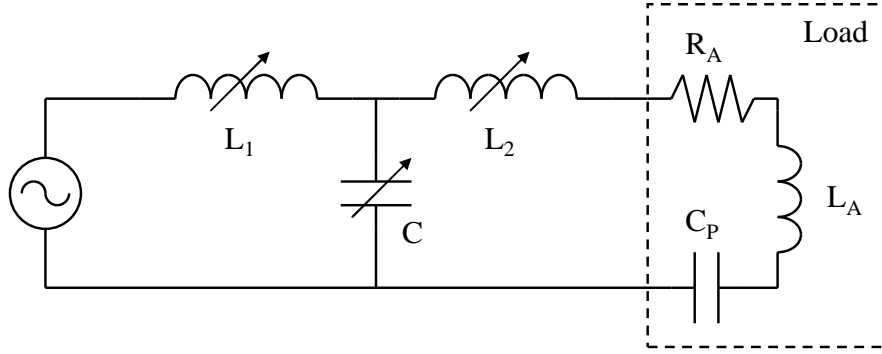
Figure 155. T-type matching network.

The equivalent impedance seen by the load is the series summation of the antenna reactance, the reactance from the second inductor, and the parallel combination of the capacitor and the first inductor in series with the source.

$$Z_{eq} = \left(\frac{1}{R_s + iX_{L,1}} + \frac{1}{iX_C} \right)^{-1} + i(X_{L,2} + X_A)$$

$$Z_{eq} = \left(\frac{-X_{L,1}X_C + iX_C R_S}{R_s + i(X_{L,1} + X_C)} \right) + i(X_{L,2} + X_A) \qquad (D.70)$$

Separating the terms into real and imaginary components,

$$\text{Re}(Z_{eq}) = \frac{R_S X_C^2}{R_S^2 + (X_{L,1} + X_C)^2} \qquad (D.71)$$

$$\text{Im}(Z_{eq}) = \frac{R_S^2 (X_C + X_{L,2} + X_A) - X_{L,1}X_C (X_{L,1} + X_C) + (X_{L,1} + X_C)^2 (X_{L,2} + X_A)}{R_S^2 + (X_{L,1} + X_C)^2} \qquad (D.72)$$

Since an ideal match occurs when the equivalent impedance is purely resistive and equal to the resistance of the load,

$$R_A = \frac{R_S X_C^2}{R_S^2 + \left(X_{L,1} + X_C\right)^2}$$ (D.73)

$$0 = R_S^2\left(X_C + X_{L,2} + X_A\right) - X_{L,1}X_C\left(X_{L,1} + X_C\right) + \left(X_{L,1} + X_C\right)^2\left(X_{L,2} + X_A\right)$$ (D.74)

In a T network the capacitor and the first inductor tune the real component of the impedance, while both inductors and the capacitor tune the imaginary component.

D.3 Antenna Connection

D.3.1 Antenna Types

While the matching network serves to maintain a uniform impedance throughout the RF system, there is an additional consideration in connecting to the load when the load is an antenna. Limiting the selection to those fed by two-conductor transmission lines, there are two types of antennas: monopole and dipole. Monopole antennas, often called aerials, are single lead antennas that use surrounding grounded surfaces as a signal return. Monopole antennas are commonly used in conjunction with unbalanced coaxial lines with the antenna connected to the center conductor. Dipole antennas, in contrast, are fed with a balanced transmission line with each conductor feeding a symmetric portion of the antenna. These segments can either be separate, as in the case of a simple dipole antenna, or connected, as in the case of a loop antenna. Examples of these antennas are shown in Figure 156.
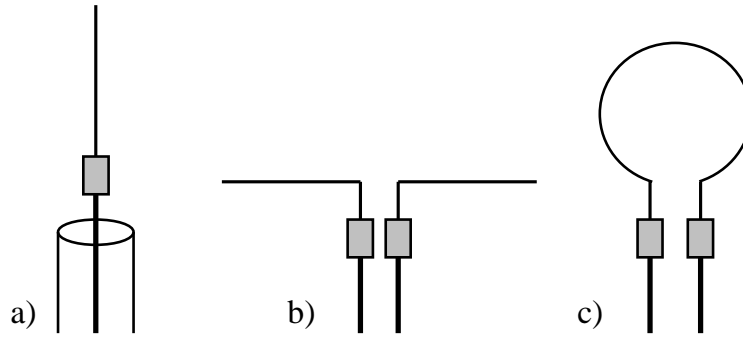
Figure 156. Sample antennas: (a) monopole antenna connected to coax line; (b) dipole and (c) loop antenna connected to balanced line.

The double saddle antenna used in the helicon plasma source is a dipole antenna, and thus normally would be fed with a balanced line. However, coaxial unbalanced lines offer several advantages over balanced lines. The first is that the coaxial lines contain the signal and do not have any near-field radiation. This is especially useful when connecting to an antenna that is part of a thruster, where conductive components would be placed in the near-field region of the line. If a balanced line was used, this could lead to the line radiating to the thruster components. Another benefit is coaxial lines can strongly constrain conductor separation without greatly limiting cable flexibility, which eases thruster and RF system design.

While feeding a dipole antenna with a coaxial transmission line is an attractive idea, it does create one problem. Generally when coaxial lines are used to feed an antenna, only the center conductor is used; however, a dipole antenna requires a connection to both conductors of the transmission line. This necessitates connecting one terminal of the antenna to the shield of the coax line. Discussion in Section D.1.3.2, however, noted that the wave propagating through the line passes only through an inner layer of the outer conductor. If the outer conductor is connected to one of the antenna terminals, this

326

creates a connection between the inner and outer layers of the outer conductor, allowing a portion of the antenna current to pass back along the outer conductor on the outer surface. This creates two problems - the first is that the antenna is now asymmetrically fed, as part of the current passing through the inner conductor is passed back along the outer layer of the conductor, rather than the antenna. The second problem is the outer conductor is now radiating and acts as a second broadcasting antenna. Both of these problems make it more difficult to effectively match the impedance, and causes non-uniform ionization within the helicon discharge and within the vacuum chamber as a whole.

D.3.2 Baluns

Despite the difficulties in feeding a dipole antenna with a coax transmission line, the benefits of using the more flexible coax line merit solving the issue rather than simply using a balanced line. The common solution to feeding dipole antennas with an unbalanced line is to include a balun between the coax line and the antenna. A balun converts a transmission line from balanced to unbalanced, (the name balun is derived from "**bal**anced to **un**balanced"). For this kind of application, there are two types of baluns that can be used: transformer and choke. Transformer baluns use a voltage transformer to create two output leads that have equal magnitude of potential from ground, though in opposite directions. A choke balun does not include a DC break, but instead adds a large inductive impedance on the outer conductor that suppresses the current passing along the outer layer of the outer conductor. Figure 157 shows a schematic of the problem, as well as the two solutions.
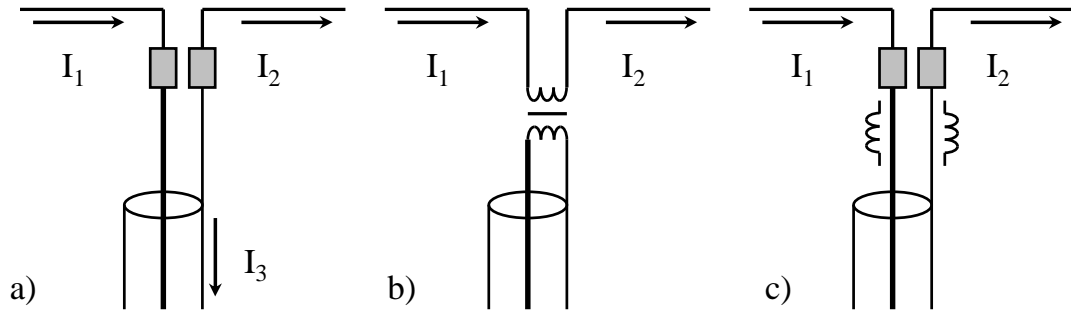
Figure 157. Dipole antenna connection to a unbalanced coax line. (a) Direction connection with contaminated outer conductor, (b) transformer balun connection, and (c) choke balun connection.

The most common form of a transformer balun is ferrite toroid with two windings, one for each transmission line. The number of turns in each winding is generally the same, although different turn counts can be used when a larger or smaller voltage is desired. Another feature of toroidal baluns is that it creates a DC break between the two lines. An alternative configuration that uses less winding material is an autotransformer balun. An autotransformer consists of a single winding around a ferrite rod where the center conductor of the unbalanced line is connected to one end of the coil along with one conductor of the balanced line. The other conductor is connected to the other end of the coil and the outer shield of the unbalanced line connects to a tap on the coil. The exact placement of the tap determines the relative voltage step of the transformer. Autotransformers do not have a DC break between the two transmission lines, but require fewer windings and can use a smaller ferrite core. In either configuration, if a 1:1 voltage ratio is used, the balun is referred to as a current balun, as the input and output currents are equal. Figure 158 shows both configurations of transformer baluns.
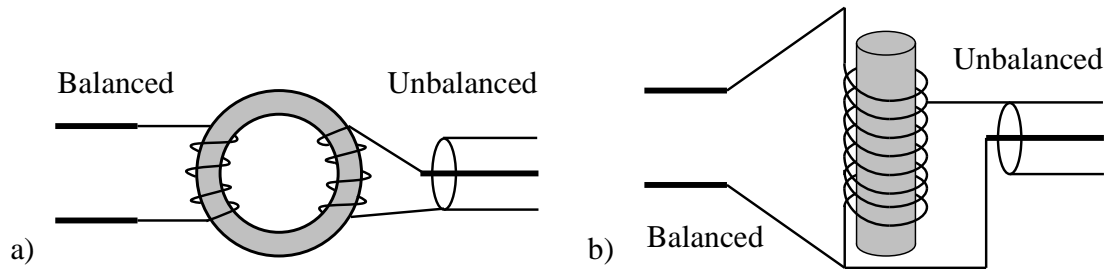
Figure 158. Transformer baluns. (a) 1:1 toroidal balun and (b) autotransformer balun.

Choke baluns differ from transformer baluns in that they do not fully create a balanced line where the voltage signal is equally carried between the two lines. Instead, a choke balun maintains the unbalanced voltage distribution and suppresses the current on the outer layer of the outer conductor by providing a large inductive impedance to RF signals. One of the most common approaches is to create an inductor out of the transmission line itself. If the length of the transmission line is large, the line can be wound into a coil around some insulating body to create an air-core inductor. If the transmission line length must be minimized, a more effective approach is to wind the line around a toroidal ferrite. Choke baluns are also referred to as current baluns, as the current through the balun is maintained. In general, about 1,000 Ω of impedance is recommended to effectively suppress the current on the outer shield.

D.3.3 Ferrite Selection

In both balun configurations the use of a ferrite core is either required or recommended for optimal performance. Hence, the selection of ferrite material is a key component to designing a balun. The defining characteristic of a ferrite material is the permeability, defined as

$$\mu = \frac{B}{H} \tag{D.75}$$

where B is the magnetic flux density, and H is the magnetic field intensity. The permeability can also be expressed in terms of the relative permeability, μ_r,

$$\mu = \mu_r \mu_0 \tag{D.76}$$

where μ_0 is the permeability of a vacuum. For some materials the permeability is effectively a scalar constant, but for ferromagnetic materials the permeability is a function of frequency and composition. At higher frequencies it is useful to consider permeability as a complex quantity,

$$\mu = \mu' + i\mu'' \tag{D.77}$$

where μ' denotes the inductive component and μ'' denotes the resistive loss component. Manufacturers often present the complex permeability in a plot of both components as a function of frequency, as shown in Figure 159. Using such a plot with a given frequency of operation, the values of the components of the complex permeability can be determined.
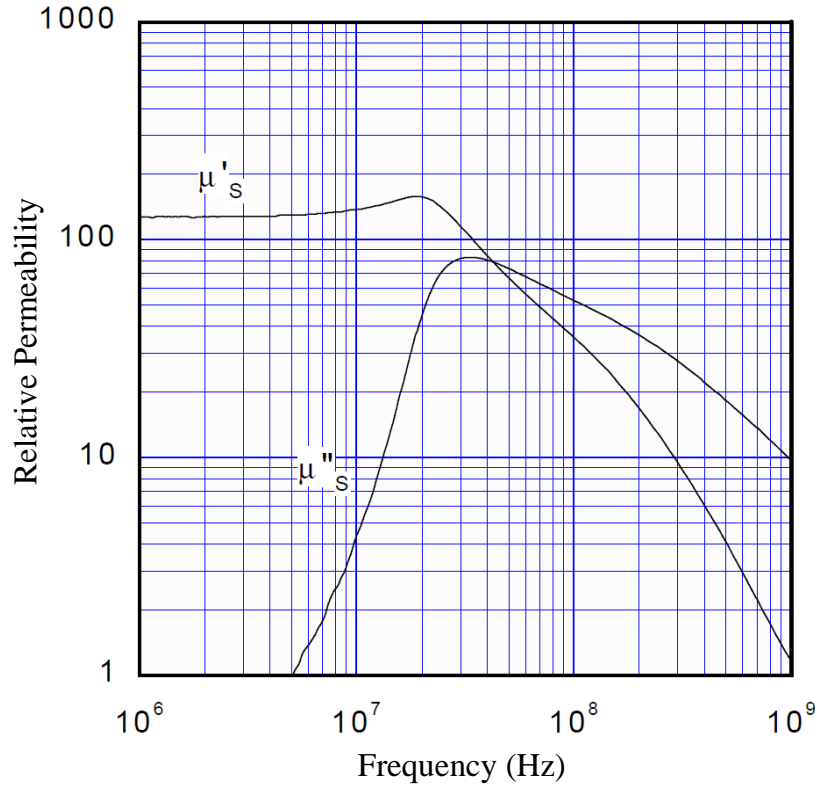
Figure 159. Complex permeability of type M NiZn ferrite.[87]

The other key selection parameter of a ferrite is the quality factor, Q, defined as

$$Q = \frac{X_L}{R} = \frac{\mu'}{\mu''}$$

(D.78)

where X_L is the inductive reactance and R is the resistance of the ferrite. The quality factor is a measure of how much of the applied impedance is lossless. A low quality factor implies much of the countering magnetic energy is dissipated through resistive heating. This is particularly important in vacuum applications where ferrites have negligible cooling. If the temperature of the ferrite exceeds the Curie temperature of the material, the material will transition from being ferromagnetic to paramagnetic. This

331

causes the effectiveness of the toroid to greatly diminish, effectively eliminating the balun of which it is a component of. Therefore it is desirable to have a ferrite that maximizes the quality factor.

The resultant design parameter of interest for the ferrite is the inductance, which for a toroid is given by

$$L = \frac{1}{2\pi} |\mu| N^2 H \ln\left(\frac{r_2}{r_1}\right)$$

(D.79)

where N is the number of turns around the toroid, H is the height, r_2 is the outer radius, and r_1 is the inner radius of the toroid. The magnitude of the permeability is

$$|\mu| = \sqrt{\mu'^2 + \mu''^2}$$

D.4 RF System Selection

The direct application of the previous sections is the design of the RF system. There are two figures of merit for the RF system: the power attenuation through the system and the directivity of transmission. Power attenuation is the loss of power through the system due to resistive losses, the primary cause of which is the transmission line. The directivity of RF transmission is primarily concerned with transmission from components other than the antenna. The directivity of the antenna itself is neglected, as the antenna is selected to match previous research that uses a double saddle antenna. The design

objective for the RF system is to minimize power attenuation and RF transmission from the line and other components.

D.4.1 Power Attenuation

The function of an RF power system in this application is to deliver an RF signal to an antenna which couples the RF power to the plasma. The two primary performance metrics of an RF system are the power attenuation from the source to the load (the plasma) and the amount of transmission from system components other than the antenna. The power attenuation is particularly important, as it decreases the effective power output of the RF system and the range of operating conditions available for testing. There are two sources of attenuation: resistive losses as the signal propagates through finite impedance, and reflective losses caused by mismatched impedances between components in the system. The latter is resolved through proper selection of components and the use of a matching network. The former can only be minimized by reducing the number of resistive components in the line. Generally, the largest contribution to attenuation is the transmission line itself.

The propagation constant is defined in Equation (D.23) in terms of real and imaginary components. The real component is called the attenuation constant and describes the resistive power loss through the line. In a loss-less line, where resistance and conductance are zero, the attenuation constant is zero. In an actual transmission line, resistance and shunt conductance are low, but non-zero. Furthermore, resistance increases with frequency, as the current only penetrates into the conductor a distance of skin depth. An estimate of the resistance per unit length of the center conductor of a coaxial transmission line is

$$R' = \frac{1}{d}\sqrt{\frac{f\mu}{\sigma\pi}} \tag{D.80}$$

where d is the diameter of the center conductor.

The attenuation constant for a realistic transmission line can be estimated by assuming that the transmission line is close to lossless, where $R'/\omega L' < 1$ and $G'/\omega C' < 1$. With this assumption, Equations (D.7) and (D.8) are substituted into Equation (D.23) and a first order Taylor expansion is used to simplify the radicands. Assuming $R'/L' > G'/C'$, the attenuation constant is

$$\alpha = \frac{R'}{2}\sqrt{\frac{C'}{L'}} = \frac{R'}{2Z_0} \tag{D.81}$$

where Z_0 is the characteristic impedance of the line. Substituting Equation (D.80) into Equation (D.81) yields

$$\alpha = \frac{1}{2dZ_0}\sqrt{\frac{f\mu}{\sigma\pi}} \tag{D.82}$$

This estimate of the attenuation constant only takes into account the resistance of the center conductor, and not the resistance of the outer shield, or dielectric losses of the line. As an example, at 10 MHz Equation (D.82) results in a line loss for RG-58/U of 0.67 dB per 100 feet. However, the documented loss for RG-58/U is 1.2 db per 100 feet. Despite this, Equation (D.82) demonstrates that even in the relatively low frequency range around

10 MHz, power attenuation from excessive cable length can be a non-negligible percentage of the transmitted power.

D.4.2 RF System Variants

Since the primary source of power dissipation is in the transmission line, one of the central design points for the system is the method for connecting the RF equipment to the antenna. There are three variants on the RF system that were developed that utilized different approaches to this transmission line connection. The first is designed around half-wavelength resonance, where a transmission line that is an odd number of half-wavelengths long does not contribute to impedance. The second minimizes the transmission line length and relocates the matching network inside the vacuum chamber. The third variant is a hybrid setup of the previous two, where the transmission line length is minimized, but the matching network remains outside of the vacuum chamber.

D.4.2.1 Resonant Line Configuration

The design methodology of the resonant line configuration is to attempt to remove the impedance of the transmission line between the matching network and the antenna. Normally when the matching network is separated from the antenna by a transmission line, the impedance of the line is added to the impedance of the load to be matched. The fixed line length for a given frequency requirement is imposed in order to create a resonating line that would make the line effectively lossless, thereby removing it from the impedance matching circuit.

There are three sections to the RF system: the source cabinet, the matching network, and the antenna. The source cabinet contains a Yaesu FT-540 HF transceiver to generate

the signal, connected with a 0.9 m RG-58 cable to an ACOM 2000A linear amplifier. Another 0.9 m length of RG-58 connects the output of the amplifier to the directional coupler of the LP-100A RF wattmeter, which measures the RF power transmitted and standing wave ratio (SWR) with an uncertainty of ±5% for power and ±0.05 for the SWR. The source cabinet is connected to the matching network with 8.1 m of RG-58. The matching network is a custom π-type consisting of two 7-1000 pF variable vacuum capacitors and a 1-35 μH variable inductor. Three Applied Motion OMHT17-075 stepper motors are remotely driven to vary the three components of the matching network. The matching network is connected to the chamber feedthrough by RG-393 of a variable length as set by the frequency. RG-393 is utilized for the higher maximum operating temperature (200 ℃ compared to 80 ℃ for RG-58). A final length of 5.3 m of RG-393 connects the interior side of the chamber feedthrough to the antenna. A schematic of the resonant line RF system is shown in Figure 160.
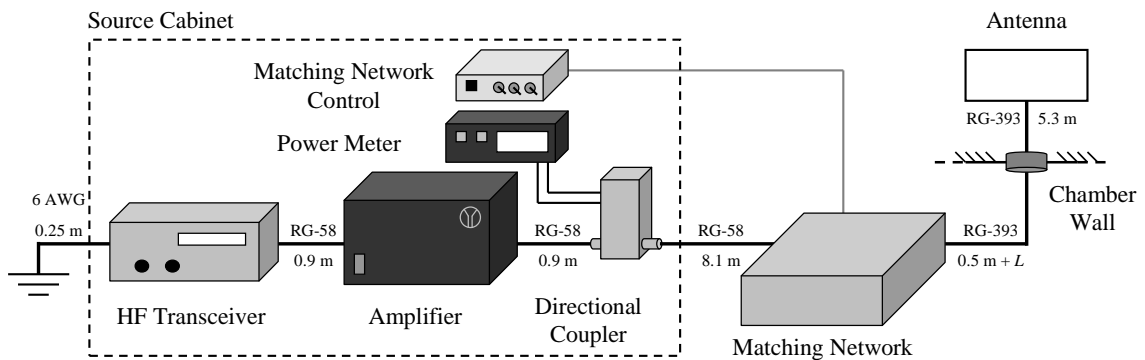
Figure 160. Resonant line RF system configuration schematic. L denotes variable cable length set by frequency, 8.3 m for 13.56 MHz.

The total length of the transmission line is dependent on the geometric restrictions of the distance between each section of the RF system and whether the resonant criterion is used for the line connecting the matching network and the antenna. The line lengths connecting the components from the transceiver to the matching network are due to the geometry of the RF cabinet and the vacuum chamber, the latter of which must be elevated above the ground to allow space for the diffusion pumps. Placement of the source cabinet on the ground below the chamber is necessary to minimize line length between the cabinet and the RF ground, which is a 1.3 cm diameter iron rod driven into the ground. The length of the transmission line from the matching network to the antenna is the section that is set by the resonant line condition. However, the line length inside the chamber of 5.3 m is the minimum necessary to reach from the feedthrough to the test setup. Therefore, the section of the transmission line where length can be varied by frequency is between the matching network and the feedthrough. There are two 0.25 cm segments attached to the feedthrough and the matching network output that terminate in N-type connectors. Between these two connections, additional cable of length L is placed to set the overall transmission line length. The resonant line condition for an operating frequency of 13.56 MHz using RG-393 requires a line length of 5.2 m for the first harmonic, which is not feasible due to geometric limitations inside the chamber. Therefore the next harmonic must be used, which uses $L = 8.3$ m of additional cable connected between the matching network and the feedthrough.

D.4.2.2 In-Vacuum Matching Network Configuration

The alternative design relocates the matching network inside the chamber. With the resonant line condition is removed, the transmission line between the matching network

337

and the antenna is again a part of the matching circuit. However, since the matching network is now located inside the chamber, this line length is reduced such that the impedance of the line is negligible compared with the load. This reduces the power attenuation caused by the transmission line and increases power transmitted into the plasma. This is called the in-vacuum RF system configuration, denoting the placement of the matching network inside the vacuum chamber.

Relocation of the matching network requires two modifications to the RF system. The first is to alter the grounding of the matching network circuit to prevent ground loops and the formation of a plasma discharge inside the network. The original circuit design grounded the shield of the coax line to the matching network chassis, where the low potential sides of the variable capacitors are also grounded. This is a sufficient configuration when the matching network is located outside of the vacuum chamber on a nonconductive surface, as the grounded chassis contains the RF signal. Inside the vacuum chamber, the low base pressure and the distance between the components and the chassis of approximately 4 cm allow the formation of a glow discharge at sufficiently high powers. The conductive chassis also creates ground loops either through contact with mounting hardware, or through ambient plasma generated from the helicon plasma source.

The solution to the ground loops and glow discharge formation is to isolate the matching circuit from the chassis and ground the chassis to the vacuum chamber. The low voltage terminals of the capacitors are connected to the shields of the input and output coax lines using 10 AWG wire insulated with fiberglass and mica. This eliminates the occurrence of generating a discharge between the matching network components and

the chassis, as well as eliminates ground loops between the matching network and the chamber. Figure 161 shows circuit diagrams of the two matching circuit designs.
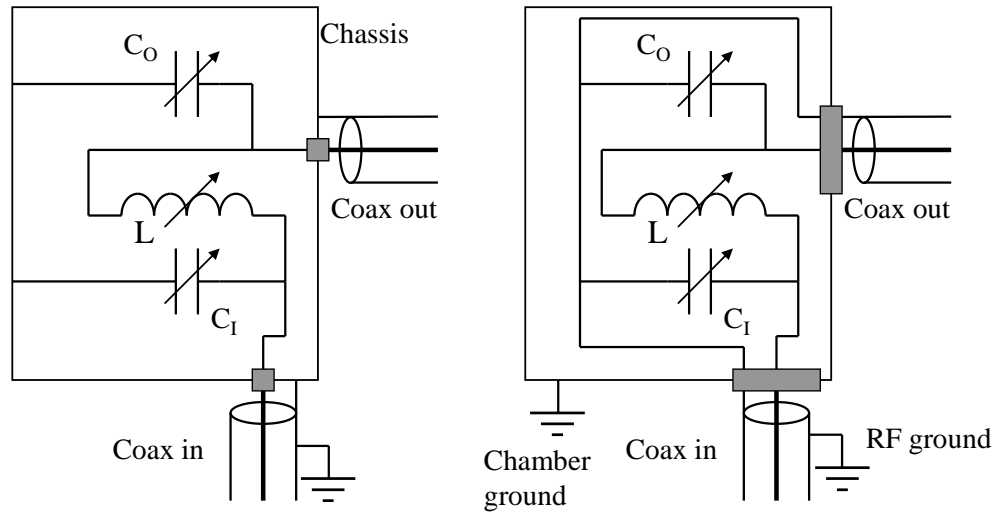
Figure 161. Matching network circuit for the resonant-line (*left*) and in-vacuum configuration (*right*).

The second modification required for the system is to the antenna connection. One result of using a coax line to connect to a loop antenna is that it causes the outer shield to broadcast the signal. In a coax line, the RF signal propagates between the inner conductor and the shield, but due to the skin depth effect only the inner surface of the shield carries the current. When a coax line is terminated at an antenna using the cable shield, the inner and outer surfaces are shorted, allowing a portion of the current to propagate along the outer surface of the shield. This can result in the cable broadcasting into the chamber and create a low density plasma discharge around the cable. The third current also unbalances the antenna and causes inhomogeneous power radiation along the antenna.

The first option for removing the outer shield current is to connect the matching network to the antenna with a balanced line. This method is undesirable, as the presence of conductive surfaces in the near-field region of a balanced line would inhibit proper coupling of the RF power into the plasma. An alternative approach is to use a choke balun to add impedance along the outer surface of the coax line and inhibit the exterior current, discussed previously in Section D.3.2. Some choke baluns are constructed by simply winding the transmission line into a coil to create the inductive impedance, but a more effective approach that minimizes line length is to pass the line through ferrite toroids, discussed in Section D.3.3.

The goal is for the choke to have at least 1,000 Ω of impedance. For the frequency of interest, 13.56 MHz, the optimal material is NiZn type M ferrites from National Magnetics Group. Due to the stiffness of the RG-393, only two turns through the choke is possible. Therefore in order to achieve the necessary impedance, sixteen toroids are used in series with an outer diameter of 8.73 cm, an inner diameter of 4.45 cm, a height of 1.25 cm, and a quality factor of 37.5. The total impedance of the choke is 1,020 Ω. The total length of coax cable from the matching network to the antenna, including the turn in the choke balun, is 2.1 m. Figure 162 shows the schematic of the in-vacuum RF system.
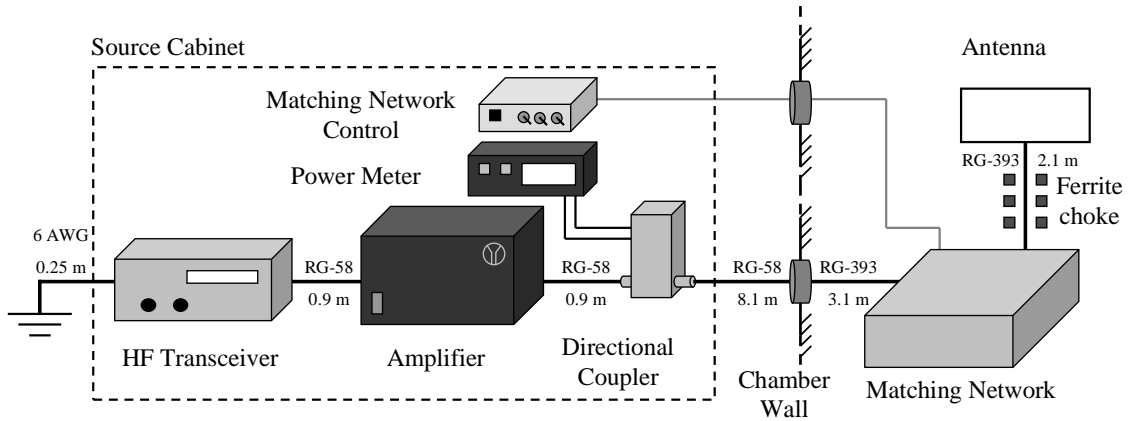
Figure 162. In-vacuum matching network RF system configuration schematic.

D.4.2.3 Minimized External Configuration

One of the primary drawbacks to the in-vacuum configuration is that the matching network does not have any external cooling. For standard operating at low power and SWR the vacuum-rated components can handle the thermal loading. However, during testing of various operating conditions which call for extensive cycling where the power and SWR spike during GHIT operation, the lack of cooling can lead to component damage. In particular, the N-type connector at signal input into the matching network is prone to failure in this configuration. Degradation of this component generally appears as an unsteady SWR during operation, which can start as small perturbations of ± 0.04 and over time increase to ± 0.2, at which point the system cannot be tuned below an SWR of 2.0. A third RF system variant is designed to incorporate the short transmission line lengths of the in-vacuum configuration while preserving the exterior matching network of the resonant line configuration. This setup is called the minimized external configuration.

The minimized external configuration is essentially the resonant line configuration with the resonant line condition removed and the transmission line between the matching

network and the antenna reduced to only what is required to reach the antenna. The total transmission line length differs slightly between the in-vacuum and minimized configurations due to the location of the matching network outside of the vacuum chamber relative to the feedthrough. A schematic of the minimized external configuration is shown in Figure 163.
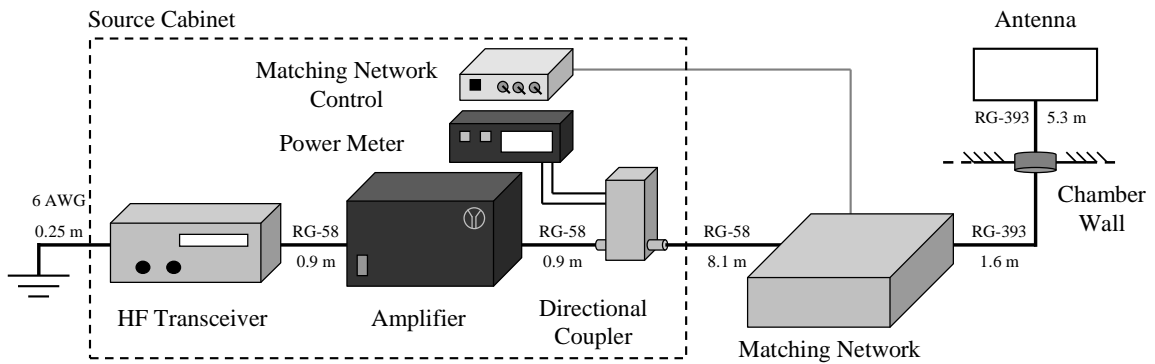
Figure 163. Minimized external RF system configuration schematic.

D.4.3 RF System Performance

The primary source of attenuation is the transmission line that connects the source cabinet to the antenna and the in-line matching network. Therefore power attenuation is measured between the location of the directional coupler inside the source cabinet and the antenna. The antenna is replaced with a 50 Ω dummy load and the system is tuned to a SWR of 1.02 or below. The forward power at a fixed source output is first measured at the source by the LP-100A. The power at the load is then measured by relocating the directional coupler to immediately before the dummy load and running the system at the exact same condition. Attenuation is measured using the procedure outlined in Section D.1.5, which is plotted as a function of SWR for all three variants in Figure 164.
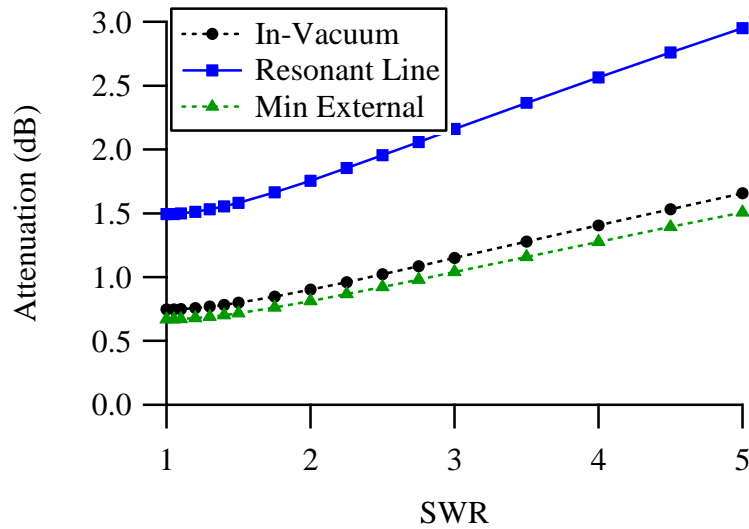
Figure 164. Power attenuation as a function of SWR and configuration.

Both the in-vacuum matching network and the minimized external configurations demonstrate a lower attenuation while at the same time reducing the length of transmission line necessary to complete the setup. The increase in power that is transmitted through the line at an SWR of 1.00 is approximately 13% of the power supplied by the source. This is an appreciable increase in power transmitted to the antenna and demonstrates that removal of the resonant line condition does not impair operation.

The justification for the resonant line condition was that the impedance of the line from the matching network to the antenna would be zero if the line length was an odd multiple of the wavelength. Thus, even a short transmission line would have greater impedance than resonant line. However, the resonant line condition assumes a lossless transmission line, which is not a practical assumption and ultimately the added line length of the resonant condition increases overall losses. Removal of the resonant line condition

also enables variation of the RF frequency over wide ranges without necessitating a change in transmission line length to avoid additional power attenuation.

The resonant line configuration was the first system developed, and is the design used during thrust testing of the helicon. Afterwards the RF system was redesigned with the two latter variants as possible options. Due to the previously mentioned difficulty with component longevity of the matching network inside the vacuum chamber, the minimized external configuration was selected for subsequent testing.

REFERENCES

[1] D. M. Goebel and I. Katz, *Fundamentals of Electric Propulsion: Ion and Hall Thrusters*, Jet Propulsion Laboratory Space Science and Technology Series, J. H. Yuen, Pasadena, CA, 2008.

[2] R. F. Boivin and E. E. Scime, "Control of Nitrogen Species in Helicon Plasmas," *Plasma Sources Science and Technology,* **14**, No. 2, pp. 283-292, 2005.

[3] F. F. Chen, "Plasma Ionization by Helicon Waves," *Plasma Physics and Controlled Fusion*, **33**, No. 4, pp. 339-364, 1991.

[4] F. F. Chen, *Helicon Plasma Sources*, in "High Density Plasma Sources," ed. Oleg A. Popov, Noyes Publications, Park Ridge, NJ, 1995.

[5] F. F. Chen, "Experiments on Helicon Plasma Sources," *Journal of Vacuum Science Technology*, **10**, No. 4, pp. 1389-1401, 1992.

[6] R. W. Boswell, "Very Efficient Plasma Generation by Whistler Waves Near the Lower Hybrid Frequency," *Plasma Physics and Controlled Fusion*, **26**, No. 10, pp. 1147-1162, 1984.

[7] A. W. Degeling, D. O. Jung, R. W. Boswell, and A. R. Ellingboe, "Plasma Production from Helicon Waves," *Physics of Plasmas*, **3**, No. 7, pp. 2788-2796, 1996.

[8] A. J. Perry, D. Vender, and R. W. Boswell, "The Application of the Helicon Source to Plasma Processing," *Journal of Vacuum Science Technology*, **9**, No. 2, pp. 310-317, 1991.

[9] A. W. Degeling, T. E. Sheridan, and R. W. Boswell, "Intense On-axis Plasma Production and Associated Relaxation Oscillations in a Large Volume Helicon Source," *Physics of Plasmas*, **6**, No. 9, pp. 3664-3673, 1999.

[10] T. Ziemba, *et al*, "High Power Helicon Thruster," *41st Joint Propulsion Conference and Exhibit*, July 2005, Tucson, Arizona, AIAA 2005-4119.

[11] C. Charles, "A Review of Recent Laboratory Double Layer Experiments," *Plasma Sources Science and Technology*, **16**, No. 4, 2007.

[12] C. Charles, *et al*, "Helicon Double Layer Thrusters," 29th *International Electric Propulsion Conference*, Princeton, NJ, 2005, IEPC-2005-290.

[13] C. Charles, R. W. Boswell, and M. A. Lieberman, "Xenon Ion Beam Characterization in a Helicon Double Layer Thruster," *Applied Physics Letters*, **89**, No. 26, 2006.

[14] M. D. West, C. Charles and R. W. Boswell, "Testing a Helicon Double Layer Thruster Immersed in a Space-Simulation Chamber," *Journal of Propulsion and Power*, **24**, No. 1, pp. 134-141, 2008.

[15] C. Charles and R. W. Boswell, "Current-Free Double-Layer Formation in a High-Density Helicon Discharge," *Applied Physics Letters*, **82**, No. 9, pp. 1356-1358, 2003.

[16] W. Cox, *et al*, "Spatial Retarding Field Energy Analyzer Measurements Downstream of a Helicon Double Layer Plasma," *Applied Physics Letters*, **93**, No. 7, 2008.

[17] J. Ling, *et al*, "Thrust Measurements in a Low-Magnetic Field High-Density Mode in the Helicon Double Layer Thruster," *Journal of Physics D: Applied Physics*, **43**, No. 30, 2010.

[18] K. Takahashi, *et al*, "Direct Thrust Measurement of a Permanent Magnet Helicon Double Layer Thruster," *Applied Physics Letters*, **98**, No. 14, 2011.

[19] S. Pottinger, *et al*, "Performance Characterization of a Helicon Double Layer Thruster Using Direct Thrust Measurements," *Journal of Applied Physics D,* **44**, No. 23, 2011.

[20] L. T. Williams and M. L. R. Walker, "Thrust Measurements of a Helicon Plasma Source," *AIAA/ASME/SAE/ASEE Joint Propulsion Conference & Exhibit*, San Diego CA, August 2011.

[21] Y. S. Hwang, I. S. Hong and G. S. Eom, "Conceptual Design of a Helicon Ion Source for High-Current DC Accelerators," *Review of Scientific Instruments*, **69**, No. 3, pp. 1344-1348, 1998.

[22] S. Mordyk, V. Miroshnichenko, D. Shulha and V. Storizhko, "Investigation of Helicon Ion Source Extraction Systems," *Review of Scientific Instruments*, **79**, No. 2, 2008.

[23] I. S. Hong, Y. S. Hwang, G. H. Lee, D. Y. Kim, H. Y. Won, G. S. Eom and W. Choe, "Ion-beam Characteristics of Novel Helicon Ion Sources for Different Plasma Parameters," *Review of Scientific Instruments*, **71**, No. 3, pp 1385-1388, 2000.

[24] B. Longmier, L. Cassady, M. Ballenger, M. Carter, F. Chang-Díaz, T. Glover, A. Ilin, G. McCaskill, C. Olsen, J. Squire, and E. Bering III, "VX-200 Magnetoplasma Thruster Performance Results Exceeding Fifty-Percent Thruster Efficiency," Journal of Propulsion and Power, AIAA, **27**, No. 4, pp. 915-920, 2011.

[25] B. W. Longmier, E. A. Bering III, M. D. Carter, L. D. Cassady, W. J. Chancery, F. R. Chang-Díaz, T. W. Glover, N. Hershkowitz, A. V. Ilin, G. E. McCaskill, C. S. Olsen, and J. P. Squire, "Ambipolar Ion Acceleration in an Expanding Magnetic Nozzle," *Plasma Sources Science and Technology*, **20**, No. 1, 2000.

[26] A. Shabshelowitz, "Study of RF Plasma Technology Applied to Air-Breathing Electric Propulsion," *Aerospace Engineering*, Ph.D. Dissertation, University of Michigan, Ann Arbor MI, 2013.

[27] M. M. Tsay and M. Martinez-Sanchez, "Simple Performance Modeling of a Radio-Frequency Ion Thruster," *30th International Electric Propulsion Conf.,* Florence, Italy, IEPC-2007-072, 2007.

[28] H. Bassner, R. Killinger, H. Leiter and J. Müller, "Development Steps of the RF-Ion Thrusters RIT," *27th International Electric Propulsion Conf.,* Pasadena, CA, IEPC-01-105, 2001.

[29] K. H. Groh and H. W. Loebt, "State-of-the-Art of Radio-Frequency Ion Thrusters," *Journal of Propulsion and Power*, **7**, No. 4, pp. 573-579, 1991.

[30] L. D. Cassady, W. J. Chancery, B. W. Longmier, C. Olsen, G. McCaskill, M. Carter, T. W. Glover, J. P. Squire, F. R. Chang-Díaz, and E. A. Bering III, "VASIMR Technologyical Advances and First Stage Performance Results," *45th AIAA Joint Propulsion Conference*, AIAA 2009-5362, Denver, CO, August 2-5, 2009.

[31] M. P. Reilly, "Three Dimensional Imaging of Helicon Wave Fields via Magnetic Induction Probes," *Nuclear Engineering*, Ph.D. Dissertation, University of Illinois, Urbana-Champaign IL, 2009.

[32] F. F. Chen, *Introduction to Plasma Physics and Controlled Fusion, Volume 1: Plasma Physics*, Second Edition, Springer Science, New York, 2006.

[33] M. Light and F. F. Chen, "Helicon Wave Excitation with Helical Antennas," *Physics of Plasmas*, **2**, No. 4, pp. 1084-1093, 1995.

[34] A. W. Degeling, N. Mikhelson, R. W. Boswell, and N. Sadeghi, "Characterization of Helicon Waves in a Magnetized Inductive Discharge," *Physics of Plasmas*, **5**, No. 3, pp. 572-579, 1998.

[35] S. Rauf, K. Bera, and K. Collins, "Self-consistent Simulation of Very High Frequency Capacitively Coupled Plasmas," *Plasma Sources Science and Technology*, **17**, No. 3, 2008.

[36] D. M. Franck, O. Grulke, and T. Klinger, "Mode Transitions in Helicon Discharges," *Physics of Plasmas*, **10**, No. 1, pp. 323-325, 2003.

[37] F. F. Chen, "RF Production of High Density Plasmas for Accelerators," *Laser and Particle Beams*, **7**, No. 3, pp. 551-559, 1989.

[38] F. F. Chen, "Landau Damping of Helicon Waves," *Australian National University Report ANU-PRL IR 85/12*, unpublished, 1985.

[39] J. L. Kline, E. E. Scime, R. F. Boivin, A. M. Keesee, and X. Xun, "RF Absorption and Ion Heating in Helicon Sources," *Physical Review Letters*, **88**, No. 19, 2002.

[40] F. F. Chen and D. D. Blackwell, "Upper Limit to Landau Damping in Helicon Discharges," *Physical Review Letters*, **82**, No. 13, pp. 2677-2680, 1999.

[41] D. Arnush, "The Role of Trivelpiece-Gould Waves in Antenna Coupling to Helicon Waves," *Physics of Plasmas*, **7**, No. 7, pp. 3042-3050, 2000.

[42] J. D. Kraus, and K. R. Carver, *Electromagnetics*, 2nd Edition, McGraw-Hill, pp. 405-406, 1973, ISBN 0-07-035396-4.

[43] A. W. Trivelpiece and R. W. Gould, "Space Charge Waves in Cylindrical Plasma Columns," *Journal of Applied Physics*, **30**, No. 11, pp. 1784-1793, 1959.

[44] K. P. Shamrai, and V. B. Taranov, "Resonances and Anti-resonances of a Plasma Column in a Helicon Plasma Source," *Physics Letters A*, **204**, No. 2, pp. 139-145, 1995.

[45] K. P. Shamrai, and V. B. Taranov, "Volume and Surface RF Power Absorption in a Helicon Plasma Source," *Plasma Sources Science and Technology*, **5**, No. 3, pp. 474-491, 1996.

[46] K. P. Shamrai, and V. B. Taranov, "Resonance Wave Discharge and Collisional Energy Absorption in a Helicon Plasma Source," *Plasma Physics and Controlled Fusion*, **36**, No. 11, pp. 1719-1735, 1994.

[47] J. G. Andrews and J. E. Allen, "Theory of a Double Sheath Between Two Plasmas," *Proceeds of the Royal Society of London, Series A"*, **320**, pp. 459-472, 1971.

[48] D. A. Herman, "The Use of Electrostatic Probes to Characterize the Discharge Plasma Structure and Identify Discharge Cathode Erosion Mechanisms in Ring-Cusp Ion Thrusters," *Aerospace Engineering*, Ph.D. Dissertation, University of Michigan, Ann Arbor MI, 2005.

[49] M. M. Balkey, R. Boivin, J. L. Kline, and E. E. Scime, "Ion Heating and Density Production in Helicon Sources near the Lower Hybrid Frequency," Plasma Sources Science and Technology, **10**, No. 2, 2001, pp. 284-294.

[50] B. E. Cherrington, "The Use of Electrostatic Probes for Plasma Diagnostics-A Review," *Plasma Chemistry and Plasma Processing,* **2**, No. 2, pp. 113-140, 1982.

[51] D. M. Goebel, (private communication, 2012).

[52] G. Aston, H. R. Kaufman, and P. J. Wilbur, "Ion Beam Divergence Characteristics of Two-Grid Accelerator Systems," *AIAA Journal,* **16**, No. 5, pp. 516-524, 1978.

[53] G. G. Raju, "Electron-atom Collision Cross Sections in Argon: An Analsys and Comments," *IEEE Transactions on Dielectrics and Electrical Insulation*, **11**, No. 4, pp. 649-673, 2004.

[54] I. Katz, B. M. Gardner, M. J. Mandell, G. A. Jongeward, M. Patterson, and R. M. Myers, "Model of Plasma Contactor Performance," *Journal of Spacecraft and Rockets*, **34**, No. 6, pp. 824-828, 1997.

[55] K. Chi, T. E. Sheridan, and R. W. Boswell, "Resonant Cavity Modes of a Bounded Helicon Discharge," *Plasma Sources Science and Technology*, **8**, No. 3, pp. 421-431, 1999.

[56] *Vacuum Measurement*, Varian, Inc., 2005, Available from: http://www.varianinc.com/cgi-bin/nav?products/vacuum/measure/index&cid=IPMHIKJQFO.

[57] MKS Product Specifications, *MKS 1179A Instruction Manual*, MKS Instruments, 2000, pp. 57.

[58] K. G. Xu amd M. L. R. Walker, "High-Power, Null-Type, Inverted Pendulum Thrust Stand," *Review of Scientific Instruments*, **80**, No. 5, 2009.

[59] D. H. Manzella and J. M. Sankovic, "Hall Thrusters Ion Beam Characterization," *31st AIAA Joint Propulsion Conference*, AIAA 95-2927, San Diego CA, July 10-12, 1995.

[60] D. L. Brown, "Investigation of Low Discharge Voltage Hall Thruster Characteristics and Evaluation of Loss Mechanisms," *Aerospace Engineering*, Ph.D. Dissertation, University of Michigan, Ann Arbor MI, 2009.

[61] M. L. R. Walker, R. R. Hofer, and A. D. Gallimore, "The Effects of Nude Faraday Probe Design and Vacuum Facility Backpressure on the Measured Ion Current Density Profile of Hall Thruster Plumes," *38th AIAA Joint Propulsion Conference*, AIAA 2002-4253, Indianapolis IN, July 7-10, 2002.

[62] R. R. Hofer, M. L. R. Walker, and A. D. Gallimore, "A Comparison of Nude and Collimated Faraday Probes for Use with Hall Thrusters," *27th International Electric Propulsion Conference*, IEPC-01-020, Pasadena CA, Oct. 15-19, 2001.

[63] L. S. Mason and R. S. Jankovsky, "1000 Hour of Testing on a 10 Kilowatt Hall Effect Thruster," *37th AIAA Joint Propulsion Conference*, AIAA 2001-3773, Salt Lake City, UT, July 8-11, 2001.

[64] K. Xu, "Ion Collimation and In-Channel Potentail Shaping Using In-Channel Electrodes for Hall Effect Thrusters," *Aerospace Engineering*, Ph.D. Dissertation, Georgia Institute of Technology, 2012.

[65] D. L. Brown and A. D. Gallimore, "Evaluation of Ion Collection Area in Faraday Probes," *Review of Scientific Instruments*, **81**, No. 6, 2010.

[66] H. D Hagstrum, "Auger Ejection of Electrons From Tungsten by Noble Gas Ions," *Physical Review*, **96**, No. 2, pp. 325-335, 1954.

[67] R. R. Hofer, "Development and Characterization of High-Efficiency, High Specific Impulse Xenon Hall Thrusters," *Aerospace Engineering*, Ph.D. Dissertation, University of Michigan, Ann Arbor MI, 2004.

[68] L. B. King, "Transport-Property and Mass Spectral Measurements in the Plasma Exhaust Plume of a Hall-Effect Space Propulsion System," *Aerospace Engineering*, Ph.D. Dissertation, University of Michigan, Ann Arbor MI, 1998.

[69] I. H. Hutchinson, *Principles of Plasma Diagnostics*, Cambridge: Cambridge University Press, 1987.

[70] Keithley Product Specifications, *Series 2400 Data Sheet*, Keithley Instruments Inc., pg 5.

[71] Keithley Product Specifications, *Model 6485 Picoammeter Instruction Manual*, Keithley Instruments Inc., pg A-2, 2001.

[72] Agilent Product Specifications, *Agilent 34970A/34972A Data Acquisition/Switch Unit Service Guide*, Third Edition, Agilent Technologies, pg 22, 2012.

[73] B. E. Beal and A. D. Gallimore, "Energy Analysis of a Hall Thruster Cluster," *28th International Electric Propulsion Conference,* Toulouse, France, March 17-21, 2003.

[74] N. Hershkowitz and M. H. Cho, "Measurement of Plasma Potential Using Collecting and Emitting Probes," *Journal of Vacuum Science and Technology A*, **6**, No. 3, 1988, pp. 2054-2059.

[75] R. F. Kemp and J. M. J. Sellen, "Plasma Potential Measurements by Electron Emissive Probes," *Review of Scientific Instruments*, **37**, No. 4, 1966, pp. 455.

[76] M. A. Makowski and G. A. Emmert, "New Method to Measure Plasma Potential with Emissive Probes," *Review of Scientific Instruments*, **54**, No. 7, 1983, pp. 830-836.

[77] J. Kang, R. N. Carlile, and J. F. O'Hanlon, "A Radio Frequency Compensated Emissive Probe," *Review of Scientific Instruments*, **67**, No. 5, 1996, pp. 1818-1821.

[78] L. A. Schwager, W. L. Hsu, and D. M. Tung, "Effects of Cold Electron Emission on the Plasma Sheath," *Physics of Fluids B: Plasma Physics*, **5**, No. 2, 1996, pp. 621-630.

[79] B. M. Reid, "The Influence of Neutral Flow Rate in the Operation of Hall Thrusters," *Aerospace Engineering*, Ph.D. Dissertation, University of Michigan, Ann Arbor MI, 2009.

[80] D. L. Brown, A. D. Gallimore, "Evaluation of Plume Divergence and Facility Effects on Far-Field Faraday Probe Current Density Profiles," *31st International Electric Propulsion Conference*, Ann Arbor, Michigan, September 20-24, 2009.

[81] A. Fruchtman, "Neutral Depletion in a Collisionless Plasma," *IEEE Transactions on Plasma Science*, **36**, No. 2, 2008, pp. 403-413.

[82] D. Arnush, "The Role of Trivelpiece-Gould Waves in Antenna Coupling to Helicon Waves," *Physics of Plasmas*, **7**, No. 7, 2000, pp. 3042-3050.

[83] G. G. Borg, and R. W. Boswell, "Power Coupling to Helicon and Trivelpiece-Gould Modes in Helicon Sources," *Physics of Plasmas*, **5**, No. 3, 1998, pp. 564-571.

[84] C. Cai, "Theoretical and Numerical Studies of Plume Flows in Vacuum Chambers," *Aerospace Engineering*, Ph.D. Dissertation, University of Michigan, Ann Arbor MI, 2005.

[85] S. Giannelli, A. W. Kieckhafer, M. L. R. Walker, "Neutral Gas Expansion in a Cylindrical Helicon Discharge Chamber," *Journal of Propulsion and Power*, accepted January 2013

[86] A. V. Phelps, "Cross Sections and Swarm Coefficients for Nitrogen Ions and Neutrals in N_2 and Argon Ions and Neutrals in Ar for Energies from 0.1 eV to 10 keV," *Journal of Physical and Chemical Reference Data*, **20**, No. 3, 1991, pp. 557-573.

[87] National Magnetics Group Inc., available from: http://www.magneticsgroup.com/pdf/M.pdf, downloaded on 5/11/12.